UNIVERSITY OF CALIFORNIA,
IRVINE

Synthesis and Reactivity of Transition Metal Complexes Bearing the Tridentate Bis(2-mercapto-*p*-tolyl)amine ([SNS]H_3) Ligand

DISSERTATION

submitted in partial satisfaction of the requirements
for the degree of

DOCTOR OF PHILOSOPHY

in Chemistry

by

Kyle Evan Rosenkoetter

Dissertation Committee:
Professor Alan F. Heyduk, Chair
Professor Andrew S. Borovik
Professor William J. Evans

2017

DEDICATION

To

My family and friends

TABLE OF CONTENTS

LIST OF FIGURES

LIST OF TABLES

LIST OF SCHEMES

LIST OF EQUATIONS

ACKNOWLEDGMENTS

I would like to thank my family, whose unfaltering support and encouragement throughout every stage of my life has gotten me to this point. Words cannot describe how thankful I am to have so much support from so many family members while pursing my Ph.D. at UCI. I would also like to thank all my friends, whose support and friendship has kept me sane for the past five years.

A very special thanks to my awesome advisor, Professor Alan Heyduk, for your mentorship and guidance over the past five years. The guidance you have given me has molded me into the scientist that I am today and has thoroughly prepared me for life after graduate school.

I'd also like to thank Professor Andy Borovik and Professor Bill Evans for serving on all my committees and being open to scientific discussions throughout the years. Special thanks to Professor Jenny Yang for scientific conversations about electrochemistry.

I'm grateful for the excellent facilities available at UCI and the people who maintain and run them. Thank you Dr. Joe Ziller, Dr. Phil Dennison, Dr. John Greaves, Dr. Dmitry Fishman, Dr. Beniam Berhane, and Dr. Nathan Crawford for all you do to ensure the availability of the tools needed for research to progress here at UCI. I'd also like to thank the Borovik group for allowing use of their EPR spectrometer, the Evans group for use of their elemental analysis instrument, and the Yang lab for use and modification of their bulk electrolysis cell.

Thank you to Dr. Joe Ziller, Dr. Jordan Corbey, Jason Jones, and Mikey Wojnar for the work you've done for me in the X-ray facility.

Thank you to past Heyduk group members who helped train me when I first joined the group; Dr. Aaron Hollas, Dr. Rui Munha, and Dr. Janice Wong. Thank you to all my current group members and special thanks to those who helped with dissertation edits; Mikey Wojnar, Claudia Ramirez, Jennifer Glancy-Logan, and Dr. Aaron Hollas.

The work described herein was supported by grants from the National Science Foundation.

CURRICULUM VITAE

Kyle Rosenkoetter

8213 Palo Verde Rd., Irvine, CA 92617 ■ Cell: (775) 843-0758 ■ k.rosenkoetter@gmail.com

Qualifications

Dedicated chemist combining excellent academic credentials with over seven years of research laboratory experience between two distinct universities. Excellent knowledge in air-free manipulations (Schlenk line, glove box, high vacuum line), characterization techniques (electrochemistry, NMR, EPR, UV-Vis, EA, X-ray diffraction, ESI-MS, GC-TCD), and laboratory equipment maintenance (vacuum pumps, glove boxes, HPLC, GC, ESI-MS). Well versed in laboratory safety regulations (OSHA and EH&S) as Laboratory Safety Officer for the past five years.

Education

University of California, Irvine – Irvine, CA 2012 – 2017

Doctor of Philosophy (Ph.D.) in Chemistry, 05/2017 (GPA: 3.87)

Advisor: Alan F. Heyduk, Ph.D.

Ph.D. Thesis: *Synthesis and Reactivity of Transition Metal Complexes Bearing the Tridentate Bis(2-mercapto-p-tolyl)amine ([SNS]H_3) Ligand*

University of Nevada, Reno – Reno, NV 2007 – 2011

Bachelor of Science in Chemistry with a Minor in Mathematics, 12/2011 (GPA: 3.35)

Advisor: Jason Shearer, Ph.D.

Senior Thesis: *Investigation into the changes of the coordination environment of Amyloid-Beta and ORP peptide fragments in the presence of Cu^{2+} and Zn^{2+} ions.*

Research Laboratory Experience

University of California, Irvine – Irvine, CA

Ph.D Candidate, Graduate Student Researcher, 8/2012 to Present

Advisor: Alan F. Heyduk, Ph.D.

Synthesis of heterobimetallic complexes involving the W[SNS]$_2$ metalloligand and group 10 metal phosphine adducts

- Synthesized and characterized a novel family of heterobimetallic complexes of the general formula W[SNS]$_2$M(L) (M = Ni, Pd, Pt; L = dppe, depe, dmpe, dppp, $P^{R'2}N^{R}P^{R'2}$ (R = phenyl, benzyl; R'=phenyl), dppf, or DPEphos) to investigate their electronic properties and effects of varying the Group 10 metal in addition to the ancillary phosphine ligand. Complexes were synthesized using rigorous air-free manipulations involving Schlenk-line, glove box, and high vacuum line techniques. Complexes were characterized using methods

involving X-ray diffraction, electrochemistry (cyclic voltammetry and differential pulse voltammetry), electronic absorption spectroscopy (UV-Vis), nuclear magnetic resonance (NMR), electron paramagnetic resonance (EPR), elemental analysis (EA), and mass spectroscopy (ESI/MS).

Electrochemical proton reduction using the W[SNS]$_2$Ni(dppe) heterobimetallic complex

- Catalytic ability of the complex was monitored through cyclic voltammetry whereby the addition of acid resulted in the observation of a catalytic reduction process coincident with the first reduction of the heterobimetallic complex. Controlled potential electrolysis confirmed that the complex electrochemically generates hydrogen at a Faradaic efficiency of 80 ± 3%. The quantification of H_2 was determined using gas chromatography equipped with a thermal conductivity detector (GC-TCD).

Metal exchange of the nickel center with other divalent first-row transition metal ions

- Investigated the electronic, magnetic, and structural effects observed with the interchanging of the nickel center with other first-row transition metal ions such as cobalt and copper.

Probing the reactivity of the [SNS] ligand through the formation of square-planar Ni^{II} complexes

- Synthesis of a novel set of square-planar nickel complexes that utilize the [SNS] ligand framework with tertiary phosphines (PPh_3 and PCy_3) to demonstrate the [SNS]H_3 ligand as redox, proton, and hydrogen atom non-innocent.

University of Nevada, Reno – Reno, NV

Undergraduate Student Researcher, 6/2009 to 4/2012

Advisor: Jason Shearer, Ph.D.

Synthesis and characterization of polypeptide fragments towards understanding metal uptake and folding patterns

- Synthesized various lengths of polypeptide chains that are known to cause folding in the Amyloid-Beta proteins and octarepeate domains (ORP) found in Alzheimer's patients. Studies consisted of probing the effects of coordination environments for uptake of Cu^{2+} and Zn^{2+} into these peptide fragments. Peptide sequences were synthesized using solid state peptide synthesis. Fragments were characterized and purified using ESI-MS and high performance liquid chromatography (HPLC).
- Synthesized common inorganic metal complexes that were used as blank studies for X-ray absorption spectroscopy (XAS/XANES) experiments which were performed at the synchrotron source at Brookhaven National Laboratory.

Presentations and Publications

- **Rosenkoetter, Kyle E.**; Ziller, Joe W.; Heyduk, Alan F., Heterobimetallic Complexes of Palladium and Platinum Containing a Redox-Active $W[SNS]_2$ Metalloligand. *Dalton Transactions **2017***, 46, 5503-5507.
- **Rosenkoetter, Kyle E.**; Ziller, Joe W.; Heyduk, Alan F., A Heterobimetallic W-Ni Complex Containing a Redox-Active $W[SNS]_2$ Metalloligand. *Inorganic Chemistry **2016**, 55, 6794-6798.*
- **Rosenkoetter, Kyle E.**; Heyduk, Alan F., Electrochemical proton reduction using a redox-active $W[SNS]_2$ cofactor tethered to a Ni center. 251st ACS National Meeting & Exposition, San Diego, California, March 13-17, **2016**, INOR-96. (Talk).
- **Rosenkoetter, Kyle E.**; Heyduk, Alan F., Synthesis of heterobimetallic complexes of Co, Ni, and Cu featuring the $W[SNS]_2$ redox active co-factor. 248th ACS National Meeting & Exposition, San Francisco, CA, United States, August 10-14, **2014**, INOR-547. (Talk).
- Shearer, J.; **Rosenkoetter, K. E.**; Callan, P. E.; Pham, C., One Octarepeate Expansion to the Human Prion Protein Alters Both the Zn^{2+} and Cu^{2+} Coordination Environments within the Octarepeate Domain. *Inorganic Chemistry* **2011**, *50* (4), 1173-1175.

Fellowship Awards

- UCI Regents' Dissertation Fellowship; Awarded in September 2016 to be utilized during Spring Quarter 2017
- NRC Research Associateship award at the Naval Air Warfare Center Weapons Division: Awarded May 4th, 2017

Teaching Experience

University of California, Irvine – Irvine, CA

Laboratory Safety Officer

- Maintained laboratory regulations (Cal OSHA and EH&S) through proper training, documentation, and handling of hazardous laboratory equipment and chemicals.

Advanced Inorganic Chemistry Laboratory Teaching Assistant

- Trained senior-level students in proper research level laboratory techniques including air-free manipulations using Schlenk-line, high vacuum line, and glove box techniques in order to synthesize and characterize classic inorganic metal complexes.

Discussion Leader for Advanced Inorganic Chemistry and General Chemistry

- Taught important chemistry problem solving skills to a range of students from entry- to senior-level chemistry courses.

General Chemistry Laboratory Teaching Assistant

- Trained entry-level students in proper laboratory principles and techniques involving electronic absorption spectroscopy, acid-base titrations, colligative properties, etc.

University of Nevada, Reno – Reno, NV
General Chemistry Laboratory Teaching Assistant

- As an undergraduate research assistant, I trained entry-level students in proper laboratory principles and techniques involving electronic absorption spectroscopy, acid-base titrations, colligative properties, etc.

Professional References

Dr. Alan F. Heyduk, Professor of Chemistry
University of California, Irvine, Department of Chemistry
E-mail: aheyduk@uci.edu
Office phone: (949) 824-8806

Dr. William J. Evans, Professor of Chemistry
University of California, Irvine, Department of Chemistry
E-mail: wevans@uci.edu
Office phone: (949) 824-5174

Dr. Andrew S. Borovik, Professor of Chemistry
University of California, Irvine, Department of Chemistry
E-mail: aborovik@uci.edu
Office phone: (949) 824-1510

Dr. Jason Shearer, Professor of Chemistry
University of Nevada, Reno, Department of Chemistry
E-mail: shearer@unr.edu
Office phone: (775) 784-7785

ABSTRACT OF THE DISSERTATION

Synthesis and Reactivity of Transition Metal Complexes Bearing the Tridentate Bis(2-mercapto-*p*-tolyl)amine ([SNS]H_3) Ligand

By

Kyle Evan Rosenkoetter

Doctor of Philosophy in Chemistry

University of California, Irvine, 2017

Professor Alan F. Heyduk, Chair

The work described herein focuses on the synthesis and characterization of new heterobimetallic complexes containing the redox-active W[SNS]$_2$ metalloligand and investigation into their electronic properties and reactivity. Most recent studies have explored the redox nature of the [SNS]H_3 scaffold through the synthesis and reactivity of a novel set of square-planar nickel complexes.

Chapters 2 and **3** describe a modular synthetic approach towards generating a new series of heterobimetallic complexes with the general formula W[SNS]$_2$M(L) ([SNS] = bis(2-mercapto-*p*-tolyl)amine; M = Ni, Pd, or Pt; and L = dppe, depe, dmpe, dppp, $P^{R'2}N^{R}P^{R'2}$ (R = phenyl, benzyl; R'=phenyl), DPEphos or dppf). The complexes were prepared by a salt metathesis of Cl_2M^{II}(L) with the previously reported W[SNS]$_2$ coordination complex under reducing conditions. X-ray diffraction analysis revealed interesting coordination geometries about the appended Group 10 metal centers moving from Pt and Pd (pseudo-square planar) to the first row Ni (pseudo-tetrahedral) analogue. These complexes demonstrate formal metal–metal bond formation across the series with a tunable first oxidation potential up to 600 mV.

Chapter 4 investigates the use of $W[SNS]_2Ni(dppe)$ as a catalyst for the electrochemical reduction of protons to hydrogen. This complex was found to catalytically generate hydrogen with an overpotential of 700 mV, a TOF of 14 sec^{-1}, and a Faradaic yield of 80 ± 3 % using 4-cyanoanilinium tetrafluoroborate in non-aqueous solutions.

Chapter 5 demonstrates the effect of exchanging the nickel center of the heterobimetallic complexes discussed in **Chapters 2** and **3** with other first row transitions metal ions (i.e. cobalt and copper). Analysis into the observed metal–metal distances reveal stark differences across the series. Additionally, the copper ion containing complexes demonstrate dynamic behavior in solution.

Chapter 6 investigates the synthesis and reactivity of a series of monomeric square-planar nickel complexes of the [SNS] scaffold to demonstrate the ligand as redox, proton, and hydrogen atom non-innocent.

Appendix A illustrates the electrochemical responses observed for the monoanionic complexes from **Chapter 6** in the presence of CO_2 and CO. **Appendices B** and **C** describe the synthesis and characterization of a five-coordinate cobalt and a heterotrimetallic tungsten-nickel complex, respectively.

Chapter 1

Introduction

Redox-Active Ligands

Ligand non-innocence was first termed in the 1960s to describe a unique set of ligands that when coordinated to a metal center introduce ambiguity into the oxidation state assignment.[1] Jørgensen described the concept of ligand non-innocence through the example of a nitrosyl ligand (NO) coordinated to a metal ion (**Scheme 1.1**) and concluded that the NO ligand could exist as a nitrosyl cation, a nitric oxide radical, or nitroxide anion.[1–3] This was determined through the use of ligand field theory and analyzing the atomic contributions of molecular orbitals of metal–nitrosyl complexes, which were determined to have a large amount of orbital mixing between energetically similar ligand and metal orbitals.[1–3] As a result, this mixing lead to the ambiguity observed in both the ligand and metal oxidation state assignments.[1–3] Recently, the widespread use of X-ray diffraction techniques has provided important structural information of metal–nitrosyl complexes, whereby the M–N–O bond angle revealed a direct correlation between the ligand oxidation state and the degree of angular distortion unique to the nitrosyl cation (~180°), nitric oxide radical (~145°), and nitroxide anion (~120°).[4] These bond angle distortions have allowed for less uncertainty in assigning metal oxidation state assignments of nitrosyl containing complexes.[4]

Scheme 1.1. Possible electronic arrangements for a metal-nitrosyl complex.

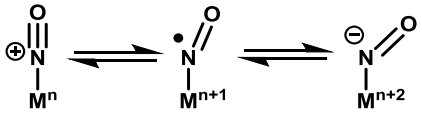

In the time leading to Jørgensen's analysis of nitrosyl ligands, early work by Harry Gray had begun to investigate square-planar cobalt and nickel centers supported by unsaturated bidentate sulfur containing ligands (**Scheme 1.2**).[5] Characterization of these dithiolene containing complexes initially reported the metal ion as a M^{IV} center supported by two dianionic thiolate ligands.[5–7] However, it was later determined that the metal was stabilized as a M^{II} ion supported

by two dithiolate radical anions.[5–7] Further evidence to support the redox-active nature of dithiolene ligands were demonstrated synthetically and electrochemically through isolation of the neutral, mono- and dianionic forms of the complexes.[5,8] In all cases, the ligand was observed to undergo well-defined ligand-centered redox activity maintaining a M^{II} metal oxidation state, illustrating that dithiolene ligands are redox non-innocent.[5,6,9,10]

Scheme 1.2. Redox activity of dithiolene complexes.[5,7]

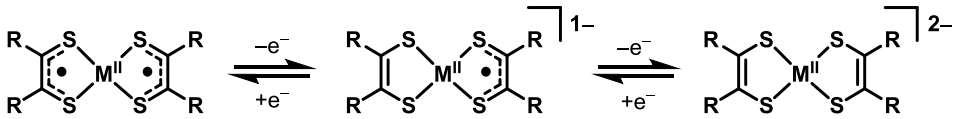

Of late, redox-active (non-innocent) ligands have come to describe any ligand capable of existing in multiple oxidation states when coordinated to a metal center.[9,11] Redox-active ligands have become increasingly prevalent in inorganic coordination chemistry over the last 50 years owing to their ability to act as electron mediators towards multi-electron transformations at earth abundant metal centers.[3,9] The widespread use of redox-active ligand scaffolds continue to grow as they form a broader range of multifunctional ligands that provide a variety of interesting and versatile approaches towards controlling the activity and selectivity of transition metal complexes towards small molecule activation.[9,12] The use of redox-active ligands in catalysis continues to expand as such ligands have been shown to act as an electron reservoir by accepting or donating electrons to a metal center for small molecule activation; actively participate in the cleavage or formation of covalent bonds; and relieve strain on the metal center as it undergoes redox changes.[12]

In catalysis, metal centered multi-electron transformations using precious metals (i.e. Pd and Pt) to initiate bond cleavage or bond formation is highly favored, however, their high cost and lack of abundancy has driven research towards studying earth-abundant metal centers supported by redox-active ligands.[9] A ligand capable of supplying equivalents of protons and electrons while supporting an electron poor metal center proves advantageous in catalysis as the metal ion can act

as a tunable redox center to maintain a low overpotential for small molecule activation.[13,14] Examples of this have been illustrated by Chirik and coworkers, who demonstrated that first-row transition metal centers once strictly hindered to single electron processes were able to perform multi-electron transformations similar to their second- and third-row analogs. This feat was achieved through a first-row transition metal ion supported by the [^{R}PDI] redox-active ligand, (**Scheme 1.3**, **c**) which conferred "nobility" to the base-metal center through metal-ligand cooperativity by providing electron equivalents from both the metal center and ligand scaffold.[6,9] Moreover, Berben *et. al.* further investigated the effects of coordinating a Lewis acidic Al^{III} metal ion to a variant of the [PDI] redox-active ligand (**Scheme 1.3**, **c**) to achieve proton reduction through ligand based transformations at a relatively low overpotential (500 mV) and high Faradaic yield (> 70%).[14] Similarly, our group has demonstrated the use of early transition metal centers (i.e. Ti, V, Zr, Ta) supported by the redox-active tetradentate $[N_2O_2]^{4-}$ (**Scheme 1.3**, **b**) and tridentate [^{iPr}NNN]$^{3-}$ (**Scheme 1.3**, **d**) scaffolds to leverage multi-electron transformations (i.e. nitrene transfer) through ligand-based redox changes.[15,16]

Scheme 1.3. Series of selected redox-active ligands.[1,5,6,10,14–17]

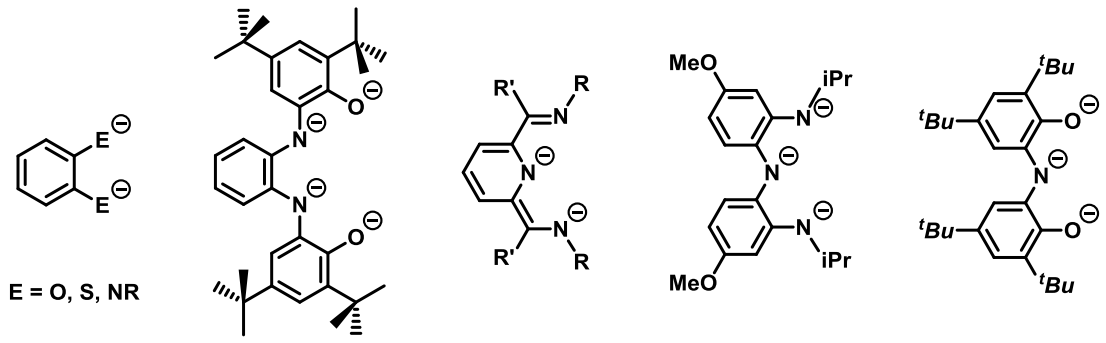

Of the redox-active ligands represented in **Scheme 1.3**, the tridentate N,N-bis(3,5-di-tert-butyl-2-phenoxide)amide ([ONO^{cat}]$^{3-}$, **Scheme 1.3**, **e**) scaffold has been among the most heavily studied

pincer-type ligand coordinated to transition metal centers.[15,18,19] The [ONO] ligand has been fully characterized in three oxidation states when coordinated to metal ions: (i) the fully-reduced catecholate trianion $[ONO^{cat}]^{3-}$; (ii) the dianionic, radical semiquinonate, $[ONO^{sq\bullet}]^{2-}$; and (iii) the monoanionic iminoquinonate, $[ONO^{q}]^{-}$. The accessible [ONO] redox states are best described through the sequential oxidation of $[ONO^{cat}]TaCl_2$ using iodobenzene dichloride. This reactivity demonstrates the redox ability of the [ONO] platform which adopts stable ligand based valence changes while the Ta^{V} center remains unchanged (**Scheme 1.4**). The electronegativity of oxygen allows for ligand oxidation to manifest itself through a carbon-based ligand radical and a contraction within the N–C bond of the ligand framework. Likewise, solid-state analyses reveal severe bond contraction in an O–C bond distance upon sequential oxidation of the ligand, consistent with the observance of localized double bond character ($[ONO^{q}]^{-}$).

Scheme 1.4. Example of [ONO]$TaCl_n$ complexes.[15]

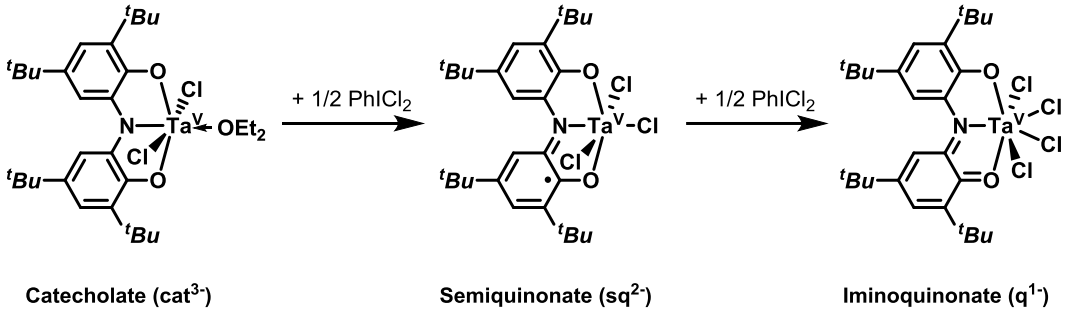

Metalloligands

A metalloligand can be formally defined as a metal complex capable of making additional bonds.[20,21] More specifically, a metalloligand is classified as a primary coordinated metal ion supported by a ligand system with which facile coordination of a secondary metal center is achieved through secondary donor sites.[20,22] The largest benefit of studying metalloligands is the ability to control the precise placement of functional groups to generate rigid frameworks that would otherwise be difficult to achieve with a flexible organic molecule.[20–22] Desirable attributes

for a metalloligand require that it offer additional binding sites and/or functional groups that can be utilized to either make a bond with a secondary metal ion or engage in other non-covalent interactions; be relatively rigid, with appended functional groups oriented in an ideal direction to allow for desirable coordination to a secondary metal center; and be stable and robust to withstand subsequent synthetic manipulations.[20,21]

A popular structural feature of metalloligands is a pair of cis-oriented thiolate donor atoms capable of bridging two metal species. Multimetallic sulfur-containing complexes are an interesting class of compounds that can serve as replicas for the active sites of metalloproteins (i.e. hydrogenase, nitrogenase, etc.).[23] Metal complexes containing coordinated sulfur groups have also been found to act as bridging ligands through their lone pairs which bind with a slightly greater σ-donating ability than harder nitrogen or oxygen donor ligands.[23–26] An example of this stems from metalloligands utilizing the Ni(N_2S_2) core, which comprises a square-planar nickel(II) center supported by a tetradentate ligand containing two amine and two thiolate donors.[27–29] The electron-rich nature of the d^8 nickel center and the cis-thiolate donors afford a strongly donating bidentate ligand that readily chelates low-valent W^0 and Pd^{II} metal centers.[28,29] Using the metalloligand approach in this case offered a unique method towards generating biological mimics of enzymatic active sites capable of performing CO addition/insertion reactions.[28,29]

Redox-Active Metalloligands

Saturation of the primary coordination sphere of a metal ion with electron rich donor atoms is an advantageous approach as it can act as a method in transforming coordination complexes into electron reservoir mimics. This allows these new systems to be capable of promoting the transfer or storage of electron equivalents for multi-electron transformations. In biological systems, these electron reservoirs usually consist of inorganic frameworks (ie. Fe-S clusters) that can undergo

redox changes, whereas in coordination chemistry their role can be fulfilled through the use of redox-active ligands.[15,30–32] While generating a metalloligand is beneficial, often the results include the formation of a sterically encumbered primary coordination sphere about the appended metal center, limiting the ability to perform inner-sphere reactivity.[33,34] Additionally, metalloligands often display electrochemical processes at highly negative reduction potentials (below −2 V, vs $Cp_2Fe^{0/+}$), limiting their practicality for small molecule activation.[33,34] To this end, extensive research has been done towards further tuning metalloligands through the incorporation of redox-active ligands.[18,35] Incorporating a ligand that can mediate both proton and electron transfer while coordinated to a positively charged Lewis acidic metal center can serve as a utility to shift the redox potentials of the species towards more positive potentials (anodically).[14] The isolation of these new systems offer an intesting strategy for the synthesis of multimetallic complexes with intriguing redox, electronic, and magnetic properties.[18,36,37]

Redox-active ligands (in both biology and catalysis) are desired for their ability to work in tandem with transition metal centers to facilitate multi-electron redox transformations and promote the activation and functionalization of small molecule substrates.[38] It is not only necessary to develop new redox-active ligand platforms but to incorporate them into binuclear systems based around affordable, earth-abundant transition metal centers. Tridentate pincer-type redox-active ligands have continued to receive increased attention over the past several years owing to their interesting electronic properties and their ability to act as electron reservoirs.[17,39–41] Additionally, their rigid ligand framework limits ligand dissociation pathways allowing for the generation of structurally robust metal complexes.[17]

Recently, our group has demonstrated that homoleptic $M[ONO]_2$ fragments can be utilized as building blocks for the preparation of multimetallic complexes.[18] Specifically, in an attempt to

isolate the reduction product of a monometallic Fe[ONO^{q}]Cl$_2$ species, the reaction afforded an iron-iron bimetallic complex consisting of a homoleptic Fe[ONO]$_2$ fragment chelated to a second five-coordinate iron center through μ_2 bridging of the phenolate moieties (**Scheme 1.5**).[18] Analysis of this bimetallic complex of the [ONO] scaffold demonstrated the ability to isolate a double mixed-valence complex consisting of two iron centers in different coordination geometries which proposes an alternative strategy for the synthesis of mulitmetallic systems embued with interesting redox and magnetic properties.[18,42]

Scheme 1.5. Synthesis of a diiron heterobimetallic complex utilizing Fe[ONO]$_2$ as a redox-active metalloligand.[18]

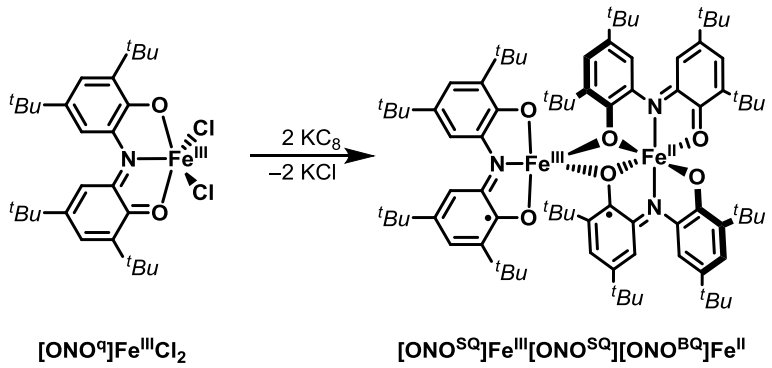

Despite the importance of sulfur-containing ligands in both biology and coordination chemisty, little investigation had been done towards generating new ligand scaffolds that exchange the hard oxygen donor atoms of the [ONO] scaffold for softer, more polarizable sulfur atoms.[17,43] The benefit of incorporating softer sulfur atoms into the ligand framework allow for a stabilizing effect of metal centers.[25] Therefore, isolation of a sulfur-containing analog to the heavily explored [ONO]H$_3$ ligand yielded the bis(2-mercapto-*p*-tolyl)amine ([SNS^{cat}]H$_3$) (**Scheme 1.6**).[17] Preparation of the ligand ([SNS]H$_3$) was performed through a four step synthesis, whereby the di-*p*-tolylamine precursor was brominated, benzyl-protected, and alkyl-lithiated to install the methyl-thioether arms in the ortho-positions. This is followed by a reduction under Birch conditions to yield the fully-reduced, triply protonated form of the ligand in high yields.[17]

Scheme 1.6. Synthesis of the $[SNS]H_3$ ligand scaffold.[17]

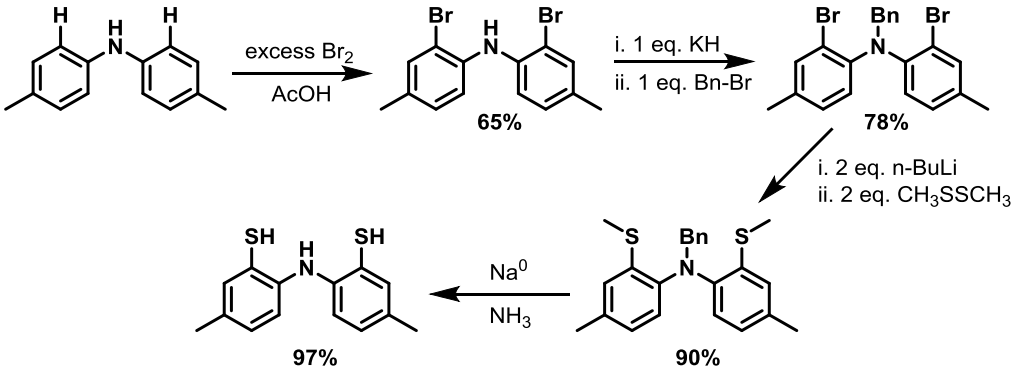

The installation of thiolate groups, which are ubiquitous in nature, offer duel functionality in coordination chemistry for their ability to act as chelating sites and to stabilize early transition metals in high oxidation states (i.e. W^{VI}, Mo^{VI}, etc.).[35,44–48] This in turn may allow tunable electronic and structural properties towards catalysis.[35,44–48] To this end, heating a toluene suspension of WCl_6 with $[SNS]H_3$ under a nitrogen atmosphere for 24 hours resulted in the isolation of a homoleptic $W[SNS]_2$ coordination complex in high yields (**Scheme 1.7**). The tungsten core is six-coordinate with a formal W^{VI} center supported by two fully-reduced, trianionic forms of the [SNS] ligand. The incorporation of two tridentate ligands saturate the tungsten ion and limit the extent of metal reactivity that can be studied, however, electrochemical characterization of this neutral tungsten monomer revealed two reversible, one-electron reductions at modest potentials of −0.61 and −1.55 V, vs $[Cp_2Fe]^{+/0}$, in THF. Using these accessible potentials, we hope to leverage the $W[SNS]_2$ synthon as a redox-active metalloligand through the appendage of secondary metal centers.

Scheme 1.7. Synthesis of the homoleptic $W[SNS]_2$ complex.

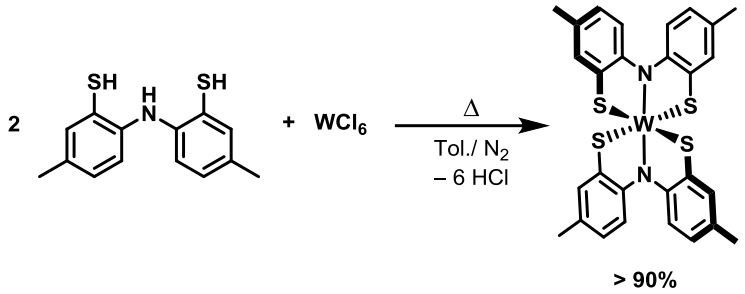

Dissertation Scope

Chapters 2 and **3** illustrate a modular synthetic approach to generating a series of heterobimetallic complexes with the general formula $W[SNS]_2M(P^{R2}R'P^{R2})$ ([SNS] = bis(2-mercapto-p-tolyl)amine; M = Ni, Pd, or Pt; and $P^{R2}R'P^{R2}$ = dppe, depe, dmpe, dppp, $P^{Ph2}N^{Ph}P^{Ph2}$, $P^{Ph2}N^{Bn}P^{Ph2}$, DPEphos, and dppf). **Chapter 4** investigates the use of $W[SNS]_2Ni(dppe)$ as a catalyst for the electrochemical reduction of protons to hydrogen in non-aqueous solutions. **Chapter 5** explores the effects of exchanging the nickel center of the heterobimetallic complex with other first-row transitions metal ions (i.e. cobalt and copper). **Chapter 6** investigates the synthesis and reactivity of a series of monomeric square-planar nickel complexes of the [SNS] ligand to demonstrate the ligand platform as redox, proton, and hydrogen atom non-innocent. **Appendix A** investigates the effects of small molecule substrates (i.e. CO and CO_2) on monoanionic complexes **16** and **17**, isolated in **Chapter 6**, under elctrochemical conditions. **Appendix B** and **C** describe the synthesis and characterization of a five-coordinate cobalt species ([SNS]Co(dppe)) and heterotrimetallic tungsten-nickel species ($W[SNS]_2[Ni(dppe)]_2$]), respectively.

References

(1) Jørgensen, C. K. *Coord. Chem. Rev.* **1966**, *1*, 164–178.
(2) Pierpont, C. G. *Coord. Chem. Rev.* **2001**, *216–217*, 99–125.
(3) Kaim, W.; Schwederski, B. *Coord. Chem. Rev.* **2010**, *254*, 1580–1588.
(4) Roncaroli, F.; Videla, M.; Slep, L. D.; Olabe, J. A. *Coord. Chem. Rev.* **2007**, *251*, 1903–

1930.
(5) Stiefel, E. I.; Waters, J. H.; Billig, E.; Gray, H. B. *J. Am. Chem. Soc.* **1965**, *87*, 3016–3017.
(6) Chirik, P. J.; Wieghardt, K. *Science (80-.).* **2010**, *327*, 794–795.
(7) Eisenberg, R.; Gray, H. B. *Inorg. Chem.* **2011**, *50*, 9741–9751.
(8) Schrauzer, G. N.; Mayweg, V. P. *J. Am. Chem. Soc.* **1965**, *87*, 1483–1489.
(9) Luca, O. R.; Crabtree, R. H. *Chem. Soc. Rev.* **2013**, *42*, 1440–1459.
(10) Sproules, S.; Wieghardt, K. *Coord. Chem. Rev.* **2010**, *254*, 1358–1382.
(11) Henthorn, J. T.; Lin, S.; Agapie, T. *J. Am. Chem. Soc.* **2015**, *137*, 1458–1464.
(12) Lyaskovskyy, V.; Bruin, B. De. **2012**.
(13) Warren, J. J.; Tronic, T. A.; Mayer, J. M. *Chem. Rev.* **2010**, *110*, 6961–7001.
(14) Thompson, E. J.; Berben, L. A. *Angew. Chemie Int. Ed.* **2015**, *54*, 11642–11646.
(15) Heyduk, A. F.; Zarkesh, R. a; Nguyen, A. I. *Inorg. Chem.* **2011**, *50*, 9849–9863.
(16) Blackmore, K. J.; Lal, N.; Ziller, J. W.; Heyduk, A. F. *J. Am. Chem. Soc.* **2008**, *130*, 2728–2729.
(17) Shaffer, D. W.; Szigethy, G.; Ziller, J. W.; Heyduk, A. F. *Inorg. Chem.* **2013**, *52*, 2110–2118.
(18) Wong, J. L.; Higgins, R. F.; Bhowmick, I.; Cao, D. X.; Szigethy, G.; Ziller, J. W.; Shores, M. P.; Heyduk, A. F. *Chem. Sci.* **2016**, *7*, 1594–1599.
(19) Szigethy, G.; Shaffer, D. W.; Heyduk, A. F. *Inorg. Chem.* **2012**, *51*, 12606–12618.
(20) Kumar, G.; Gupta, R. *Chem. Soc. Rev.* **2013**, *42*, 9403–9453.
(21) Srivastava, S.; Gupta, R. *CrystEngComm* **2016**, *18*, 9185–9208.
(22) Li, L.; Fanna, D. J.; Shepherd, N. D.; Lindoy, L. F.; Li, F. *J. Incl. Phenom. Macrocycl. Chem.* **2015**, *82*, 3–12.
(23) Forniés-Cámer, J.; Masdeu-Bultó, A. M.; Claver, C. *Inorg. Chem. Commun.* **2002**, *5*, 351–354.
(24) Lunsford, A. M.; Goldstein, K. F.; Cohan, M. A.; Denny, J. A.; Bhuvanesh, N.; Ding, S.; Hall, M. B.; Darensbourg, M. Y. *Dalt. Trans.* **2017**.
(25) Ding-Xue, K.; Poor, M.; Blinn, E. L.; Treichel, P. M. *Inorganica Chim. Acta* **1990**, *168*, 209–214.
(26) Yamada, Y.; Tsumita, M.; Hirano, A.; Miyashita, Y.; Fujisawa, K.; Okamoto, K. *Inorganica Chim. Acta* **2002**, *332*, 108–114.
(27) Hsiao, Y. M.; Chojnacki, S. S.; Hinton, P.; Reibenspies, J. H.; Darensbourg, M. Y. *Organometallics* **1993**, *12*, 870–875.
(28) Rampersad, M. V; Jeffery, S. P.; Golden, M. L.; Lee, J.; Reibenspies, J. H.; Darensbourg, D. J.; Darensbourg, M. Y. *J. Am. Chem. Soc.* **2005**, *127*, 17323–17334.
(29) Rampersad, M. V; Jeffery, S. P.; Reibenspies, J. H.; Ortiz, C. G.; Darensbourg, D. J.; Darensbourg, M. Y. *Angew. Chemie Int. Ed.* **2005**, *44*, 1217–1220.
(30) Girgis, A. Y.; Balch, A. L. *Inorg. Chem.* **1975**, *14*, 2724–2727.
(31) Choukroun, R.; Jaud, J.; Kalck, I. P.; Data, S. *Organometallics* **1986**, 67–71.
(32) Chaudhuri, P.; Hess, M.; Weyhermüller, T.; Wieghardt, K. *Angew. Chemie Int. Ed.* **1999**, *38*, 1095–1098.
(33) Tereniak, S. J.; Carlson, R. K.; Clouston, L. J.; Young, V. G.; Bill, E.; Maurice, R.; Chen, Y.-S.; Kim, H. J.; Gagliardi, L.; Lu, C. C. *J. Am. Chem. Soc.* **2014**, *136*, 1842–1855.
(34) Kuppuswamy, S.; Bezpalko, M. W.; Powers, T. M.; Wilding, M. J. T.; Brozek, C. K.; Foxman, B. M.; Thomas, C. M. *Chem. Sci.* **2014**, *5*, 1617.

(35) Bansal, D.; Hundal, G.; Gupta, R. *Eur. J. Inorg. Chem.* **2015**, *2015*, 1022–1032.
(36) Rosenkoetter, K. E.; Ziller, J. W.; Heyduk, A. F. *Inorg. Chem.* **2016**, *55*, 6794–6798.
(37) Rosenkoetter, K. E.; Ziller, J. W.; Heyduk, A. F. *Dalton Trans.* ***2017***, 46, 5503-5507.
(38) Bezpalko, M. W.; Foxman, B. M.; Thomas, C. M. *Inorg. Chem.* **2013**, *52*, 12329–12331.
(39) van der Vlugt, J. I.; Reek, J. N. H. *Angew. Chemie Int. Ed.* **2009**, *48*, 8832–8846.
(40) Gibson, V. C.; Redshaw, C.; Solan, G. A. *Chem. Rev.* **2007**, *107*, 1745–1776.
(41) Ivakhnenko, E. P.; Starikov, A. G.; Minkin, V. I.; Lyssenko, K. A.; Antipin, M. Y.; Simakov, V. I.; Korobov, M. S.; Borodkin, G. S.; Knyazev, P. A. *Inorg. Chem.* **2011**, *50*, 7022–7032.
(42) Robin, M. B.; Day, P. Radiochemistry, H. J. E. and A. G. S. B. T.-A. in I. C. and, Ed.; Academic Press, 1968; Vol. Volume 10, pp. 247–422.
(43) Burgess, B. K. *Chem. Rev.* **1990**, *90*, 1377–1406.
(44) Rauchfuss, T. B.; Roundhill, D. M. *J. Am. Chem. Soc.* **1975**, 3386–3392.
(45) Chatt, J.; Hart, F. A. *J. Chem. Soc.* **1953**, 2363–2371.
(46) DePamphilis, B. V; Averill, B. A.; Herskovitz, T.; Que, L.; Holm, R. H. *J. Am. Chem. Soc.* **1974**, *96*, 4159–4167.
(47) Darkwa, J. *Inorganica Chim. Acta* **1996**, *257*, 137–141.
(48) Verkade, J. G. *Inorg. Chem.* **1992**, *31*, 5331–5335.

Chapter 2

Heterobimetallic Complexes of Group 10 Metals

Containing a Redox-Active W[SNS]$_2$ Metalloligand

Portions of this work have been reported previously:

Rosenkoetter, Kyle E.; Ziller, Joe W.; Heyduk, Alan F., A Heterobimetallic W-Ni Complex Containing a Redox-Active W[SNS]$_2$ Metalloligand. *Inorganic Chemistry* ***2016****, 55, 6794-6798.*

Rosenkoetter, Kyle E.; Ziller, Joe W.; Heyduk, Alan F., Heterobimetallic Complexes of Palladium and Platinum Containing a Redox-Active W[SNS]$_2$ Metalloligand. *Dalton Transactions* ***2017****, 46, 5503-5507.*

Introduction

Heterobimetallic complexes play an integral role in biology and synthetic coordination chemistry.[1–3] In biology, metalloenzymes perform multielectron reactions such as proton reduction, nitrogen fixation, or water oxidation through the use of base metal bimetallic active sites with associated redox-active cofactors acting as an electron reservoir.[4–6] The active site bimetallic cores typically pair mid- and late-first row transition metal ions together imbuing metal centers with enhanced electronics and the ability to perform a diverse range of chemical reactions.[7–17] In coordination chemistry, a variety of synthetic ligand architectures have been used to support multimetallic complexes as structural and functional models for these types of metalloenzymes.[18–23] In particular, thiolate donor ligands have been particularly useful in the preparation of both structural and functional models for hydrogenase enzymes, where bimetallic active sites are often supported by bridging thiolate donor ligands.[24,25]

Investigation into heterobimetallic complexes that utilize metalloligand building blocks continues to grow in the field of coordination chemistry for their ability to bring together two different metal centers with disparate electronic properties and reactivities.[16] Often, the design strategies for accessing heterobimetallic structures rely on specialized ligand scaffolds that incorporate chemically distinct binding sites for each metal.[17,18,21,26–29] An alternative strategy is to utilize monometallic building blocks or metalloligands that can be bound to another metal fragment to generate a heterobimetallic structure.[30] The use of a metalloligand bound to a late-transition metal offers a distinctive method for generating innovative heterobimetallic complexes without the use of inherently complex ligand architectures.[21,27,28] **Scheme 2.1** illustrates different approaches investigated throughout the years towards generating heterobimetallic complexes by tailoring a ligand scaffold to accept a secondary metal center in a variety of coordination modes.

Scheme 2.1. Heterobimetallic complexes using different ligand design strategies.[16,17,28,31–33]

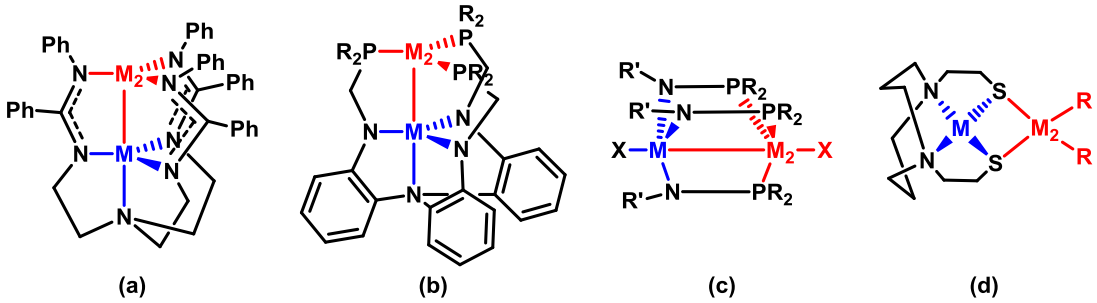

Continued efforts towards incorporating both early- and late-metal centers into heterobimetallic species has led to further understanding of the importance of metal–metal cooperativity and its effects on reactivity patterns.[17,27,28] The groups of Lu and Thomas have investigated these metal–metal interactions by utilizing ligand scaffolds that incoorperate either hepta-coordinate amino-[17] or phosphino-amido units (**Scheme 2.1**, a-c).[18,27,28,34,35] These types of frameworks are advantageous as the amide fragments can stabilize early-transition metal ions while the softer phosphine donors can stabilize late-transition metal ions. By enforcing the proximity between a nucleophilic late transition metal center with a more electrophilic early/mid transition metal, a polarization occurs within the complex and proves advantageous for small molecules activation.[36,37] Similarly, Darensbourg *et al*. has generated square-planar nickel(II) species that comprise a tetradentate ligand containing two amine and two thiolate donors, a Ni(N_2S_2) core (**Scheme 2.1**, d).[32,38,39] The electron-rich nature of the d^8 metal center and the cis-thiolate donors afford a strongly donating bidentate ligand that readily chelates to another metal center.[32,39]

The recent discovery of a diiron heterobimetallic complex consisting of a Fe[ONO]$_2$ metalloligand coordinated to a secondary Fe[ONO] fragment enticed our investigation towards exploiting the recently discovered W[SNS]$_2$ coordination complex towards similar heterobimetallic formation. The pair of cis-oriented thiolate donor atoms of the homoleptic

tungsten complex appear poised to accept a secondary metal center with ease. Herein we have developed a synthetic route towards obtaining heterobimetallic systems that leverage $W[SNS]_2$ as a metalloligand under reducing conditions to undergo a salt metathesis with $Cl_2M(dppe)$ species (M = Ni, Pd, and Pt).

Results and Discussion

Synthesis and Characterization of Complexes 1-3.

New heterobimetallic complexes of the general formula $W[SNS]_2M(dppe)$ (M = Ni (**1**), Pd (**2**), and Pt (**3**); dppe =1,2-bis(diphenylphosphino)ethane) were prepared via salt metathesis from $Cl_2M(dppe)$ and $W[SNS]_2$ (**Scheme 2.2**). To this end, reduction of $W[SNS]_2$ with two equivalents of potassium graphite (KC_8) in tetrahydrofuran (THF) at low temperatures afforded a maroon solution with a black precipitate (graphite) and a yellow hue around the rim. One equivalent of the desired $Cl_2M(dppe)$[40–43] complex was then added to the solution of the reduced tungsten synthon resulting in an immediate color change unique to the appended Group 10 metal fragment (Ni = brown; Pd = forest green; Pt = blue/green). Filtration of the reaction mixture to remove graphite (C_8) and potassium chloride (KCl) followed by concentration of the mother liquor and the addition of diethyl ether or pentane afforded $W[SNS]_2M(dppe)$ in high yields across the series (> 70%). Single crystals of each complex were obtained through slow diffusion of a concentrated analyte solution of THF (**1**) or CH_2Cl_2 (**2** and **3**) into pentane at room temperature.

Scheme 2.2. Synthesis of heterobimetallic complexes **1-3**.

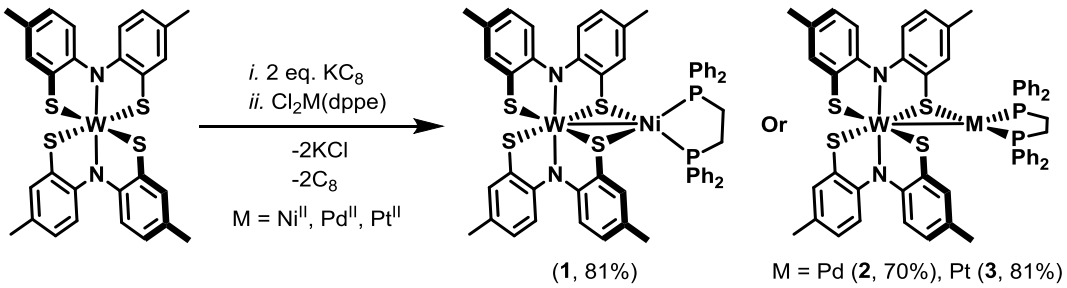

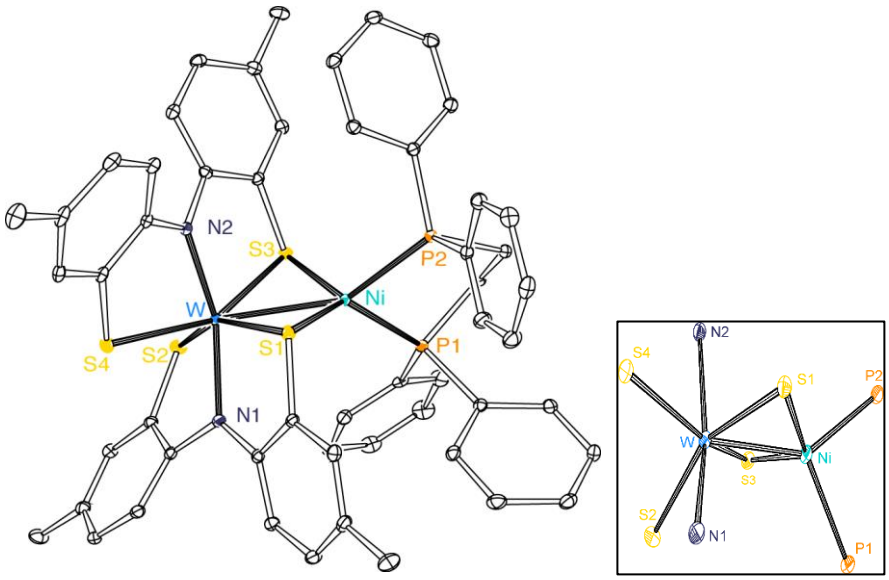

Figure 2.1. ORTEP diagram for complex **1** (Ni) with thermal ellipsoids shown at 50% probability. Hydrogen atoms have been omitted for clarity. Inset shows the geometry about the tungsten core.

X-ray diffraction studies on a single crystal of W[SNS]$_2$Ni(dppe) (**1**) revealed a bimetallic complex with a W−Ni bond supported by two bridging thiolate donors. **Figure 2.1** shows the structure of W[SNS]$_2$Ni(dppe) as an ORTEP diagram and a table of bond lengths and angles are provided in **Table 2.1**. The bimetallic complex can be described as a W[SNS]$_2$ unit bound as a chelating ligand to a Ni(dppe) fragment. The nickel center is four-coordinate (disregarding the W−Ni bond) with a pseudo-tetrahedral geometry comprising the two phosphine donors and two thiolates that bridge from the W[SNS]$_2$ cofactor. The P−Ni−P angle of 87.58° is consistent with the constricted bite angle of the dppe ligand. The Ni−P distances of 2.228 Å are longer than those typically observed for nickel(II) complexes of the dppe ligand.[40,44–46] In contrast, the Ni−S bond distances of 2.190 Å are shorter than those of nickel(II) complexes containing bridging thiolate ligands.[44–46] The W−Ni distance of 2.536(3) Å falls within the sum of the covalent radii of these two metal ions (tungsten, 1.62 Å; nickel, 1.24 Å)[47] consistent with the formation of a metal−metal bond. Previously reported examples of tungsten−nickel complexes containing a metal−metal bond were all found longer than that measured for W[SNS]$_2$Ni(dppe).[48] Within the W[SNS]$_2$ cofactor,

the W−S distances range from 2.365 to 2.433 Å, with the bridging thiolates falling between the two extremes represented by the nonbridging thiolates. These distances are similar to the average W−S distance of 2.367 Å in the neutral, isolated $W[SNS]_2$ complex.[49] The average W−N distance of 2.091 Å in the bimetallic complex is elongated slightly compared to the W−N distance observed for the $W[SNS]_2$ monomer (2.072 Å).

Descending the Group 10 metal series, solid-state structures of the heterobimetallic palladium and platinum congeners revealed a distorted square-planar geometry through the bonding to a distal thiolate of a single [SNS] ligand and a formal metal–metal interaction with the tungsten center of the metalloligand (**Figure 2.2**). The formal metal–metal interactions lie at distances of 2.837 and 2.832 Å for complexes **2** (Pd) and **3** (Pt), respectively. These interactions fall within the sum of the covalent radii tolerances for both metal combinations (tungsten, 1.62 Å; palladium, 1.39 Å; platinum, 1.36 Å).[47] The metal–metal bond of **2** (2.837 Å) is slightly elongated from a known W–Pd bond (2.831 Å),[50] while the metal–metal bond of **3** (2.832 Å) is slightly contracted from a known W–Pt containing complex (2.861 Å), both are consistent with the formation of a W–M single bond.[51] Complexes **2** and **3** reveal characteristic P–M–P bite angles of 86.30° for the dppe ligand.[52,53] Based on the average Pd–P distances of 2.300 Å, the complex appears similar to other Pd^{II}–phosphine lengths which range between 2.232–2.370 Å.[53–55] Similarly, the average Pt–P bond lengths (2.259 Å) correspond well with known Pt^{II}–phosphine bond distances ranging between 2.202 and 2.320 Å.[56–61] In contrast, a M^0–P bond distance would be expected to range from 2.330–2.350 Å.[62,63] A slight contraction in the M–S bond distances are observed going from Pd (2.323 Å) to Pt (2.314 Å), with a similar finding in the average M–P distances from 2.312 to 2.265 Å, respectively, consistent with the radii of the respective metal ions. With the structures being isomorphorous to one another, it is no surprise that only slight deviations in the M–S and

M–P bonds are observed. Within the $W[SNS]_2$ metalloligand cores of **2** and **3**, the W–S distances range from 2.360 to 2.460 Å, with the bridging thiolate establishing the upper limit in each case. These distances are similar to the average W–S distances in the neutral, isolated $W[SNS]_2$ complex (2.367 Å).[49] The average W–N distances of 2.091 Å are slightly elongated from the monomeric $W[SNS]_2$ (2.072 Å).

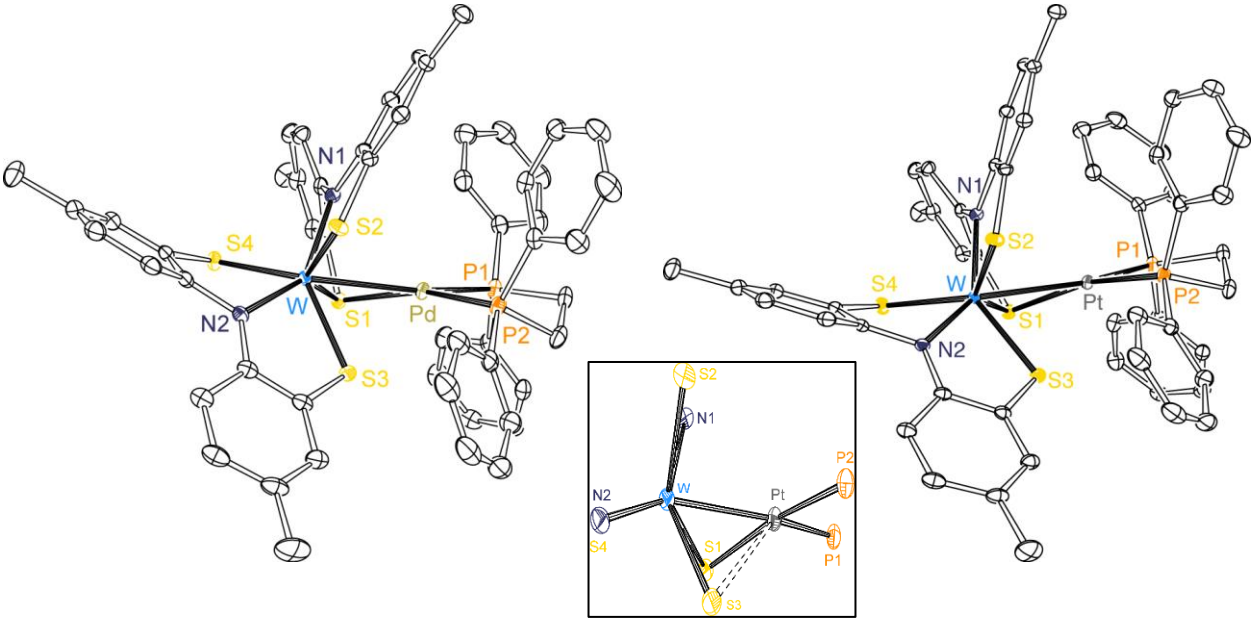

Figure 2.2. ORTEP diagrams for complexes **2** (Pd) and **3** (Pt) with thermal ellipsoids shown at 50% probability. Hydrogen atoms and a solvent molecule (CH_2Cl_2) have been omitted for clarity from both. Inset shows the geometry about the tungsten core.

Table 2.1. Selected bond lengths (Å) and angles (°) for complexes **1-3**.

	$W[SNS]_2Ni(dppe)$ (**1**)	$W[SNS]_2Pd(dppe)$ (**2**)	$W[SNS]_2Pt(dppe)$ (**3**)
	Bond Distances / Å		
W(1) – M(1)	2.5358(1)	2.8374(2)	2.83188(17)
W(1) – S(1)	2.3925(5)	2.4412(5)	2.4590(6)
W(1) – S(3)	2.4145(5)	2.3649(5)	2.3599(6)
M(1) – S(1)	2.1912(5)	2.3227(5)	2.3144(6)
M(1) – S(3)	2.1892(5)	2.8893(5)	2.9264(6)
M(1) – P(1)	2.2285(5)	2.2885(5)	2.2527(7)
M(1) – P(2)	2.2266(5)	2.3118(5)	2.2646(7)
	Bond Angles / °		
S(1) – W(1) – S(3)	102.280(16)	83.677(15)	84.96(2)
S(1) – M(1) – S(3)	117.413(19)	–	–
P(1) – M(1) – P(2)	87.586(19)	86.257(18)	86.30(2)
P(1) – M(1) – S(1)	132.40(2)	104.787(17)	104.13(2)
P(1) – M(1) – S(3)	98.897(19)	–	–
P(2) – M(1) – S(1)	104.092(19)	162.563(17)	163.85(2)
P(2) – M(1) – S(3)	112.43(2)	–	–
P(1) – M(1) – W(1)	125.790(16)	157.888(13)	157.857(18)
W(1) – S(1) – M(1)	67.008(14)	73.062(12)	72.707(17)
W(1) – M(1) – P(2)	145.960(16)	115.442(14)	115.336(18)
τ_4 value	0.78	0.28	0.27

The angular structural parameter (τ_4) is a common calculation based on solid-state metrics for four-coordinate metal centers established by Yang *et al*.[64] This value is used to illustrate the degree of distortion from an ideal geometry as an ideal tetrahedral coordination environment would yield a τ_4 value of 1.0 while a value of 0.0 is expected for an ideal square-planar coordination environment. To give insight into the distortion about the Group 10 metal ions, the structural parameter was calculated for each four-coordinate metal center (disregarding the W–Ni bond in **1**).[64] Using **Equation 2.1**, defining α and β as the two largest valence angles about the Group 10 metal center with θ as $\cos^{-1}(-1/3) = 109.5°$, τ_4 values of 0.78, 0.28, and 0.27 were calculated for complexes **1-3**, respectively, illustrating a degree of distortion from each of their ideal geometries.

$$\tau_4 = \frac{360° - (\alpha + \beta)}{360° - 2\theta} \qquad (\mathbf{2.1})$$

Lastly, the overall tungsten geometry of the $W[SNS]_2$ metalloligand in complexes **1-3** were found to lie between a trigonal prismatic and a trigonal antiprismatic geometry in all cases. The primary measurements of trigonal prismatic versus trigonal antiprismatic geometry is defined by the twist angle (θ) between opposite trigonal faces (**Figure 2.3**). In all complexes, two trigonal planes can be defined by the nitrogen and a single sulfur atom from one [SNS] ligand and a single sulfur atom from the other ligand (N(1)–S(1)–S(4) and N(2)–S(2)–S(3)), whereby the twist angle is then defined as the torsion angle between the vertices of the trigonal planes and the centroids of those planes.[49,65] A second metrical parameter used to determine the degree of distortion for trigonal systems is the prismatic compression, defined as the ratio of the prism height (h) to the average length of the trigonal face (s). An ideal trigonal prism demonstrates a twist angle, θ, of 0° with an s/h ratio of 1.00 while an ideal trigonal antiprism has a twist angle of 60° and a s/h ratio of 1.22.[65] **Table 2.2** demonstrates the values calculated for complexes **1**-**3**. Using this approach complex **1** displays a distorted trigonal antiprismatic geometry with an average twist angle of 30°, consistent with the observed prismatic compression of 1.16. On the other hand, complexes **2** and **3** appear to adopt a tungsten core best described as a trigonal prismatic geometry with twist angles less than 12° and prismatic compression ratios of 1.04.[49,65]

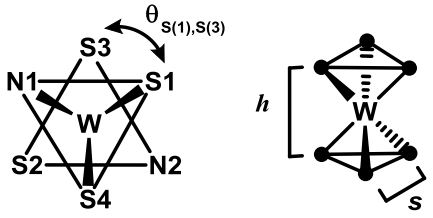

Figure 2.3. Diagrams of metrical parameters calculated for the $W[SNS]_2$ core of complexes **1-3**.[49,65]

Table 2.2. Additional measured and calculated metrical parameters for complexes **1-3**, as defined in **Figure 2.3**.

	$W[SNS]_2Ni(dppe)$ (**1**)	$W[SNS]_2Pd(dppe)$ (**2**)	$W[SNS]_2Pt(dppe)$ (**3**)
$\theta_{S4,N2}$	40.3°	3.2°	2.0°
$\theta_{S1,S3}$	13.1°	10.1°	11.4°
$\theta_{N1,S2}$	35.8°	10.6°	9.1°
s/h	1.16	1.04	1.04

Based on the observed bond metrics, two plausible metal oxidation state assignments can be made for the bimetallic $W[SNS]_2Ni(dppe)$ complex (**1**). The first plausible assignment would comprise tungsten(V) and nickel(I) centers, with the unpaired electrons on each metal center pairing to form the metal−metal bond and a diamagnetic ground state. The second plausible assignment would comprise tungsten(VI) and nickel(0) centers, with the metal−metal bond arising from a nickel→tungsten dative interaction.[66] A third alternative assignment, based on the oxidation states of the metal synthons, would be tungsten(IV) (from the doubly reduced $W[SNS]_2$ synthon) and nickel(II); however, two factors refute such an assignment. First, the geometry of the nickel center in $W[SNS]_2Ni(dppe)$ is inconsistent with a multitude of known nickel(II) diphosphine dithiolate complexes in which the nickel center adopts a square-planar geometry.[24,25] Second, the diamagnetism of $W[SNS]_2Ni(dppe)$ then would require a W−Ni double bond, which is unlikely because π interaction of a tungsten 5d orbital with a nickel 3d orbital would be expected to be weak.[67]

Similarly, three plausible metal oxidation state assignments can be made for the bimetallic palladium (**2**) and platinum (**3**) complexes. Based on the structural data, the [SNS] ligands of both **2** and **3** appear to remain in their fully-reduced, trianionic states and as such the possible oxidation state assignments for the metals are W^{IV}–M^{II}, W^{V}–M^{I}, or W^{VI}–M^{0}. Despite palladium and platinum having a high proclivity to remain M^0 or M^{II}, we favor the intermediate assignment in which the bridging thiolate acts as an L-type donor to tungsten and an X-type donor to palladium

or platinum. This assignment leaves one unpaired electron on each metal center capable of forming the formal metal–metal interaction observed in the solid-state.

Spectroscopic Characterization of Complexes 1-3.

The electronic structure of the heterobimetallic complexes were further investigated using electronic absorption spectroscopy (UV-vis). Dissolution of black crystals of $W[SNS]_2Ni(dppe)$ in THF afforded a dark-yellow/brown solution manifesting intense absorbance bands in the visible region at 436 nm (21,000 M^{-1} cm^{-1}) and 616 nm (7,100 M^{-1} cm^{-1}) (**Figure 2.4**). The palladium congener yielded three intense transitions at 381 nm (18,000 M^{-1} cm^{-1}), 430 nm (20,000 M^{-1} cm^{-1}), and 633 nm (14,000 M^{-1} cm^{-1}) while the third-row derivative, platinum, demonstrated two intense transitions at 414 nm (19,000 M^{-1} cm^{-1}) and 582 nm (14,000 M^{-1} cm^{-1}). All electronic absorption bands observed for complexes **1-3** are consistent with charge transfer transitions based upon their extinction coefficients ($\varepsilon > 10^4$ M^{-1} cm^{-1}, **Figure 2.4**, **Table 2.3**). The heavier metal analogs demonstrate a blue shift in their lowest-energy transition moving down the Periodic Table from 633 nm (15,800 cm^{-1}) for complex **2** to 582 nm (17,200 cm^{-1}) for complex **3**.

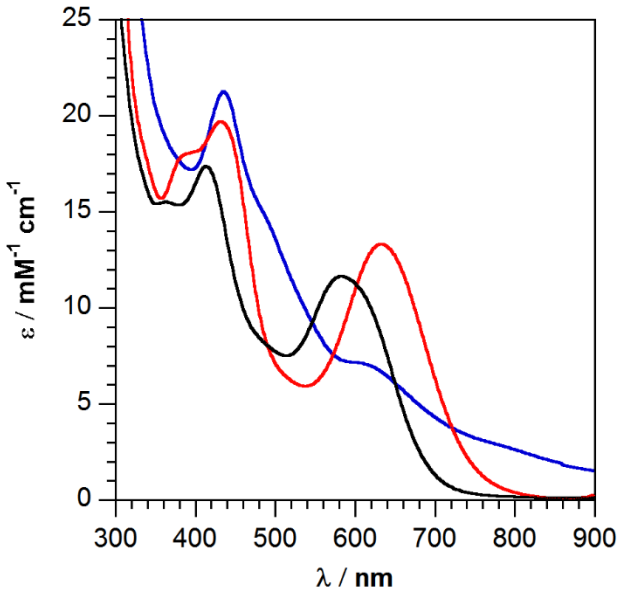

Figure 2.4. Electronic absorption spectra for complexes **1** (blue), **2** (red), and **3** (black) collected in THF.

Table 2.3. Spectroscopic data collected for complexes **1-3**.

	λ / nm (ε / $M^{-1}cm^{-1}$)[a]	**$^{31}P\{^{1}H\}$ NMR (ppm)[b]**
$W[SNS]_2Ni(dppe)$ (**1**) (blue)	436 (21,000), 616 (7,100)	49.8
$W[SNS]_2Pd(dppe)$ (**2**) (red)	381 (18,000), 430 (20,000), 633 (14,000)	56.6, 82.1
$W[SNS]_2Pt(dppe)$ (**3**) (black)	414 (19,000), 582 (14,000)	51.3, 81.4

[a]Collected in THF. [b]Collected in $CDCl_3$.

Nuclear magnetic resonance (NMR) revealed diamagnetic ground states for complexes **1-3**. The presence of the Ni(dppe) fragment was readily established in complex **1** by $^{31}P\{^{1}H\}$ NMR, which revealed a sharp singlet at 49.8 ppm, significantly shifted upfield from the $Cl_2Ni(dppe)$ starting complex (58 ppm). The characteristic proton resonances of the $W[SNS]_2$ fragment of **1** could be readily observed in the ^{1}H NMR spectrum through the observance of two sharp singlet resonances at 2.13 and 2.32 ppm. These resonances are consistent with the two inequivalent sets of methyl groups of the SNS ligands, indicative of reduced symmetry relative to the isolated $W[SNS]_2$ starting material. The methylene protons of the dppe ligand appear as a broad singlet at 2.55 ppm, indicating that the ligand backbone can flex in solution. Due to the asymmetry about the distorted square-planar cores of **2** and **3**, and lack of C_2 symmetry for the molecules, ^{1}H NMR spectroscopy yielded broad and complicated spectra for each complex. However, less ambiguity was observed in the $^{31}P\{^{1}H\}$ NMR, which support the asymmetric geometry of the complexes observed in the solid state. $^{31}P\{^{1}H\}$ NMR revealed a pair of doublets for palladium derivative **2** at 56.6 and 82.1 ppm displaying a $^{2}J_{PP}$ coupling constant of 123 Hz, concluding two chemically inequivalent phosphorous donor atoms in a cis-configuration.[68–70] Platinum derivative **3** appears as two triplet resonances centered at 51.3 ppm ($^{1}J_{PtP}$ = 4190 Hz) and 81.4 ppm ($^{1}J_{PtP}$ = 2950 Hz) with characteristic ^{195}Pt satellites giving coupling constants consistent with ^{195}Pt–^{31}P coupling. Because of the observed asymmetry in the $^{31}P\{^{1}H\}$ NMR, the rate of dynamic exchange between the cis-oriented phosphorus atoms in complex **2** were investigated using variable temperature (VT)

$^{31}P\{^{1}H\}$ NMR spectroscopy. Upon heating samples of **2** dissolved in tetrachloroethane-d_2 ($C_2D_2Cl_4$), the $^{31}P\{^{1}H\}$ NMR resonances broaden between 298 and 360 K, coalesce at 370 K, and continue to sharpen into a single resonance at 71.5 ppm at temperatures above 370 K (**Figure 2.5**). Holding the sample at these elevated temperatures for extended time periods resulted in some thermal decomposition as evidenced by the appearance of signals consistent with $Cl_2Pd(dppe)$ (64.3 ppm). Despite this minor decomposition, an analysis of the temperature dependence of the signals for **2** gave activation parameters of $\Delta H^{\ddagger} = 14.6 \pm 3$ kcal mol^{-1} and $\Delta S^{\ddagger} = -0.8$ cal K^{-1}mol^{-1} (**Figure 2.6, Eq 2.2**).[71,72] These values are consistent with an intramolecular process that equilibrates the two different phosphorous environments.[73,74] A possible mechanism for this equilibration would be an exchange of the Pd–S(1) bond for a Pd–S(3) bond (i.e., the palladium rocking back and forth between the two sulfur donors).

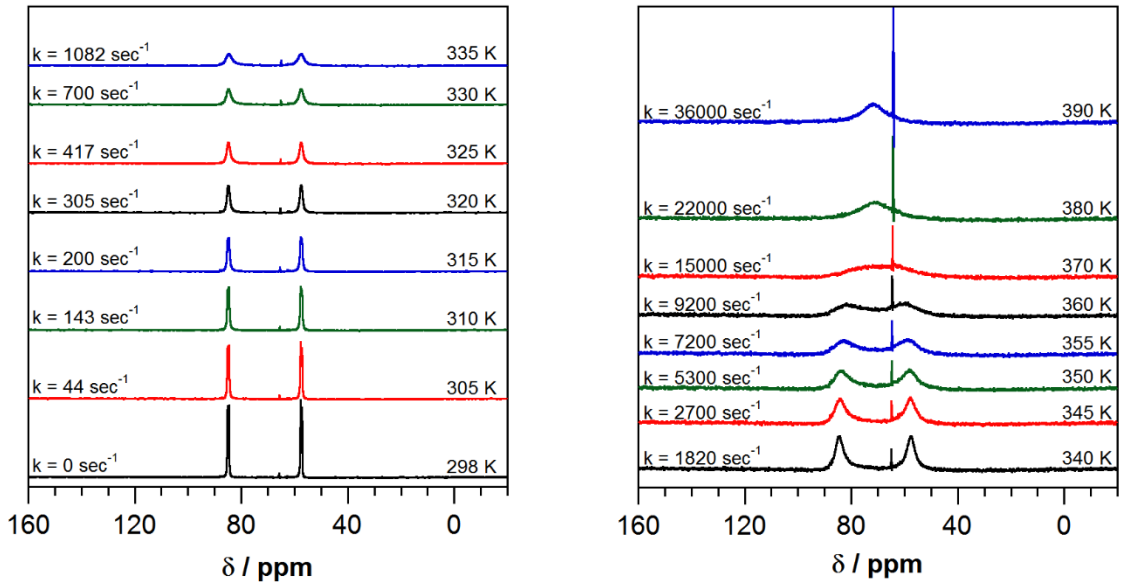

Figure 2.5. $^{31}P\{^{1}H\}$ VT NMR studies of complex **2** in tetrachloroethane-d_2 at elevated temperatures displaying thermal decomposition of **2** to $Cl_2Pd(dppe)$ with the growth of the signal at 64.3 ppm.

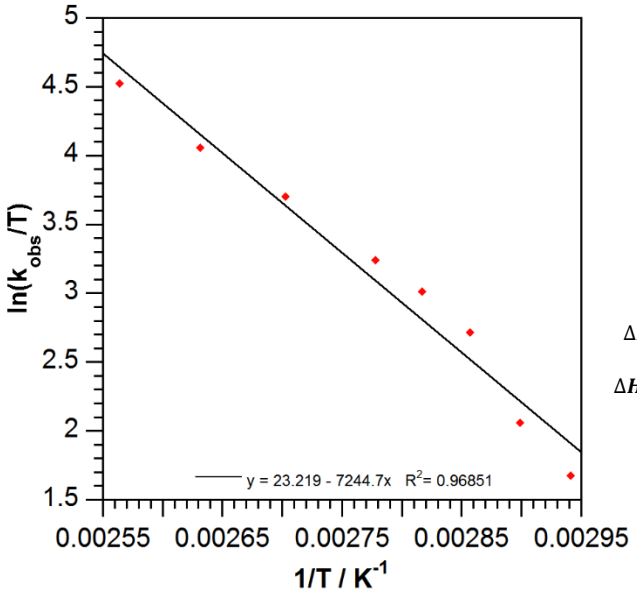

$$ln\left(\frac{k_{obs}}{T}\right) = \frac{-\Delta H^{\ddagger}}{R} * \left(\frac{1}{T}\right) + ln\left(\frac{k_B}{h}\right) + \frac{\Delta S^{\ddagger}}{R} \qquad (2.2)$$

$$slope = \frac{-\Delta H^{\ddagger}}{R} \qquad y - intercept = ln\left(\frac{k_B}{h}\right) + \frac{\Delta S^{\ddagger}}{R}$$

$$\Delta H^{\ddagger} = -(-7245) * R \qquad \Delta S^{\ddagger} = \left(23.22 - \ln\left(\frac{k_B}{h}\right)\right) * R$$

$$\Delta H^{\ddagger} = 14.6\ kcal\ mol^{-1} \qquad \Delta S^{\ddagger} = -0.8\ cal\ mol^{-1}$$

Figure 2.6. Eyring plot and equations for calculating the activation parameters for complex **2**. R is the gas constant in cal K^{-1} mol^{-1}, k_B is the Boltzmann constant in J K^{-1}, and h is planks constant in J sec^{-1}.

Using the same approach as above, the rate of dynamic exchange of the phosphorus atoms in **3** were also monitored by $^{31}P\{^{1}H\}$ NMR spectroscopy over a similar temperature range. Complex **3** revealed dynamic behavior in solution; however, sample decomposition was much more prevalent at elevated temperatures (**Figure 2.7**) as the intensity of a signal consistent with $Cl_2Pt(dppe)$ at 41.4 ppm continued to increase at temperatures greater than 370 K. There was no observable sign of coalescence, however, an associated color change from an emerald green to a dark maroon solution was observed after heating. This color change is indicative of dissociation of the $W[SNS]_2$ metalloligand from the Pt center. This thermal decomposition prevented a detailed analysis of activation parameters for **3**.

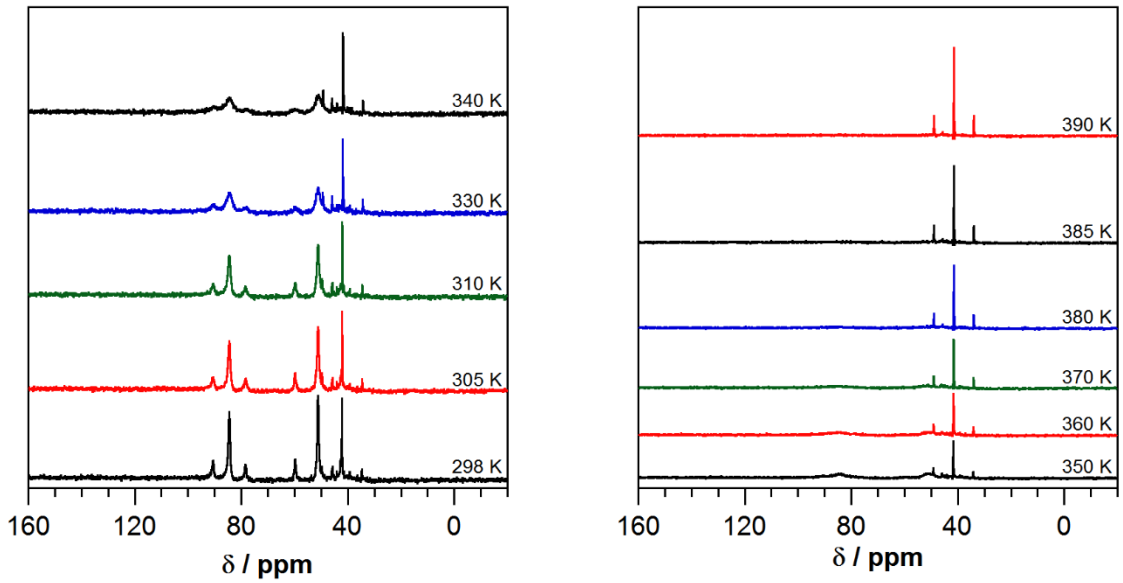

Figure 2.7. $^{31}P\{^{1}H\}$ VT NMR studies of complex **3** in tetrachloroethane-d_2 at elevated temperatures displaying thermal decomposition of **3** to $Cl_2Pt(dppe)$ with the growth of the signal at 41.4 ppm.

Electrochemistry

Electrochemical analysis performed on THF solutions displayed rich electrochemistry for complexes **1-3**. **Figure 2.8** illustrates the cyclic voltammograms of complexes **1-3** in a solution of THF containing 0.3 M $[Bu_4N][PF_6]$ as the supporting electrolyte. All potentials were referenced to $[Cp_2Fe]^{+/0}$ using an internal standard. Complex **1** displays two reversible ($i_{pc}/i_{pa} \cong 1$) one-electron reductions at −1.43 and −2.14 V, while two partially reversible one-electron oxidations were observed at −0.39 V ($i_{pc}/i_{pa} \cong 0.57$) and −0.07 V ($i_{pc}/i_{pa} \cong 0.75$). Both the reductions and oxidations of $W[SNS]_2Ni(dppe)$ are cathodically shifted relative to the redox potentials of the parent $W[SNS]_2$ complex.[49] This result is consistent with the more reduced nature of the heterobimetallic complex compared to the $W[SNS]_2$ monomer. Under the same electrochemical conditions, $Cl_2Ni(dppe)$ shows two irreversible reductive processes at −1.50 and −2.25 V versus $[Cp_2Fe]^{+/0}$. Analogously, both palladium derivative **2** and platinum derivative **3** show a reversible ($i_{pc}/i_{pa} \cong 1$) one-electron oxidation, appearing at −0.65 and −0.81 V, respectively. In the palladium

derivative the shape of the CV wave suggests that there is a minor conformational rearrangement after the first oxidation. A second one-electron oxidation that is partially reversible also was observed for each complex at more positive potentials (red dotted trace for **2** and **3**). This second oxidation gives rise to daughter signals observed near –1.00 V for each complex. Under reducing potentials, the palladium and platinum derivatives show somewhat different behavior. In the case of palladium derivative **2**, a reversible one-electron reduction was observed at –1.47 V followed by an irreversible second reduction at –1.83 V (green dotted trace). For the platinum derivative **3**, no reduction was observed out to a potential of –1.70 V, however, an irreversible process was observed at –1.80 V (green dotted trace). For both palladium and platinum derivatives, the irreversible processes near –1.80 V spawned daughter peaks that were observed at −1.04 and −1.30 V, for **2** and **3**, respectively, upon repeated scanning.

Further analysis of the observed redox potentials for complexes **1-3** reveal interesting aspects between the series. Firstly, an obvious and drastic cathodic shift within the first oxidative process ($E_3°'$) descending the Group 10 metal series is observed. The first oxidative process appears to shift by roughly 420 mV cathodically, indicating that the first oxidation is largely dependent on the appended metal center. This trend is consistent with the heterobimetallic complexes exhibiting more reduced character descending the series, characteristically making the complexes easier to oxidize. In contrast, the second observed oxidative process ($E_4°'$) in **1-3** and the first reductive process ($E_2°'$) in **1** and **2** remain relatively unchanged despite the appended metal center, indicative of displaying more tungsten metalloligand character. Based on the DFT (discussed in detail below) this first oxidative process of **1** is consistent with a nickel based event, however, **2** and **3**, appear more consistent with an oxidation of the tungsten metalloligand.

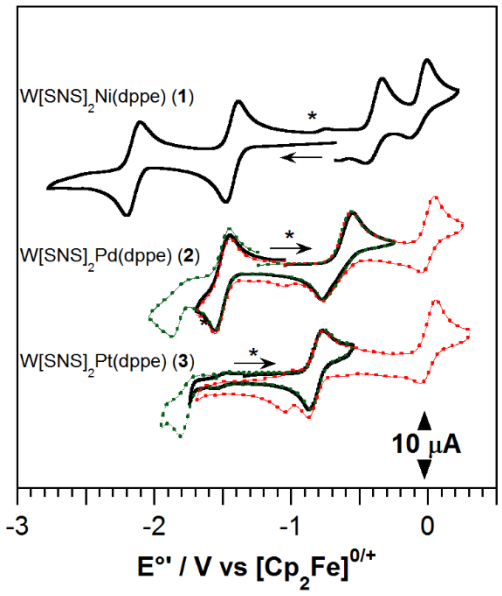

Figure 2.8. Cyclic voltammograms for W[SNS]$_2$Ni(dppe) (*top*), W[SNS]$_2$Pd(dppe) (*middle*), and W[SNS]$_2$Pt(dppe) (*bottom*). All voltammograms were recorded at a 1 mM analyte concentration in 0.3M [NBu$_4$][PF$_6$] in dry, degassed, THF under a nitrogen atmosphere using a 3 mm glassy carbon working electrode, Pt wire counter electrode, and $Ag^{0/+}$ wire pseudo-reference electrode at room temperature at 200 mV sec^{-1} scan rates.

Table 2.4. Electrochemical data for W[SNS]$_2$Ni(dppe) (**1**)**,** W[SNS]$_2$Pd(dppe) (**2**), and W[SNS]$_2$Pt(dppe) (**3**) dissolved in a THF solution containing 0.3M [NBu$_4$][PF$_6$].

	$E_1°'$ $(W–M)^{1–/2–}$	E_{pc}'	$E_2°'$ $(W–M)^{0/1–}$	$E_3°'$ $(W–M)^{1+/0}$	$E_4°'$ $(W–M)^{2+/1+}$
W[SNS]$_2$Ni(dppe) (**1**)	–2.14	*b*	–1.43	–0.39	+0.05
W[SNS]$_2$Pd(dppe) (**2**)	*b*	–1.83[a]	–1.48	–0.65	+0.03
W[SNS]$_2$Pt(dppe) (**3**)	*b*	–1.80[a]	*b*	–0.81	+0.05

[a]Irreversible event [b]Not observed

Theoretical Calculations

To help visualize the frontier electronic structures of **1-3**, DFT computations were carried out. Final geometry optimizations were carried out at the TPSS/TZVP level of theory after initial refinement of the solid-state structures using a more computationally inexpensive SVP basis set. The computed structures agree well with the solid-state structures. The computed W–M bond distances falls within 0.1 Å and 0.04 Å of the measured values for **1** and **2**/**3**, respectively. The

computed metal–ligand bond distances in all cases fall within 0.06 Å while bond distances within the ligand backbones fall within 0.012 Å of the measured values.

Primary interest of the computational studies were to evaluate the relative energies and to determine the Mulliken distributions to investigate the frontier orbitals of complexes **1-3**. The computed electronic structures are consistent with a redox-active $W[SNS]_2$ metalloligand comprising electron-rich $[SNS]^{3-}$ ligands and an electron-poor tungsten center. **Figure 2.9** shows the frontier orbital energies for **1-3** alongside the computed Kohn-Sham orbitals for all complexes. In the case of **1**, the HOMO-1 demonstrates localized [SNS] ligand character with a noticeable decrease in contribution moving to the HOMO, demonstrating split contribution among both [SNS] and the Ni center. The computed orbitals for palladium derivative **2** are indistinguishable from the orbitals for **3**. The HOMO and the HOMO-1 are localized on the [SNS] ligands in complexes **2** and **3** and are further supported by Mulliken population analyses (**Table 2.5**), which indicate that these orbitals have ≥70% [SNS] ligand character. In contrast, in the empty LUMO and LUMO+1 the [SNS] ligand contribution drops below 50% with a significant increase in tungsten character. The frontier orbital energetics for **1-3** are very similar to one another with the only notable difference being in the energy of the LUMO, which gives a maximum energy difference of 0.29 eV between the nickel and platinum derivative. This data suggests that removal of an electron from the HOMO of **1** (oxidation) may result by the removal from a nickel based orbital, while the HOMO on **2** and **3** appears more consistent with a removal from the tungsten metalloligand.

Secondary interest of the computational studies were to evaluate the energy levels involved in the metal–metal bonding of the complexes. Interestingly, the relative energy level that appears responsible for the formal metal–metal bonding in complex **1** are buried deep in energy within the

HOMO-6 (not shown). On the other hand, the heavier metal analogs appear to demonstrate the formation of the metal–metal bonding within the HOMO-1 levels between what appears to be mixing of a tungsten d_{xz} and a palladium/platinum d_{x2-y2} orbital.

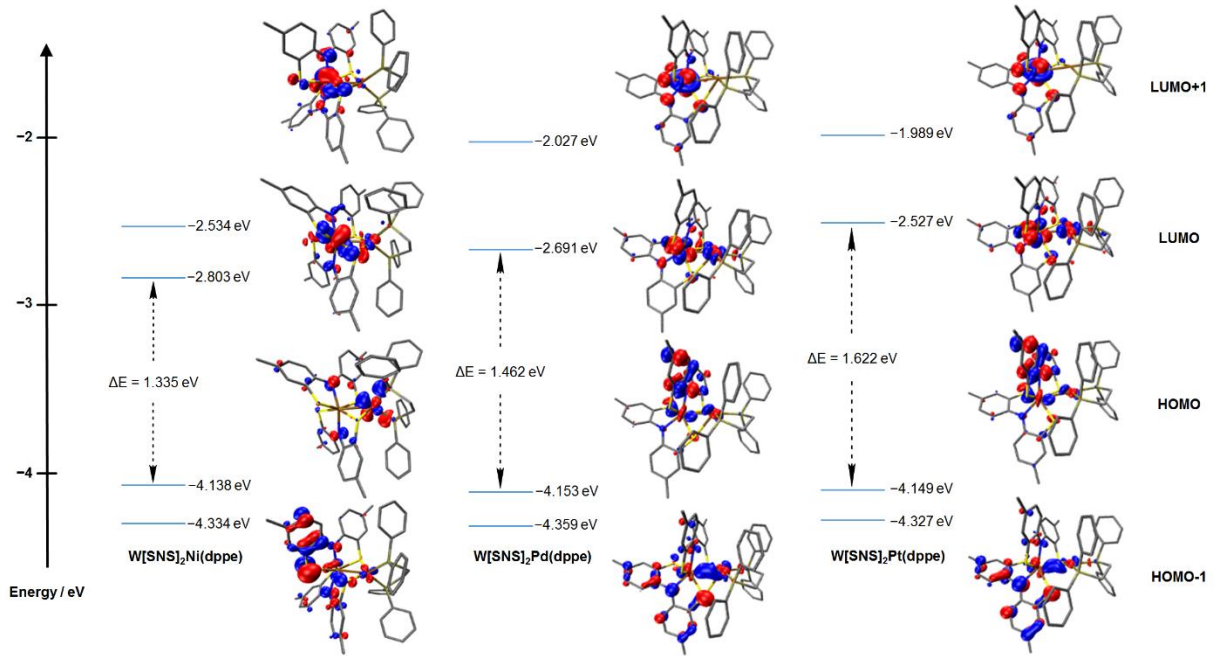

Figure 2.9. Frontier Kohn-Sham molecular orbitals and energies for complexes **1**-**3** using the TPSS/def2-TZVP level of theory. Rendering was performed using VMD for Windows.

Table 2.5. Mulliken population analysis distributions for complexes **1**-**3**.

	$W[SNS]_2Ni(dppe)$ (**1**)				$W[SNS]_2Pd(dppe)$ (**2**)				$W[SNS]_2Pt(dppe)$ (**3**)			
	W (%)	Ni (%)	P (%)	[SNS] (%)	W (%)	Pd (%)	P (%)	[SNS] (%)	W (%)	Pt (%)	P (%)	[SNS] (%)
HOMO-1	8.45	7.48	0.00	84.06	13.37	9.02	8.40	69.21	11.31	5.22	5.60	77.87
HOMO	1.83	40.13	15.80	42.23	13.49	6.94	5.57	74.00	14.01	4.46	4.25	77.28
LUMO	45.37	13.79	3.26	37.58	34.69	12.19	8.50	44.62	33.15	9.24	8.99	48.62
LUMO+1	48.13	1.65	0.00	50.22	52.89	1.20	0.00	45.91	52.57	0.64	1.09	45.70

Conclusion

Herein we demonstrate a modular synthetic approach to generate a novel family of heterobimetallic complexes utilizing $W[SNS]_2$ as a metalloligand to the Group 10 metal series. The overall structural motifs are similar to diiron and iron−zinc complexes recently prepared in our laboratories,[30] except in the cases of complexes **1**-**3**, unusual tungsten−metal bonds are formed.

The assignment of metal oxidation states in complexes **1-3** are of interest, especially given the parallel between the $[SNS]^{3-}$ ligand platform and the well-established oxygen analog, bis(3,5-di-*tert*-butylphenolato)amide ($[ONO^{cat}]^{3-}$).[75,76] Structural and spectroscopic evidence support the assignment of complexes **1-3** adopting W^{V}–M^{I} cores with the metal−metal bond arising from the pairing of the odd electrons on the tungsten and Group 10 metal centers (note: a $W^{VI} \leftarrow M^{0}$ assignment also offers a similar polarization of valence electrons over the bimetallic core). In the case of **1**, the tungsten metalloligand acts as a chelating ligand through two L-type donors to the Ni^{I} center, allowing for the pairing of the unpaired electrons. In the case of **2** and **3**, this intermediate assignment would involve a bridging thiolate acting as an L-type donor to tungsten and an X-type donor to palladium or platinum. This arrangement leaves one unpaired electron on each metal to form the metal–metal bond. This W^{V}–M^{I} electron configuration is most consistent with the limited experimental data collected. Notably, the W–S(1) and M–S(1) bond distances suggest a stronger interaction with the M center than with the W center. This arrangement may also explain the activation barrier measured by $^{31}P\{^{1}H\}$ NMR spectroscopy for the symmetrization of the W–Pd core in **2**, since cleavage of an X-type Pd–S(1) bond would be expected to have a higher enthalpy requirement than a L-type dative bond. Further work describing the reactivity of complex **1** towards electrochemical proton reduction is described in detail in **Chapter 4**.

Experimental

General Considerations. The compounds and reactions reported below show various levels of air- and moisture-sensitivity, therefore all manipulations were carried out using standard vacuum-line, Schlenk-line and glovebox techniques unless otherwise noted. Hydrocarbon and ethereal solvents were sparged with argon before being deoxygenated and dried by passage through Q5 and activated alumina columns, respectively. Halogenated solvents were sparged with argon and

dried by passage through two activated alumina columns. To test for effective oxygen and water removal, aliquots of each solvent were treated with a few drops of a purple solution of sodium benzophenone ketyl radical in THF. $CDCl_3$ was dried over CaH_2 and vacuum distilled prior to use. Tetrachloroethane-d_2 ($C_2D_2Cl_4$) was used as received and dried over sieves. $NiCl_2{\cdot}6H_2O$ (sigma), $PdCl_2$ (sigma), K_2PtCl_4 (Fisher), and 1,2-bis(diphenylphosphino)ethane (dppe) (Fisher) were all used as received. The ligand $[SNS^{cat}]H_3$[49] in addition to complexes $W[SNS]_2$[49], $(DMSO)_2PtCl_2$[41], $Cl_2Pt(dppe)$[42], $Cl_2Pd(dppe)$[43], and $Cl_2Ni(dppe)$[40] were all prepared according to previously reported procedures.

Spectroscopic Methods. Elemental analyses were conducted on a Perkin-Elmer 2400 Series II CHNS elemental analyzer. NMR spectra were collected on Bruker Avance 400 and 600 MHz spectrometers in dry, degassed $CDCl_3$ or $C_2D_2Cl_4$. ^1H NMR spectra were referenced to TMS using the residual proteo impurities of the solvent (7.26 ppm for $CDCl_3$). All $^{31}P\{^1H\}$ NMR spectra were referenced with an external standard of phosphoric acid (H_3PO_4, 85%). Chemical shifts are reported using the standard δ notation in parts per million. Electronic absorption spectra were recorded with a Perkin-Elmer Lambda 900 UV-vis spectrophotometer and a Jasco V-670 absorption spectrometer as solutions in dry, degassed THF contained in 1-cm quartz cells. Electrospray ionization mass spectrometry (ESI-MS) data were collected on a Waters LCT Premier mass-spectrometer using dry, degassed CH_2Cl_2 or THF.

Electrochemical Methods. Electrochemical data were collected with a Gamry Series G 300 Potentiostat/Galvanostat/ZRA (Gamry Instruments, Warminster, PA, USA) using a 3.0 mm glassy carbon working electrode, a platinum wire auxiliary electrode, and a silver wire pseudo-reference electrode. Electrochemical experiments were performed at 25°C in a glovebox under an atmosphere of N_2. Electrochemical samples were 1.0 mM analyte solutions in THF containing 0.3

M $[NBu_4][PF_6]$ as the supporting electrolyte. All potentials were referenced to the $[Cp_2Fe]^{0/+}$ couple using ferrocene or decamethylferrocene as an internal standard. Ferrocene and decamethylferrocene (Acros) were purified by sublimation under reduced pressure and tetra-*n*-butylammonium hexafluorophosphate (Acros) was recrystallized from ethanol three times and dried under vacuum.

Theoretical Calculations. All calculations were performed employing the non-empirical tpss density functional theory using the quantum chemistry program package TURBOMOLE.[77] For computational efficiency, initial geometry optimizations were performed using moderate split-valence plus polarization basis sets (def2-SVP).[78] Structures were refined using basis sets of triple zeta valence plus polarization (def2-TZVP) quality.[79] Crystal structures obtained from X-ray diffraction experiments were used as starting points for the geometry optimization; no molecular symmetry was imposed.

Crystallographic Methods. X-ray diffraction data was collected on a single crystal mounted on a glass fiber using paratone oil. Data was acquired using a Bruker SMART APEX II diffractometer equipped with a CCD detector at 88 K using Mo Kα radiation (λ = 0.71073 Å), which was wavelength selected with a single-crystal graphite monochromator. The SMART program package was used to determine unit-cell parameters and for data collection. The raw frame data were processed using SAINT and SADABS to yield the reflection data file. Subsequent calculations were carried out using the SHELXTL program suite. The structures were solved by direct methods and refined on F^2 by full-matrix least-squares techniques. Analytical scattering factors for neutral atoms were used throughout the analyses. Hydrogen atoms were generated in calculated positions and refined using a riding model. ORTEP diagrams were generated using *ORTEP-3* for Windows.

Table 2.6. Data collection and refinement parameters for complexes **1-3**.

	$W[SNS]_2Ni(dppe)$ (**1**)	$W[SNS]_2Pd(dppe)$ (**2**)	$W[SNS]_2Pt(dppe)$ (**3**)
empirical formula	$C_{54}H_{48}N_2NiP_2S_4W$	$C_{54}H_{48}N_2PdP_2S_4W{\bullet}CH_2Cl_2$	$C_{54}H_{48}N_2PtP_2S_4W{\bullet}CH_2Cl_2$
formula weight [g/mol]	1157.68	1290.29	1378.99
crystal system	Monoclinic	Monoclinic	Monoclinic
space group	$P2_1/c$	$P2_1/n$	$P2_1/n$
T [K]	88(2) K	88(2) K	143(2) K
a [Å]	19.4209(12)	14.0682(13)	14.0874(8)
b [Å]	15.6957(9)	15.7304(14)	15.6390(9)
c [Å]	16.2513(10)	24.270(2)	24.3593(14)
a [deg]	90	90	90
b [deg]	106.7842(7)	104.3314(11)	104.6962(6)
g [deg]	90	90	90
V [$Å^3$]	4742.8(5)	5203.86	5191.1(5)
Z	4	4	4
refl collected	57922	63378	58665
data/restr/param	12020/0/581	13098/0/626	12232/0/608
R_1 [$I > 2\sigma(I)$][a]	0.0199	0.0185	0.0203
wR_2(all data)[a]	0.0455	0.0444	0.0482
GOF[a]	1.041	1.033	1.025

[a] $R_1 = \Sigma||F_o|-|F_c|| / \Sigma|F_o|$, $wR_2 = [\Sigma[w(F_o^2-F_c^2)^2] / \Sigma[w(F_o^2)^2]\ ]^{1/2}$, $GOF = S = [\Sigma[w(F_o^2-F_c^2)^2] / (n-p)]^{1/2}$

General Synthesis of Complexes 1-3. To a 100 mL Schlenk flask, potassium metal and graphite were heated with a heat gun to form two equivalents of KC_8 as a bronze powder. The flask was charged with 30 mL of THF and frozen in a liquid nitrogen cold well. Upon thawing, $W[SNS]_2$ was added to the stirring solution to generate $K_2W[SNS]_2$ *in situ.* as a dark maroon solution with a yellow/orange hue around the rim. After 10 minutes, $Cl_2M(dppe)$ was added to the solution and stirred at room temperature for one hour. The reaction mixture was filtered through celite to remove graphite and KCl to yield a uniquely colored filtrate (see below). The filtrate was concentrated to roughly 5 mL and a solid was crashed out of solution using Et_2O (**1**) or pentane (**2** and **3**). The solid was collected on a glass frit and washed with pentane (2 x 10 mL) and Et_2O (2 x 20 mL). The complex was transferred to a 20 mL scintillation vial and dried under vacuum.

$W[SNS]_2$Ni(dppe) (1). Reagents used: K (180 mg, 4.62 mmol, 2.05 equiv.); C_8 (450 mg, 4.69 mmol, 2.05 equiv.); $W[SNS]_2$ (1.60 g, 2.29 mmol, 0.975 equiv.); $Cl_2Ni(dppe)$ (1.20 g, 2.28 mmol,

0.975 equiv.). The filtrate was collected as a yellow/brown solution prior to evaporation of mother liquor. The complex was collected as a black powder (2.14 g, 81%). X-ray quality crystals were obtained by diffusion of pentane into a THF solution of the complex at 25°C. Anal. Calc. $WS_4N_2NiP_2C_{54}H_{48}$: C, 55.96; H, 4.15; N, 2.42%. Found: C, 55.69; H, 4.13; N, 1.98%. ^{1}H NMR (500 MHz, $CDCl_3$) δ / ppm: 7.39 (br.s., 2H, aryl-H), 7.32 (d, J = 4.2 Hz, 2H, aryl-H), 7.28 (br.s., 3H, aryl-H), 7.25 (m, 4H, aryl-H), 7.07 (m, 4H, aryl-H), 6.93 (m, 6H, aryl-H), 6.73 (m, 6H, aryl-H), 6.48 (d, J = 6.8 Hz, 2H, aryl-H), 2.55 (m, 4H, CH_2), 2.32 (s, 6H, CH_3), 2.13 (s, 6H, CH_3). ^{31}P {^{1}H}-NMR (162 MHz, $CDCl_3$) δ / ppm: 49.8 (s). UV-vis (THF) λ_{max} / nm (ε / $M^{-1}cm^{-1}$): 436 (21,000), 616 (7,100). UV-vis (MeCN) λ_{max} / nm (ε / $M^{-1}cm^{-1}$): 436 (16,300), 616 (5,300). MS (ESI+) (CH_2Cl_2) *m/z*: 1158.11 $(M)^+$.

W[SNS]$_2$Pd(dppe) (2). Reagents used: K (40 mg, 1.0 mmol, 2.0 equiv.); C_8 (99 mg, 1.0 mmol, 2.0 equiv.); W[SNS]$_2$ (362 mg, 0.518 mmol, 1.04 equiv.); Cl_2Pd(dppe) (298 mg, 0.518 mmol, 1.04 equiv.). The filtrate was collected as a forest green solution prior to evaporation of the mother liquor. The solid was collected as a dark green powder (430 mg, 70%). X-ray quality crystals were obtained by slow diffusion of pentane into a CH_2Cl_2 solution of the complex at ambient temperature, dark purple/green crystals obtained. Anal. Calc. $C_{54}H_{48}N_2PdP_2S_4W{\bullet}CH_2Cl_2$: C, 51.19; H, 3.91; N, 2.17%. Found: C, 51.29; H, 3.72; N, 2.16%. ^{31}P {^{1}H}-NMR (236 MHz, $CDCl_3$) δ / ppm: 56.60 ($^2J_{PP}$ = 123.5 Hz), 82.10 ($^2J_{PP}$ = 123.5 Hz). UV-Vis (THF) λ_{max} / nm (ε / M^{-1} cm^{-1}): 381 (18,000), 430 (20,000), 633 (14,000). ESI-MS(+) (THF): *m/z* 1238.91 $(M+MeOH)^+$.

W[SNS]$_2$Pt(dppe) (3). Reagents used: K (31 mg, 0.78 mmol, 2.0 equiv.); C_8 (74 mg, 0.77 mmol, 2.0 equiv.); W[SNS]$_2$ (273 mg, 0.390 mmol, 1.00 equiv.); Cl_2Pt(dppe) (265 mg, 0.380 mmol, 0.974 equiv.). The filtrate was collected as a blue/green solution prior to evaporation of the mother liquor. The solid was collected as a black powder (420 mg, 81%). X-ray quality crystals were

obtained by diffusion of pentane into a CH_2Cl_2 solution of the complex at ambient temperature, purple crystals obtained. Anal. Calc. $C_{54}H_{48}N_2PtP_2S_4W{\bullet}CH_2Cl_2$: C, 47.94; H, 3.66; N, 2.03%. Found: C, 47.95; H, 3.50; N, 1.86%. ^{31}P $\{^1H\}$-NMR (236 MHz, $CDCl_3$) δ / ppm: 51.34 ($^1J_{PtP}$ = 4191 Hz), 83.40 ($^1J_{PtP}$ = 2954 Hz). UV-Vis (THF) λ_{max} / nm (ε / M^{-1} cm^{-1}): 414 (19,000), 582 (14,000). ESI-MS(+) (CH_2Cl_2): *m/z* 1325.16 $(M+MeOH)^+$.

References

(1) Mulder, D. W.; Shepard, E. M.; Meuser, J. E.; Joshi, N.; King, P. W.; Posewitz, M. C.; Broderick, J. B.; Peters, J. W. *Structure* **2011**, *19*, 1038–1052.
(2) Schilter, D.; Fuller, A. L.; Gray, D. L. *Eur. J. Inorg. Chem.* **2015**, *2015*, 4638–4642.
(3) Fontecilla-Camps, J. C.; Volbeda, A.; Cavazza, C.; Nicolet, Y. *Chem. Rev.* **2007**, *107*, 4273–4303.
(4) Karlin, K. D. *Science (80-.).* **1993**, *261*, 701–708.
(5) Holm, R. H.; Kennepohl, P.; Solomon, E. I. *Chem. Rev.* **1996**, *96*, 2239–2314.
(6) McEvoy, J. P.; Brudvig, G. W. *Chem. Rev.* **2006**, *106*, 4455–4483.
(7) Chaudhuri, P.; Hess, M.; Weyhermüller, T.; Wieghardt, K. *Angew. Chemie Int. Ed.* **1999**, *38*, 1095–1098.
(8) Ivakhnenko, E. P.; Starikov, A. G.; Minkin, V. I.; Lyssenko, K. A.; Antipin, M. Y.; Simakov, V. I.; Korobov, M. S.; Borodkin, G. S.; Knyazev, P. A. *Inorg. Chem.* **2011**, *50*, 7022–7032.
(9) Kletzin, a; Adams, M. W. *FEMS Microbiol. Rev.* **1996**, *18*, 5–63.
(10) Kalck, P.; Wheatley, N.; Bergman, R. G. *Chem. Rev.* **2001**, *101*, 207–208.
(11) Krogman, J. P.; Thomas, C. M. *Chem. Commun. (Camb).* **2014**, *50*, 5115–5127.
(12) Choukroun, R.; Jaud, J.; Kalck, I. P.; Data, S. *Organometallics* **1986**, 67–71.
(13) Dalle-Donne, I.; Aldini, G.; Carini, M.; Colombo, R.; Rossi, R.; Milzani, A. *J. Cell. Mol. Med.* **2006**, *10*, 389–406.
(14) Holm, R. H. *Chem. Soc. Rev.* **1981**, *10*, 455–490.
(15) Dross, F.; Geisler, V.; Lenger, R.; Theis, F.; Krafft, T.; Fahrenholz, F.; Kojro, E.; Duchene, A.; Tripier, D.; Juvenal, K. *Eur. J. Biochem.* **1992**, *206*, 93–102.
(16) Kumar, G.; Gupta, R. *Chem. Soc. Rev.* **2013**, *42*, 9403–9453.
(17) Tereniak, S. J.; Carlson, R. K.; Clouston, L. J.; Young, V. G.; Bill, E.; Maurice, R.; Chen, Y.-S.; Kim, H. J.; Gagliardi, L.; Lu, C. C. *J. Am. Chem. Soc.* **2014**, *136*, 1842–1855.
(18) Clouston, L. J.; Siedschlag, R. B.; Rudd, P. A.; Planas, N.; Hu, S.; Miller, A. D.; Gagliardi, L.; Lu, C. C. *J. Am. Chem. Soc.* **2013**, *135*, 13142–13148.
(19) MacKay, B. A.; Fryzuk, M. D. *Chem. Rev.* **2004**, *104*, 385–402.
(20) Lee, S. C.; Lo, W.; Holm, R. H. *Chem. Rev.* **2014**, *114*, 3579–3600.
(21) Kanady, J. S.; Lin, P.-H.; Carsch, K. M.; Nielsen, R. J.; Takase, M. K.; Goddard, W. A.; Agapie, T. *J. Am. Chem. Soc.* **2014**, *136*, 14373–14376.
(22) Powers, T. M.; Betley, T. A. *J. Am. Chem. Soc.* **2013**, *135*, 12289–12296.
(23) Blakemore, J. D.; Crabtree, R. H.; Brudvig, G. W. *Chem. Rev.* **2015**, *115*, 12974–13005.
(24) Denny, J. A.; Darensbourg, M. Y. *Chem. Rev.* **2015**, *115*, 5248–5273.

(25) Rauchfuss, T. B. *Acc. Chem. Res.* **2015**, *48*, 2107–2116.
(26) Lin, P.-H.; Takase, M. K.; Agapie, T. *Inorg. Chem.* **2015**, *54*, 59–64.
(27) Cooper, B. G.; Fafard, C. M.; Foxman, B. M.; Thomas, C. M. *Organometallics* **2010**, *29*, 5179–5186.
(28) Kuppuswamy, S.; Bezpalko, M. W.; Powers, T. M.; Wilding, M. J. T.; Brozek, C. K.; Foxman, B. M.; Thomas, C. M. *Chem. Sci.* **2014**, *5*, 1617.
(29) Cammarota, R. C.; Lu, C. C. *J. Am. Chem. Soc.* **2015**, *137*, 12486–12489.
(30) Wong, J. L.; Higgins, R. F.; Bhowmick, I.; Cao, D. X.; Szigethy, G.; Ziller, J. W.; Shores, M. P.; Heyduk, A. F. *Chem. Sci.* **2016**, *7*, 1594–1599.
(31) Pereira, M. T.; Antelo, J. M.; Adrio, L. A.; Martínez, J.; Ortigueira, J. M.; López-Torres, M.; Vila, J. M. *Organometallics* **2014**, *33*, 3265–3274.
(32) Rampersad, M. V; Jeffery, S. P.; Reibenspies, J. H.; Ortiz, C. G.; Darensbourg, D. J.; Darensbourg, M. Y. *Angew. Chemie Int. Ed.* **2005**, *44*, 1217–1220.
(33) Bezpalko, M. W.; Foxman, B. M.; Thomas, C. M. *Inorg. Chem.* **2013**, *52*, 12329–12331.
(34) Kuppuswamy, S.; Cooper, B. G.; Bezpalko, M. W.; Foxman, B. M.; Powers, T. M.; Thomas, C. M. *Inorg. Chem.* **2012**, *51*, 1866–1873.
(35) Marquard, S. L.; Bezpalko, M. W.; Foxman, B. M.; Thomas, C. M. *Organometallics* **2014**, *33*, 2071–2079.
(36) Cooper, B. G.; Napoline, J. W.; Thomas, C. M. *Catal. Rev.* **2012**, *54*, 1–40.
(37) Greenwood, B. P.; Forman, S. I.; Rowe, G. T.; Chen, C.-H.; Foxman, B. M.; Thomas, C. M. *Inorg. Chem.* **2009**, *48*, 6251–6260.
(38) Hsiao, Y. M.; Chojnacki, S. S.; Hinton, P.; Reibenspies, J. H.; Darensbourg, M. Y. *Organometallics* **1993**, *12*, 870–875.
(39) Rampersad, M. V; Jeffery, S. P.; Golden, M. L.; Lee, J.; Reibenspies, J. H.; Darensbourg, D. J.; Darensbourg, M. Y. *J. Am. Chem. Soc.* **2005**, *127*, 17323–17334.
(40) Busby, R.; Hursthouse, M. B.; Jarrett, P. S.; Lehrnann, C. W.; Malik, K. M. A.; Phillips, C. *J. Am. Chem. Soc. Dalt. Trans* **1993**, 3767–3770.
(41) Coucouvanis, D. *Inorganic Syntheses*; 2002; Vol. 33.
(42) Shavaleev, N. M.; Adams, H.; Best, J.; Weinstein, J. a. *J. Organomet. Chem.* **2007**, *692*, 921–925.
(43) Abukari, M. A.; Suzuki, T.; Kita, M. *Polyhedron* **2013**, *52*, 364–369.
(44) Carroll, M. E.; Barton, B. E.; Gray, D. L.; Mack, A. E.; Rauchfuss, T. B. *Inorg. Chem.* **2011**, *50*, 9554–9563.
(45) Redin, K.; Wilson, A. D.; Newell, R.; DuBois, M. R.; DuBois, D. L. *Inorg. Chem.* **2007**, *46*, 1268–1276.
(46) Schilter, D.; Rauchfuss, T. B.; Stein, M. *Inorg. Chem.* **2012**, *51*, 8931–8941.
(47) Cordero, B.; Gómez, V.; Platero-Prats, A. E.; Revés, M.; Echeverría, J.; Cremades, E.; Barragán, F.; Alvarez, S. *Dalton Trans.* **2008**, 2832–2838.
(48) Bartlone, A. F.; Chetcuti, M. J.; Fanwick, P. E.; Hallert, K. J. *Inorg. Chem.* **1993**, *32*, 1435–1441.
(49) Shaffer, D. W.; Szigethy, G.; Ziller, J. W.; Heyduk, A. F. *Inorg. Chem.* **2013**, *52*, 2110–2118.
(50) Cianfriglia, P.; Narducci, V.; Sterzo, C. Lo; Viola, E.; Sapienza, L.; Moro, P. A.; Roma, I.-; Bocelli, G.; Kodenkandath, T. A. *Organometallics* **1996**, 5220–5230.
(51) Ashworth, T. V; Howard, J. A. K.; Laguna, M.; Stone, F. G. A. *J. Chem. Soc. Dalt. Trans.* **1980**, 1593–1600.

(52) Zuzek, A. A.; Reynolds, S. C.; Glueck, D. S.; Golen, J. A.; Rheingold, A. L. *Organometallics* **2011**, *30*, 1812–1817.
(53) Zhuravel, M. A.; Glueck, D. S.; Incarvito, C. D.; Rheingold, A. L. *Organometallics* **1999**, 4673–4676.
(54) Magill, A. M.; Yates, B. F.; Cavell, K. J.; Skelton, W.; White, A. H. *Dalt. Trans.* **2007**, 3398–3406.
(55) Budzelaa, P. H. M.; Leeuwen, P. W. N. M. van; Roobeek, C. F. *Organometallics* **1992**, *11*, 23–25.
(56) Fun, H.-K.; Chantrapromma, S.; Liu, Y.-C.; Chen, Z.-F.; Liang, H. *Acta Crystallogr. Sect. E* **2006**, *62*, m1252--m1254.
(57) Miao, J.; Hu, C.; Feng, X.; Chen, H.; Nie, Y. *Acta Crystallogr. Sect. E* **2009**, *65*, m1025.
(58) Johansson, M. H.; Otto, S. *Acta Crystallogr. Sect. C* **2000**, *56*, e12--e15.
(59) Edelbach, B. L.; Vicic, D. A.; Lachicotte, R. J.; Jones, W. D. *Organometallics* **1998**, *17*, 4784–4794.
(60) Low, J. J.; Goddard, W. A. *J. Am. Chem. Soc.* **1986**, *108*, 6115–6128.
(61) Sunkel, K.; Birk, U.; Rob, C. *Organometallics* **1994**, 1679–1687.
(62) Kraaijkamp, J. G.; van Koten, G.; Vrieze, K.; Grove, D. M.; Klop, E. A.; Spek, A. L.; Schmidpeter, A. *J. Organomet. Chem.* **1983**, *256*, 375–389.
(63) Ellis, J. W.; Harrison, K. N.; Hoye, P. A. T.; Orpen, A. G.; Pringle, P. G.; Smith, M. B. *Inorg. Chem.* **1992**, *31*, 3026–3033.
(64) Yang, L.; Powell, D. R.; Houser, R. P. *Dalton Trans.* **2007**, 955–964.
(65) Stiefel, E. I.; Brown, G. F. *Inorg. Chem.* **1972**, *11*, 434–436.
(66) Bauer, J.; Braunschweig, H.; Dewhurst, R. D. *Chem. Rev.* **2012**, *112*, 4329–4346.
(67) Cotton, F. A.; Murillo, C. A.; Walton, R. A. *Multiple bonds between metal atoms*; Springer Science: New York, 2005.
(68) Carty, A. J. *Inorg. Chem.* **1976**, *15*, 1956–1959.
(69) Pregosin, P. S. *Coord. Chem. Rev.* **2008**, *252*, 2156–2170.
(70) Hunt, C. T.; Balch, A. L. *Inorg. Chem.* **1982**, *21*, 1641–1644.
(71) Kost, D.; Carlson, E. H.; Raban, M. *J. Chem. Soc. D* **1971**, 656–657.
(72) Bain, A. D. *Prog. Nucl. Magn. Reson. Spectrosc.* **2003**, *43*, 63–103.
(73) Ledford, J.; Shultz, C. S.; Gates, D. P.; White, P. S.; DeSimone, J. M.; Brookhart, M. *Organometallics* **2001**, *20*, 5266–5276.
(74) Bunten, K. A.; Farrar, D. H.; Poë, A. J.; Lough, A. J. *Organometallics* **2000**, *19*, 3674–3682.
(75) Zarkesh, R. A.; Ziller, J. W.; Heyduk, A. F. *Angew. Chemie Int. Ed.* **2008**, *47*, 4715–4718.
(76) Szigethy, G.; Shaffer, D. W.; Heyduk, A. F. *Inorg. Chem.* **2012**, *51*, 12606–12618.
(77) Furche, F.; Ahlrichs, R.; Hättig, C.; Klopper, W.; Sierka, M.; Weigend, F. *Wiley Interdiscip. Rev. Comput. Mol. Sci.* **2014**, *4*, 91–100.
(78) Schäfer, A.; Horn, H.; Ahlrichs, R. *J. Chem. Phys.* **1992**, *97*, 2571–2577.
(79) Schäfer, A.; Huber, C.; Ahlrichs, R. *J. Chem. Phys.* **1994**, *100*, 5829–5835.

Chapter 3

Ancillary Phosphine Donor Effects on a Series of $W[SNS]_2Ni(P^{R2}R'P^{R2})$ Heterobimetallic Complexes

Introduction

Bidentate phosphines are important ancillary ligands for transition metal complexes.[1] The electron-donating properties of a bidentate phosphine often alter the electron richness of the metal center while generating rigid coordination environments capable of modifying the binding and reactivity of small molecule substrates.[1] While Tolman's cone angle concept for monodentate phosphines has become widely accepted, the extension towards bidentate phosphines has been much more limited.[2–4] An attractive aspect of bidentate phosphines is the ability to tailor a ligand backbone to achieve a desirable distance of separation between the phosphorus donor atoms. This spacing is determined by the constraints imposed by the ligand backbone and is directly involved in determining the P–M–P bite angles of transition metal complexes.[2,5,6] A P–M–P bite angle is directly dependent on three main factors (i) the substituents on the phosphine donor atom; (ii) the M–$P_{centroid}$ distance (used as a more consistent form of the M–P length); and (iii) the phosphorus–phosphorus separation distance.[2,5,6] **Figure 3.1** demonstrates the overall trend observed with bidentate phosphines in literature in which a decrease in the M–$P_{centroid}$ bond distance results in an increase in the P–M–P bite angle as the phosphorus–phosphorus separation remains the same.[2,7]

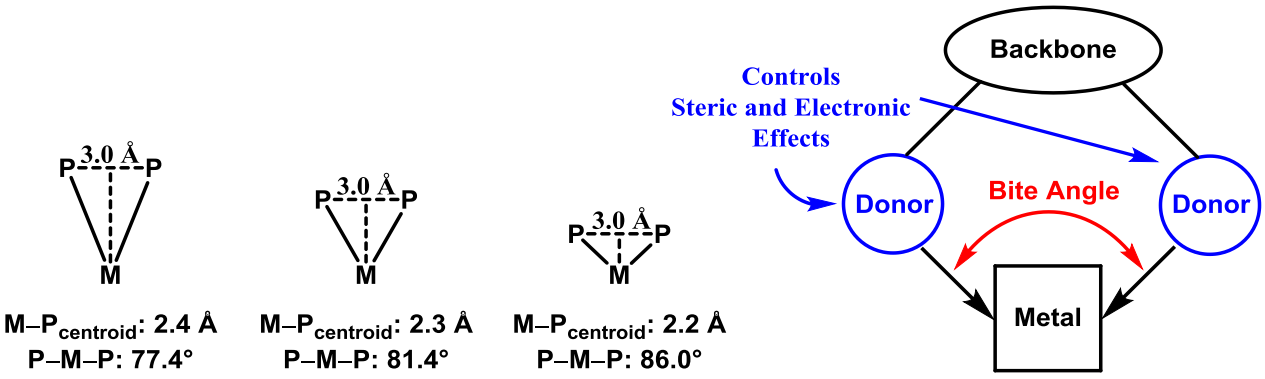

Figure 3.1. Visual representations of the bite angle for bidentate phosphines coordinated to metal centers.[2,7]

Phosphine ligands have continued to show the ability to stabilize transition metal complexes for widespread use in catalytic reactions.[8] Bidentate phosphines in particular demonstrate

multifunctional use in catalysis through the incorporation of steric bulk on the donor atom, the ability to tune the electronic properties of the metal center, and their ability to stabilize low-valent metal centers.[2,7–12] Through these investigations, bidentate phosphines have been found to offer more control over regio- and stereo-selectivity in many catalytic reactions over their monodentate analogs.[1,2,13–19] Additionally, bite angles observed in transition metal catalysts have been explored to determine their effects on catalytic efficiency in reactions such as hydroformylation, hydrocyanation, cross-coupling reactions, Diels–Alder, and other high enantioselective reactions.[5,6,20–23] In most cases, it was correlated that catalytic ability was dependent on the size of the metal–phosphine bite angle.[5,6,20–23] This increase in catalytic efficiency is postulated to be attributed to the flexibility of the bidentate backbone, whereby an arm-off η_1 intermediate may be accessible to allow substrate binding for facile small molecule activation to occur.[2]

Substitution of substituents on phosphine ligands have long been recognized to cause behavior changes in transition metal centers through steric and electronic effects.[24] These effects will be investigated through the synthesis of a family of tungsten-nickel heterobimetallic complexes that involve bidentate phosphine ligands. The phosphines of choice will substitute phosphorus substituents for stronger donors in addition to altering the chelating ring size through the appendage of systematically larger bidentate phosphine ligands. These studies will offer a better understanding into the role of the ancillary phosphine towards electronic and steric effects in our family of tungsten–nickel heterobimetallic complexes.

Results and Discussion

Synthesis and Structural Characterization

A family of heterobimetallic complexes analogous to previously discussed **1** were investigated through substitution of both the phosphine donor substituents and the chelate linker. Using the synthetic approach previously discussed in **Chapter 2**, treatment of W[SNS]$_2$ with two equivalents of potassium graphite followed by a salt metathesis with one equivalent of $Cl_2Ni(P^{R2}R'P^{R2})$ ($P^{R2}R'P^{R2}$ = depe (**4**), dmpe **(5**), dppp (**6**), $P^{Ph2}N^{Ph}P^{Ph2}$ (**7**), $P^{Ph2}N^{Bn}P^{Ph2}$ (**8**), DPEphos (**9**), and dppf (**10**)) afforded heterobimetallic complexes **4-10** as dark powders in greater than 40% yields. ESI-MS data confirmed the formation of the desired species with parent ion signals at *m/z* values of 964.1, 908.1, 1169.9, 1247.0, 1261.0, 1295.9, and 1314.1 for complexes **4-10**, respectively (**Scheme 3.1**). Single crystals of complexes **4**, **7**, and **9** were obtained by slow diffusion of pentane into a saturated THF solution of the complex at room temperature.

Scheme 3.1. Synthesis of heterobimetallic complexes **4-10**.

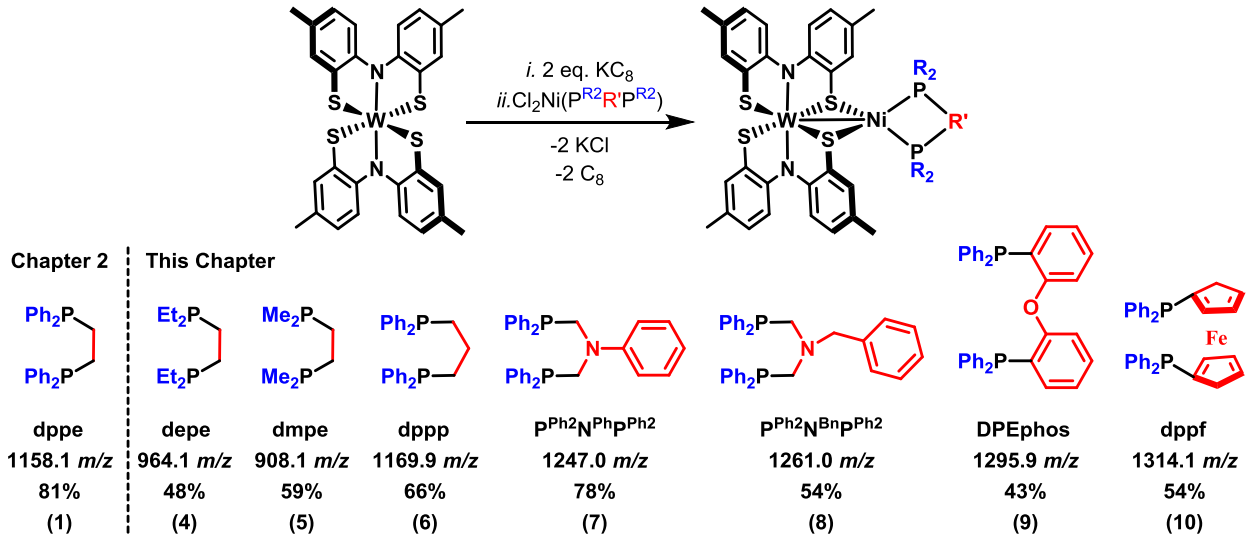

X-ray diffraction studies on single crystals of W[SNS]$_2$Ni(depe) (**4**), W[SNS]$_2$Ni($P^{Ph2}N^{Ph}P^{Ph2}$) (**7**), and W[SNS]$_2$Ni(DPEphos) (**9**) revealed bimetallic complexes with a W–Ni bond supported by two bridging thiolate donors, isomorphous to the aforementioned W[SNS]$_2$Ni(dppe) (**1**,

Chapter 2). **Figure 3.2** illustrates the solid-state structures of **4**, **7**, and **9** as ORTEP diagrams and a table of selected bond distances and angles are provided in **Table 3.1**. The bimetallic complexes can be best described as a $W[SNS]_2$ unit bound as a chelating ligand to the $Ni(P^{R2}R'P^{R2})$ fragments. The nickel centers are four-coordinate (disregarding the W−Ni bonds) with a pseudo-tetrahedral geometry comprising the two phosphine donors and two thiolates that bridge from the $W[SNS]_2$ cofactor. Applying the angular structural parameter (τ_4) for four-coordinate metal centers to complexes **4**, **7**, and **9** revealed values of 0.82, 0.87, and 0.78, respectively, indicating distortion from ideal tetrahedral geometry. The average valence angles about the nickel centers lie between 88.58° and 128.0°, consistent with the calculated τ_4 values and a distortion from ideal tetrahedral geometry. The P−Ni−P bite angles of 88.58°, 94.32°, and 104.4° are indicative of the observed bite angles for depe, $P^{Ph2}N^{Ph}P^{Ph2}$, and DPEphos, respectively.[2,25] The Ni−P distances (d_{avg} / Å: **4** = 2.231, **7** = 2.243, and **9** = 2.250) are longer than those typically observed for nickel(II) complexes of the respective chelating phosphine, however, the Ni−S bond distances (d_{avg} / Å: **4** = 2.160, **7** = 2.173, and **9** = 2.165) are slightly shorter than those of nickel(II) complexes containing bridging thiolate ligands.[2,26–28] The W−Ni distances of 2.531 Å, 2.593 Å, and 2.642 Å for complexes **4**, **7**, and **9**, respectively, fall within the sum of the covalent radii of these two metal ions (tungsten, 1.62 Å; nickel, 1.24 Å)[29] suggesting the formation of a formal metal−metal bond in all three cases. Within the $W[SNS]_2$ cofactor, the average W−S distances that bridge the tungsten and nickel centers (d_{avg} / Å: **4** = 2.420, **7** = 2.408, and **9** = 2.432) agree well with the observed bridging thiolate distances of **1** (d_{avg} = 2.404 Å), however, are elongated from the W–S bond distances of the neutral, isolated $W[SNS]_2$ complex (2.367 Å).

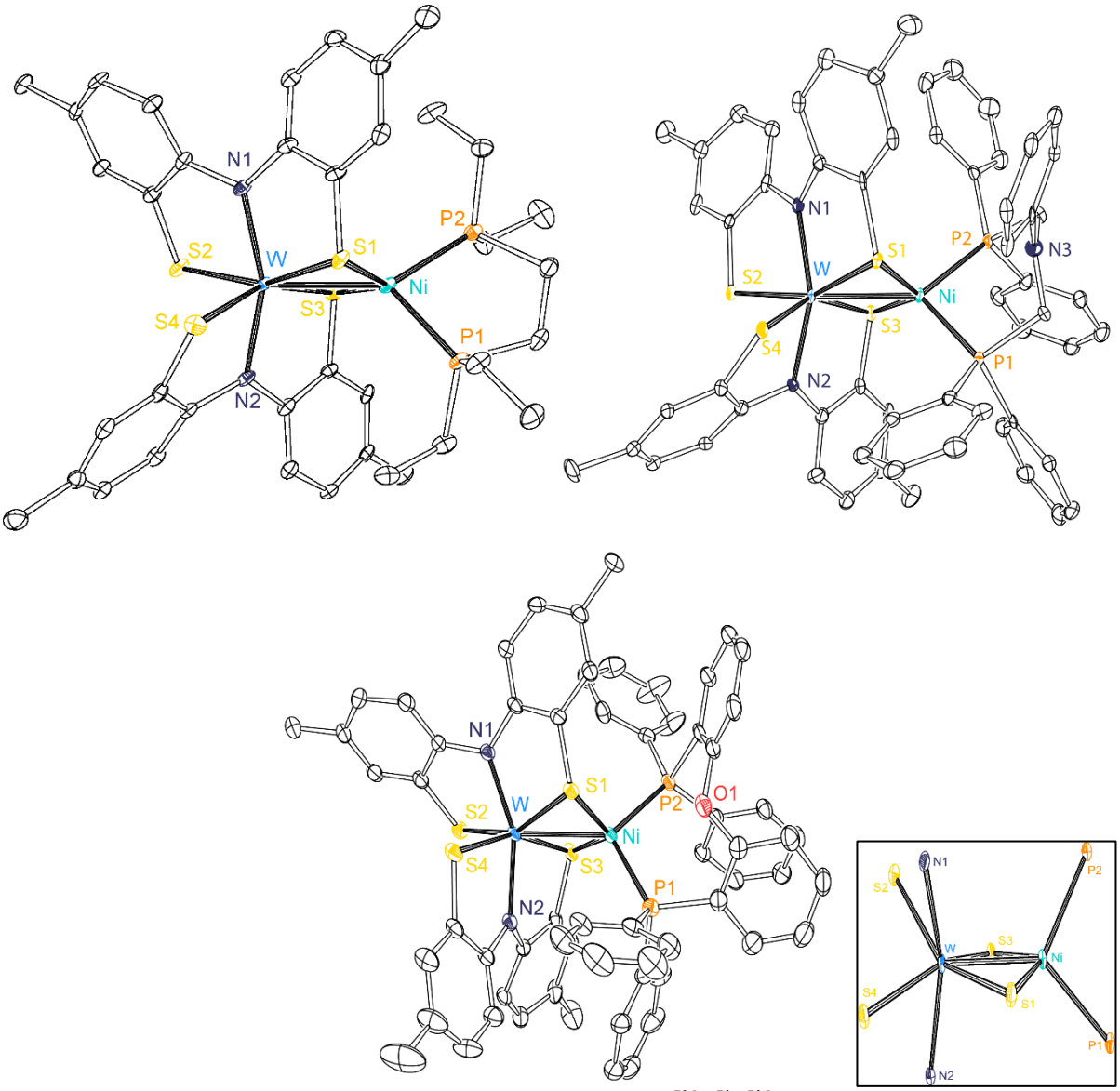

Figure 3.2. ORTEP diagrams for complexes **4** (depe) (top, *left*); **7** ($P^{Ph2}N^{Ph}P^{Ph2}$) (top, *right*); and **9** (DPEphos) (bottom) with thermal ellipsoids shown at 50% probability. Hydrogen atoms have been omitted for clarity. Solvent molecules from **7** (THF) and **9** (2-THFs) were removed for clarity. Inset shows the geometry about the tungsten core of **7** (analogous to **4** and **9**).

Table 3.1. Selected bond metrics for complexes **4**, **7**, and **9**.

	$W[SNS]_2Ni(depe)$ (**4**)	$W[SNS]_2Ni(P^{Ph2}N^{Ph}P^{Ph2})$ (**7**)	$W[SNS]_2Ni(DPEphos)$ (**9**)
	Bond Distances / Å		
W – Ni	2.5310(6)	2.5934(3)	2.6416(4)
W – S1	2.4250(8)	2.4014(5)	2.4488(7)
W – S3	2.4142(8)	2.4141(5)	2.4153(7)
Ni – S1	2.1603(9)	2.1752(6)	2.1651(8)
Ni – S3	2.1578(9)	2.1707(6)	2.1655(8)
Ni – P1	2.2269(9)	2.2444(6)	2.2737(9)
Ni – P2	2.2344(10)	2.2423(6)	2.2255(8)
	Bond Angles / °		
S1 – W – S3	102.75(3)	101.958(17)	98.85(2)
S1 – Ni – S3	122.21(4)	118.83(2)	117.11(3)
P1 – Ni – P2	88.58(3)	94.32(2)	104.43(3)
P1 – Ni – S1	122.53(3)	128.00(2)	119.90(3)
P1 – Ni – S3	99.89(3)	95.46(2)	100.20(3)
P2 – Ni – S1	98.94(3)	101.81(2)	103.08(3)
P2 – Ni – S3	121.20(3)	117.10(2)	111.52(3)
τ_4 value	0.82	0.87	0.78

The overall tungsten geometry of the $W[SNS]_2$ metalloligand in complexes **4**, **7**, and **9** was found to lie between trigonal prismatic and trigonal antiprismatic geometry in each case. The primary measurements of trigonal prismatic versus trigonal antiprismatic geometry is defined by the twist angle (θ) between opposite trigonal faces (**Chapter 2**, **Figure 2.3,** page 21). In all complexes, two trigonal planes can be defined by the nitrogen and a single sulfur atom from one [SNS] ligand and a single sulfur atom from the second [SNS] ligand (N(1)–S(1)–S(4) and N(2)–S(2)–S(3)), whereby the twist angle is then defined as the torsion angle between the vertices of the trigonal planes and the centroids of those planes.[30,31] A second metrical parameter used for determining the degree of distortion for trigonal systems is the prismatic compression, defined as the ratio of the prism height (h) to the average length of the trigonal face (s). An ideal trigonal prism demonstrates a twist angle (θ) of 0° with an s/h ratio of 1.00 while an ideal trigonal antiprism has a twist angle of 60° and a s/h ratio of 1.22.[31] **Table 3.2** displays the values calculated based off the twist angles and the observed prismatic compression. Calculated values for **4**, **7**, and **9** each

display a distortion from an ideal anti-prismatic geometry with average twist angles greater than 35°. These large deviations in the twist angles are consistent with the observed prismatic compression (s/h) ratios (> 1.05) concluding a distortion from ideal trigonal anti-prismatic geometry.

Table 3.2. Additional measured and calculated parameters for complexes **1**, **4**, **7**, and **9**, as defined by **Figure 2.3**.

	$W[SNS]_2Ni(dppe)$ (**1**)	$W[SNS]_2Ni(depe)$ (**4**)	$W[SNS]_2Ni(P^{Ph2}N^{Ph}P^{Ph2})$ (**7**)	$W[SNS]_2Ni(DPEphos)$ (**9**)
$\theta_{S4,N2}$	40.3°	47.0°	29.4°	42.6°
$\theta_{S1,S3}$	13.1°	29.0°	28.8°	25.4°
$\theta_{N1,S2}$	35.8°	34.1°	55.2°	36.3°
s/h	1.16	1.05	1.10	1.06

Investigation into the effects of the chelating phosphines towards the observed metal–metal bond of complexes **4**, **7**, and **9** are of interest. Substituent substitution on the chelating phosphine atoms from a weaker, sterically bulky donor (**1**, Ph) to a stronger, less sterically hindered donor (**4**, Et) revealed a negligible contraction of 0.01 Å in the observed metal–metal bond, concluding that donor effects nor steric bulk of the phosphine substituents play a large role in the metal–metal bond length. Increasing the complexity within the phosphine backbone by incorporating a six- or eight-membered chelate ring, however, resulted in an elongation of the metal–metal bond by up to 0.11 Å when compared to the five-membered chelate of **4**. This elongation in the in the W–Ni bond distance is directly related to the bite angle and $Ni–P_{centroid}$ distance. The distance between the nickel center and the centroid of the two phosphorous atoms ($Ni–P_{centroid}$) yielded a linear trend versus the bite angles observed for complexes **1**, **4**, **7**, and **9** indicating that as the bite angle decreases, the $Ni–P_{centroid}$ bond distance increases, consistent with the observed lengthening in the Ni–P bond distances (**Figure 3.3**, **Table 3.1**). This observation suggests that the bidentate phosphines follow the same relative trend also observed by Tolman *et al*. with monodentate phosphines, with which the cone angles were directly related to the M–P bond distances.[3,4]

Similarly, a relatively linear trend is observed between the W–Ni bond and the phosphine bite angle concluding that as the bite angle increases, the metal–metal bond of the complex increases.

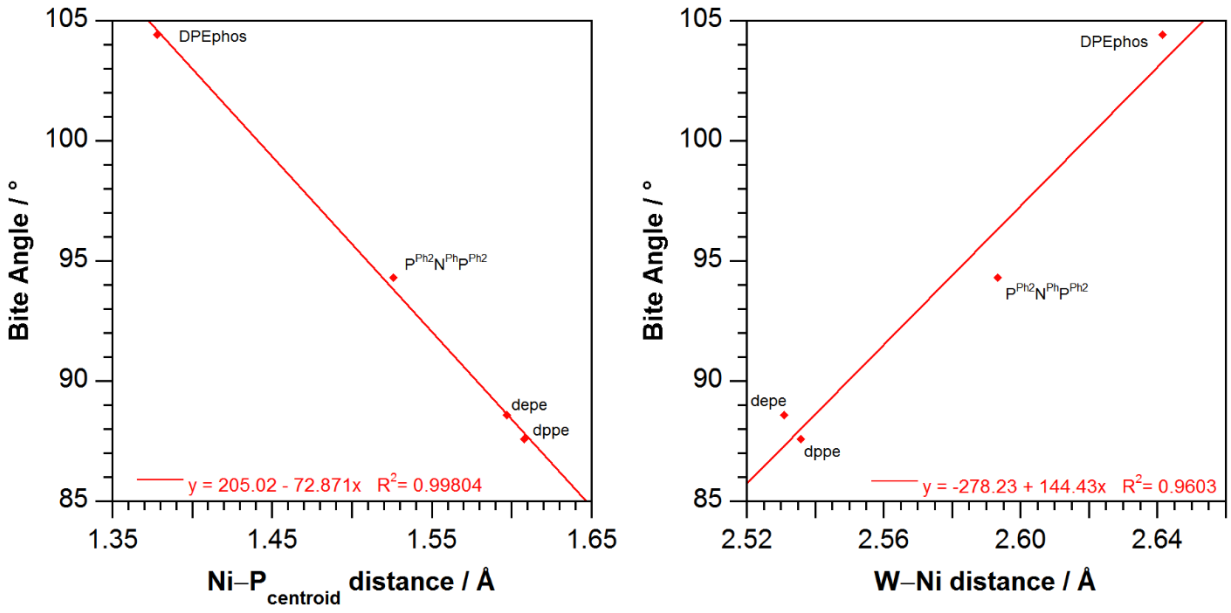

Figure 3.3. (*left*) Bite angle vs Ni–$P_{centroid}$ bond distance and (*right*) Bite angle vs W–Ni bond distances for complexes **1** (dppe), **4** (depe), **7** ($P^{Ph2}N^{Ph}P^{Ph2}$), and **9** (DPEphos).

Spectroscopic Characterization of Complexes 4-10

The electronic structures of complexes **4-10** were further investigated through electronic absorption spectroscopy (UV-vis). All electronic absorption spectra for complexes **4-10** are shown in **Figure 3.4** with collected values listed in **Table 3.3**. Dissolution of the family of heterobimetallic complexes in THF afforded dark solutions manifesting intense absorbance bands in the visible region between 400 – 700 nm indicative of charge transfer bands based on their extinction coefficients (5800 – 21000 M^{-1} cm^{-1}, **Figure 3.4**). Comparison of **1** (dppe, 436 nm, 23000 cm^{-1}), **4** (depe, 421 nm, 23700 cm^{-1}), and **5** (dmpe, 420 nm, 23800 cm^{-1}) conclude that the exchange of the phosphine substituents resulted in a blue-shift in the observed charge transfer band (Δ_{max} = 800 cm^{-1}). Analogously, comparison of **1** (dppe, 436 nm, 23000 cm^{-1}), **6** (dppp, 438 nm, 22800 cm^{-1}), **7** ($P^{Ph2}N^{Ph}P^{Ph2}$, 441 nm, 22700 cm^{-1}), **8** ($P^{Ph2}N^{Bn}P^{Ph2}$, 438 nm, 22800 cm^{-1}), **9** (DPEphos,

443 nm, 22600 cm^{-1}), and **10** (dppf, 441 nm, 22700 cm^{-1}) conclude that the exchange of the phosphine linker resulted in a red-shift in the observed charge transfer band (Δ_{max} = 400 cm^{-1}).

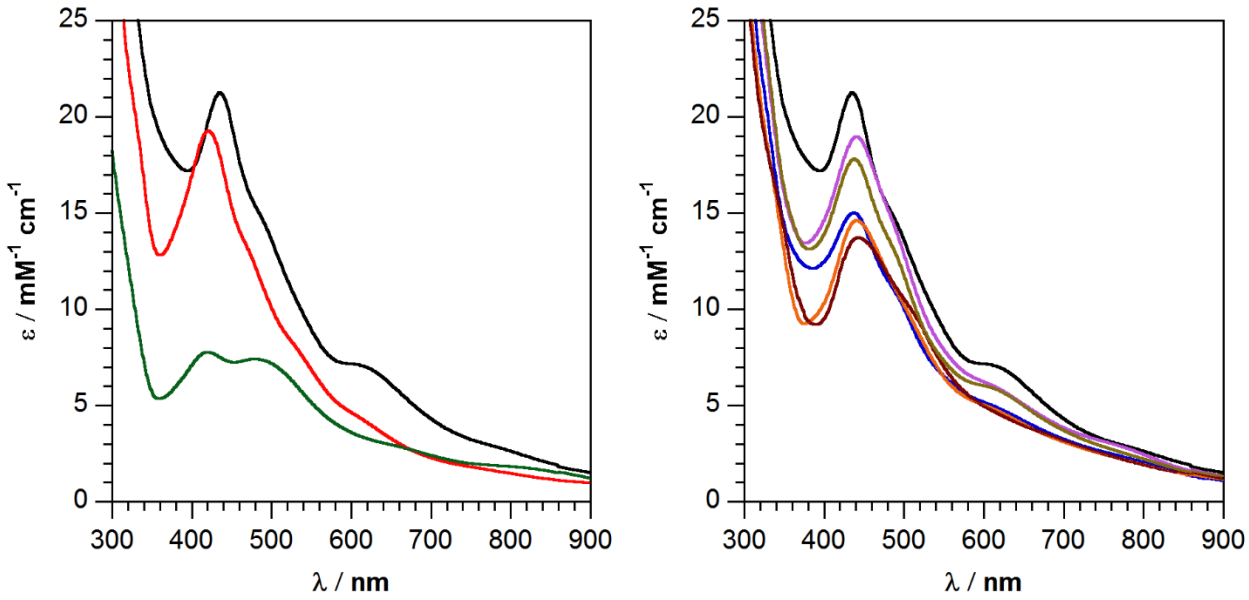

Figure 3.4. Electronic absorption spectra for (*left*) W[SNS]$_2$Ni(dppe) (**1**, black), W[SNS]$_2$Ni(depe) (**4**, red), and W[SNS]$_2$Ni(dmpe) (**5**, green); and (*right*) W[SNS]$_2$Ni(dppe) (**1**, black), W[SNS]$_2$Ni(dppp) (**6**, blue), W[SNS]$_2$Ni($P^{Ph2}N^{Ph}P^{Ph2}$) (**7**, purple), W[SNS]$_2$Ni($P^{Ph2}N^{Bn}P^{Ph2}$) (**8**, gold), W[SNS]$_2$Ni(DPEphos) (**9**, maroon), and W[SNS]$_2$Ni(dppf) (**10**, orange) collected in THF.

Table 3.3. Spectroscopic data for complexes **1** and **4-10**.

	λ / nm (ε / M^{-1} cm^{-1})[a]	^{31}P NMR (δ / ppm)[b]
W[SNS]$_2$Ni(dppe) (**1**, black)	436 (21000), 494 (sh, 14200), 616 (7100)	49.0
W[SNS]$_2$Ni(depe) (**4**, red)	421 (19300)	50.9
W[SNS]$_2$Ni(dmpe) (**5**, green)	420 (7750), 478 (7400)	31.4
W[SNS]$_2$Ni(dppp) (**6**, blue)	438 (15000), 495 (sh, 10500)	30.5
W[SNS]$_2$Ni($P^{Ph2}N^{Ph}P^{Ph2}$) (**7**, purple)	441 (19000), 497 (sh, 13000), 616 (5900)	21.2
W[SNS]$_2$Ni($P^{Ph2}N^{Bn}P^{Ph2}$) (**8**, gold)	438 (17800), 494 (sh, 12400), 616 (5800)	25.7
W[SNS]$_2$Ni(DPEphos) (**9**, maroon)	443 (13700), 515 (sh, 9700)	35.2
W[SNS]$_2$Ni(dppf) (**10**, orange)	441 (14600), 503 (sh, 10000), 610 (4850)	32.7

[a]Collected in THF. [b]Collected in $CDCl_3$.

Analogous to aforementioned **1**, complexes **4-10** display diamagnetic character and as such were readily characterized through ^{1}H and ^{31}P{^{1}H} NMR. The presence of the Ni($P^{R2}R'P^{R2}$) fragment in each case was readily established by the ^{31}P{^{1}H} NMR spectra, displaying sharp singlet resonances characteristic of symmetric phosphorus atoms ranging between 21 to 51 ppm (**Table 3.3**). In ^{1}H NMR, complexes **7** and **8** display characteristic doublet resonances

corresponding to the methylene protons of the pendent amine between 3.91 and 4.49 ppm. Similarly, **10** displayed unique resonances between 4.24 and 4.67 ppm, consistent with the proton resonances for the cyclopentadiene (Cp) rings of the ferrocenyl unit. For the $W[SNS]_2$ fragment, the ^1H NMR spectra revealed the presence of the inequivalent methyl substituents of the [SNS] backbone between 2.36 and 2.10 ppm as either a singlet (**5** and **6**, fast exchange), doublet (**4**, **7**, **8**, and **10**, intermediate exchange), or two standalone singlet (**9**, no exchange) resonances. The observance of exchange between the methyl resonances of the [SNS] backbone are indicative of fluxionality within the complexes in solution.

Electrochemistry

Cyclic voltammograms were collected on complexes **4-10** in dry, degassed THF using 1 mM analyte and 0.3 M $[Bu_4N][PF_6]$ as the supporting electrolyte revealed rich electrochemistry across the family of complexes. These studies revealed multiple one-electron reductive and oxidative processes within the THF solvent window (**Figure 3.5**). All measured potentials were referenced to $[Cp_2Fe]^{0/+}$ using an internal standard and are listed in **Table 3.4**. Complexes **4-10** exhibit two reductive events centered between −1.49 V and −2.18 V with two oxidative processes (except for **9** (DPEphos) observed between −0.62 V and 0.19 V. Substitution of the ancillary phosphine appended to the nickel center does not demonstrate a large effect on either of the reductive processes observed in **4-10** (Δ_{max} < 130 mV shift) indicating little influence from the appended nickel–phosphine adduct. This is indicative of the reductive processes demonstrating tungsten metalloligand character. The two reductive processes observed in all cases appear reversible ($i_{pc}/i_{pa} \cong 1$), while in the case of **9** and **10**, the second reductive event appears to lose its reversible character. This may indicate a structural rearrangement that is not supported by the larger chelating phosphines. Scanning beyond the second reductive process of complexes **9** and **10** gave rise to

daughter signals observed near −0.55 V. In contrast, an observable trend is discovered within the oxidative range for complexes **4-10**. Firstly, substitution of the phosphine substituents shifted the first oxidative process cathodically by up to 300 mV, consistent with the appendage of a stronger donor ligand to the nickel center to yield the observable trend of Me > Et > Ph. Secondly, variation of the phosphine linker resulted in a large anodic shift in the first oxidative process by up to 300 mV compared to **1**, indicating that the ancillary phosphine ligands act as weaker donors to the nickel center as the chelating ring is increased (dppe > dppp, $P^{Ph2}N^{Ph}P^{Ph2}$, $P^{Ph2}N^{Bn}P^{Ph2}$ > DPEphos, dppf). This results in a highly tunable oxidative process dependent on both the exchange of the phosphine substituents and the phosphine linker. These results suggest that the first oxidative process is heavily influenced by the appended ancillary phosphine appearing consistent with a nickel based event ($Ni^{I/II}$ couple).

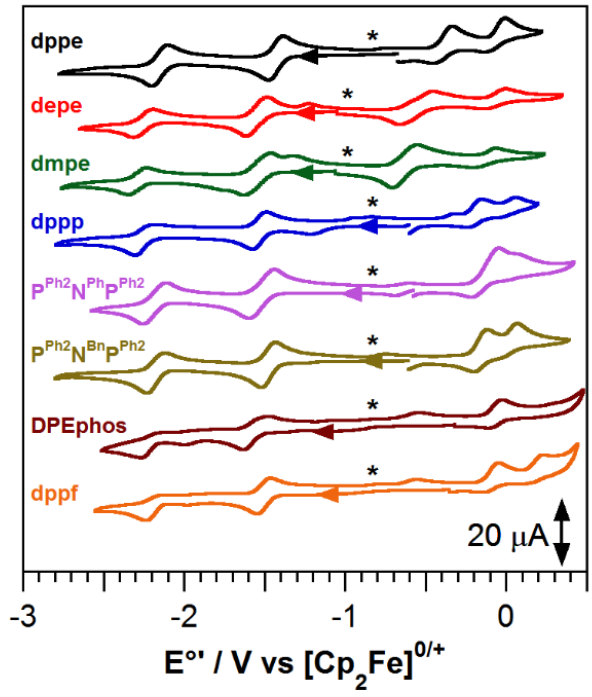

Figure 3.5. Cyclic voltammograms for W[SNS]$_2$Ni(dppe) (**1**, black), W[SNS]$_2$Ni(depe) (**4**, red), W[SNS]$_2$Ni(dmpe) (**5**, green), W[SNS]$_2$Ni(dppp) (**6**, blue), W[SNS]$_2$Ni($P^{Ph2}N^{Ph}P^{Ph2}$) (**7**, purple), W[SNS]$_2$Ni($P^{Ph2}N^{Bn}P^{Ph2}$) (**8**, gold), W[SNS]$_2$Ni(DPEphos) (**9**, maroon), and W[SNS]$_2$Ni(dppf) (**10**, orange). All CVs were recorded at a 1 mM analyte concentration in 0.3 M [NBu_4][PF_6] in dry, degassed THF under a nitrogen atmosphere using a 3 mm glassy carbon working electrode, Pt wire counter electrode, and a silver wire pseudo-reference electrode at room temperature at 50 mV sec^{-1} scan rates.

Table 3.4. Electrochemical data for **1** and **4-10** dissolved in a THF solution containing 0.3M $[NBu_4][PF_6]$.

	$E_1°'$ $[M]^{2-/1-}$	$E_2°'$ $[M]^{1-/0}$	$E_3°'$ $[M]^{0/1+}$	$E_4°'$ $[M]^{1+/2+}$
$W[SNS]_2Ni$(dppe) (**1**, black)	−2.14	−1.43	−0.32	−0.07
$W[SNS]_2Ni$(depe) (**4**, red)	−2.27	−1.56	−0.54	−0.06[b]
$W[SNS]_2Ni$(dmpe) (**5**, green)	−2.30	−1.54	−0.62	−0.10[b]
$W[SNS]_2Ni$(dppp) (**6**, blue)	−2.20	−1.49	−0.15	0.10[b]
$W[SNS]_2Ni(P^{Ph2}N^{Ph}P^{Ph2})$ (**7**, purple)	−2.18	−1.52	−0.13	0.07[b]
$W[SNS]_2Ni(P^{Ph2}N^{Bn}P^{Ph2})$ (**8**, gold)	−2.18	−1.47	−0.16	0.07[b]
$W[SNS]_2Ni$(DPEphos) (**9**, maroon)	−2.20[b]	−1.55	−0.07[b]	*a*
$W[SNS]_2Ni$(dppf) (**10**, orange)	−2.18[b]	−1.50	−0.09[b]	0.19[b]

[a]Not observed. [b]Irreversible event

Conclusion

Herein a modular synthetic approach was adopted to expand a family of tungsten–nickel heterobimetallic complexes. The goal was to investigate bidentate ancillary phosphine effects on the electronic structures of our newly formed W–Ni complexes. Solid-state structures of **4**, **7**, and **9** revealed analogous structures to aforementioned **1**, whereby a formal W–Ni bond is supported by a chelating $W[SNS]_2$ metalloligand to nickel phosphine adducts. Structural and spectroscopic evidence collected on complexes **4-10** support the assignments of a W^{V}−Ni^{I} heterobimetallic core with a metal−metal bond arising from the pairing of the odd electrons on the tungsten and nickel metal centers (note: a $W^{VI} \leftarrow Ni^{0}$ assignment also offers a similar polarization of valence electrons over the bimetallic core). Exchange of the phosphines indicate the ability to tune the first oxidative process both anodically and cathodically by up to 300 mV. A cathodic shift was observed with implementation of stronger sigma donating R-groups (ethyl and methyl) onto the phosphorus donor atoms, while an anodic shift can be obtained with increasing the length of the phosphine linker. The collected electrochemical data suggests that the donor strength of the bidentate phosphines appear to decrease as the size of the linker increases (dppe > dppp, $P^{Ph2}N^{Ph}P^{Ph2}$, $P^{Ph2}N^{Bn}P^{Ph2}$ > DPEphos, dppf). Due to the well-behaved electrochemical processes observed, it was of interest to investigate these heterobimetallic species for the activation of small molecule

substrates. To this end, $W[SNS]_2Ni(dppe)$ (**1**) was tested as a molecular catalyst for electrochemical proton reduction (**Chapter 4**).

Experimental

General Considerations. The compounds and reactions reported below show various levels of air- and moisture-sensitivity, therefore all manipulations were carried out using standard vacuum-line, Schlenk-line and glovebox techniques unless otherwise noted. Hydrocarbon and ethereal solvents were sparged with argon before being deoxygenated and dried by passage through Q5 and activated alumina columns, respectively. Halogenated solvents were sparged with argon and dried by passage through two activated alumina columns. To test for effective oxygen and water removal, aliquots of each solvent were treated with a few drops of a purple solution of sodium benzophenone ketyl radical in THF. $CDCl_3$ was dried over CaH_2 and vacuum distilled prior to use. $NiCl_2{\cdot}6H_2O$ (sigma), $NiCl_2$ (anhydrous) (sigma), 1,2-bis(diethylphosphino)ethane (depe) (sigma), 1,2-bis(dimethylphosphino)ethane (dmpe) (sigma), 1,2-bis(diphenylphosphino)propane (dppp) (sigma), 1,1'-bis(diphenylphosphino)ferrocene (dppf) (sigma), bis[(2-diphenylphosphino)phenyl]ether (DPEphos) (sigma) were all used as received. Ligands $[SNS^{cat}]H_3$[30] and $P^{Ph2}N^{R}P^{Ph2}$ (R = Ph and Bn)[25] in addition to complexes $W[SNS]_2$[30] and $Cl_2Ni(P^{R2}R'P^{R2})$[13,32] species were all prepared according to previously reported procedures.

Spectroscopic Methods. NMR spectra were collected on Bruker Avance 400 and 600 MHz spectrometers in dry, degassed $CDCl_3$. ^1H NMR spectra were referenced to TMS using the residual proteo impurities of the solvent (7.26 ppm for $CDCl_3$). All $^{31}P\{^1H\}$ NMR spectra were referenced with an external standard of phosphoric acid (H_3PO_4, 85%). Chemical shifts are reported using the standard δ notation in parts per million. Electronic absorption spectra were recorded with a Jasco V-670 absorption spectrometer as solutions in dry, degassed THF contained in 1-cm quartz

cells. Electrospray ionization mass-spectrometry (ESI-MS) data were collected on a Waters LCT Premier mass-spectrometer using dry, degassed CH_2Cl_2 or THF.

Electrochemical Methods. Electrochemical data were collected with a Gamry Series G 300 Potentiostat/Galvanostat/ZRA (Gamry Instruments, Warminster, PA, USA) using a 3.0 mm glassy carbon working electrode, a platinum wire auxiliary electrode, and a silver wire pseudo-reference electrode. Electrochemical experiments were performed at 25°C in a glovebox under an atmosphere of N_2. Electrochemical samples were 1.0 mM analyte solutions in THF containing 0.3 M $[NBu_4][PF_6]$ as the supporting electrolyte. All potentials were referenced to the $[Cp_2Fe]^{0/+}$ couple using ferrocene or decamethylferrocene as an internal standard. Ferrocene and decamethylferrocene (Acros) were purified by sublimation under reduced pressure and tetra-*n*-butylammonium hexafluorophosphate (Acros) was recrystallized from ethanol three times and dried under vacuum.

Crystallographic Methods. X-ray diffraction data were collected on a single crystal mounted on a glass fiber using paratone oil. Data was acquired using a Bruker SMART APEX II diffractometer equipped with a CCD detector at 88 K using Mo Kα radiation (λ = 0.71073 Å), which was wavelength selected with a single-crystal graphite monochromator. The SMART program package was used to determine unit-cell parameters and for data collection. The raw frame data were processed using SAINT and SADABS to yield the reflection data file. Subsequent calculations were carried out using the SHELXTL program suite. The structures were solved by direct methods and refined on F^2 by full-matrix least-squares techniques. Analytical scattering factors for neutral atoms were used throughout the analyses. Hydrogen atoms were generated in calculated positions and refined using a riding model. ORTEP diagrams were generated using *ORTEP-3* for Windows.

Table 3.5. Data collection and refinement parameters for complexes **4**, **7**, and **9**.

	$W[SNS]_2Ni(depe)$ (**4**)	$W[SNS]_2Ni(P^{Ph2}N^{Ph}P^{Ph2})$ (**7**)	$W[SNS]_2Ni(DPEphos)$ (**9**)
empirical formula	$C_{38}H_{48}N_2NiP_2S_4W$	$C_{60}H_{53}N_3NiP_2S_4W \bullet C_4H_8O$	$C_{64}H_{52}N_2NiOP_2S_4W \bullet 2(C_4H_8O)$
formula weight [g/mol]	965.52	1320.89	1442.02
crystal system	Monoclinic	Monoclinic	Monoclinic
space group	$P2_1/n$	$P2_1/n$	$P2_1/n$
T [K]	88(2)	133(2)	133(2)
a [Å]	12.363(2)	16.0044(9)	12.6066(8)
b [Å]	14.508(3)	19.5950(11)	23.1925(14)
c [Å]	22.262(4)	17.8106(10)	21.9287(13)
a [deg]	90	90	90
b [deg]	105.684(2)	92.8278(7)	101.8793(7)
g [deg]	90	90	90
V [$Å^3$]	3844.1(12)	5578.7(5)	6274.2(7)
Z	4	4	4
refl collected	45644	63970	71909
data/restr/param	9609/0/441	12307/0/689	13832/0/728
R_1 [$I > 2\sigma(I)$][a]	0.0293	0.0207	0.0294
wR_2(all data)[a]	0.0688	0.0499	0.0772
GOF[a]	1.025	1.035	1.033

[a] $R_1 = \Sigma||F_o|-|F_c|| / \Sigma|F_o|$, $wR_2 = [\Sigma[w(F_o^2-F_c^2)^2] / \Sigma[w(F_o^2)^2]\ ]^{1/2}$, $GOF = S = [\Sigma[w(F_o^2-F_c^2)^2] / (n-p)]^{1/2}$

General Synthesis of Complexes 4 and 5. A 20 mL scintillation vial was charged with a magnetic stir bar, previously isolated $K_2W[SNS]_2$, and 10 mL of dry, degassed THF. To the solution, solid $Cl_2Ni(P^{R2}R'P^{R2})$ ($P^{R2}R'P^{R2}$ = depe or dmpe) was added as a slurry in 5 mL of THF. An immediate color change was observed. The reaction mixture was stirred for three hours followed by filtration through celite on a fritted glass filter to remove KCl. The filtrate was then concentrated to 2 mL and a solid was crashed from solution using pentane (15 mL). Solid was collected on a glass frit, washed with pentane (2 x 10 mL), and dried under vacuum.

$W[SNS]_2Ni(depe)$ (4). Reagents used: $K_2W[SNS]_2$ (101 mg, 0.129 mmol, 0.992 equiv.); $Cl_2Ni(depe)$ (44 mg, 0.13 mmol, 1.0 equiv.). The filtrate was collected as a red solution prior to evaporation of the mother liquor. The complex was collected as a brown powder (60 mg, 48%). ^1H NMR (400 MHz, $CDCl_3$ (w/ TMS)) δ / ppm: 7.37 (m, 4H, aryl-H), 7.19 (m, 4H, aryl-H), 6.69

(m, 4H, aryl-H), 2.30 (d, *J*=8.41 Hz, 12H, -CH_3 [SNS]), 1.70 (m, 6H, alkyl-H), 1.56 (m, 3H, alkyl-H), 1.05 (m, 3H, alkyl-H), 0.66 (m, 6H alkyl-H), 0.51 (m, 6H, alkyl-H). ^{31}P {^1H}-NMR (162 MHz, $CDCl_3$) δ / ppm: 50.9 (s). UV-vis (THF) λ_{max} / nm (ε / $M^{-1}cm^{-1}$): 421 (19300). MS (ESI+) (CH_2Cl_2) *m/z*: 964.1 $(M)^+$, 966.1 $(M+2)^+$.

W[SNS]$_2$Ni(dmpe) (5). Reagents used: $K_2W[SNS]_2$ (101 mg, 0.129 mmol, 0.992 equiv.); $Cl_2Ni(dmpe)$ (37 mg, 0.13 mmol, 1.0 equiv). The filtrate was collected as a red solution prior to evaporation of the mother liquor. The complex was collected as a brown powder (70 mg, 59%). ^1H NMR (400 MHz, $CDCl_3$ (w/ TMS)) δ / ppm: 7.48 (m, 4H, aryl-H), 7.38 (m, 4H, aryl-H), 6.75 (m, 4H, aryl-H), 2.35 (s, 12H, -CH_3 [SNS]), 1.35 (m, 16H, alkyl-H). ^{31}P {^1H}-NMR (162 MHz, $CDCl_3$) δ / ppm: 31.4 (s). UV-vis (THF) λ_{max} / nm (ε / $M^{-1}cm^{-1}$): 420 (7750), 478 (7400). MS (ESI+) (CH_2Cl_2) *m/z*: 908.1 $(M)^+$.

General Synthesis of Complexes 6-10. To a 100 mL Schlenk flask, potassium metal and graphite were heated with a heat gun to form two equivalents of KC_8 as a bronze powder. The flask was charged with 30 mL of THF and frozen in a liquid nitrogen cold well. Upon thawing, $W[SNS]_2$ was added to the stirring solution to generate $K_2W[SNS]_2$ *in situ.* as a dark maroon solution with a yellow hue around the rim. After 10 minutes, $Cl_2Ni(P^{R2}R'P^{R2})$ was added to the solution and stirred at room temperature for one hour. The reaction mixture was filtered through celite to remove graphite and KCl and yield a dark yellow/brown filtrate. The filtrate was concentrated to roughly 5 mL and a solid was crashed out of solution using pentane. The solids were collected on a glass frit and washed with pentane (2 x 10 mL) and Et_2O (2 x 20 mL). The complexes were transferred to a 20 mL scintillation vial and dried under vacuum to yield black powders.

W[SNS]$_2$Ni(dppp) (6). Reagents used: K (25 mg, 0.64 mmol, 2.0 equiv.); C_8 (61 mg, 0.66 mmol, 2.0 equiv.); $W[SNS]_2$ (226 mg, 0.323 mmol, 1.00 equiv.); $Cl_2Ni(dppp)$ (175 mg, 0.323 mmol, 1.0

equiv.). The complex was collected as a black powder (250 mg, 66%). ^{1}H NMR (400 MHz, $CDCl_3$) δ / ppm: 7.51 (m, 4H, aryl-H) 7.43 (m, 4H, aryl-H) 7.17 (m, 4H, aryl-H) 7.11 (m, 4H, aryl-H), 7.05 (m, 4H, aryl-H), 6.98 (m, 4H, aryl-H), 6.88 (m, 4H, aryl-H), 6.56 (m, 4H, aryl-H), 2.36 (s, 12H, -CH_3 [SNS]) 2.27 (m, 6H, -CH_2). ^{31}P {^{1}H}-NMR (162 MHz, $CDCl_3$) δ / ppm: 30.5 (s). UV-vis (THF) λ_{max} / nm (ε / $M^{-1}cm^{-1}$): 438 (15000), 495 (sh, 10500). MS (ESI+) (THF) *m*/*z*: 1169.9 $(M)^+$, 1171.9 $(M+2)^+$.

W[SNS]$_2$Ni($P^{Ph2}N^{Ph}P^{Ph2}$) (7). Reagents used: K (11.5 mg, 0.294 mmol, 2.00 equiv.); C_8 (28.4 mg, 0.296 mmol, 2.00 equiv.); W[SNS]$_2$ (104 mg, 0.148 mmol, 1.00 equiv.); $Cl_2Ni(P^{Ph2}N^{Ph}P^{Ph2})$ (107 mg, 0.145 mmol, 1.00 equiv.). The complex was collected as a black powder (145 mg, 78%). ^{1}H NMR (500 MHz, $CDCl_3$) δ / ppm: 7.52 (d, *J*=7.24 Hz, 2H, aryl-H), 7.24 (br s, 4H, aryl-H), 7.18 (m, 5H, aryl-H), 7.02 (m, 13H, aryl-H), 6.83 (m, 4H, aryl-H), 6.69 (d, *J*=7.04 Hz, 2H, aryl-H), 6.57 (m, 7H, aryl-H), 4.49 (d, *J*=13.50 Hz, 2H, -CH_2), 4.31 (d, *J*=13.50 Hz, 2H, -CH_2), 2.29 (d, *J*=16.63 Hz, 12H, -CH_3 [SNS]). ^{31}P {^{1}H}-NMR (162 MHz, $CDCl_3$) δ / ppm: 21.2 (s). UV-vis (THF) λ_{max} / nm (ε / $M^{-1}cm^{-1}$): 441 (19000), 497 (sh, 13000), 616 (5900). MS (ESI+) (THF): 1247.0 $(M)^+$, 1249.0 $(M+2)^+$.

W[SNS]$_2$Ni($P^{Ph2}N^{Bn}P^{Ph2}$) (8). Reagents used: K (25 mg, 0.64 mmol, 2.0 equiv.); C_8 (63 mg, 0.66 mmol, 2.0 equiv.); W[SNS]$_2$ (224 mg, 0.320 mmol, 1.00 equiv.); $Cl_2Ni(P^{Ph2}N^{Bn}P^{Ph2}$ (200 mg, 0.323 mmol, 1.00 equiv.). The complex was collected as a black powder (215 mg, 54%). ^{1}H NMR (500 MHz, $CDCl_3$) δ / ppm: 7.29 (m, 2H, aryl-H), 7.15 (m, 10H, aryl-H), 7.04 (m, 2H, aryl-H), 6.95 (m, 10H, aryl-H), 6.81 (m, 6H, aryl-H), 6.65 (d, *J*=8.61 Hz, 2H, aryl-H), 6.51 (m, 5H, aryl-H), 3.91 (d, *J*=12.91 Hz, 2H, -CH_2), 3.82 (d, *J*=3.13 Hz, 2H, -CH_2), 3.67 (d, *J*=13.11 Hz, 2H, -CH_2), 2.29 (d, *J*=2.93 Hz, 12H, -CH_3 [SNS]). ^{31}P {^{1}H}-NMR (162 MHz, $CDCl_3$) δ / ppm: 25.7

(s). UV-vis (THF) λ_{max} / nm (ε / $M^{-1}cm^{-1}$): 438 (17800), 494 (sh, 12400), 616 (5800). MS (ESI+) (THF): 1261.0 $(M)^+$, 1263.0 $(M+2)^+$.

W[SNS]$_2$Ni(DPEphos) (9). Reagents used: K (26 mg, 0.66 mmol, 2.0 equiv.); C_8 (68 mg, 0.71 mmol, 2.0 equiv.); W[SNS]$_2$ (234 mg, 0.334 mmol, 1.00 equiv.); Cl_2Ni(DPEphos) (222 mg, 0.332 mmol, 1.00 equiv.). The complex was collected as a black powder (185 mg, 43%). ^{1}H NMR (500 MHz, $CDCl_3$) δ / ppm:. 7.46 (m, 2H, aryl-H), 7.10 (m, 4H, aryl-H), 7.03 (m, 7H, aryl-H), 6.92 (m, 6H, aryl-H), 6.78 (m, 12H, aryl-H), 6.62 (m, 2H, aryl-H), 6.53 (m, 2H, aryl-H), 6.29 (m, 3H, aryl-H), 6.11 (m, 2H, aryl-H), 2.30 (s, 6H, -CH_3 [SNS]), 2.11 (s, 6H, -CH_3 [SNS]). ^{31}P {^{1}H}-NMR (162 MHz, $CDCl_3$) δ / ppm: 35.2 (s). UV-vis (THF) λ_{max} / nm (ε / $M^{-1}cm^{-1}$): 443 (13700), 515 (sh, 9700). MS (ESI+) (THF): 1295.9 $(M)^+$, 1297.9 $(M+2)^+$.

W[SNS]$_2$Ni(dppf) (10). Reagents used: K (23.5 mg, 0.601 mmol, 2.00 equiv.); C_8 (58 mg, 0.60 mmol, 2.0 equiv.); W[SNS]$_2$ (206 mg, 0.294 mmol, 1.00 equiv.); Cl_2Ni(dppf) (200 mg, 0.293 mmol, 1.00 equiv.). The complex was collected as a black powder (209 mg, 54%). ^{1}H NMR (400 MHz, $CDCl_3$) δ / ppm: 7.15 (m, 10H, aryl-H), 6.87 (m, 18H, aryl-H), 6.66 (m, 2H, aryl-H), 6.57 (m, 2H, aryl-H), 4.67 (m, 2H, -Cp), 4.43 (m, 2H, -Cp), 4.36 (m, 2H, -Cp), 4.24 (m, 2H, -Cp), 2.30 (d, *J*=1.76 Hz, 12H, -CH_3 [SNS]). ^{31}P {^{1}H}-NMR (162 MHz, $CDCl_3$) δ / ppm: 32.7 (s). UV-vis (THF) λ_{max} / nm (ε / $M^{-1}cm^{-1}$): 441 (14600), 503 (sh, 10000), 610 (4850). MS (ESI+) (THF): 1314.1 $(M)^+$, 1316.1 $(M+2)^+$.

References

(1) Flener Lovitt, C.; Frenking, G.; Girolami, G. S. *Organometallics* **2012**, *31*, 4122–4132.
(2) Dierkes, P.; van Leeuwen, P. *J. Chem. Soc.{,} Dalt. Trans.* **1999**, 1519–1530.
(3) Tolman, C. A. *J. Am. Chem. Soc.* **1970**, *92*, 2956–2965.
(4) Müller, T. E.; Mingos, D. M. P. *Transit. Met. Chem.* **1995**, *20*, 533–539.
(5) Casey, C. P.; Whiteker, G. T.; Melville, M. G.; Petrovich, L. M.; Gavney, J. A.; Powell, D. R. *J. Am. Chem. Soc.* **1992**, *114*, 5535–5543.
(6) Kranenburg, M.; Kamer, P. C. J.; van Leeuwen, P. W. N. M.; Vogt, D.; Keim, W. *J. Chem. Soc.{,} Chem. Commun.* **1995**, 2177–2178.

(7) Gillespie, J. A.; Dodds, D. L.; Kamer, P. C. J. *Dalt. Trans.* **2010**, *39*, 2751–2764.
(8) Dubois, D. L.; Miedaner, A. *Inorg. Chem.* **1986**, 4642–4650.
(9) Minahan, D. M. A.; Hill, W. E.; McAuliffe, C. A. *Coord. Chem. Rev.* **1984**, *55*, 31–54.
(10) Miedaner, A.; Haltiwanger, R. C.; Dubois, D. L. *Inorg. Chem.* **1991**, 417–427.
(11) Guerrero, J.; Cortez, L.; Lemus, L.; Farías, L.; Costamagna, J.; Pettinari, C.; Rossi, M.; Caruso, F. *Inorganica Chim. Acta* **2010**, *363*, 3809–3816.
(12) McCormick, T.; Jia, W.-L.; Wang, S. *Inorg. Chem.* **2006**, *45*, 147–155.
(13) Busby, R.; Hursthouse, M. B.; Jarrett, P. S.; Lehrnann, C. W.; Malik, K. M. A.; Phillips, C. *J. Am. Chem. Soc. Dalt. Trans* **1993**, 3767–3770.
(14) Ramakrishna, D.; Bhat, B. R. *Inorg. Chem. Commun.* **2011**, *14*, 690–693.
(15) Grutters, M. M. P.; Müller, C.; Vogt, D. *J. Am. Chem. Soc.* **2006**, *128*, 7414–7415.
(16) Shavaleev, N. M.; Adams, H.; Best, J.; Weinstein, J. a. *J. Organomet. Chem.* **2007**, *692*, 921–925.
(17) Housecroft, C. E.; Shaykh, B. A. M.; Rheingold, A. L.; Haggerty, B. S. *Inorg. Chem.* **1991**, *30*, 125–130.
(18) Lassahn, P.; Lozan, V.; Wu, B.; Weller, S.; Janiak, C. *Dalton Trans.* **2003**, 4437–4450.
(19) Berners-Price, S. J.; Johnson, R. K.; Mirabelli, C. K.; Faucette, L. F.; McCabe, F. L.; Sadler, P. J. *Inorg. Chem.* **1987**, *26*, 3383–3387.
(20) Trost, B. M.; Murphy, D. J. *Organometallics* **1985**, *4*, 1143–1145.
(21) Hayashi, T.; Konishi, M.; Kobori, Y.; Kumada, M.; Higuchi, T.; Hirotsu, K. *J. Am. Chem. Soc.* **1984**, *106*, 158–163.
(22) Hayashi, T.; Tamao, K.; Katsuro, Y.; Nakae, I.; Kumada, M. *Tetrahedron Lett.* **1980**, *21*, 1871–1874.
(23) Kawabata, Y.; Hayashi, T.; Ogata, I. *J. Chem. Soc.{,} Chem. Commun.* **1979**, 462–463.
(24) Tolman, C. A. *Chem. Rev.* **1977**, *77*, 313–348.
(25) Kilgore, U. J.; Roberts, J. a S.; Pool, D. H.; Appel, A. M.; Stewart, M. P.; DuBois, M. R.; Dougherty, W. G.; Kassel, W. S.; Bullock, R. M.; DuBois, D. L. *J. Am. Chem. Soc.* **2011**, *133*, 5861–5872.
(26) Carroll, M. E.; Barton, B. E.; Gray, D. L.; Mack, A. E.; Rauchfuss, T. B. *Inorg. Chem.* **2011**, *50*, 9554–9563.
(27) Redin, K.; Wilson, A. D.; Newell, R.; DuBois, M. R.; DuBois, D. L. *Inorg. Chem.* **2007**, *46*, 1268–1276.
(28) Schilter, D.; Rauchfuss, T. B.; Stein, M. *Inorg. Chem.* **2012**, *51*, 8931–8941.
(29) Cordero, B.; Gómez, V.; Platero-Prats, A. E.; Revés, M.; Echeverría, J.; Cremades, E.; Barragán, F.; Alvarez, S. *Dalton Trans.* **2008**, 2832–2838.
(30) Shaffer, D. W.; Szigethy, G.; Ziller, J. W.; Heyduk, A. F. *Inorg. Chem.* **2013**, *52*, 2110–2118.
(31) Stiefel, E. I.; Brown, G. F. *Inorg. Chem.* **1972**, *11*, 434–436.
(32) Standley, E. A.; Smith, S. J.; Müller, P.; Jamison, T. F. *Organometallics* **2014**, *33*, 2012–2018.

Chapter 4

Electrochemical Proton Reduction Studies with the Recently Developed W[SNS]$_2$Ni(dppe) Heterobimetallic Complex

Portions of this work have been reported previously:

Rosenkoetter, Kyle E.; Ziller, Joe W.; Heyduk, Alan F., A Heterobimetallic W-Ni Complex Containing a Redox-Active W[SNS]$_2$ Metalloligand. *Inorganic Chemistry* ***2016***, *55, 6794-6798.*

Introduction

Production of carbon-neutral chemical fuels (i.e., H_2) using earth abundant metal centers is a fundamental requirement to sustain the global demand imposed by the world's energy infrastructure.[1] Hydrogen is particularly of great interest due to its renewability when generated from the reduction of protons (ideally from water).[2] Although platinum and the Fe–Ni and Ni–Ni hydrogenases are excellent catalysts for hydrogen activation, their high cost (Pt) and usability (hydrogenase enzymes) limit their widespread effectiveness.[1] Controlling the intermolecular movement of protons using first row transition metal centers is a necessity for catalytic processes that require multiple equivalents of protons and electrons (i.e. $2H^+ + 2e^- \rightarrow H_2$).[3] This sort of process is performed at ease in hydrogenase enzymes through specific channels of proton relays that facilitate the exchange of protons between the catalyst active site and the surrounding protein matrix.[3]

The incorporation of sulfur into transition metal complexes have continued to be heavily investigated since the 1960s, due to their ubiquitous presence nature.[12–16] Structural integrity of metal–sulfur containing complexes in addition to their often reversible redox behavior has driven research to explore thiolate containing complexes for multielectron transformations.[12–17] As of late, Holland *et al*. and Jones *et al.* have demonstrated the ability to generate square planar cobalt and nickel complexes supported by one (Jones) or two (Holland) 1,2-benzenedithiol (bdt) moieties.[12,16] Jones supported their nickel system through the incorporation of a bidentate ancillary phosphine ligand (dppf).[16] Both groups demonstrated these thiolate derived complexes as highly active electrochemical proton reduction catalysts in non-aqueous solutions.[12,16]

Research continues to develop and investigate new synthetic complexes that incorporate pendent bases, or proton relays, into the second coordination sphere.[3–5] Recently, work has been

done to generate hydrogenase mimics through first row transition metal centers supported by redox-active cofactors with a azadithiolate moiety positioned to induce proton shuttling.[6–8] Similarly, groups at the Pacific Northwest National Lab (PNNL) have demonstrated the ability to generate square-planar nickel(II) complexes supported by bidentate phosphine ligands that incorporate a pendent amine strategically positioned to allow facile proton shuttling to the metal center.[9] Specifically positioned bases in this second coordination sphere have proven to increase the rates of intra- and intermolecular proton transfer in addition to activating other small molecules such as H_2 and CO.[3,8,10,11]

Based on literature precedent, our previously discussed W[SNS]$_2$Ni(dppe) (**1**, **Chapter 2**) complex was treated with an acid source to study the activity of the heterobimetallic complex towards electrochemical proton reduction in non-aqueous solutions. With the complex containing a redox-active metalloligand coordinated to a low-valent first-row transition metal ion supported by an ancillary phosphine, it stands to reason that the species may show enhanced metal–metal cooperativity to reduce small molecule substrates, in this case protons to hydrogen.

Results and Discussion

Proton Reduction Studies of W[SNS]$_2$Ni(dppe) (1) in THF

Cyclic voltammetry experiments carried out on THF solutions of W[SNS]$_2$Ni(dppe) with the addition of acid (4-cyanoanilinium tetrafluoroborate, $pK_a^{MeCN} = 7.0$)[3] resulted in the observation of a catalytic reduction process coincident with the first reduction of the heterobimetallic complex. **Figure 4.1** shows the effect of added 4-cyanoanilinium tetrafluoroborate on the cyclic voltammogram of W[SNS]$_2$Ni(dppe). At 2.5 mM acid concentration and a scan rate of 50 mV sec^{-1}, a catalytic reduction process was observed, with $E_{cat} = -1.38$ V versus $[Cp_2Fe]^{+/0}$ ($E_{cat/2} = -1.33$ V). Further additions of acid resulted in a continued increase in catalytic current until

reaching a plateau after the addition of 40 mM acid, demonstrating that catalysis is no long hindered by the acid concentration in solution (i.e. acid-independent). Throughout the acid addition experiments, the two oxidative processes for $W[SNS]_2Ni(dppe)$ remain essentially unchanged.

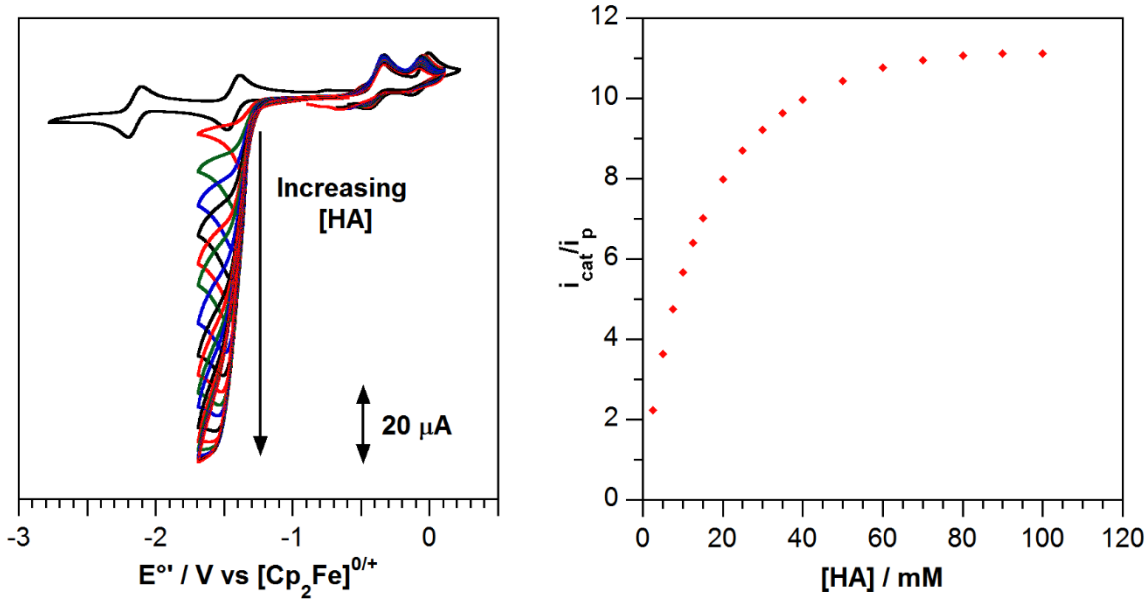

Figure 4.1. (*left*) Cyclic voltammograms of 1.0 mM $W[SNS]_2Ni(dppe)$ in THF containing 0.3 M $[Bu_4N][PF_6]$ with increasing concentrations of 4-cyanoanilinium tetrafluoroborate, $[HA][BF_4]$ (0-100 mM); (*right*) The ratio of catalytic current to the current in the absence of added acid (i_{cat}/i_p) as a function of the acid concentration. Data were collected using a glassy carbon working electrode at a scan rate of 50 mV sec^{-1}.

The shape of the catalytic wave is consistent with catalysis under purely kinetic conditions in which the consumption of acid is competitive with its diffusion to the electrode. Increasing acid concentrations resulted in an increase in the cathodic current, which eventually plateaued at an i_{cat}/i_p value of 11, as shown in **Figure 4.1**. In this acid-independent regime, the pseudo-first-order rate constant (k_{obs}) for proton reduction is 12 sec^{-1}, as calculated from the scan rate (ν), the number of electrons transferred (n = 2 for the reduction of protons to hydrogen), the ideal gas constant (R), the temperature (T), and Faraday's constant (F), according to **Equation 4.1**.[18–21]

$$\frac{i_{cat}}{i_p} = \frac{n}{0.4463}\sqrt{\frac{RTk_{obs}}{nFv}} \qquad \textbf{(4.1)}$$

Under the same conditions, but in the absence of $W[SNS]_2Ni(dppe)$, proton reduction at the glassy-carbon electrode was observed only at potentials more negative than −2 V, vs $[Cp_2Fe]^{+/0}$ (**Figure 4.2**). To ensure that the catalysis did not originate with the deposition of a heterogeneous catalyst onto the electrode surface,[22,23] immediately following cyclic voltammetry experiments the electrode was removed from solution, gently rinsed with clean solvent, and placed in an acid solution with no added $W[SNS]_2Ni(dppe)$. Subsequent cyclic voltammogram experiments demonstrated proton reduction only at potentials below −2 V (**Figure 4.2**). Further electrochemical experiments employing only the $W[SNS]_2$ component or various Ni(dppe) sources did not afford the same electrocatalysis as that observed for $W[SNS]_2Ni(dppe)$. While these experiments cannot unequivocally rule out the presence of nanoparticle catalysts, together they suggest that the heterobimetallic complex acts as a molecular catalyst for proton reduction.

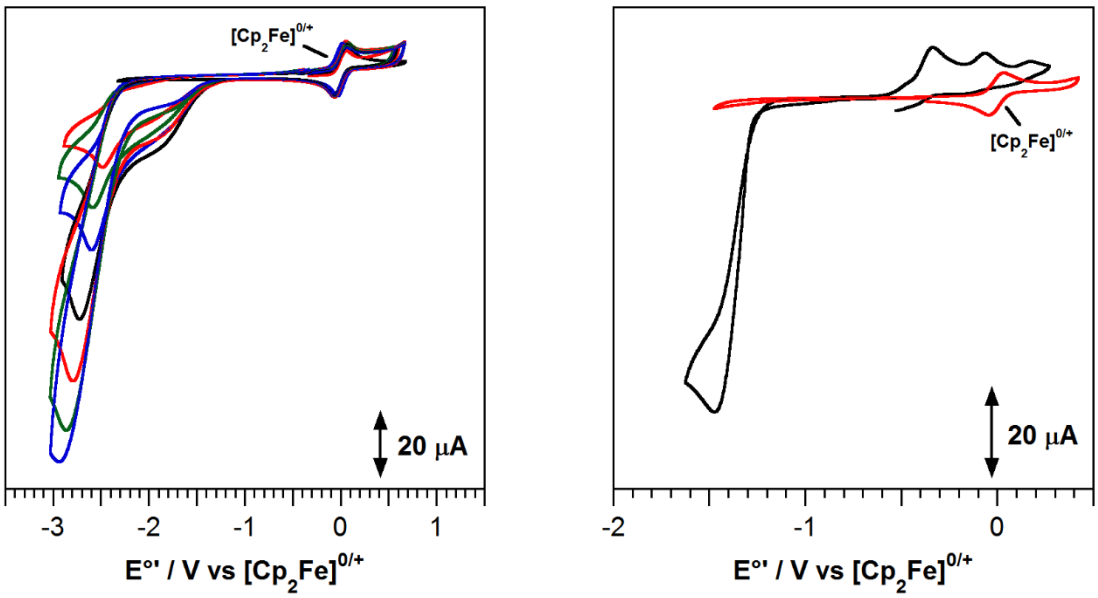

Figure 4.2. (*left*) Cyclic voltammograms collected of 4-cyanoanilinium tetrafluoroborate (HA, 0-25 mM) in the absence of catalyst in THF; (*right*) Cyclic voltammograms collected of (black) 1 mM catalyst in the presence of 25 mM HA and (red) after electrode has been gently washed with THF and placed in a fresh THF solution in the presence of ferrocene/electrolyte and 25 mM HA. All CVs were recorded at a 1 mM analyte concentration in 0.3 M $[NBu_4][PF_6]$. All scans were performed under a nitrogen atmosphere using a 3 mm glassy carbon working electrode, Pt wire counter electrode, and silver wire pseudo-reference electrode at room temperature. All CVs were collected at 50 mV sec^{-1} scan rates.

Catalyst dependence studies (**Figure 4.3**) confirm a direct relationship between the current and catalyst concentration. This is evident from the observed linear dependence in the acid-dependent regions (0-15 mM) in which doubling the catalyst loadings doubled the catalytic current observed. Similarly, the acid-independent regions appear to double in current intensity as the catalyst concentration is doubled. This result further suggests that the complex is acts as a molecular catalyst for the reduction of protons to hydrogen in non-aqueous solutions.

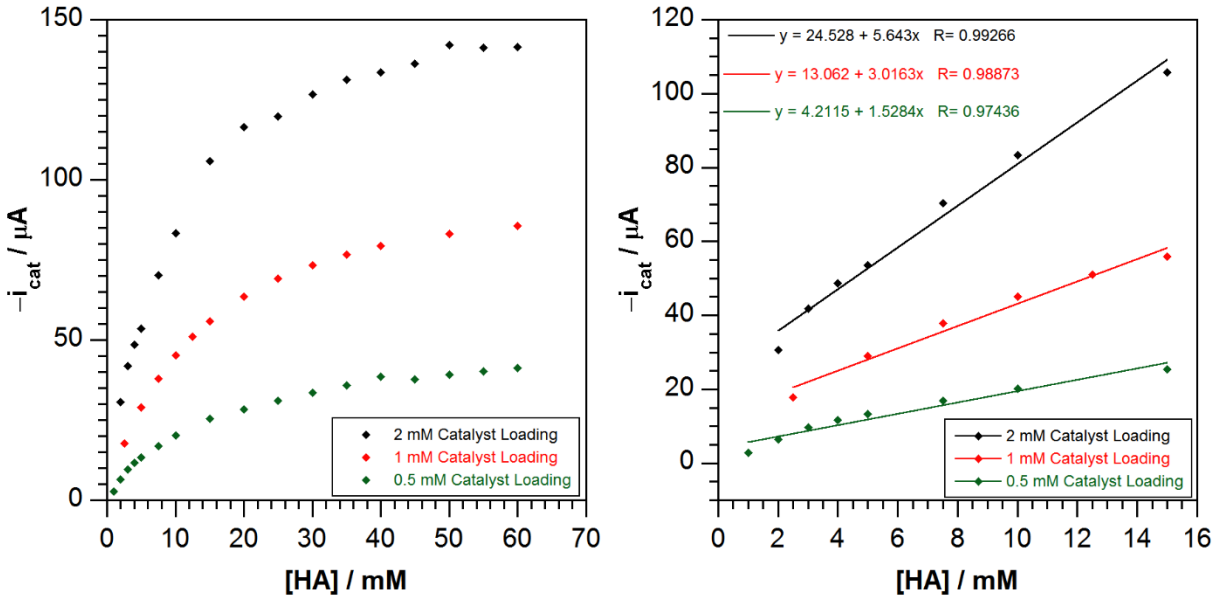

Figure 4.3. (*left*) Peak current ($-i_{cat}$) vs 4-cyanoanilinium tetrafluoroborate (0-60 mM) taken in the presence of (black) 2.0 mM, (red) 1.0 mM, and (green) 0.5 mM W[SNS]$_2$Ni(dppe) in THF; (*right*) Zoom-in on acid-dependent region of $-i_{cat}$ vs [HA] (0-15 mM). Cyclic voltammograms were recorded in 0.3 M [NBu$_4$][PF$_6$] in dry, degassed THF under a nitrogen atmosphere using a 3 mm glassy carbon working electrode, Pt wire counter electrode, and silver wire pseudo-reference electrode at room temperature at 50 mV sec^{-1} scan rates.

Proton Reduction Studies for W[SNS]$_2$Ni(dppe) (1) in MeCN

Due to the sparingly soluble nature of the complex in MeCN, an electronic absorption study (UV-vis) was performed to determine the concentration of a completely saturated analyte solution in MeCN. To this end, a concentrated stock solution of W[SNS]$_2$Ni(dppe) in 5.0 mL of THF (16.5 mg, 0.014 mmol, 2.85 mM) was generated to establish a calibration curve in MeCN. By diluting aliquots of the stock THF solution to 5 mL in MeCN, a three point calibration curve (inset, **Figure**

4.4) was obtained to determine the maximum solubility of W[SNS]$_2$Ni(dppe) in MeCN. The complex concentration was determined by monitoring the characteristic charge transfer band at 436 nm (ε = 16,300 $M^{-1}cm^{-1}$, **Figure 4.4**). Based on the results of two trials, the concentration for a saturated MeCN solution was found to be 0.16 mM. It is important to note that no distinguishable differences were observed from allowing the suspensions to stir for more than 30 minutes (**Table 4.1**). As a precaution, a ^{1}H and ^{31}P NMR spectra were also collected on a CD_3CN solution of W[SNS]$_2$Ni(dppe) to verify complex integrity was maintained.

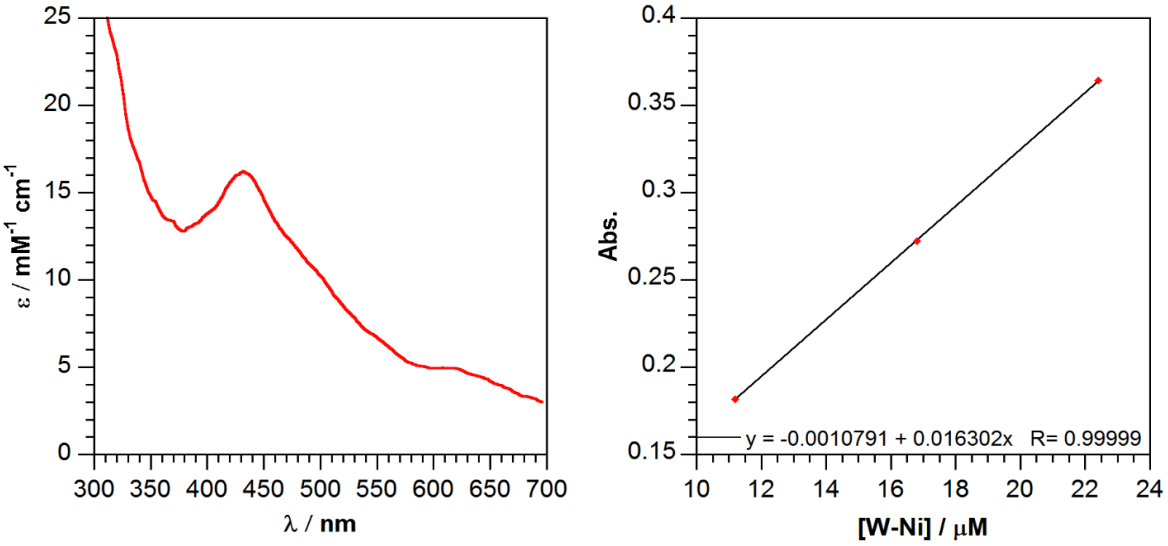

Figure 4.4. (*left*) Electronic absorption for W[SNS]$_2$Ni(dppe) (**1**) collected in MeCN with a characteristic charge transfer band at 436 nm (ε = 16,300 $M^{-1}cm^{-1}$); (*right*) Three point calibration curve for extinction coefficient determination.

Table 4.1. Experimental values obtained for a saturated solution of W[SNS]$_2$Ni(dppe) in MeCN.

Trial (#)	Stir Time (hr)	Amount of Solvent (mL)	Abs (λ_{max} = 436 nm)	W[SNS]$_2$Ni(dppe) (mmol)	W[SNS]$_2$Ni(dppe) (mM)
1	0.5	10	0.494	0.00152	0.15
2	24	30	0.566	0.00521	0.17
				Average:	0.16 mM

Electrochemical studies (CV and DPV) performed on a completely saturated MeCN solution of **1** revealed very similar traces to those collected in THF solution. **Figure 4.5** demonstrates cyclic voltammograms (CV) collected on a 1 mM analyte THF solution and a 0.16 mM analyte MeCN solution. Similarly, a differential pulse voltammogram (DPV) collected on a 0.16 mM

MeCN solution of W[SNS]$_2$Ni(dppe) was obtained to confirm the observed events in the CV (**Figure 4.5**). Cyclic voltammetry revealed two reductive and two oxidative events, consistent with the electrochemical processes observed in a THF solution. The reductive events occur at −1.93 and −1.29 V, while the oxidative processes are observed at −0.40 and 0.61 V, vs $Cp_2Fe^{0/+}$. The reductive processes are shifted 200 mV more positive (anodically) in MeCN, likely due to solvent effects.

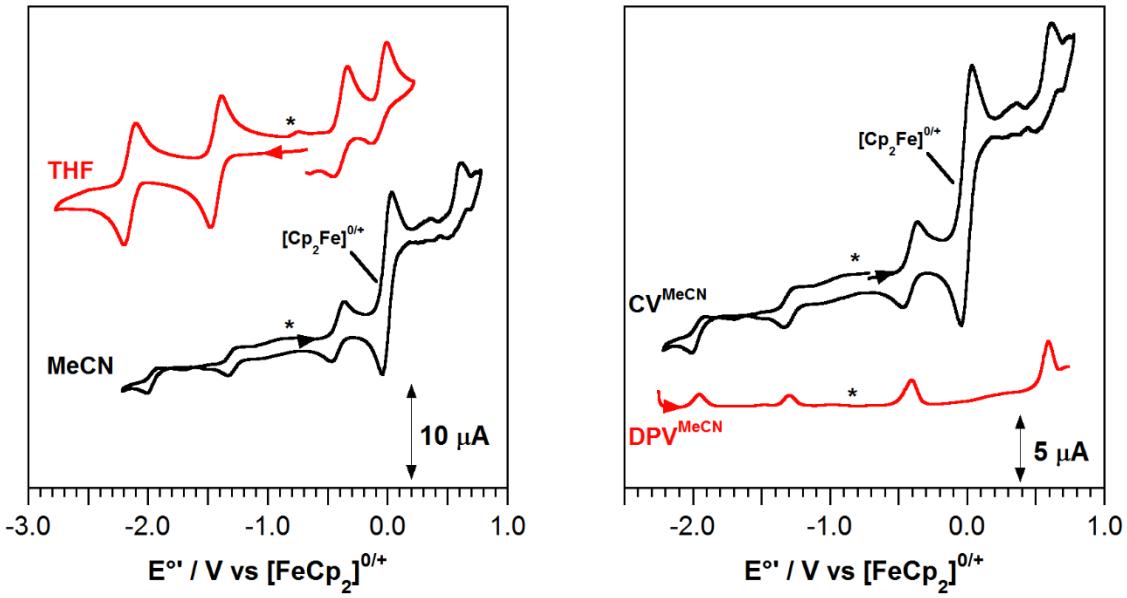

Figure 4.5. (*left*) Cyclic voltammograms of (red) 1 mM W[SNS]$_2$Ni(dppe) in THF (0.3 M [NBu$_4$][PF$_6$]) and (black) 0.16 mM W[SNS]$_2$Ni(dppe) in MeCN; (*right*) (black) Cyclic voltammogram and (red) differential pulse voltammogram (DPV) for 0.16 mM W[SNS]$_2$Ni(dppe) in MeCN. All scans were recorded in 0.1 M [NBu$_4$][PF$_6$] in dry, degassed MeCN under a nitrogen atmosphere using a 3 mm glassy carbon working electrode, Pt wire counter electrode, and silver wire pseudo-reference electrode at room temperature. CVs were collected at 50 mV sec^{-1} scan rates.

Table 4.2. Electrochemical data for W[SNS]$_2$Ni(dppe) in THF and MeCN solutions containing 0.1M [NBu$_4$][PF$_6$].

	E_1°' $[M]^{2-/1-}$	E_2°' $[M]^{1-/0}$	E_3°' $[M]^{0/1+}$	E_4°' $[M]^{1+/2+}$
W[SNS]$_2$Ni(dppe)^{THF}	−2.14	−1.43	−0.32	0.05
W[SNS]$_2$Ni(dppe)^{MeCN}	−1.93	−1.29	−0.40	0.61[a]

[a]Irreversible event

Cyclic voltammetry experiments carried out on MeCN solutions of W[SNS]$_2$Ni(dppe) with the addition of acid (4-cyanoanilinium tetrafluoroborate, pK_a^{MeCN} = 7.0)[3] resulted in the observation

of a catalytic reduction process coincident with the first reduction of the heterobimetallic complex. **Figure 4.6** shows the effect of added 4-cyanoanilinium tetrafluoroborate on the cyclic voltammogram of W[SNS]$_2$Ni(dppe). Additions of acid resulted in a continued increase in catalytic current until a plateau was reached after the addition of 100 mM acid, demonstrating that catalysis is no long hindered by the acid concentration in solution (i.e. acid-independent). Throughout the acid addition experiments, the two oxidative processes for W[SNS]$_2$Ni(dppe) remain essentially unchanged. The data revealed an E_{cat} = −1.25 V ($E_{cat/2}$ = −1.14 V) versus $[Cp_2Fe]^{+/0}$, with an i_{cat}/i_p ratio of 14 and a calculated k_{obs} = 19 sec^{-1}. The data collected are qualitatively similar to the THF results (E_{cat} = −1.38 V ($E_{cat/2}$ = −1.33 V), i_{cat}/i_p = 11, and k_{obs} = 12 sec^{-1}).

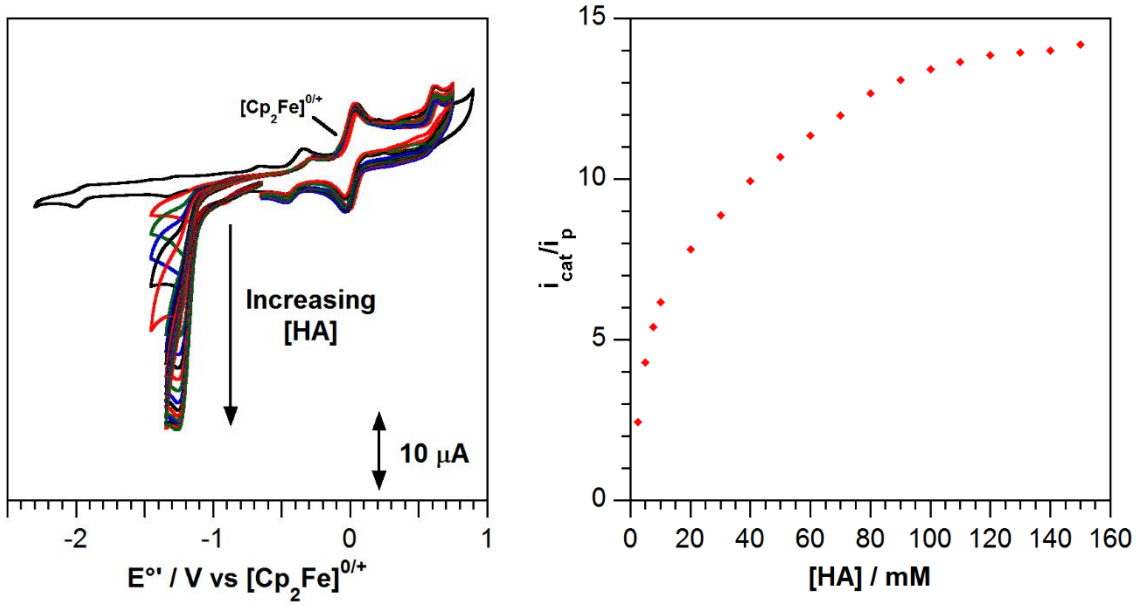

Figure 4.6. (*left*) Cyclic voltammograms of 0.16 mM W[SNS]$_2$Ni(dppe) in MeCN containing 0.1 M $[Bu_4N][PF_6]$ with increasing concentrations of 4-cyanoanilinium tetrafluoroborate, $[HA][BF_4]$ (0-150 mM); (*right*) The ratio of catalytic current to the current in the absence of added acid (i_{cat}/i_p) as a function of the acid concentration. Data were collected using a glassy carbon working electrode at a scan rate of 50 mV sec^{-1}.

To verify that the complex is still acting as a molecular catalyst, blank trials in MeCN solutions were performed to confirm that the observed catalytic activity is not due to electrodeposition of nanoparticles to the electrode surface. To this end, acid titration experiments were conducted using

4-cyanoanilinium tetrafluoroborate (0-25 mM) in an MeCN solution with supporting electrolyte in the presence of ferrocene. As observed in **Figure 4.7**, catalytic onsets begin to grow in at potentials more negative of −1.6 V, vs. $[Cp_2Fe]^{0/+}$, in MeCN (E_{cat} = −2.30 V). This is consistent with the glassy carbon electrode reducing protons to generate hydrogen.[23] Additionally, a dip test was performed to eliminate electrodeposition of a heterogeneous material upon to the electrode surface as the active catalyst. This was performed in the same fashion as all other CV-based acid titrations, however, after the addition of 25 mM acid, the electrode was removed, rinsed gently with MeCN, and placed in a new electrolyte solution containing 25 mM of acid and Cp_2Fe. Following this step, no catalytic wave was observed within the desired window, consistent with the absence of heterogeneous material deposited on the electrode surface acting as the active catalyst. This suggests that complex **1** acts as a molecular catalyst for proton reduction at the observed potential (E_{cat}) −1.25, vs $[Cp_2Fe]^{0/+}$, in MeCN.

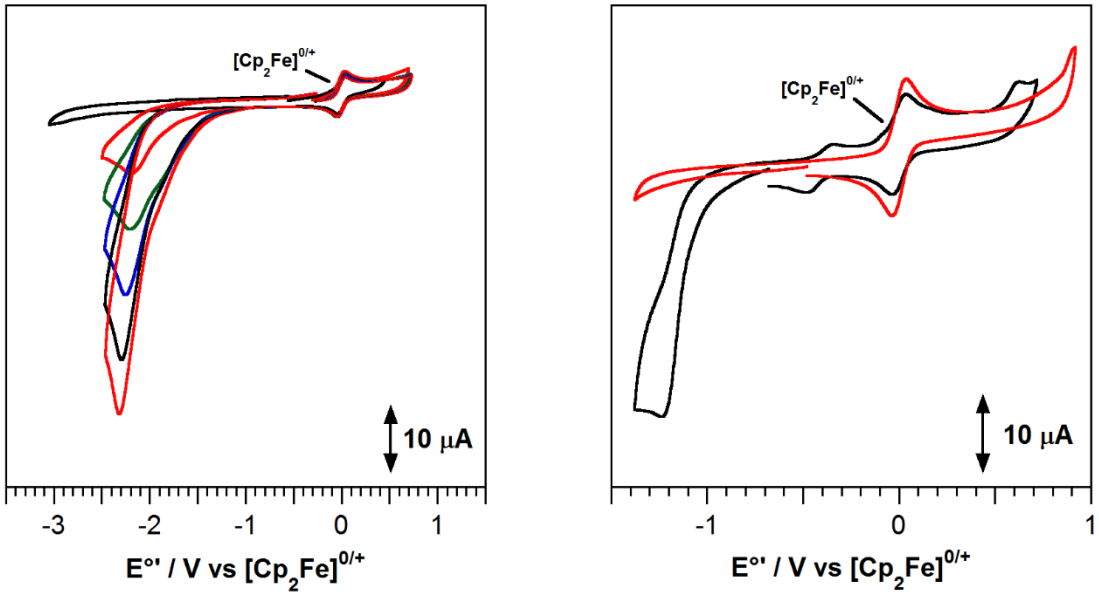

Figure 4.7. (*left*) Cyclic voltammograms collected of 4-cyanoanilinium tetrafluoroborate (HA, 0-25 mM) in the absence of catalyst in MeCN; (*right*) Cyclic voltammograms collected of (black) 0.16 mM catalyst in the presence of 25 mM HA and (red) after electrode has been gently washed with MeCN and placed in a fresh MeCN solution in the presence of ferrocene/electrolyte and 25 mM HA. All CVs were recorded at a fully saturated analyte concentration (0.16 mM) in 0.1 M $[NBu_4][PF_6]$. All scans were performed under a nitrogen atmosphere using a 3 mm glassy carbon working electrode, Pt wire counter electrode, and silver wire pseudo-reference electrode at room temperature. All CVs were collected at 50 mV sec^{-1} scan rates.

k_{obs}, TOF, and Overpotential in THF and MeCN

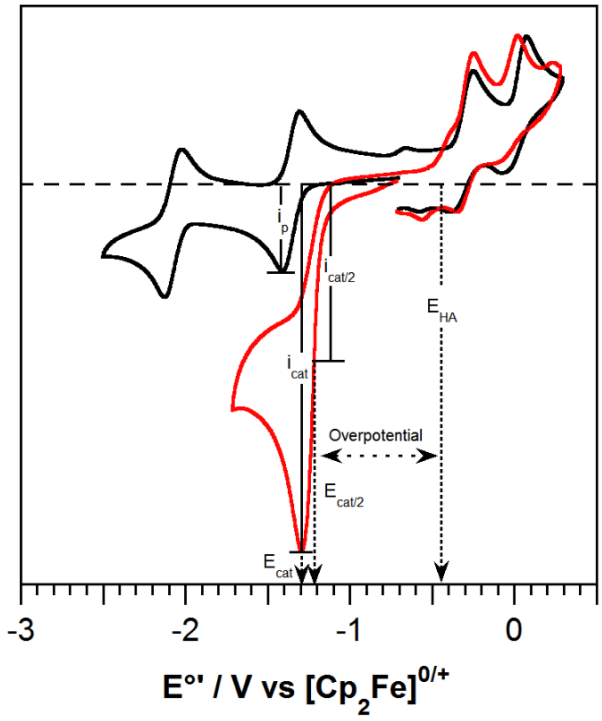

Figure 4.8. Illustrated guide used to determine the k_{obs} and overpotential (η) for experimentally collected CVs. Shown with CVs collected in THF. Actual E_{HA} in THF for 4-cyanoanilinium tetrafluoroborate cannot be calculated as the pK_a for this acid in THF is unknown. E_{HA} shown above is the thermodynamic potential for 4-cyanoanilinium tetrafluoroborate in MeCN (−0.442 V).

Analysis of the collected cyclic voltammograms of catalyst with and without acid (HA) present allow for the determination of the catalytic rate constant (k_{obs}), turnover frequency (TOF), and calculated overpotential. **Figure 4.8** demonstrates an illustrated guide to understanding the necessary aspects of the catalytic response towards determining these factors. The scans shown below were collected from a THF solution of W[SNS]$_2$Ni(dppe). The catalytic current (i_{cat}) is defined as the max current in the presence of acid, while i_p is defined as the current passed in the absence of acid. The overpotential can then be determined from the difference of the half-wave potential ($E_{cat/2}$) and the thermodynamic potential needed to reduce protons to hydrogen in non-aqueous solutions (E_{HA}). Unfortunately, the overpotential cannot be calculated in THF solutions due to the pK_a of 4-cyanoanilinium tetrafluoroborate not being known, therefore, the

thermodynamic potential (E_{HA}) for 4-cyanoanilinium tetrafluoroborate is reported herein as an MeCN solution (−0.442 V).[2]

Using **Figure 4.8** as a guide, the rate constant (k_{obs}) and turnover frequency (TOF) observed for complex **1** in THF and MeCN solutions could be determined. The observed rate constant was calculated using aforementioned **Equation 4.1**, whereby the ratio of the catalytic current (i_{cat}) to the peak current in the absence of acid (i_p) can be obtained from the acid containing cyclic voltammogram traces. Using n = 2 for the number of electrons, a maximum k_{obs} of 12 sec^{-1} is achievable in the presence of 100 mM acid concentration at 50 mV sec^{-1} scan rates in THF solutions. Similarly, a maximum k_{obs} of 19 sec^{-1} can be obtained in the presence of 150 mM acid concentration at 50 mV sec^{-1} scan rates in MeCN solutions. The turnover frequency (TOF) of the complex can be obtained from the acid independent region (plateau) of the i_{cat}/i_p plots (**Figures 4.1** and **4.6**), giving TOFs of 11 sec^{-1} and 14 sec^{-1} in THF and MeCN, respectively, at a scan rate of 50 mV sec^{-1}.

The overpotential for a molecular electrocatalyst for H_2 production is defined as the difference between the thermodynamic potential for the reduction of an acid (BH^+) and the potential for the observed catalytic wave ($E_{cat/2}$).[2,24] The thermodynamic potential for an acid source (E_{HA}) is defined by the standard state potential for the H^+/H_2 couple ($E°_{H+/H2}$) and the pK_a of the acid source. Using $E°_{H+/H2}$ = −0.028 V, vs $[Cp_2Fe]^{0/+}$ in MeCN,[2] in conjunction with the pK_a of 4-cyanoanilinium tetrafluoroborate (pK_a^{MeCN} = 7.0),[3] the thermodynamic potential (E_{HA}) can be calculated as −0.442 V using **Equation 4.2**. Furthermore, subtracting the catalytic wave ($E_{cat/2}$) from the thermodynamic potential for the acid (E_{HA}), the overpotential (η, **Equation 4.3**) needed to achieve proton reduction was determined to be 700 mV in MeCN. The overpotential was not calculated in THF as the pK_a of 4-cyanoanilinium tetrafluoroborate is unknown in THF.

$$E_{HA} = E^{\circ}_{H^+/H_2} - \left(\frac{2.303RT}{F}\right)(pK_a(BH^+)) \quad \textbf{(4.2)}$$

$$\eta = \left|E_{cat/2} - E_{HA}\right| \quad \textbf{(4.3)}$$

While natural hydrogenase enzymes operate at low overpotentials (<100 mV) and very fast turnover frequencies for the reduction of protons to hydrogen, great strides have been made towards optimizing molecular catalyst to mimic these biological systems.[2,12] Monometallic nickel electrocatalysts observed in the literature reveal overpotentials that range from 220 mV to 470 mV and turnover frequencies as slow as < 1 sec^{-1} or as fast as 170,000 sec^{-1} with greater than 95% faradaic efficiency.[1,3,12,9] Despite these low overpotentials and fast turnover frequencies, these systems do not utilize a heterobimetallic core, as such they become less comparable to complex **1**. Recently, however, a tungsten-localized proton-reduction electrocatalyst was reported for the superficially similar complex $(CO)_4W(pdt)Ni(dppe)$ (pdt^{2-} = 1,3-propanedithiolate) which demonstrated similar attributes in potential ($E_{cat/2} = -1.21$), $i_{cat}/i_p = 15.4$, and turnover frequency (47 sec^{-1}).[25]

Controlled Potential Coulometry in MeCN

Controlled-potential electrolysis (CPE) experiments were conducted to identify the product of proton reduction and determine the Faradaic efficiency. Attempts to carry out CPE in a THF solution resulted in solvent polymerization within the counter-electrode compartment (due to the high acid concentrations and long electrolysis times).[26,27] CPE experiments were carried out at −1.0 V on a 30 mL MeCN solution containing 0.16 mM $W[SNS]_2Ni(dppe)$, 3.7 mM acid (23 equiv), and 0.1 M $[Bu_4N][PF_6]$ electrolyte (see experimental section for further details). A gas sample of the headspace was collected by a gastight syringe and analyzed by gas chromatography with thermal conductivity detection (GC-TCD) which confirmed the production of hydrogen gas with a Faradaic yield of 80 ± 3%.

Analysis of the current versus time plot over the course of CPE experiments suggest catalyst decomposition (**Figure 4.9**). At early electrolysis times, the catalyst turnover rate is high, as indicated by the high current; however, the activity decreases over the course of the experiment until it appears completely deactivated after 2000 sec. Headspace analysis as a function of time confirmed that hydrogen production occurs early in the electrolysis, before decomposition of the heterobimetallic complex. Spectroscopic analyses of the final solution from the CPE trials demonstrated the loss of the charge transfer band at 436 nm that is diagnostic for the $W[SNS]_2Ni(dppe)$ complex.

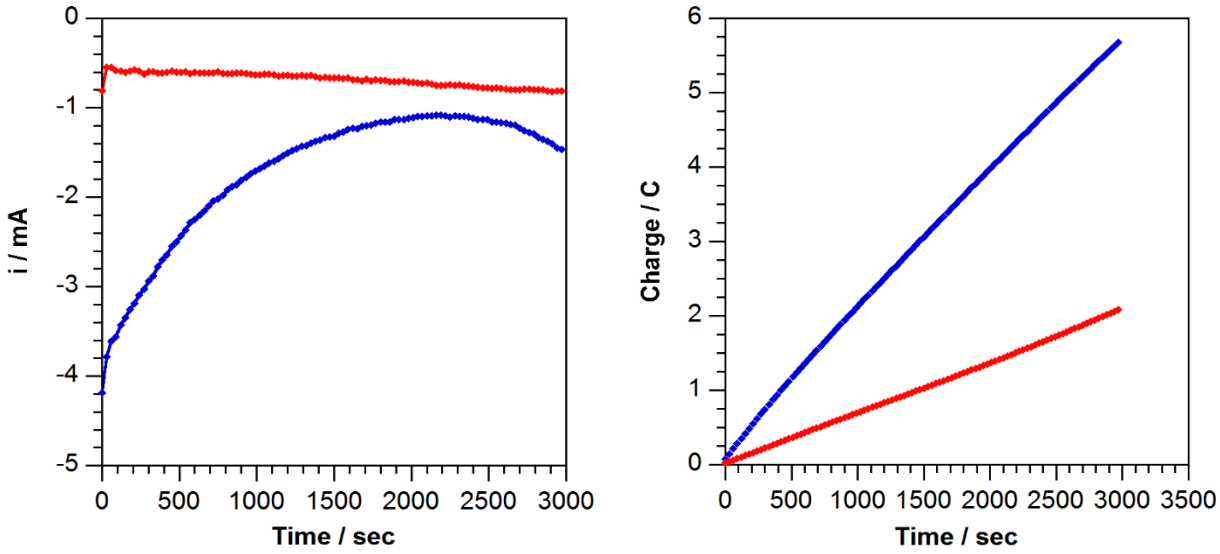

Figure 4.9. (*left*) Average sample current vs. time plot; and (*right*) average charge vs. time plot. Each case displaying (red) blank CPE experiment in the absence of catalyst and (blue) CPE experiment in the presence of 0.16 mM catalyst.

Table 4.3. Bulk electrolysis data collected with and without blank correction.

	Q_{trial} (C)	Theoretical Yield of H_2 (µmol)	Catalyst (µmol)	H_2 (µmol)	Headspace (% H_2)	Duration (sec)	Faradaic Yield (%)	TON (s^{-1})
Raw Data (Avg)	5.895	30.5	4.8	19.4	0.194	3000	63 ± 1	4.0
Blank (Avg)	2.08	10.8	–	3.61	0.036	3000	–	–
Corrected Data	3.815	19.8	4.8	15.8	0.158	3000	80 ± 3	3.3

Faradaic Yield Calculations

The Faradaic yield for an electrocatalyst can be determined through **Equations 4.4-4.8**. Data analysis of the elution plots were performed using the program Agilent OpenLab, whereby the integration of the curve associated with H_2 elution was obtained. This area in conjunction with a calibration curve (**Figure 4.9**) yielded the percentage of hydrogen present in the headspace post-electrolysis. By correcting for any Faradaic/non-Faradaic charge passed and any hydrogen produced in the absence of catalyst, the average values collected from blank trials were subtracted from the experimental values to determine the Faradaic yield for the system. Using a calibration curve developed prior to electrolysis (**Figure 4.9**), the percentage of H_2 in the headspace of the bulk electrolysis cell was obtained through the use of **Equation 4.4**.

$$y = 562.23x - 26.313 \quad \textbf{(4.4)}$$

$$62.2551 = 562.23X - 26.313$$

$$X = 0.158\ \%\ H_2\ produced$$

The percentage of H_2 can then be converted to the volume (L) of H_2 produced through multiplication by the available headspace volume of the electrolysis cell using **Equation 4.5** (total electrolysis cell volume obtained prior to experiment through mass difference using DI water).

$$\left(\frac{0.158\ \%}{100}\right) * \left[\begin{matrix}(Headspace\ volume) = \\ 283\ mL\ (Total\ cell\ volume) - 11.3\ mL\ (counter\ compartment) - 27\ mL\ (solvent\ and\ electrodes)\end{matrix}\right]$$

$$\left(\frac{0.158\%}{100}\right) * (0.2447\ L) = 3.85\ x\ 10^{-4}\ L\ H_2\ produced \quad \textbf{(4.5)}$$

Using the ideal gas law, **Equation 4.6**, the liters of H_2 produced can be converted into moles of H_2 generated, assuming a constant 1 atm of pressure inside the cell. Using Henry's law, at 1 atm and 298 K, the solubility of H_2 in MeCN was found to be negligible under our conditions (~7.9 x 10^{-8} moles) and was therefore excluded from calculations.[28]

$$PV = nRT \quad \textbf{(4.6)}$$

$$(1\ atm) * (3.85\ x\ 10^{-4}\ L) = n\left(0.082 \frac{atmL}{molK}\right)(298.15\ K)$$

$$n = 1.578\ x\ 10^{-5}\ moles\ of\ H_2\ produced$$

Now that the moles of H_2 produced from the bulk electrolysis experiment are known, the theoretical amount of moles of H_2 that could be generated based on the total amount of current passed (3.815 C after subtraction of the blank trial) can be calculated using **Equation 4.7**. In addition, the faradaic yield of the catalyst can be determined through the use of **Equation 4.8**. Using these equations, heterobimetallic complex **1** was found to act as a molecular catalyst for the electrochemical reduction of protons to hydrogen with a Faradaic yield of 80 ± 3 %.

$$Theo.Moles = 3.815\ C * \left(\frac{1\ F}{96485\ C}\right) * \left(\frac{1\ mole\ electron}{1\ F}\right) * \left(\frac{1\ mole\ H_2}{2\ mole\ electrons}\right) \quad \textbf{(4.7)}$$

$$= 1.977\ x\ 10^{-5}\ Theoretical\ Moles\ H_2\ Produced$$

$$\left(\frac{1.578\ x\ 10^{-5}\ moles\ H_2\ generated}{1.977\ x\ 10^{-5}\ Theo.moles\ H_2}\right) * 100 = 79.79\ \%\ Faradaic\ Yield \quad \textbf{(4.8)}$$

Conclusion

Coordination of the $W[SNS]_2$ unit to the nickel center imbues the heterobimetallic complex with rich redox properties at mild potentials, therefore the $W[SNS]_2$ fragment can be viewed as a redox-active metalloligand within the complex. These redox properties enable the complex to function as an electrocatalyst for the reduction of protons to hydrogen in non-aqueous solution. At this point, little is known regarding the mechanism of proton reduction. While the electrochemical data suggest that one-electron reduction of $W[SNS]_2$Ni(dppe) precedes protonation, the locus of protonation and subsequent hydrogen evolution is unclear. Two distinct possibilities are (*i*) that proton reduction occurs at the nickel center, which is well-known for monometallic nickel phosphine complexes[3,16,29] or (*ii*) that proton reduction occurs at the tungsten center.[25,30] One aspect that refutes the former is that the nickel centers capable of proton reduction are often times unsaturated square-planar nickel complexes, where the nickel ion in our species is a coordinatively

saturated tetrahedral nickel center. Closer examination of the previously mentioned $(CO)_4W(pdt)Ni(dppe)$ complex revealed a square-planar, nickel(II) metalloligand bound to an electron-rich tungsten(0) carbonyl fragment.[25] While this electron distribution might favor protonation at tungsten, the $W[SNS]_2Ni(dppe)$ complex reported here is oppositely polarized, with an electron-rich nickel center and an electron-poor tungsten. In this case, it seems unlikely that proton reduction would occur at the tungsten metal ion; however, it may still be possible for proton reduction to occur at the non-bridging thiolate sulfur donors, distal to the nickel center, as has been observed for ruthenium complexes with thiolate ligands.[31] Similarly, protonation of one of the nitrogen atoms of the [SNS] scaffold cannot be ruled out as a potential site for protonation to occur.

Experimental

General Considerations. The compounds and reactions reported show various levels of air- and moisture-sensitivity, therefore all manipulations were carried out using standard vacuum-line, Schlenk-line and glovebox techniques unless otherwise noted. Hydrocarbon and ethereal solvents were sparged with argon before being deoxygenated and dried by passage through Q5 and activated alumina columns, respectively. Halogenated solvents were sparged with argon and dried by passage through two activated alumina columns. To test for effective oxygen and water removal, aliquots of each solvent were treated with a few drops of a purple solution of sodium benzophenone ketyl radical in THF. The ligand and complexes: $[SNS^{cat}]H_3$,[32] $W[SNS]_2$,[32] $Cl_2Ni(dppe)$,[33] $W[SNS]_2Ni(dppe)$,[34] and 4-cyanoanilinium tetrafluoroborate[35] were all prepared according to previously reported procedures.

Characterization Methods. Electronic absorption spectra were recorded with a Jasco V-670 absorption spectrometer or a Cary 60 UV-vis spectrometer equipped with fiber optic cables to allow for samples to remain under an inert atmosphere as solutions in dry, degassed THF or MeCN contained in 1-cm quartz cells.

Electrochemical Methods. Electrochemical data were collected with a Gamry Series G 300 Potentiostat/Galvanostat/ZRA (Gamry Instruments, Warminster, PA, USA) using a 3.0 mm glassy carbon working electrode, a platinum wire auxiliary electrode, and a silver wire pseudo-reference electrode. Electrochemical experiments were performed at 25°C in a glovebox under an atmosphere of N_2. Electrochemical samples were 1.0 mM (0.16 mM in MeCN) analyte solutions in THF containing 0.3 M (0.1 M in MeCN) $[NBu_4][PF_6]$ as the supporting electrolyte. All potentials were referenced to the $[Cp_2Fe]^{0/+}$ couple using ferrocene or decamethylferrocene as an internal standard. Ferrocene and decamethylferrocene (Acros) were purified by sublimation under reduced pressure and tetra-*n*-butylammonium hexafluorophosphate (Acros) was recrystallized from ethanol three times and dried under vacuum.

Blank Trials. Blank studies were performed to verify that the observed catalytic activity is due to the complex and not the glassy carbon working electrode. To this end, acid titration experiments were conducted using 4-cyanoanilinium tetrafluoroborate (0-25 mM) in electrolyte solutions of THF or MeCN in the presence of ferrocene. As observed in **Figure 4.2** and **4.7**, catalytic responses peak at potentials more negative of −2 V vs. $[Cp_2Fe]^{0/+}$ in THF (E_{cat} = −2.71 V) and MeCN (E_{cat} = −2.30 V), consistent with the glassy carbon electrode reducing protons to generate hydrogen. Additionally, a dip test concluded that no catalytic wave was observed within the desired window, consistent with the absence of a heterogeneous deposit on the electrode surface performing the proton reduction at potentials (E_{cat}) −1.51 and −1.26 V, vs $[Cp_2Fe]^{0/+}$, in THF and MeCN, respectively.

GC-TCD Instrument Parameters. Headspace analyses were performed using an Agilent 7890B GC system equipped with a thermal conductivity detector (TCD) to quantitatively determine the percent of molecular hydrogen generated during bulk electrolysis experiments. The GC-TCD

system was equipped with a HP-Molesieve (Cat. # 19095P-MS6) column of 30 m length, 0.530 mm diameter, and having a 25 µm film. The method used for H_2 separation consisted of a 4 minute run with an inlet temperature of 200°C (splitless), a detector temperature of 220°C, a 40°C isotherm, and a flow rate of 4.7 mL min^{-1} for the nitrogen carrier gas. The retention time of molecular hydrogen under these conditions was 2.26 min (**Figure 4.10**). Hydrogen was quantified for the method using a calibration curve which was generated from injecting six known volumes of H_2 into the sealed bulk electrolysis vessel under 1 atm of N_2 and allowed to stir and mix for 15 minutes. After 15 minutes, a 1.6 mL sample of the headspace was removed using a gastight syringe. Eight 200 µL injections were then made at each percentage of H_2 to give a linear fit of y = 562.23x – 26.313 (**Figure 4.10**). Between CPE sample trials, a burnoff run was performed to remove MeCN vapors from the column by heating the oven to 250°C for 60 minutes.

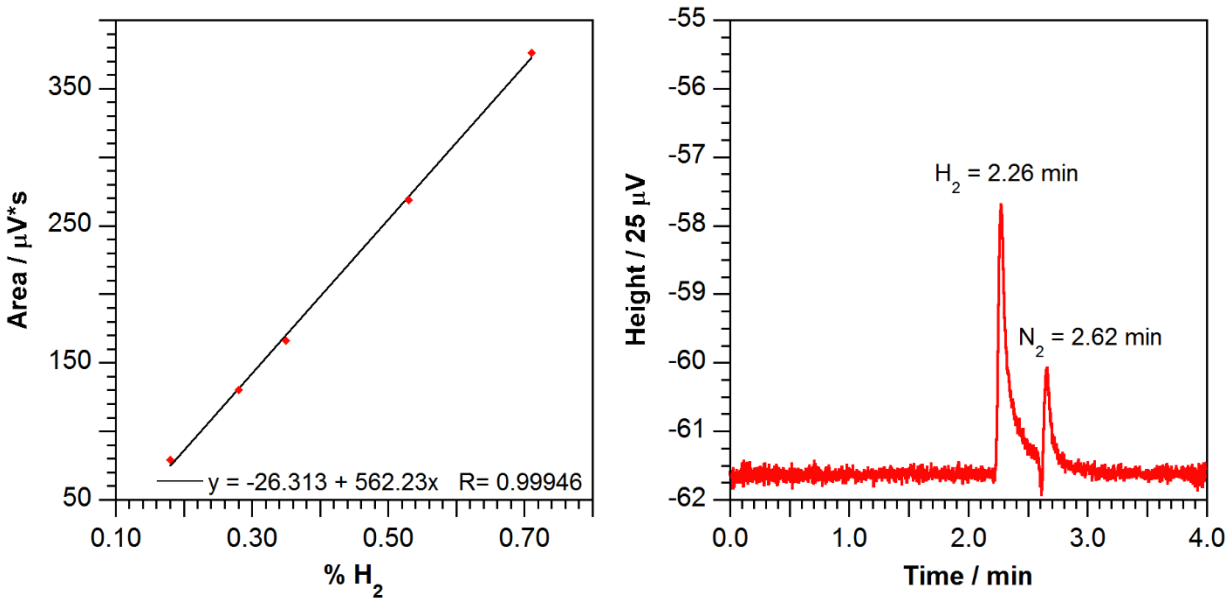

Figure 4.10. (*left*) Calibration curve utilized to determine percentage of H_2 produced during CPE experiments; and (*right*) Sample GC-TCD spectra obtained post-electrolysis.

Controlled Potential Electrolysis (CPE). Controlled-potential electrolysis experiments were carried out on an MeCN solution (0.1 M $[Bu_4N][PF_6]$) under a nitrogen atmosphere using a

standard three-electrode setup in a five-neck flask having a total volume of 283 mL (including 11.3 mL for the counter compartment). The five-neck flask was assembled under a strong flow of nitrogen with two of the necks accepting an electrode connected to a tungsten lead through a nickel sleeve that had been sealed through a 14/20 ground glass stopper. The counter electrode was fed through a pierced septum in its own custom sealed fritted tube. The other two necks were covered using one fresh ribbed rubber septum and one flow adaptor which were used for sampling the headspace and for inlet/outlet purging of nitrogen, respectively. The working electrode consisted of a copper wire attached to a reticulated vitreous carbon cylinder; the reference electrode was a Ag wire placed in a 1 mm glass tube terminated by a Vycor fritted disk and filled with MeCN/electrolyte (0.1 M $[NBu_4][PF_6]$) solution; and the counter electrode consisted of a copper wire attached to a reticulated vitreous carbon cylinder in a 10 mm glass tube terminated with a fine fritted disk and filled with 1-2 mL of the CPE solution. A saturated analyte solution (0.16 mM) was made by suspending 10 mg of $W[SNS]_2Ni(dppe)$ in 30 mL of MeCN/electrolyte and stirred for 30 minutes. The undissolved solid was filtered away and the filtrate was collected into a fresh 50 mL round bottom flask, sealed with a septum and taped closed. A solution of 4-cyanoanilinium tetrafluoroborate (23 mg, ~23 eq.) in 1.0 mL of dry, degassed MeCN was made in a 20 mL scintillation vial, capped with a large inverted septum and taped. Both solutions were prepared in the glovebox. The catalyst and electrolyte solution were then cannula transferred to the CPE vessel, after which an initial cyclic voltammogram was obtained. A syringe transfer of the acid solution to the CPE vessel was then conducted. A second cyclic voltammogram was taken to determine the electrolysis potential for the experiment. Controlled potential coulometry was performed at −1.00 V for 3000 sec using this approach. After 3000 seconds, a 1.6 mL sample of the headspace was removed via gastight syringe. Eight 200 µL injections were analyzed by GC-

TCD. Using the moles of H_2 produced and the charge passed, taking into account the blank trials which demonstrated some faradaic (spongy carbon induced proton reduction) and non-faradaic charge being passed during electrolysis, a Faradaic yield could be calculated for H_2 production (**Table 4.3**).

References

(1) Hoffert, W. a; Roberts, J. a S.; Morris Bullock, R.; Helm, M. L. *Chem. Commun. (Camb).* **2013**, *49*, 7767–7769.
(2) Bullock, R. M.; Appel, A. M.; Helm, M. L. *Chem. Commun. (Camb).* **2014**, *50*, 3125–3143.
(3) Kilgore, U. J.; Roberts, J. a S.; Pool, D. H.; Appel, A. M.; Stewart, M. P.; DuBois, M. R.; Dougherty, W. G.; Kassel, W. S.; Bullock, R. M.; DuBois, D. L. *J. Am. Chem. Soc.* **2011**, *133*, 5861–5872.
(4) Tereniak, S. J.; Carlson, R. K.; Clouston, L. J.; Young, V. G.; Bill, E.; Maurice, R.; Chen, Y.-S.; Kim, H. J.; Gagliardi, L.; Lu, C. C. *J. Am. Chem. Soc.* **2014**, *136*, 1842–1855.
(5) Cooper, B. G.; Fafard, C. M.; Foxman, B. M.; Thomas, C. M. *Organometallics* **2010**, *29*, 5179–5186.
(6) Rauchfuss, T. B. *Acc. Chem. Res.* **2015**, *48*, 2107–2116.
(7) Bourrez, M.; Steinmetz, R.; Gloaguen, F. *Inorg. Chem.* **2014**, *53*, 10667–10673.
(8) Smith, S. E.; Yang, J. Y.; DuBois, D. L.; Bullock, R. M. *Angew. Chem. Int. Ed. Engl.* **2012**, *51*, 3152–3155.
(9) Wiese, S.; Kilgore, U. J.; Ho, M. H.; Raugei, S.; Dubois, D. L.; Bullock, R. M.; Helm, M. L. *ACS Catal.* **2013**, *3*, 2527–2535.
(10) Appel, A. M.; Pool, D. H.; Hagan, M. O.; Shaw, W. J.; Yang, J. Y.; Dubois, M. R.; Dubois, D. L.; Bullock, R. M. *J. Am. Chem. Soc.* **2011**, *1*, 777–785.
(11) Yang, J. Y.; Bullock, R. M.; Dougherty, W. G.; Kassel, W. S.; Twamley, B.; DuBois, D. L.; Rakowski DuBois, M. *Dalt. Trans.* **2010**, *39*, 3001–3010.
(12) Mcnamara, W. R.; Han, Z.; Alperin, P. J.; Brennessel, W. W.; Holland, P. L.; Eisenberg, R. *J. Am. Chem. Soc.* **2011**, 15368–15371.
(13) Sproules, S.; Wieghardt, K. *Coord. Chem. Rev.* **2010**, *254*, 1358–1382.
(14) Rabaça, S.; Almeida, M. *Coord. Chem. Rev.* **2010**, *254*, 1493–1508.
(15) Herich, P.; Kameníček, J.; Kuča, K.; Pohanka, M.; Olšovský, M. *Polyhedron* **2009**, *28*, 3565–3569.
(16) Gan, L.; Groy, T. L.; Tarakeshwar, P.; Mazinani, S. K. S.; Shearer, J.; Mujica, V.; Jones, A. K. *J. Am. Chem. Soc.* **2015**, *137*, 1109–1115.
(17) DuBois, M. R. *Chem. Rev.* **1989**, *89*, 1–9.
(18) Pool, D. H.; Stewart, M. P.; O'Hagan, M.; Shaw, W. J.; Roberts, J. A. S.; Bullock, R. M.; DuBois, D. L. *Proc. Natl. Acad. Sci. U. S. A.* **2012**, *109*, 15634–15639.
(19) Savéant, J.-M. *Chem. Rev.* **2008**, *108*, 2348–2378.
(20) Saveant, J. M.; Vianello, E. *Electrochim. Acta* **1965**, *10*, 905–920.
(21) Nicholson, R. S.; Shain, I. *Anal. Chem.* **1964**, *36*, 706–723.
(22) Fang, M.; Engelhard, M. H.; Zhu, Z.; Helm, M. L.; Roberts, J. A. S. *ACS Catal.* **2014**, *4*,

90–98.
(23) McCarthy, B. D.; Martin, D. J.; Rountree, E. S.; Ullman, A. C.; Dempsey, J. L. *Inorg. Chem.* **2014**, *53*, 8350–8361.
(24) Appel, A. M.; Lee, S.-J.; Franz, J. A.; DuBois, D. L.; Rakowski DuBois, M.; Twamley, B. *Organometallics* **2009**, *28*, 749–754.
(25) Schilter, D.; Fuller, A. L.; Gray, D. L. *Eur. J. Inorg. Chem.* **2015**, *2015*, 4638–4642.
(26) Dey, A. N.; Rudd, E. J. *J. Electrochem. Soc.* **1974**, *121*, 1294–1298.
(27) Pruckmayr, G.; Wu, T. K. *Macromolecules* **1978**, *11*, 662–668.
(28) Brunner, E. *J. Chem. Eng. Data* **1985**, *30*, 269–273.
(29) Wilson, A. D.; Newell, R. H.; McNevin, M. J.; Muckerman, J. T.; Rakowski DuBois, M.; DuBois, D. L. *J. Am. Chem. Soc.* **2006**, *128*, 358–366.
(30) Schilter, D.; Rauchfuss, T. B.; Stein, M. *Inorg. Chem.* **2012**, *51*, 8931–8941.
(31) Haddad, A. Z.; Kumar, D.; Ouch Sampson, K.; Matzner, A. M.; Mashuta, M. S.; Grapperhaus, C. A. *J. Am. Chem. Soc.* **2015**, *137*, 9238–9241.
(32) Shaffer, D. W.; Szigethy, G.; Ziller, J. W.; Heyduk, A. F. *Inorg. Chem.* **2013**, *52*, 2110–2118.
(33) Busby, R.; Hursthouse, M. B.; Jarrett, P. S.; Lehrnann, C. W.; Malik, K. M. A.; Phillips, C. *J. Am. Chem. Soc. Dalt. Trans* **1993**, 3767–3770.
(34) Rosenkoetter, K. E.; Ziller, J. W.; Heyduk, A. F. *Inorg. Chem.* **2016**, *55*, 6794–6798.
(35) Appel, A. M.; DuBois, D. L.; DuBois, M. R. *J. Am. Chem. Soc.* **2005**, *127*, 12717–12726.

Chapter 5

Heterobimetallic Complexes of Cobalt and Copper Containing a Redox-Active W[SNS]$_2$ Metalloligand

Introduction

Metal−metal bonds present interesting opportunities in coordination chemistry to investigate new functionality for transition-metal complexes.[1] Although the field of coordination chemistry is primarily dominated by homometallic metal complexes, the ability to tether two different metal centers (heterobimetallic) has allowed for a larger scope of exploration into metal−metal bonds.[2] The formation of bonds between metal centers is often a delicate process as the same electronic properties that allow metal−ligand bonding to occur also allow for direct metal-to-metal interactions through formation of covalent, polar covalent, or dative bonds.[1,3] This often requires the valence orbitals involved to be sufficiently diffuse to afford substantial orbital overlap, however, a competition arises between binding additional ligands or a second metal center.[4] The strength of a metal–metal bond is largely dependent on the number of available electrons and the radial and angular properties of the valence orbitals involved in bonding.[2–4] This overlap can stem from a weak interaction that can barely be viewed as a bond to a strong covalent interaction capable of forming multiple bonds (i.e. double, triple, or quadruple).[2–4] Unfortunately, the formation of a metal–metal bond often times leads to ambiguous metal oxidation state assignments. This has led to controversy in electronic structure theory, particularly where orbital overlap is weak despite the electrons being strongly coupled with one another.[2,4–6] Currently, molecular metal–metal bonding is largely characterized through X-ray crystallography whereby the intermetallic bond distance defines the metal–metal interaction for the complex, however, this method tends to break down with the incorporation of redox-active metal centers.[2]

Over the last 50 years research has continued to thoroughly investigate the role of metal–metal bonds in catalysis as they have been implicated as a common structural motif in both molecular catalysis and active-sites of enzymes.[2,7–10] The metal–metal interaction observed in these types of

systems play a large role in tuning the activity and/or selectivity of the catalyst.[1] A common example of metal–metal bond containing intermediates in coordination chemistry can be observed in catalytic C–H bond functionalization, demonstrating that metal–metal cooperativity is necessary to achieve catalytic turnover.[2,11,12] In biology, the Ni−Fe hydrogenase active site is thought to have a short-lived Ni–Fe interaction forming an integral intermediate for the evolution of H_2 as the metal–metal bond stabilizes the intermediate within the catalytic cycle and serves as a proton acceptor.[2,3,7,13,14]

This unique feature of a formal metal–metal bond has been prevalent within all aforementioned complexes (**1-10**), however, investigation of the substitution of the metal center for non-group 10 metal ions has not been studied within our heterobimetallic systems. To this end, we sought to synthesize and characterize first-row analogs of the previously discussed W[SNS]$_2$Ni(dppe) heterobimetallic complex (**1**) through the substitution of the appended nickel center for cobalt and copper to investigate the effects of metal exchange on the metal–metal interaction. Similarly, ligand effects were investigated with exchange of 1,2-bis(diphenylphosphino)ethane (dppe) for 4,4-di-t-butyl-bipyridine (dtbbpy) to monitor the effects of incorporating a harder, bidentate nitrogen containing donor ligand on the metal–metal distance in copper containing complexes.

Results and Discussion

Synthesis and Structural Characterization of Complexes 11-13.

A heterobimetallic complex of the formula W[SNS]$_2$Co(dppe) (**11**) was synthesized using a similar approach as previously described in **Chapters 2** and **3** (**Scheme 5.1**). ESI-MS data confirmed the formation of the neutral bimetallic complex with a parent ion signal at a *m/z* value of 1160 ($(M+H)^+$). A byproduct of this reaction is a five-coordinate monometallic cobalt center supported by a single [SNS] and dppe ligand. This complex is discussed in detail in **Appendix B**.

Efforts to isolate a single crystal of **11** for X-ray diffraction techniques were unsuccessful, however, a solid-state structure of the product of the stoichiometric reduction of **11** with an equivalent of decamethylcobaltocene ([Cp_2*Co]) afforded an immediate color change to generate **11**$^{-}$. ESI-MS data confirmed the formation of the reduced species with a parent ion signal (negative mode) at a *m/z* value of 1159 ($(M)^{-}$). Single crystals of **11**$^{-}$ were obtained by slow diffusion of a concentrated analyte solution of THF into diethyl ether at room temperature.

Scheme 5.1. Synthesis of heterobimetallic complexes **11** and **11**$^{-}$.

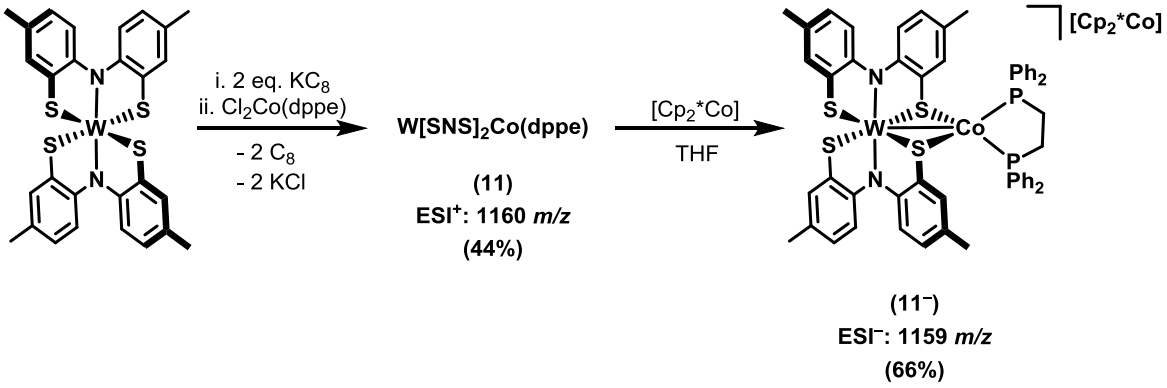

X-ray diffraction studies on single crystals of **11**$^{-}$ revealed a bimetallic complex with a W–Co bond supported by two bridging thiolate donors from the W[SNS]$_2$ metalloligand, isostructural to the previously investigated Ni analog (**1**). **Figure 5.1** shows the structure of **11**$^{-}$ as an ORTEP diagram and a table of bond lengths and angles are provided in **Table 5.1**. The bimetallic complex is best described as a W[SNS]$_2$ unit bound as a chelating ligand to a Co(dppe) fragment. The cobalt center is four-coordinate (disregarding the W–Co bond) with a pseudo-tetrahedral coordination geometry comprising the two phosphine donors and two thiolates that bridge from the W[SNS]$_2$ cofactor. Application of the structural angular parameter for four-coordinate metal centers revealed a τ_4 value of 0.84 for the cobalt ion, concluding a distorted tetrahedral coordination geometry. Further investigation into the valence angles about the cobalt center revealed angles between 87.53–125.70°, supporting the calculated τ_4 value. The P–Co–P angle of 87.53° is

consistent with the constricted bite angle of the dppe ligand.[15] The average Co–P distance of 2.211 Å appears similar to Co^{II}–P bonds (2.205−2.230 Å), while Co^{I}– and Co^{III}–P lengths have been observed between 2.108–2.154 Å and 2.264–2.334 Å, respectively.[15–20] However, the average Co–S distance of 2.170 Å for **11**$^{-}$ appears more consistent with a Co^{I}–S length (2.158–2.174 Å) as opposed to Co^{II}–S (2.294–2.331 Å) or Co^{III}–S (2.229–2.315 Å) bond distances observed in the literature.[21–24] Finally, the W–Co distance of 2.548 Å falls within the sum of the covalent radii for the two metal ions (tungsten, 1.62 Å; cobalt, 1.26 Å) and is severely contracted from known tungsten–cobalt heterobimetallic complexes observed in literature (2.598–2.817 Å), indicative of a formal tungsten–cobalt single bond.[25–27]

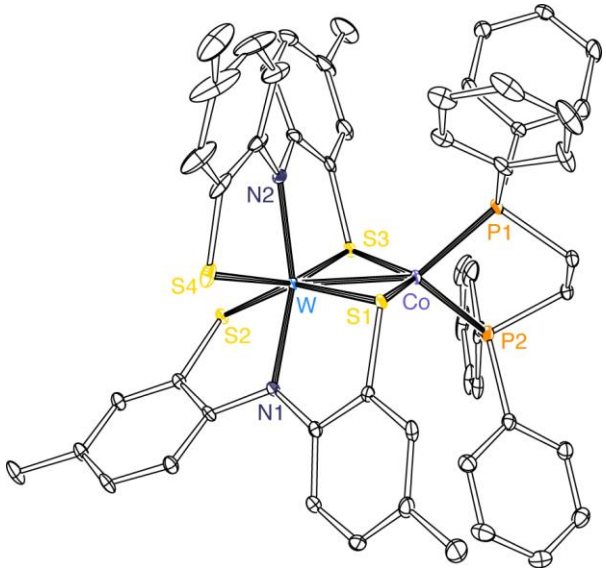

Figure 5.1. ORTEP diagram for complex **11**$^{-}$ with thermal ellipsoids shown at 50% probability. Hydrogen atoms and a counter cation ($[Cp_2^*Co]^+$) have been omitted for clarity.

Using the same modular approach outlined above, copper containing heterobimetallic complexes of the general formula $W[SNS]_2Cu(L)$ (L = 1,2-bis(diphenylphosphino)ethane (dppe) or 4,4′-di-*t*-butyl-2,2′-bipyridine (dtbbpy)) were obtained in high yields (> 76%, **Scheme 5.2**). ESI-MS data confirmed the formation of the desired heterobimetallic complexes **12** and **13** with parent ion signals at *m/z* values of 1163 and 1033, respectively. Single crystals of complexes **12**

and **13** were grown from the slow diffusion of a concentrated analyte solution of THF into diethyl ether or pentane at −35°C (**12**) or room temperature (**13**).

Scheme 5.2. Synthesis of heterobimetallic complexes **12** and **13**.

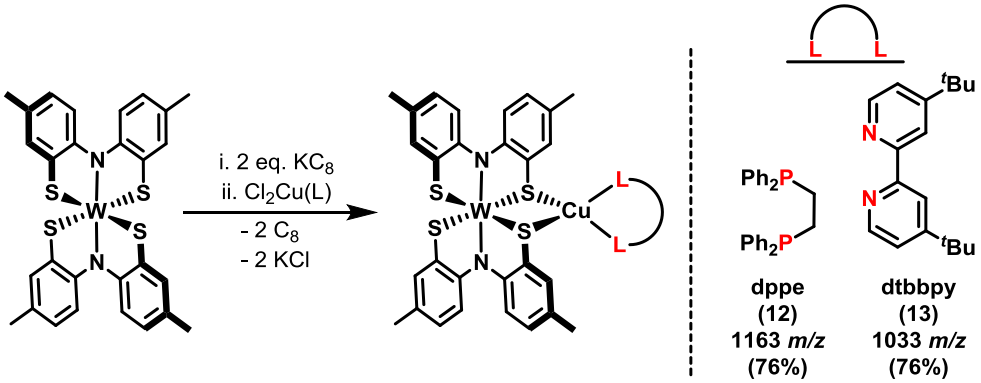

X-ray diffraction studies on single crystals of **12** and **13** revealed bimetallic complexes supported by two bridging thiolate donors from the W[SNS]$_2$ metalloligand. **Figure 5.2** illustrates the solid-state structures of **12** and **13** as ORTEP diagrams with a table of selected bond lengths and angles provided in **Table 5.1**. The bimetallic complexes are best described as a W[SNS]$_2$ fragment bound as a chelating ligand to a Cu(L) fragment (L = dppe or dtbbpy). The copper center are four-coordinate in both cases with a pseudo-tetrahedral coordination geometry comprising the two phosphine/nitrogen donor atoms of the ancillary ligand and the two thiolates that bridge from the W[SNS]$_2$ metalloligand. Applying the angular structural parameter for four-coordinate complexes, τ_4 values of 0.78 and 0.88 were calculated for **12** and **13**, respectively. Further investigation into the valence angles of the copper centers of **12** and **13** revealed angles between 81.28–126.10°, consistent with the observed distortion from ideal tetrahedral geometry and further support of the calculated τ_4 values. The L–Cu–L (L = P or N) bite angles of 89.93° (**12**) and 81.27° (**13**) reveal the constricted angle typically observed for dppe and dtbbpy ligands, respectively.[15,28–30] The average Cu–P bond distance of 2.286 Å in **12** appears most similar with Cu^{I}–P bond distances observed in the literature (2.197–2.309 Å).[28,30–36] In contrast Cu^{II}–P bond distances have

been observed within the range of 2.219–2.243 Å.[37] The average Cu–N bond length of 2.022 Å in **13** appears comparable with both Cu^{I}–N (2.018–2.118 Å) and Cu^{II}–N (1.997–2.075 Å) bond distances observed in literature.[29,38–41] The average Cu–S distances of **12** (2.339 Å) and **13** (2.281 Å) match those of Cu^{I}–S (2.349–2.420 Å) and Cu^{II}–S bond distances (2.303–2.320 Å), respectively.[28,31,42–46] Finally, investigations into the tungsten–copper bond length revealed distances of 3.004 Å (**12**) and 2.755 Å (**13**). In the case of **12**, the metal–metal distance is extended outside the sum of the covalent radii for the two metal centers (tungsten, 1.62 Å; copper, 1.32 Å) concluding no metal–metal interaction. However, the bond length of **13** appears to fall within the sum of the covalent radii for the two metal ions and allows for a plausible metal–metal bond to form between the metal centers. Within the literature, few tungsten–copper molecular structures have been reported, however, in all described cases the tungsten center is bridging the copper ion through thiolate donors to yield metal–metal distances (not bonded) ranging between 2.641–2.833 Å.[47,48]

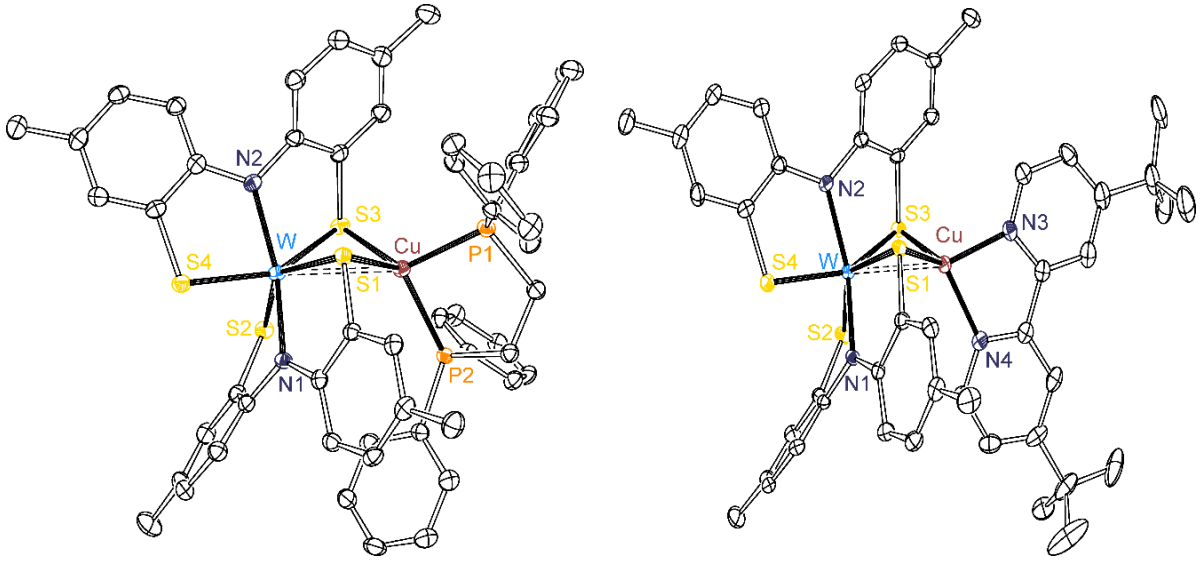

Figure 5.2. ORTEP diagrams of complexes **12** and **13**. Thermal ellipsoids are shown at 50% probability. Hydrogen atoms have been omitted for clarity.

Table 5.1. Selected bond lengths and angles for complexes **11⁻**, **12**, and **13**.

	[W[SNS]$_2$Co(dppe)][CoCp$_2$*] (**11⁻**)	W[SNS]$_2$Cu(dppe) (**12**)	W[SNS]$_2$Cu(dtbbpy) (**13**)
	Bond Distances / Å		
W–M	2.5483(4)	3.0043(5)	2.7547(4)
W–S1	2.4040(7)	2.3769(9)	2.3909(7)
W–S3	2.3987(7)	2.4669(10)	2.4430(7)
M–S1	2.1839(7)	2.3805(10)	2.2880(7)
M–S3	2.1559(7)	2.2980(10)	2.2742(8)
M–P1	2.2037(8)	2.2940(11)	–
M–P2	2.2178(8)	2.2777(10)	–
M–N3	–	–	2.028(2)
M–N4	–	–	2.016(2)
	Bond Angles / °		
S1–W–S3	103.56(2)	90.11(3)	94.93(2)
S1–M–S3	120.78(3)	94.25(4)	102.67(3)
P1–M–P2	87.53(3)	89.93(4)	–
S1–M–P1	125.70(3)	123.07(4)	–
S1–M–P2	96.07(3)	102.54(4)	–
S3–M–P1	102.02(3)	122.19(4)	–
S3–M–P2	121.23(3)	126.10(4)	–
N3–M–N4	–	–	81.28(9)
S1–M–N3	–	–	113.57(7)
S1–M–N4	–	–	122.02(7)
S3–M–N3	–	–	119.45(7)
S3–M–N4	–	–	117.64(7)
τ_4 value	0.84	0.78	0.88

The overall tungsten geometry within the metalloligand of complexes **11⁻**, **12**, and **13** were found to lie between a trigonal prismatic and trigonal antiprismatic geometry in all cases. The primary measurements of trigonal prismatic versus trigonal antiprismatic geometry is defined by the twist angle (θ) between opposite trigonal faces (**Chapter 2**, **Figure 2.3**, page 21). In all complexes, two trigonal planes can be defined by the nitrogen and a single sulfur atom from one [SNS] ligand and a single sulfur atom from the other ligand (N(1)–S(1)–S(4) and N(2)–S(2)–S(3)), whereby the twist angle is then defined as the torsion angle between the vertices of the trigonal planes and the centroids of those planes.[49,50] A second metrical parameter used to determine the degree of distortion for trigonal systems is the prismatic compression ratio, defined as the ratio of

the prism height (h) to the average length of the trigonal face (s). Under these parameters an ideal trigonal prism demonstrates a twist angle (θ) of 0° with an s/h ratio of 1.00 while an ideal trigonal antiprism affords a twist angle of 60° and a s/h ratio of 1.22.[50] **Table 5.2** demonstrates the values calculated for complexes **11⁻**, **12**, and **13**. Using this approach, the tungsten center of complex **11⁻** appears most consistent with a trigonal anti-prismatic geometry with an average twist angle of 38.7° and a s/h ratio of 1.09. In contrast, the twist angles of **12** and **13** resemble a distortion from both trigonal prismatic and trigonal anti-prismatic geometries with average twist angles of 16° while the calculated prismatic compression ratios (> 1.10) suggest a geometry more similar to a trigonal anti-prismatic geometry.[49,50]

Table 5.2. Additional measured and calculated metrical parameters for complexes **11⁻**, **12**, and **13**.

	[W[SNS]$_2$Co(dppe)][CoCp$_2$*] (**11⁻**)	W[SNS]$_2$Cu(dppe) (**12**)	W[SNS]$_2$Cu(dtbbpy) (**13**)
$\theta_{S4,N2}$	31.4°	26.1°	25.9°
$\theta_{S1,S3}$	31.4°	5.1°	1.6°
$\theta_{N1,S2}$	53.4°	20.6°	21.0°
s/h	1.09	1.10	1.12

Lastly, the oxidation state assignments of the metal centers in complexes **11** and **11⁻** are of interest. In all cases, the [SNS] ligands appear most consistent with maintaining their fully reduced, trianionic forms. Despite not obtaining a solid-state structure for complex **11**, using the supported oxidation state assignments for previously explored complexes **1-10**, complex **11** appears likely to adopt either a $W^{V}(d^1)$–$Co^{I}(d^8)$ or $W^{IV}(d^2)$–$Co^{II}(d^7)$ configuration. Using these putative assignments for **11**, three plausible oxidation state assignments can be made for **11⁻**. The first plausible oxidation state assignment could arise from either a reduction of the tungsten center (from $W^{V}(d^1)$–$Co^{I}(d^8)$) or a reduction of the cobalt center (from $W^{IV}(d^2)$–$Co^{II}(d^7)$) to give a $W^{IV}(d^2)$–$Co^{I}(d^8)$ heterobimetallic core. Either center becoming reduced would give two unpaired electrons on each metal center capable of forming (i) a W–Co double bond or (ii) a single bond

with anti-ferromagnetic coupling of the remaining unpaired electrons. In this case, diamagnetic character may require a W–Co double bond, however, formation of a double bond is unlikely due to the π interaction of a W 5d orbital with a Co 3d orbital would be expected to be weak.[51] A second plausible oxidation state assignment would require the reduction of the tungsten center of $W^{IV}(d^2)$–$Co^{II}(d^7)$ to give a $W^{III}(d^3)$–$Co^{II}(d^7)$ configuration. This assignment would yield a bimetallic core capable of forming a metal–metal bond and an overall diamagnetic ground state. The third plausible oxidation state assignment consists of the reduction of the cobalt center of $W^{V}(d^1)$–$Co^{I}(d^8)$ to give a $W^{V}(d^1)$–$Co^{0}(d^9)$ configuration. This assignment is refuted as the formation of a cobalt(0) containing complex is expected to be rare.[19,52] Of the three, the most plausible oxidation state assignment for **11**$^-$ is the formation of a $W^{III}(d^3)$–Co^{II}(l.s. d^7) heterobimetallic core. In this case, the assignment suggests that neutral **11** would likely adopt a $W^{IV}(d^2)$–Co^{II}(l.s. d^7) core.

Less ambiguous oxidation state assignments can be made for copper analogs **12** and **13** based on the observed bond metrics. Investigation into the metal–metal distance between the tungsten and copper in both cases reveal evidence for the plausible oxidation states of the bimetallic cores. In the case of complex **12**, the metal–metal distance is extended outside the sum of the covalent radii and therefore suggests that the copper center is reduced to a Cu^{I} d^{10} ion with a closed shell d-manifold. This renders the copper ion unable to form a formal metal–metal bond with the tungsten metalloligand center. This observation in the solid-state structure gives a putative oxidation state assignment for **12** as W^{V}–Cu^{I} leaving a single unpaired electron on the tungsten center. Interestingly, the exchange of the bidentate phosphine ligand, known for stabilizing low-valent metal centers (i.e. M^0 and M^{I}), for a bipyridine ligand, known to stabilize intermediate-valent metal centers (i.e. M^{II}), allowed the copper center of **13** to become closer in proximity to the tungsten

center of the metalloligand. This is likely due to steric effects of the ancillary ligand which allowed for an observed metal–metal distance within the sum of the covalent radii for the two metal ions and formally may be classified as a metal–metal bond. Despite this short distance (2.755 Å), two plausible oxidation state assignments can be made for **13**, a W^{V}–Cu^{I} or W^{IV}–Cu^{II} heterobimetallic core. Each configuration would result in the formation of a single unpaired electron on the tungsten center, with the latter generating a formal metal–metal bond. Overall, further spectroscopic analysis is needed to confirm these putative oxidation state assignments for **11-13**.

Spectroscopic Characterization of Complexes 11-13

The heterobimetallic complexes were further investigated using electronic absorption (UV-vis) spectroscopy. All electronic absorption spectra are shown in **Figure 5.3** with all collected data displayed in **Table 5.3**. Dissolution of complexes **11-13** in THF afforded dark colored solutions manifesting intense absorbance bands in the visible region consistent with charge transfer transitions based on their observed extinction coefficients (426-490 nm, 14400–18400 M^{-1} cm^{-1}).

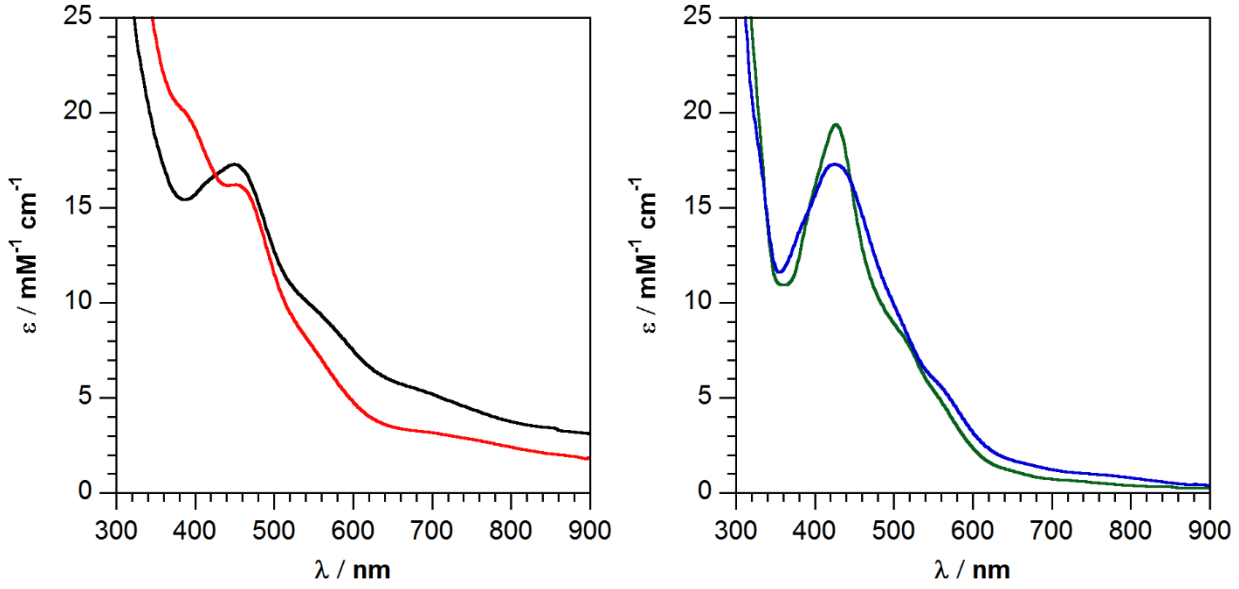

Figure 5.3. Electronic absorption spectra for (*left*) W[SNS]$_2$Co(dppe) (**11**, black) and [W[SNS]$_2$Co(dppe)][Cp_2*Co] (**11**$^{-}$, red); and (*right*) W[SNS]$_2$Cu(dppe) (**12**, green) and W[SNS]$_2$Cu(dtbbpy) (**13**, blue).

Table 5.3. Electronic absorption data for complexes **11-13**.

	λ / nm (ε/$M^{-1}cm^{-1}$)
$W[SNS]_2Co(dppe)$ (**11**, black)	416 (sh, 16400), 450 (17300)
$[W[SNS]_2Co(dppe)][Cp_2*Co]$ (**11**$^-$, red)	390 (sh, 19900), 452 (16200)
$W[SNS]_2Cu(dppe)$ (**12**, green)	426 (19400)
$W[SNS]_2Cu(dtbbpy)$ (**13**, blue)	425 (17300)

Due to their paramagnetic nature, nuclear magnetic resonance (Evans' Method) and electron paramagnetic resonance (EPR) spectroscopy were utilized on complexes **11-13**. Solution magnetic moment measurements were performed using Evans' Method analysis to reveal effective magnetic moments for **11**, **12**, and **13** of 1.84, 1.78, and 1.89 μ_B, respectively, consistent with a spin only s = ½ value of 1.73 μ_B at room temperature in $CDCl_3$. EPR spectra collected on THF solutions of **11-13** revealed isotropic signals centered at g = 1.96 resembling a single nuclear spin of I = ½ with hyperfine coupling (A) of 60 (**11**), 61 (**12**), 61 (**13**) Gauss at 298 K. The corresponding coupling appears to be best described by the nuclear spin of ^{183}W (14.28 %, I = ½).[53] Frozen glass solutions of **11-13** in THF collected at 77 K revealed s = ½ systems as complex **11** revealed a rhombic signal with g_x = 1.99, g_y = 1.96, and g_z = 1.93; complex **12** revealed an isotropic signal centered at g = 1.96; and complex **13** revealed a rhombic signal with g_x = 1.98, g_y = 1.96, and g_z = 1.94. The collected EPR spectra with g-values observed below 2.00 are distinctive for a tungsten center with a less than half-filled d-manifold, concluding that the unpaired electron is localized on the tungsten center in all cases.[6,53–55]

Nuclear magnetic resonance spectroscopy (^1H and ^{31}P NMR) was utilized to characterize the diamagnetic reduction product **11**$^-$. The presence of the Co(dppe) fragment in **11**$^-$ was readily established by the $^{31}P\{^1H\}$ NMR spectra, displaying a broad singlet at 96.4 ppm. ^1H NMR revealed a characteristic broad singlet at 1.90 ppm, illustrating the methylene protons of the dppe backbone. The $W[SNS]_2$ fragment revealed the presence of the methyl substituents of the [SNS]

backbone at 2.08 and 2.23 ppm, consistent with reduced symmetry from the neutral, monomeric $W[SNS]_2$. Similarly, the methyl resonances of the $[Cp_2^*Co]$ anion were observed as a broad singlet at 1.29 ppm.

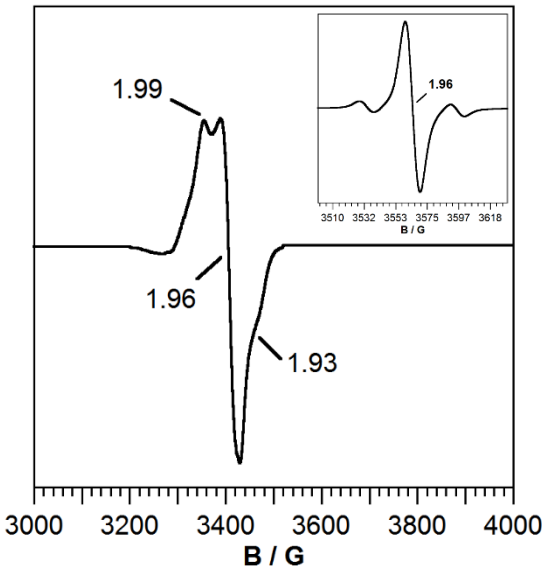

Figure 5.4. EPR spectra collected for $W[SNS]_2Co(dppe)$ (**11**, black) at 77 K and 298 K (inset). All spectra were collected in dry, degassed THF.

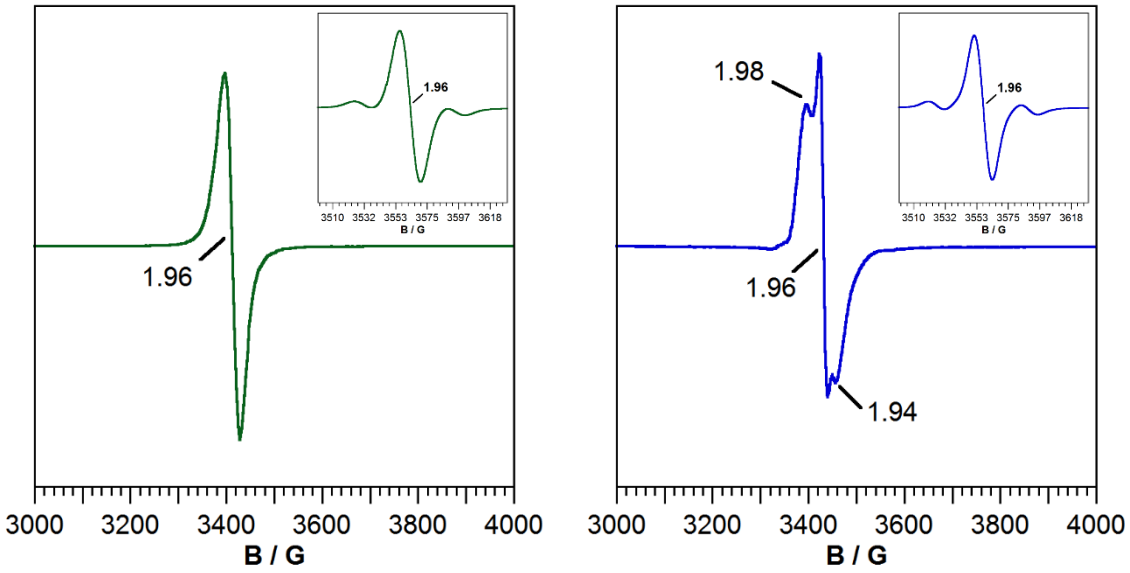

Figure 5.5. EPR spectra collected for *(left)* $W[SNS]_2Cu(dppe)$ (**12**, green) at 77 K and 298 K (inset); and *(right)* $W[SNS]_2Cu(dtbbpy)$ (**13**, blue) at 77 K and 298 K (inset). All spectra were collected in dry, degassed THF.

Table 5.4. Magnetic data collected for complexes **11-13**.

	Spin (s)	μ_B[a] (BM)	g-value[b]	g-value[c]	^{31}P NMR[d] (ppm)
W[SNS]$_2$Co(dppe) (**11**, black)	1/2	1.84	1.96 (A = 60 G)	g_x = 1.99; g_y = 1.96; g_z = 1.93	–
[**11**][Cp_2*Co] (**11**$^-$)	0	–	–	–	96.4
W[SNS]$_2$Cu(dppe) (**12**, green)	1/2	1.78	1.96 (A = 61 G)	1.96	–
W[SNS]$_2$Cu(dtbbpy) (**13**, blue)	1/2	1.89	1.96 (A = 61 G)	g_x = 1.98; g_y = 1.96; g_z = 1.94	–

[a]Room temperature (298 K) magnetic moment collected as a solution ($CDCl_3$) by Evans' method. [b]EPR collected on THF solutions at 298 K. [c]EPR collected on THF solutions at 77 K. [d] $^{31}P\{^1H\}$ NMR collected on $CDCl_3$ solutions at 298 K.

EPR spectra can reveal important information about the electronic configuration of complexes **11-13** and provide further understanding of the plausible metal oxidation state assignments. Based on both the room temperature (298 K) and frozen (77 K) spectra obtained for complex **11**, it appears consistent with an unpaired electron localized upon the tungsten center of the metalloligand. This suggests an oxidation state assignment for **11** as a $W^{IV}(d^2)$–Co^{II}(l.s. d^7) heterobimetallic core. A low spin cobalt configuration in a distorted tetrahedral coordination environment would allow for the pairing of a single electron from both metal centers to form a formal metal–metal bond. This assignment would leave a single unpaired electron localized on the tungsten center (identified via EPR). The second, less likely configuration of **11** would consist of a $W^V(d^1)$–$Co^I(d^8)$ core where the cobalt center may adopt a high spin or low spin configuration. A high spin configuration for this arrangement would allow for a single metal–metal bond to occur, however, the unpaired electron would remain on the cobalt center and yield a characteristic 8-line hyperfine cobalt EPR signal (not observed, ^{59}Co; 100% abundance, I = 7/2).[56] If a low spin Co^I configuration is preferred, an unpaired electron would remain on the tungsten center, however, no metal-metal bond would occur. Overall we favor the assignment of $W^{IV}(d^2)$–Co^{II}(l.s. d^7) for the neutral complex **11**. A similar analysis can be performed on complexes **12** and **13**. Based on the observed EPR signals, either a W^V–Cu^I or a W^{IV}–Cu^{II} heterobimetallic core may be adopted. Based on the solid-state structure, **12** is confirmed to adopt a W^V–Cu^I with no metal–metal bond

and an unpaired electron localized on the tungsten center of the metalloligand. Unfortunately, EPR does not definitively determine the existence of a metal–metal bond, therefore, the oxidation state assignments for **13** remain as either a W^{V}–Cu^{I} or a W^{IV}–Cu^{II} heterobimetallic core.

Mass-Spectroscopy Crossover Experiments for Complexes 12 and 13

Mass-spectroscopy crossover experiments were devised to investigate the dynamic nature of the chelating $W[SNS]_2$ metalloligand to the appended Cu(dppe) (**12**) and Cu(dtbbpy) (**13**) fragments. Due to **12** and **13** being highly labile in solution, electrochemical analysis was unsuccessful to yield clean traces of each complex. To fully investigate the lability of these tungsten–copper complexes, a series of molybdenum–copper analogs were synthesized by a colleague (Mikey Wojnar) with the formulas of $Mo[SNS]_2Cu$(dppe) (**12a**) and $Mo[SNS]_2Cu$(dtbbpy) (**13a**). The unique ESI-MS isotope patterns observed for $W[SNS]_2Cu$(dppe) (**12**, 1163 *m/z*), $Mo[SNS]_2Cu$(dppe) (**12a**, 1074 *m/z*), $W[SNS]_2Cu$(dtbbpy) (**13**, 1033 *m/z*), and $Mo[SNS]_2Cu$(dtbbpy) (**13a**, 944 *m/z*) allowed for quantitative investigation into the degree of lability in solution and in the gas phase. A series of three experiments were performed: (i) $W[SNS]_2Cu$(dppe) (**12**, 1163 *m/z*) combined with $Mo[SNS]_2Cu$(dtbbpy) (**13a**, 944 *m/z*); (ii) addition of free dtbbpy ligand (1 eq. and 5 eq.) with $W[SNS]_2Cu$(dppe) (**12**, 1163 *m/z*); and (iii) addition of free dppe ligand (1 eq and 5 eq.) with $W[SNS]_2Cu$(dtbbpy) (**13**, 1033 *m/z*).

$W[SNS]_2Cu$(dppe) (12) with $Mo[SNS]_2Cu$(dtbbpy) (13a). To prove the lability of the series of copper complexes in solution, the heterobimetallic complexes were treated with one another under an inert atmosphere in dry, degassed THF. Dissolution of **12** and **13a** in separate 20 mL scintillation vials resulted in initial ESI-MS data consistent with their characteristic parent ion signals with *m/z* values of 1163 and 944, respectively (**Figure 5.6**, black traces). Importantly, **12** and **13a** make up the maximum range for the heterobimetallic complexes and do not demonstrate

other parent ion signals within the *m/z* range of 1150 and 1000. The individual samples were combined and stirred for five minutes. An aliquot was then removed and diluted with 1 mL of dry, degassed THF. The resulting ESI-MS spectrum revealed the growth of parent ion signals at *m/z* values of 1074 and 1033, demonstrating the formation of Mo[SNS]$_2$Cu(dppe) (**12a**) and W[SNS]$_2$Cu(dtbbpy) (**13**), respectively (**Figure 5.6**, blue trace). Observing all four unique isotope patterns concluded the dynamic nature of the complexes in solution and the gas phase.

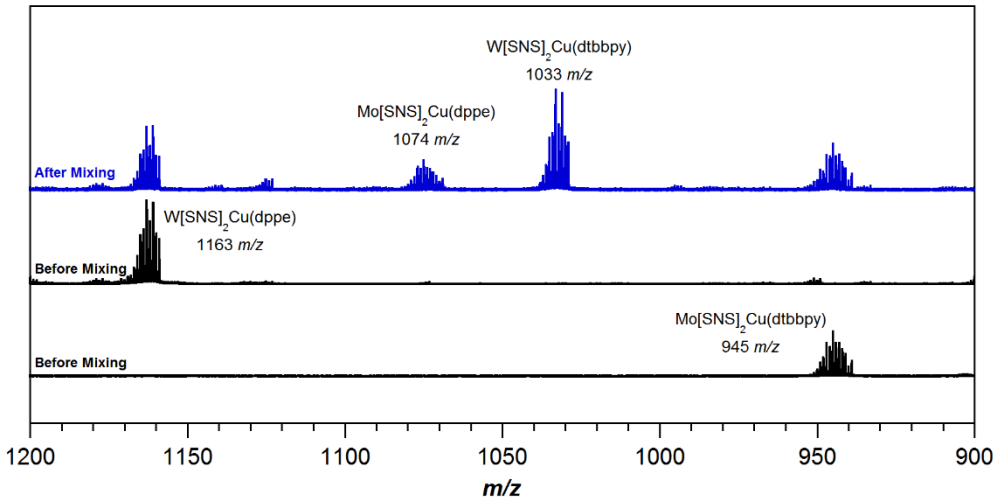

Figure 5.6. ESI-MS crossover experiment with *m/z* data collected for Mo[SNS]$_2$Cu(dtbbpy) (bottom, black), W[SNS]$_2$Cu(dppe) (middle, black), and mixture (top, blue). All experiments were performed on THF solutions.

W[SNS]$_2$Cu(dppe) (12) with free dtbbpy ligand. To verify that the aforementioned activity does not proceed through a ligand exchange equilibrium, **12** was treated with one and five equivalents of free dtbbpy ligand. Dissolution of crystalline material of **12** in a 20 mL scintillation vial revealed initial ESI-MS data that demonstrated two parent ion signals between 1300 and 500 *m/z*, heterobimetallic **12** (1163 *m/z*) and homoleptic Cu(dppe)$_2$ (860 *m/z*) (**Figure 5.7**, black trace). Addition of a single equivalent of free dtbbpy ligand to **12** resulted in the disappearance of both initial signals at *m/z* values of 1163 and 860 while the growth of a new parent ion signal at a *m/z* value of 729 was observed. This signal establishes the formation of the mixed ligand copper species, (dtbbpy)Cu(dppe) (**Figure 5.7**, red trace). The presence of excess dtbbpy ligand (5 eq.)

resulted in two parent ion signals at *m/z* values of 729 and 599 consistent with (dtbbpy)Cu(dppe) and Cu(dtbbpy)$_2$, respectively (**Figure 5.7**, blue trace). The results of this crossover experiment suggest that dppe is a stronger chelating ligand to the copper center than dtbbpy, indicative of the observed mixed ligand copper species, (dtbbpy)Cu(dppe), preserved even in the presence of excess dtbbpy. Similarly, the results suggest that the dynamic nature of the complex proceeds through both the dissociation of the copper fragment from the tungsten metalloligand and a ligand dissociation pathway.

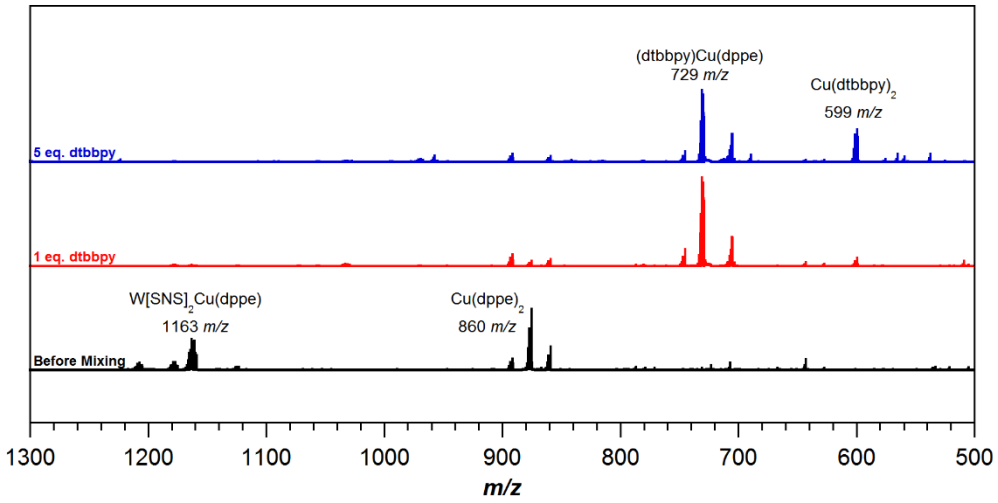

Figure 5.7. ESI-MS crossover experiment data collected for W[SNS]$_2$Cu(dppe) (black), the addition of 1 eq. of free dtbbpy (red), and the addition of 5 eq. of free dtbbpy (blue). All experiments were performed on THF solutions.

W[SNS]$_2$Cu(dtbbpy) (13) with free dppe ligand. As an analogous experiment to that described above, **13** was treated with one and five equivalents of free dppe ligand. Dissolution of crystalline material of **13** in THF revealed initial ESI-MS data that demonstrated two parent ion signals between 1300 and 500 *m/z*, heterobimetallic **13** (1033 *m/z*) and Cu(dtbbpy)$_2$ (599 *m/z*) (**Figure 5.8**, black trace). Addition of a single equivalent of free dppe ligand resulted in the disappearance of both starting parent ions signals at *m/z* values of 1033 and 599 and resulted in the growth of new parent ion signals at *m/z* values of 1163, 860, and 729 consistent with the formation of W[SNS]$_2$Cu(dppe) (**12**), Cu(dppe)$_2$, and (dtbbpy)Cu(dppe), respectively (**Figure 5.8**, red trace).

Treatment of **13** with excess dppe (5 eq.) resulted in the observance of a single parent ion signal at a *m/z* value of 860 concluding the formation of $Cu(dppe)_2$ in solution (**Figure 5.8**, blue trace). The results of this crossover experiment suggest that dppe coordinates stronger than the metalloligand and dtbbpy. Observation of a parent signal at 1163 *m/z* after the addition of one equivalent of dppe suggests minor ligand dissociation pathways are present, however, the major product observed is the homoleptic $Cu(dppe)_2$ complex, which appears to proceed through the initial formation of the mixed ligand (dtbbpy)Cu(dppe) complex. The results from this experiment suggest a similar finding as above, whereby the dynamic nature of the complexes in solution may undergo both Cu(L) fragment dissociation in addition to ligand dissociation pathways. This finding also demonstrates that free Cu(L) fragments in solution can trap excess chelating ligand to form both the mixed ligand and homoleptic copper complexes.

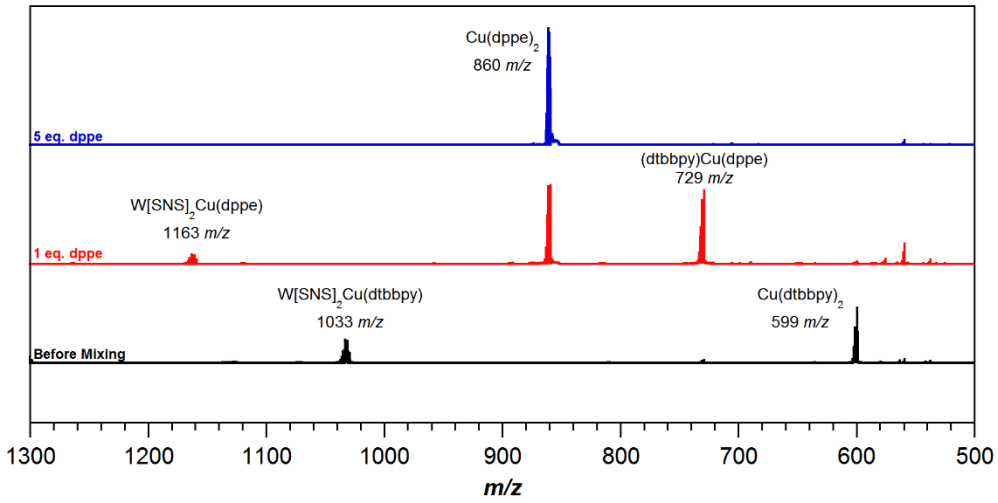

Figure 5.8. ESI-MS crossover experiment data collected for $W[SNS]_2Cu(dtbbpy)$ (black), the addition of 1 eq. of free dppe (red), and the addition of 5 eq. of free dppe (blue). All experiments were performed on THF solutions.

The results of the aforementioned ESI-MS crossover experiments suggest that complexes **12** and **13** are highly labile in solution and that the Cu(L) fragments may not strongly coordinate to the tungsten metalloligand. Based on the observed parent ion signals, the chelating strength of the ligands appear to increase from $W[SNS]_2 \rightarrow$dtbbpy$\rightarrow$dppe. These results appear to demonstrate a

weak interaction between the tungsten metalloligand and the copper fragments. The dynamic nature is likely due to the heterobimetallic complexes being held together by electrostatic interactions that occur between a $W^{V}[SNS]_2$ anion and a $Cu^{I}(L)$ cation. This dynamic nature of the copper fragments in solution may suggest that no metal–metal interaction is observed within the tungsten–copper core of **12** and **13**, as the complexes may be expected to be more robust. This type of interaction would explain the lability in solution in addition to the ability of the $Cu^{I}(L)$ cation fragment to trap additional equivalents of a stronger chelating ligand. Unfortunately, the observed homoleptic $Cu(L)_2$ complexes within initial scans of the pure crystalline material suggest that some complex degradation may be associated upon injection into the ESI-MS instrument illustrating that ligand dissociation cannot be completely ruled out as a possible pathway from these crossover experiments.

Conclusion

Herein we expand a family of heterobimetallic complexes through the exchange of the secondary metal center for cobalt (**11/11**$^{-}$) and copper (**12/13**) ions using the modular approach established in **Chapters 2** and **3**. Based on the all characterization methods discussed, the oxidation state assignments for neutral **11** appear most consistent with a $W^{IV}(d^2)$–Co^{II} (l.s. d^7) core. This configuration is favored for two reasons: (i) the observed EPR signal for **11** demonstrated tungsten metalloligand character with no cobalt contribution; and (ii) the reduction of **11** to generate **11**$^{-}$ resulted in isolation of a complex with a diamagnetic ground state accessed through the pairing of an unpaired electron on the tungsten center. This in turn yields an oxidation state assignment for **11**$^{-}$ best described as a $W^{III}(d^3)$–Co^{II}(l.s. d^7) heterobimetallic core (note: A $W^{IV}(d^2)$–$Co^{I}(d^8)$ core may also be plausible). Additionally, oxidation states that involve the reduction of the cobalt center is thought to be difficult due to literature precedent indicating that the $Co^{II/I}$

reduction couple is often observed at potentials below −2.5 V, vs $Cp_2Fe^{0/+}$, rendering a cobalt redox change unlikely during synthesis.[57–61] Based on the characterization evidence described, complexes **12** and **13** are best described as having a W^{V}–Cu^{I} heterobimetallic core with no formal metal–metal interaction observed between the metal centers. Known tungsten–copper molecular structures have been reported in the literature with similar structural motifs as in our systems (i.e. thiolate bridges), however, in all described cases the copper centers are formally in their 1+ oxidation state giving a filled d-orbital manifold unable to formally overlap to form a metal–metal interaction.[47,48] Structural and spectroscopic evidence support these oxidation state assignments for complexes **11-13**. Complexes **12** and **13** were also found to be highly labile in solution, supporting a chelating effect in the copper containing heterobimetallic complexes.

Preliminary investigation into heterobimetallic complexes **1** (Ni), **11** (**11**$^{-}$, Co), and **12** (Cu) reveal that the reduced tungsten metalloligand (formed *in situ.*) acts as both a chelating ligand and as a reducing agent to the desired M^{II} starting materials. This reducing potential appears to be more negative than the observed $M^{II/I}$ couple for both nickel and copper analogs further justifying the oxidation state assignments for **1** and **12** as W^{V}–M^{I}. In contrast, installation of a cobalt ion resulted in a complex more consistent with a W^{IV}–Co^{II} core, suggesting that the $Co^{II/I}$ redox couple lies at potentials below −2.15 V, vs $Cp_2Fe^{0/+}$.[49,62] Overall, the isolation of these complexes offer a unique approach towards generating new heterobimetallic complexes with interesting electronic and structural properties that may be advantageous for the activation of small molecule substrates.

Experimental

General Considerations. The compounds and reactions reported below show various levels of air- and moisture-sensitivity, therefore all manipulations were carried out using standard vacuum-line, Schlenk-line and glovebox techniques unless otherwise noted. Hydrocarbon and ethereal

solvents were sparged with argon before being deoxygenated and dried by passage through Q5 and activated alumina columns, respectively. Halogenated solvents were sparged with argon and dried by passage through two activated alumina columns. To test for effective oxygen and water removal, aliquots of each solvent were treated with a few drops of a purple solution of sodium benzophenone ketyl radical in THF. [Bis(diphenylphosphino)ethane]cobalt(II) chloride (sigma), Anhydrous $CuCl_2$ (Fisher), $Cl_2Cu{\cdot}H_2O$ (Sigma), 1,2-bis(diphenylphosphino)ethane (dppe) (Fisher), and 4,4′-Di-*tert*-butyl-2,2′-dipyridyl (dtbbpy) (Sigma) were all used as received. The ligand $[SNS^{cat}]H_3$[49] and coordination complex $W[SNS]_2$[49] were both prepared according to previously reported procedures. The starting Cl_2Cu(dppe) complex was synthesized using a similar approach as demonstrated for the nickel analog,[63] however, was performed in THF under a nitrogen atmosphere.

Spectroscopic Methods. Elemental analyses were conducted on a Perkin-Elmer 2400 Series II CHNS elemental analyzer. Electronic absorption spectra were recorded with a Jasco V-670 absorption spectrometer as solutions in dry, degassed THF contained in 1-cm quartz cells. Electrospray ionization mass-spectrometry (ESI-MS) data were collected on a Waters LCT Premier mass-spectrometer using dry, degassed CH_2Cl_2 or THF. X-band (9.352 GHz) EPR spectra were collected on THF solutions at room temperature (298 K) and frozen glass (77 K) using a Bruker EMX spectrometer equipped with an ER041XG microwave bridge using the following spectrometer settings: attenuation = 20 dB, microwave power = 1.997 mW, frequency = 9.352 GHz, modulation amplitude = 10.02 G, gain = 1.00×10^3, conversion time = 40.91 ms, time constant = 81.92 ms, sweep width = 5500 G, and resolution = 1024 points.

Crystallographic Methods. X-ray diffraction data for all complexes were collected on single crystals mounted on a glass fiber using paratone oil. Data was acquired using a Bruker SMART

APEX II diffractometer equipped with a CCD detector at 88 K using Mo Kα radiation (λ = 0.71073 Å), which was wavelength selected with a single-crystal graphite monochromator. The SMART program package was used to determine unit-cell parameters and for data collection. The raw frame data were processed using SAINT and SADABS to yield the reflection data file. Subsequent calculations were carried out using the SHELXTL program suite. The structures were solved by direct methods and refined on F^2 by full-matrix least-squares techniques. Analytical scattering factors for neutral atoms were used throughout the analyses. Hydrogen atoms were generated in calculated positions and refined using a riding model. ORTEP diagrams were generated using *ORTEP-3* for Windows.

Table 5.5. Data collection and refinement parameters for complexes **11**$^-$, **12**, and **13**.

	[W[SNS]$_2$Co(dppe)][CoCp$_2$*] (**11**$^-$)	W[SNS]$_2$Cu(dppe) (**12**)	W[SNS]$_2$Cu(dtbbpy) (**13**)
empirical formula	$C_{54}H_{48}CoN_2P_2S_4W \bullet C_{20}H_{30}Co$	$C_{54}H_{48}N_2CuP_2S_4W$	$C_{46}H_{48}CuN_4S_4W$
formula weight [g/mol]	1487.27	1162.51	1032.51
crystal system	Triclinic	Monoclinic	Tetragonal
space group	*P*1bar	$P2_1/c$	$I4_1/a$
T [K]	88(2) K	88(2) K	133(2) K
a [Å]	12.4810(13)	24.8020(19)	39.047(2)
b [Å]	15.1343(16)	11.6449(9)	39.047(2)
c [Å]	19.258(2)	19.7135(15)	11.4991(6)
a [deg]	75.4241(13)	90	90
b [deg]	87.1621(13)	111.4699(8)	90
g [deg]	69.8439(13)	90	90
V [Å^3]	3302.3(6)	5298.5(7)	17532(2)
Z	2	4	16
refl collected	40911	56255	103692
data/restr/param	16354/0/820	11677/0/581	10938/0/515
R_1 [I > 2σ(I)][a]	0.0299	0.0339	0.0279
wR_2(all data)[a]	0.0620	0.081	0.0592
GOF[a]	1.011	1.124	1.023

[a] $R_1 = \Sigma||F_o|-|F_c|| / \Sigma|F_o|$, $wR_2 = [\Sigma[w(F_o^2-F_c^2)^2] / \Sigma[w(F_o^2)^2]\ ]^{1/2}$, GOF = S = $[\Sigma[w(F_o^2-F_c^2)^2] / (n-p)]^{1/2}$

Crossover Experiments. All manipulations were performed in a nitrogen filled glovebox. Reactions were conducted in a 20 mL scintillation vial equipped with a magnetic stir bar. The complexes were dissolved in separate scintillation vials using 5 mL of dry, degassed THF. An

initial aliquot of the solution was removed, diluted using 1 mL of THF, transferred into a 1 mL amber ESI-MS vial and covered with Teflon tape. The sample was placed in a secondary 20 mL scintillation vial filled with the glovebox atmosphere prior to injection on a waters LCT Premier mass-spectrometer in ESI+ mode. All samples were analyzed by mass spectrometry before and after being combined with the desired species.

General Synthesis of W[SNS]$_2$M(L) (M = Co or Cu; L = dppe or dtbbpy) To a 100 mL Schlenk flask, potassium metal and graphite were heated with a heat gun to form two equiv. of KC_8 as a bronze powder. The flask was charged with 30 mL of dry THF and frozen in a liquid nitrogen cold well. Upon thawing, W[SNS]$_2$ was added to the stirring solution to generate K_2W[SNS]$_2$. After 10 minutes, Cl_2M(L) was added to the solution and stirred at room temperature for one hour. The reaction mixture was filtered through celite on a fritted glass filter to remove graphite and KCl and yield a dark colored filtrate. The filtrate was then concentrated to roughly 5 mL and a solid was crashed out of solution using pentane or diethyl ether. The solid was collected on a glass frit and washed with pentane (2 x 20 mL), toluene (1 x 2mL), and followed by Et_2O (2 x 20 mL). The collected solid was dried under vacuum.

W[SNS]$_2$Co(dppe) (11). Reagents used: K (44 mg, 1.1 mmol, 2.0 equiv.); C_8 (106 mg, 1.10 mmol, 2.03 equiv.); W[SNS]$_2$ (380 mg, 0.543 mmol, 0.978 equiv.); Cl_2Co(dppe) (290 mg, 0.549 mmol, 0.989 equiv.). The solid was collected as a dark brown powder (280 mg, 44%). UV-Vis (THF) λ_{max} / nm (ε / M^{-1} cm^{-1}): 416 (sh, 16400), 450 (17300). MS (ESI+) (CH_2Cl_2) *m*/*z*: 1160.24 $(M+H)^+$.

[W[SNS]$_2$Co(dppe)][Cp$_2$*Co] (11$^-$). A 20 mL scintillation vial equipped with a magnetic stir bar was charged with complex **11** (60 mg, 0.052 mmol, 0.96 equiv.) and 10 mL of dry THF. To the mixture, a homogenous solution of Cp$_2$*Co (18 mg, 0.055 mmol, 1.0 equiv.) in 2 mL of THF was added slowly. An immediate color change from brown to red maroon was observed. The reaction

mixture was stirred for one hour. The reaction mixture was then concentrated to roughly 3 mL and a solid was crashed out of solution using pentane. Complex **11**$^{-}$ was collected as a red/maroon powder (52 mg, 66%). X-ray quality crystals were obtained by diffusion of diethyl ether into a THF solution of the complex at ambient temperature, black crystals obtained. Anal. Calc. $C_{54}H_{48}CoN_2P_2S_4W{\bullet}C_{20}H_{30}Co$: C, 59.76; H, 5.29; N, 1.88%. Found: C, 58.81; H, 5.42; N, 2.04%. ^{1}H NMR (500 MHz, THF-d_8) δ / ppm: 7.42 (m, 2H, aryl-H), 7.31 (m, 2H, aryl-H), 7.19 (d, J = 14.5 Hz, 5H, aryl-H), 7.06 (br.s., 4H, aryl-H), 6.83 (m, 4H, aryl-H), 6.70 (m, 5H, aryl-H), 6.60 (m, 2H, aryl-H), 6.46 (m, 2H, aryl-H), 6.28 (m, 2H, aryl-H), 6.16 (m, 2H, aryl-H), 5.95 (m, 2H, aryl-H), 2.23 (s, 6H, -CH_3), 2.08 (s, 6H, -CH_3), 1.90 (s, 4H, -CH_2), 1.29 (br.s., 30H, -Cp_2*). ^{31}P {^{1}H}-NMR (162 MHz, $CDCl_3$) δ / ppm: 96.36 (br.s.). UV-Vis (THF) λ_{max} / nm (ε / $M^{-1}cm^{-1}$): 390 (sh, 19900), 452 (16200). MS (ESI−) (CH_2Cl_2) *m*/*z*: 1159.06 $(M)^-$.

W[SNS]$_2$Cu(dppe) (12). Reagents used: K (138 mg, 3.54 mmol, 2.01 equiv.); C_8 (340 mg, 3.54 mmol, 2.01 equiv.); W[SNS]$_2$ (1.23 g, 1.76 mmol, 1.00 equiv); Cl_2Cu(dppe) (930 mg, 1.75 mmol, 1.00 equiv.). The desired product was collected as a brown powder (1.55g, 76%). X-ray quality crystals were obtained by diffusion of pentane or diethyl ether into a THF solution of the complex at ambient temperature for one day, followed by two days at -35°C, black crystals obtained. Anal. Calc. $WS_4N_2CuP_2C_{54}H_{48}$: C, 55.81; H, 4.13; N, 2.41%. Found: C, 56.03; H, 4.48; N, 2.65%. UV-Vis (THF) λ_{max} / nm (ε / $M^{-1}cm^{-1}$): 426 (19400). MS (ESI+) (THF): *m*/*z* 1163.06 $(M)^+$.

W[SNS]$_2$Cu(dtbbpy) (13). Reagents used: K (55 mg, 1.4 mmol, 2.0 equiv.); C_8 (137 mg, 1.43 mmol, 2.02 equiv.); W[SNS]$_2$ (492 mg, 0.703 mmol, 1.00 equiv); Cl_2Cu(dtbbpy) (217 mg, 0.320 mmol, 1.00 equiv.). The desired product was collected as a black powder (550 mg, 76%). X-ray quality crystals were obtained by diffusion of pentane into a THF solution of the complex at ambient temperature, black crystals obtained. Anal. Calc. $WS_4N_4CuC_{46}H_{48}$: C, 53.51; H, 4.69; N,

5.43%. Found: C, 53.37; H, 4.62; N, 5.18 %. UV-Vis (THF) λ_{max} / nm (ε / $M^{-1}cm^{-1}$): 425 (17300).

MS (ESI+) (THF): *m*/*z* 1033.48 $(M)^+$.

References

(1) Powers, I. G.; Uyeda, C. *ACS Catal.* **2017**, *7*, 936–958.
(2) Eisenhart, R. J.; Clouston, L. J.; Lu, C. C. *Acc. Chem. Res.* **2015**, *48*, 2885–2894.
(3) Lindahl, P. A. *J. Inorg. Biochem.* **2012**, *106*, 172–178.
(4) McGrady, J. E. In *Molecular Metal-Metal Bonds*; Wiley-VCH Verlag GmbH & Co. KGaA, 2015; pp. 1–22.
(5) Farrugia, L. J.; Evans, C. *Comptes Rendus Chim.* **2005**, *8*, 1566–1583.
(6) Clouston, L. J.; Bernales, V.; Cammarota, R. C.; Carlson, R. K.; Bill, E.; Gagliardi, L.; Lu, C. C. *Inorg. Chem.* **2015**, *54*, 11669–11679.
(7) Fontecilla-Camps, J. C.; Volbeda, A.; Cavazza, C.; Nicolet, Y. *Chem. Rev.* **2007**, *107*, 4273–4303.
(8) Rauchfuss, T. B. *Acc. Chem. Res.* **2015**, *48*, 2107–2116.
(9) Cooper, B. G.; Fafard, C. M.; Foxman, B. M.; Thomas, C. M. *Organometallics* **2010**, *29*, 5179–5186.
(10) Karlin, K. D. *Science (80-.).* **1993**, *261*, 701–708.
(11) Mazzacano, T. J.; Mankad, N. P. *J. Am. Chem. Soc.* **2013**, *135*, 17258–17261.
(12) Powers, D. C.; Xiao, D. Y.; Geibel, M. A. L.; Ritter, T. *J. Am. Chem. Soc.* **2010**, *132*, 14530–14536.
(13) Lubitz, W.; Ogata, H.; Rüdiger, O.; Reijerse, E. *Chem. Rev.* **2014**, *114*, 4081–4148.
(14) Schilter, D.; Rauchfuss, T. B.; Stein, M. *Inorg. Chem.* **2012**, *51*, 8931–8941.
(15) Nagasawa, T.; Nagata, T. *Biochim. Biophys. Acta - Bioenerg.* **2007**, *1767*, 666–670.
(16) Bertrand, J. A.; Plymale, D. L. *Inorg. Chem.* **1966**, *5*, 879–884.
(17) Falvello, L.; Gerloch, M. *Acta Cryst.* **1979**, *B35*, 2547–2550.
(18) Fryzuk, M. D.; Leznoff, D. B.; Thompson, R. C.; Rettig, S. J. *J. Am. Chem. Soc.* **1998**, *120*, 10126–10135.
(19) Deblon, S.; Liesum, L.; Harmer, J.; Schönberg, H.; Schweiger, A.; Grützmacher, H. *Chem. – A Eur. J.* **2002**, *8*, 601–611.
(20) Papp, T.; Kollár, L.; Kégl, T. **2014**, *2014*, 1–5.
(21) Halder, P.; Paine, T. K. *Indian J. Chem.* **2011**, *50A*, 1394–1402.
(22) Fallani, G.; Morassi, R.; Zanobini, F. *Inorganica Chim. Acta* **1975**, *12*, 147–154.
(23) Pladzyk, A.; Baranowska, K.; Gudat, D.; Godlewska, S.; Wieczerzak, M.; Chojnacki, J.; Bulman, M.; Januszewicz, K.; Dołęga, A. *Polyhedron* **2011**, *30*, 1191–1200.
(24) Mcnamara, W. R.; Han, Z.; Alperin, P. J.; Brennessel, W. W.; Holland, P. L.; Eisenberg, R. *J. Am. Chem. Soc.* **2011**, 15368–15371.
(25) Wu, K.; Lin, P.; Wu, X.; Chen, L. *Laser Chem.* **2000**, *18*, 193–201.
(26) Chetcuti, M. J.; Gordon, J. C.; Fanwick, P. E. *Inorg. Chem.* **1990**, *29*, 3781–3787.
(27) D. King, J.; J. Mays, M.; E. Pateman, G.; R. Raithby, P.; A. Rennie, M.; A. Solan, G.; Choi, N.; Conole, G.; McPartlin, M. *J. Chem. Soc.{,} Dalt. Trans.* **1999**, 1–22.
(28) Nguyen, L. M.; Dellinger, M. E.; Lee, J. T.; Quinlan, R. A.; Rheingold, A. L.; Pike, R. D. *Inorganica Chim. Acta* **2005**, *358*, 1331–1336.
(29) Wing-Wah Yam, V.; Pui, Y.-L.; Li, W.-P.; Kam-Wing Lo, K.; Cheung, K.-K. *J. Chem.*

Soc.{,} Dalt. Trans. **1998**, 3615–3622.
(30) Dehghanpour, S.; Bouslimani, N.; Welter, R.; Mojahed, F. *Polyhedron* **2007**, *26*, 154–162.
(31) Bowmaker, G. A.; Hanna, J. V; King, S. P.; Marchetti, F.; Pettinari, C.; Pizzabiocca, A.; Skelton, B. W.; Sobolev, A. N.; Tăbăcaru, A.; White, A. H. *Eur. J. Inorg. Chem.* **2014**, *2014*, 6104–6116.
(32) Gill, J. T.; Mayerle, J. J.; Welcker, P. S.; Lewis, D. F.; Ucko, D. A.; Barton, D. J.; Stowens, D.; Lippard, S. J. *Inorg. Chem.* **1976**, *15*, 1155–1168.
(33) Walters, M. K. *Antonian Sch. Honor. Progr.* **2012**.
(34) Saravanabharathi, D.; Nethaji, M.; Samuelson, a. . *Polyhedron* **2002**, *21*, 2793–2800.
(35) Hattori, Y.; Nishikawa, M.; Kusamoto, T.; Kume, S.; Nishihara, H. *Inorg. Chem.* **2014**, *53*, 2831–2840.
(36) Xin, X.-L.; Chen, M.; Ai, Y.; Yang, F.; Li, X.-L.; Li, F. *Inorg. Chem.* **2014**, *53*, 2922–2931.
(37) Hao, Y. Z.; Tianzhi, Y. U.; Hang, H. Z.; Hang, P. Z.; An, D. F.; Ong, W. D. *Anal. Sci.* **2008**, *24*, 181–182.
(38) Henary, M.; Wootton, J. L.; Khan, S. I.; Zink, J. I. *Inorg. Chem.* **1997**, *36*, 796–801.
(39) Dudley, R. J.; Hathaway, B. J.; Hodgson, P. G.; Mulcahy, J. K.; Tomlinson, A. A. G. *J. Inorg. Nucl. Chem.* **1974**, *36*, 1947–1950.
(40) Pasynskii, A. A.; Skabitskii, I. V; Karpacheva, M. V. *Russ. J. Coord. Chem.* **2013**, *39*, 229–233.
(41) Selvakumar, B.; Rajendiran, V.; Uma Maheswari, P.; Stoeckli-Evans, H.; Palaniandavar, M. *J. Inorg. Biochem.* **2006**, *100*, 316–330.
(42) Li, Z.; Lin, P.; Du, S. *J. Mol. Struct.* **2008**, *892*, 182–187.
(43) Li, Z.-H.; Lin, P.; Du, S.-W. *Polyhedron* **2008**, *27*, 232–240.
(44) Groysman, S.; Majumdar, A.; Zheng, S.-L.; Holm, R. H. *Inorg. Chem.* **2010**, *49*, 1082–1089.
(45) Beheshti, A.; Clegg, W.; Dale, S. H.; Solimankhani, A. *Polyhedron* **2008**, *27*, 777–782.
(46) Capdevila, M.; Carrasco, Y.; Gonzalez-Duarte, P.; Lledos, A.; Sola, J.; Ujaque, G.; Capdevila, M.; Clegg, W.; A. Coxall, R.; Gonzalez-Duarte, P. *Chem. Commun.* **1998**, 597–598.
(47) Shamsur Rahman, A. B. M.; Boller, H.; Klepp, K. O. *Inorganica Chim. Acta* **2000**, *305*, 91–94.
(48) Guo, J.; Sheng, T.; Zhang, W.; Wu, X.; Lin, P.; Wang, Q.; Lu, J. *Inorg. Chem.* **1998**, *37*, 3689–3697.
(49) Shaffer, D. W.; Szigethy, G.; Ziller, J. W.; Heyduk, A. F. *Inorg. Chem.* **2013**, *52*, 2110–2118.
(50) Stiefel, E. I.; Brown, G. F. *Inorg. Chem.* **1972**, *11*, 434–436.
(51) Cotton, F. A.; Murillo, C. A.; Walton, R. A. *Multiple bonds between metal atoms*; Springer Science: New York, 2005.
(52) Klein, H.-F. *Angew. Chemie Int. Ed.* **1971**, *10*, 343.
(53) Almendra, M. J.; Brondino, C. D.; Gavel, O.; Pereira, A. S.; Tavares, P.; Bursakov, S.; Duarte, R.; Caldeira, J.; Moura, J. J. G.; Moura, I. *Biochemistry* **1999**, *38*, 16366–16372.
(54) Johnson, J. L.; Rajagopalan, K. V. *J. Biol. chemitry* **1976**, *251*, 5505–5511.
(55) Schmitz, R. A.; Albracht, S. P. J.; Thauer, R. K. *FEBS Lett.* **1992**, *309*, 78–81.
(56) Twitchen, D. J.; Baker, J. M.; Newton, M. E.; Johnston, K. *Phys. Rev. B* **2000**, *61*, 9–11.
(57) Cibian, M.; Derossi, S.; Hanan, G. S. *Dalt. Trans.* **2011**, *40*, 1038–1040.

(58) Cameron, P. J.; Peter, L. M.; Zakeeruddin, S. M.; Grätzel, M. *Coord. Chem. Rev.* **2004**, *248*, 1447–1453.
(59) D'Souza, F.; Villard, A.; Van Caemelbecke, E.; Franzen, M.; Boschi, T.; Tagliatesta, P.; Kadish, K. M. *Inorg. Chem.* **1993**, *32*, 4042–4048.
(60) Vasilevskis, J.; Olson, D. C. *Inorg. Chem.* **1971**, *10*, 1228–1235.
(61) Roy, S.; Sharma, B.; Pécaut, J.; Simon, P.; Fontecave, M.; Tran, P. D.; Derat, E.; Artero, V. *J. Am. Chem. Soc.* **2017**.
(62) Rosenkoetter, K. E.; Ziller, J. W.; Heyduk, A. F. *Inorg. Chem.* **2016**, *55*, 6794–6798.
(63) Darkwa, J. *Inorganica Chim. Acta* **1996**, *257*, 137–141.

Chapter 6

Probing the Redox-Active Nature of Square-Planar Nickel Complexes Supported by the [SNS] Ligand

Introduction

Proton transfer (PT) and electron transfer (ET) are two of the most fundamental processes in chemistry.[1] Most active research that investigates small molecule activation requires the distribution of equivalents of both protons and electrons, generally in a concerted pathway, to achieve catalytic reactivity.[1,2] Such reactions are termed as proton-coupled electron-transfer (PCET) reactions, or hydrogen-atom transfer (HAT), and are very important reaction pathways in a variety of biochemical, electrochemical, and small molecule reactions.[1,2] Examples of important hydrogen-atom transfer reactions can be observed in biology from radical scavenging antioxidants to enzymatic/biomimetic transformations or in coordination chemistry through C–H bond functionalization.[3–8]

Transition metal ions supported by redox-active ligands have demonstrated to be quite useful in the storage or transfer of multiple equivalents of protons or electrons, however, monometallic systems capable of delivering equivalents of both protons and electrons are quite rare.[9–14] Berben at UC-Davis has demonstrated the use of a tridentate [^{R}PDI] pincer ligand (**Scheme 1.3**, page 4) supporting an aluminum center capable of performing electrochemical proton reduction at modest potentials.[10] In this case the metal center tuned the redox potential to achieve low overpotentials while the ligand supplied the equivalents of protons and electrons.[10] Moreover, the Agapie group at CalTech has demonstrated the use of π-bound molybdenum-quinonoid moieties supported by pendent phosphines capable of distributing four equivalents of electrons towards the reduction of dioxygen.[11,15] The quinonoid of the ligand backbone allows for binding to the metal center through the π-system, initiating reactivity to occur with the weak O–H bonds of the quinonoid fragment for H-atom transfer.[11,15] The ability for redox processes and hydrogen atom transfer to occur from the ligand backbone, allow for the metal and ligand to work in a cooperative fashion to transfer a

total of two protons (2 H^+) and four electrons (2 e^- catechol→quinone; 2 e^- Mo^0→Mo^{II}) towards small molecule substrates.[11,15]

A ligand that is both redox-active and capable of actively delivering an acidic proton to a small molecule substrate has an active utility for use as a hydrogen-atom donor reagent. Given the importance of H-atom transfer in a variety of small molecule reactions, the development of H-atom non-innocent ligands in addition to understanding the fundamental thermodynamics of metallated systems could allow for new avenues in catalyst design. Herein, we set out to prove that the [SNS]H_3 ligand is capable of undergoing redox transformations as well as performing hydrogen-atom donation through the synthesis of a series of square-planar nickel complexes.

Results and Discussion

Synthesis and Structural Characterization

A family of square-planar nickel complexes of the general formula [SNS]Ni(L) (L = PPh_3 or PCy_3) were obtained through a two-step, one pot synthesis via ligand deprotonation followed by salt metathesis (**Scheme 6.1**).[16,17] Treatment of [SNS]H_3 with excess triethylamine followed by the addition of $Cl_2Ni(L)_2$ (L = PPh_3 (**14**) or PCy_3 (**15**)) under aerobic conditions yielded a dark blue/green powder (**14**) and a dark blue powder (**15**). Each were readily crystallized from MeCN solutions. The monoanionic forms of the complexes (**16** and **17**) could be obtained through the deprotonation of the [SNS]H_3 ligand using three equivalents of potassium hydride to produce an immediate precipitation of the putative [SNS]K_3 ligand. To the suspension, the desired divalent nickel phosphine complex was added to produce the monoanionic forms of the square-planar family in high yields (>70%) with associated color changes unique to each complex (PPh_3 = forest green; PCy_3 = powder blue). X-ray quality crystals of the monoanionic complexes were obtained through slow diffusion of either an MeCN (**16**) or THF (**17**) solution of the analyte into Et_2O (**16**)

or pentane (**17**) in the presence of the potassium chelating agent 2,2,2-cryptand at room temperature. Finally, under an inert atmosphere, the selective deprotonation of the thiolates was achieved through the use of two equivalents of triethylamine followed by the addition of $Cl_2Ni(L)$ to provide the orange powders of complexes **18** and **19**. These species were readily crystallized from THF (**18**) or MeCN (**19**) to yield transparent orange crystals. Electrospray ionization mass-spectrometry (ESI-MS) performed on the isolated complexes revealed parent ion signals consistent with the desired compositions of **14** (1194 *m/z*), **15** (596 *m/z*), **16 (**617 *m/z*), **17** (635 *m/z)*, **18** (580 *m/z)*, and **19** (597 *m/z*) as solutions of THF or MeCN. ESI-MS suggests that **14** maintains its dimerized solid-state structure in solution.

Scheme 6.1. Synthesis of square-planar nickel complexes **14-19**.

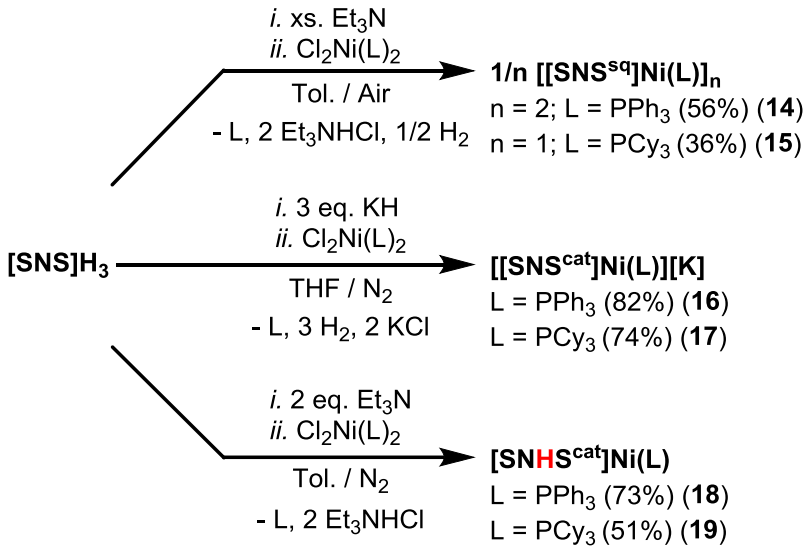

X-ray diffraction studies on single crystals of complex **14** revealed a dimeric structure consisting of the stacking of two pseudo-square planar nickel monomers while complex **15** demonstrated a monomeric pseudo-square planar species. **Figure 6.1** shows the solid-state structures of complexes **14** and **15** as ORTEP diagrams with a table of selected bond lengths and angles provided in **Table 6.1.** Complex **14** revealed severe distortion from an ideal square-planar geometry through a calculated structural parameter (τ_4) of 0.32 (ideal square planar = 0.0).

Additionally, the distortion can also be observed in the P–Ni–N angle of 139.55°, skewed roughly 40° from linearity (180°). This distortion seemed to be caused by the "limited" cone angle of the triphenylphosphine ligand (145°).[18] Increasing the steric effect of the ancillary phosphine by using the larger tricyclohexylphosphine (PCy_3, ∠179°), a cone angle 34° larger than triphenylphosphine, demonstrated the isolation of monomeric **15**.[18] Complex **15** is observed to adopt a more ideal square-planar geometry, confirmed through a τ_4 value of 0.03. Investigation into the angles around the nickel center of **15** revealed average angles of 90° and 178° consistent with the calculated τ_4 values.

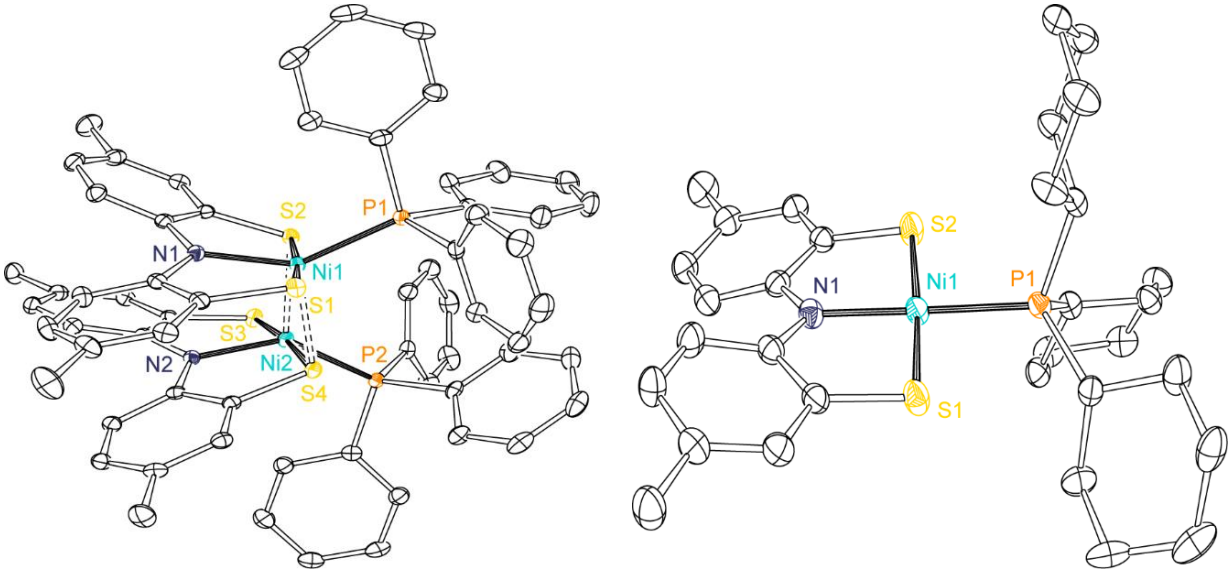

Figure 6.1. ORTEP diagrams for complexes (*left*) [[SNS]Ni(PPh_3)]$_2$ (**14**); and (*right*) [SNS]Ni(PCy_3) (**15**) with thermal ellipsoids shown at 50% probability. Hydrogen atoms have been omitted for clarity from both. Two solvent molecules (MeCN) were removed from **14**.

Further analysis of the solid-state metrics about the metal and ligand framework of **14** and **15** revealed minimal differences between the two analogs. The average Ni–S bond distances of **14** and **15** were found to be 2.198 and 2.173 Å, respectively. In dimeric **14**, the average Ni–S bond distance (2.418 Å) observed connecting the two monomers extend just outside the sum of the covalent radii for the individual atoms (Ni = 1.24 and S = 1.05 Å), consistent with no formal bonding between the two.[19] The average Ni–N bond distances were found to lie at 1.908 and 1.921

Å for complexes **14** and **15**, respectively. The Ni–P bond distances of 2.196 and 2.218 Å of **14** and **15**, respectively, remain relatively the same (Δ = 0.022 Å) despite exchange of PPh_3 for PCy_3. Interrogation into the bond distances of the ligand backbone reveal similar findings with average S–C distances of 1.742 Å and average N–C distances of 1.386 Å for both complexes. Putative oxidation assignments for complexes **14** and **15** suggest an overall singly oxidized complex with isolation under aerobic conditions.

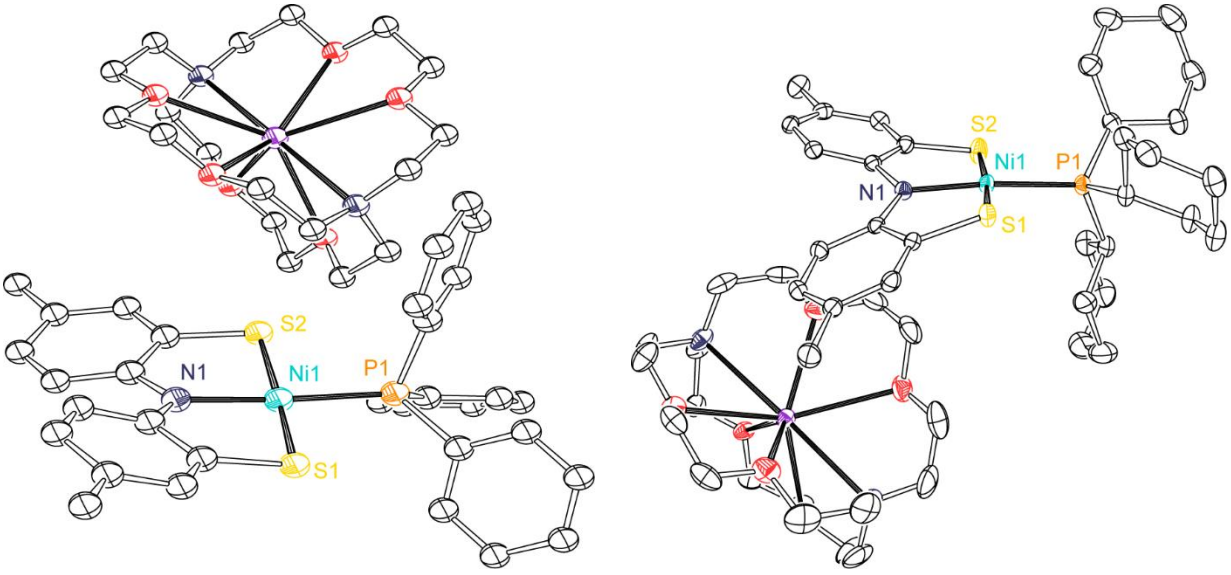

Figure 6.2. ORTEP diagrams for complexes (*left*) [[SNS]Ni(PPh_3)][K] (**16**); and (*right*) [[SNS]Ni(PCy_3)][K] (**17**) with 2,2,2-cryptand and thermal ellipsoids shown at 50% probability. Hydrogen atoms have been omitted for clarity from both. A solvent molecule was removed from each (**16** – MeCN; **17** – THF).

X-ray diffraction studies on single crystals of complexes **16** and **17** revealed monoanionic pseudo-square planar nickel centers with an observed outer sphere potassium cation trapped by the sequestering agent 2,2,2-crytand. The solid state structures for **16** and **17** are shown as ORTEP diagrams in **Figure 6.2**. Structural parameters (τ_4) of 0.07 and 0.08 were calculated for complexes **16** and **17**, respectively, demonstrating near ideal square-planar geometry. Angles about the nickel center in each species revealed average angles of 90° and 175°, consistent with the calculated structural parameter. Bond metric analysis of complexes **16** and **17** reveal negligible

differences between the two analogs. The two complexes display the same average Ni–S bond distances of 2.172 Å and very similar Ni–N distances of 1.896 Å (**16**) and 1.908 Å (**17**). The Ni–P bond distances lie at 2.171 and 2.202 Å for complexes **16** and **17**, respectively, where a slight elongation is observed between exchange of the ancillary phosphine from PPh_3 for PCy_3 ($\Delta = 0.03$ Å). The average S–C bond distances of the ligand backbone for both **16** and **17** were found to be 1.757 and 1.752 Å, respectively, while the average N–C bond distances were found to be 1.399 and 1.397 Å, respectively.

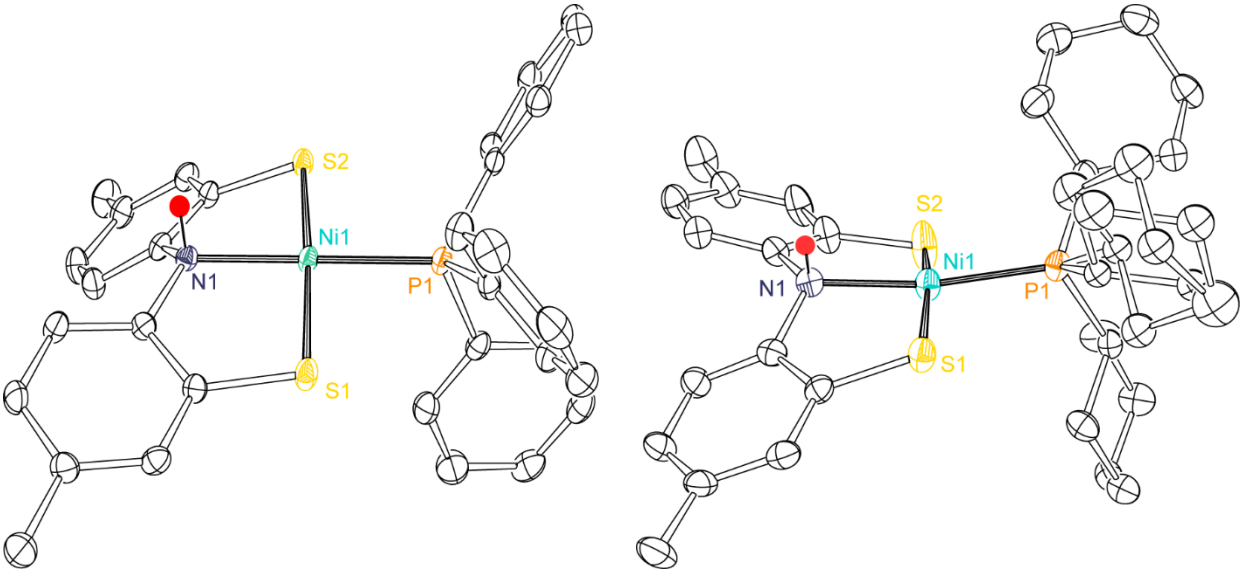

Figure 6.3. ORTEP diagrams for complexes (*left*) [SNHS]Ni(PPh_3) (**18**); and (*right*) [SNHS]Ni(PCy_3) (**19**) with thermal ellipsoids shown at 50% probability. Hydrogen atoms have been omitted for clarity from both (except the N–H protons shown in red). Two solvent molecules (THF) were removed for clarity from **18**.

X-ray diffraction studies on single crystals of **18** and **19** revealed the singly protonated [SNHS] ligand framework supporting pseudo-square planar nickel centers. **Figure 6.3** illustrates the solid-state structures of **18** and **19** as ORTEP diagrams. The nickel centers of **18** and **19** display calculated τ_4 values of 0.08 and 0.17, respectively. The angles observed about the nickel center in each case were found to lie between 86.94 and 93.95° while linear angles extended from 169.6 to 179.5°, consistent with the calculated structural parameters. An average Ni–S bond distance of 1.764 and 1.753 Å were observed for complexes **18** and **19**, respectively, with Ni–N bond distances

of 1.965 and 1.986 Å, respectively. The Ni–P bond distances of 2.168 (**18**) and 2.198 Å (**19**) demonstrate a slight elongation of 0.03 Å. The S–C and N–C bond distances of the [SNHS] ligand backbone for both complexes were found between 1.751–1.777 Å and 1.461–1.475 Å, respectively.

Oxidation state assignments for the nickel centers of **14-19** are of interest. The observed range of Ni–S bond distances for complexes **14-19** (2.167–2.212 Å) agree well with known Ni^{II}–S containing complexes in the literature which have displayed a similar range of 2.170–2.240 Å.[20–22] The average Ni–N bond distances of **14-17** ($Ni–N_{avg}$ = 1.909 Å) are all consistent with the interaction between a Ni^{II} ion and an sp^2 hybridized nitrogen ion, observed in the literature between 1.845 and 1.923 Å.[23–26] In contrast, the Ni–N bond distances of **18** and **19** are substantially elongated to lengths of 1.960 and 1.980 Å, respectively, however, each are indicative of the interaction of an sp^3 hybridized nitrogen to a Ni^{II} ion (1.920–2.010 Å).[23,27] The Ni–P bond distances also agree well with divalent nickel phosphine containing complexes in the literature with observed bond distances of 2.130–2.240 Å.[20,28] The data suggests that complexes **14-19** adopt a nickel(II) center.

Based on the nickel center likely not undergoing redox changes within the series, investigation turned towards the [SNS] scaffolds for ligand based valence changes. No noticeable differences were observed within the S–C bond distances across the series, which may be due to the polarizability of the sulfur atoms. Alternatively, investigation of the nitrogen ion revealed structural anomalies. A large twist is observed in the solid-state structures of **18** and **19**, with C(1)–C(6)–N(1)–Ni(1) torsion angles > 27°, while complexes **14-17** demonstrate the same twist < 17° ($\Delta > 10°$). This twist appears directly related to the associated hybridization change for the nitrogen center upon complexation ($sp^2 \rightarrow sp^3$). Additional evidence of this hybridization change

stems from the observed τ_4 values for the nitrogen ions of **18** and **19** which both exhibited τ_4 values of 0.90 (T_d = 1.0). Despite the tridentate [ONO] and [SNS] ligands being electronically different, structural information collected from metallated [ONO] species can be used to establish N–C single and double bond character within the tridentate ring system. Based on metallated [ONO] complexes, typical N(sp^2)–C(sp^2) single bond (1.370–1.470 Å),[23,25,29,30] N(sp^3)–C(sp^2) single bond (1.470–1.500 Å)[23,25], and N(sp^2)–C(sp^2) double bond (1.260–1.350 Å)[23,25] distances have been reported for tridentate ring systems involving a central nitrogen atom. These distances may offer insight into the bonding environment about the nitrogen center of the [SNS] analog to aide in ligand oxidation state assignment. With the observed distances of the N–C bonds in **14-17**, the range of distances (1.380–1.470 Å) appear consistent with a N(sp^2)–C(sp^2) single bond in each case. Furthermore, the N–C distances of 1.465 and 1.473 Å in ligand protonated **18** and **19**, respectively, appear consistent with a N(sp^3)–C(sp^2) single bond in each case. With this polarization, the sulfur retains a large amount of spin density and therefore delocalizes less density to the C–S, N–C, or C–C bonds of the ring system, resulting in negligible bond fluctuations within the ligand backbone.[31] Overall it appears that the bond metrics of the ligand scaffolds do not greatly change across the series.

Table 6.1. Selected bond lengths and bond angles for complexes **14-19**.

	[[SNS$^{sq\bullet}$]Ni(PPh$_3$)]$_2$ (**14**)	[[SNS^{cat}]Ni(PPh$_3$)] [Kcrypt] (**16**)	[SNHS^{cat}]Ni(PPh$_3$) (**18**)
	Bond Distances / Å		
Ni1 – P1	2.2090(4)	2.1711(6)	2.1683(5)
Ni1 – S1	2.2117(4)	2.1742(6)	2.1630(5)
Ni1 – S2	2.1856(4)	2.1688(6)	2.1872(5)
Ni1 – N1	1.9067(12)	1.8973(15)	1.9652(14)
S1 – C1	1.7466(15)	1.7610(18)	1.7559(18)
S2 – C12	1.7436(15)	1.7526(19)	1.7714(18)
N1 – C6	1.3936(18)	1.395(2)	1.461(2)
N1 – C7	1.3797(18)	1.402(2)	1.469(2)
Ni1 – S4	2.4267(5)	–	–
Ni2 – S2	2.4079(6)	–	–
	Bond Angles / °		
P1 – Ni1 – S1	88.553(15)	92.804(19)	89.914(19)
P1 – Ni1 – S2	93.058(15)	90.34(2)	93.012(18)
S1 – Ni1 – N1	87.48(4)	88.33(5)	89.72(4)
S2 – Ni1 – N1	87.84(4)	88.22(5)	87.38(4)
S1 – Ni1 – S2	174.151(16)	174.22(2)	172.72(2)
P1 – Ni1 – N1	142.81(4)	175.97(5)	179.53(5)
	Torsion Angle / °		
C1 – C6 – N1 – Ni1	18.17°	16.92°	34.17°
τ_4 value	0.32	0.07	0.08
	[[SNS$^{sq\bullet}$]Ni(PCy$_3$)]$_2$ (**15**)	[[SNS^{cat}]Ni(PCy$_3$)] [Kcrypt] (**17**)	[SNHS^{cat}]Ni(PCy$_3$) (**19**)
	Bond Distances / Å		
Ni1 – P1	2.2192(6)	2.2025(7)	2.1983(6)
Ni1 – S1	2.1814(7)	2.1694(7)	2.175(4)
Ni1 – S2	2.1665(7)	2.1749(7)	2.1865(6)
Ni1 – N1	1.9224(18)	1.9085(19)	1.9843(16)
S1 – C1	1.743(2)	1.754(2)	1.755(4)
S2 – C12	1.742(2)	1.750(2)	1.751(2)
N1 – C6	1.392(3)	1.398(3)	1.471(2)
N1 – C7	1.390(3)	1.395(3)	1.475(2)
	Bond Angles / °		
P1 – Ni1 – S1	91.79(2)	93.10(3)	92.05(10)
P1 – Ni1 – S2	91.40(2)	91.52(3)	93.95(2)
S1 – Ni1 – N1	88.18(6)	87.61(6)	88.54(11)
S2 – Ni1 – N1	88.61(6)	88.07(6)	86.94(5)
S1 – Ni1 – S2	176.59(2)	174.64(3)	170.33(7)
P1 – Ni1 – N1	179.00(6)	174.15(6)	169.55(5)
	Torsion Angle / °		
C1 – C6 – N1 – Ni1	12.19°	15.37°	27.56°
τ_4 value	0.03	0.08	0.17

The metrical data collected for complexes **14-19** agree with Ni^{II} centers supported by a redox-active [SNS] ligand platform. Complexes **14** and **15** appear supported by an oxidized, dianionic form of the ligand, [$SNS^{sq\bullet}$], containing what may to be a ligand based radical (likely localized on a sulfur atom). Dimer formation in **14** appears weakly coupled as the use of a sterically bulkier monodentate phosphine, PCy_3, resulted in the formation of a neutral monomeric species.[32] Monoanionic forms **16** and **17** appear consistent with a fully reduced [SNS^{cat}] ligand scaffold with no evidence for metal based reduction to form the Ni^{I} species. Furthermore, selective deprotonation of the [SNS^{cat}]H_3 ligand afforded the isolation of complexes **18** and **19**, both consistent with the fully reduced, singly-protonated, dianionic form of the ligand, [$SNHS^{cat}$]. The bond metrics observed for **14-19** show no substantial differences across the ligand backbones which indicate that further characterization evidence is required to confirm the oxidation state assignments outlined above.

Spectroscopic Characterization of Complexes 14-19

The electronic structures of **14-19** were further investigated using electronic absorption spectroscopy (UV-vis). All spectroscopic data collected for complexes **14-19** are provided in **Table 6.2**. Complexes **14-19** exhibit at least one charge-transfer transition within the visible region given the magnitude of their extinction coefficients (236-677 nm, 2,000–31,300 ε / $M^{-1}cm^{-1}$, **Figure 6.4**). Interestingly, complexes **14** and **15** exhibit broad low-energy transitions at 661 nm and 677 nm, respectively. This low-energy transition is unique to each family of square-planar complexes and appear only in the putative singly oxidized form of the ligand, [$SNS^{sq\bullet}$]. It has been previously demonstrated that electronic absorption is a very powerful tool in addressing ligand based oxidations for metallated [ONO] complexes, whereby the [$ONO^{sq\bullet}$] form of the ligand reveals characteristic broad low-energy transitions between 500 and 1100 nm.[29] These transitions

are characterized as π→π* transitions due to their metal-independent nature, however, in the case of the [SNS] ligand, it appears that the broad low-energy transition is effected by the exchange of the ancillary phosphine ligand. This is consistent with a metal-dependent transition, suggesting a metal to ligand charge transfer transition (MLCT, Ni→S).[33–35] Additionally, work on dithiolene complexes have illustrated intense electronic transitions in the near infrared (>600 nm) region as strong evidence for ligand oxidation.[31] These transitions at ~670 nm appear to offer a spectroscopic handle for distinguishing between the [SNS^{cat}] and [SNS^{sq}•] forms of the ligand.

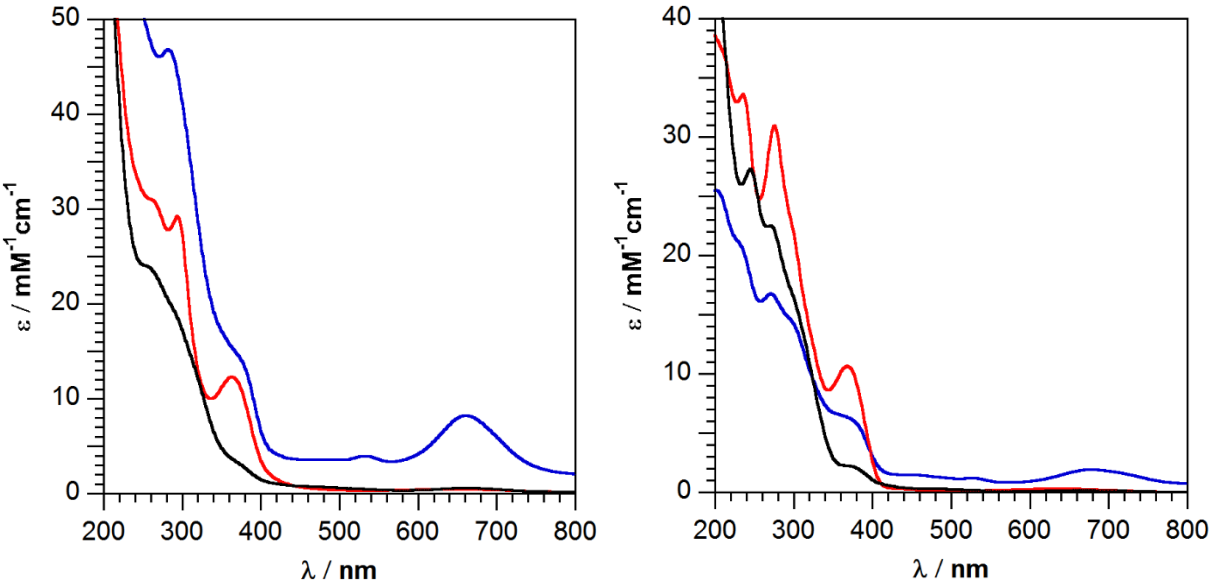

Figure 6.4. Electronic absorption spectra collected in MeCN for (*left*) PPh_3 derivatives **14** (blue), **16** (red), and **18** (black); (*right*) PCy_3 derivatives **15** (blue), **17** (red), and **19** (black).

Table 6.2. Spectroscopic data for complexes **14-19**.

	λ / nm (ε / M^{-1} cm^{-1})[a]	g-value	^{31}P NMR (δ / ppm)[b]
[[SNS^{sq}•]Ni(PPh_3)]$_2$ (**14**)	282 (46800); 378 (sh, 13700); 661 (8200)	2.01, 1.94[c]	26.0
[[SNS^{cat}]Ni(PPh_3)][K] (**16**)	294 (29200); 364 (12300)	–	36.0
[SNHS^{cat}]Ni(PPh_3) (**18**)	260 (23700)	–	29.0
[SNS^{sq}•]Ni(PCy_3) (**15**)	271 (16700); 300 (14200); 376 (6100); 677 (1900)	2.04, 2.01, 1.97[d]	–
[[SNS^{cat}]Ni(PCy_3)][K] (**17**)	236 (33600); 276 (31000); 368 (10700)	–	33.0
[SNHS^{cat}]Ni(PCy_3) (**19**)	244 (27000); 270 (22500); 374 (sh, 2200)	–	33.9

[a]CH_3CN. [b]CH_3CN-d_3. [c]Paramagnetic species collected in frozen benzene at 77K, ($g_\perp$, $g_\parallel$). [d]Collected in frozen THF at 10K, (g_x, g_y, g_z).

To probe the magnetic properties of complexes **14** and **15**, electron paramagnetic resonance (EPR) and nuclear magnetic resonance (NMR) spectroscopy were utilized. Despite both

complexes suspected of containing a ligand localized radical, formally [SNS$^{sq\bullet}$], **14** is readily characterized through ^{1}H and ^{31}P{^{1}H} NMR due to likely antiferromagnetic coupling occurring between the two monomers in polar solvents (MeCN or THF). This diamagnetic character lead to a singlet resonance observed in the ^{31}P{^{1}H} NMR at 26.0 ppm. Interestingly, this coupling can be interrupted through dissolution of **14** with non-polar benzene to yield a paramagnetic species which was analyzed through the use of electron paramagnetic resonance (EPR) (**Figure 6.5**). EPR spectra collected at room temperature (298 K) on **14** and **15** demonstrated isotropic signals centered at g = 2.003 and g = 2.01, respectively, consistent with s = ½ ground states (*insets*, **Figure 6.5**). Cooling the samples to 77K (**14**) or 10K (**15**), an axially compressed signal with $g_{|} = 2.01$ and $g_{||} = 1.94$ and a rhombic signal with g-values of $g_x = 2.03$, $g_y = 2.01$, and $g_z = 1.97$, respectively, were observed (**Figure 6.5**). Sulfur based radicals previously reported in Ni–S containing complexes demonstrate g-values in a range of 2.14−1.97,[36–38] while a Ni^{I} or Ni^{III} systems containing a metal centered radical are expected to give characteristic rhombic signals with g-values of $g_x = 2.29–2.11$, $g_y = 2.12–2.04$, $g_z = 2.04–2.002$.[39–43] The data suggests that **14** and **15**, although believed to be largely sulfur localized, demonstrate influence from the nickel(II) center.

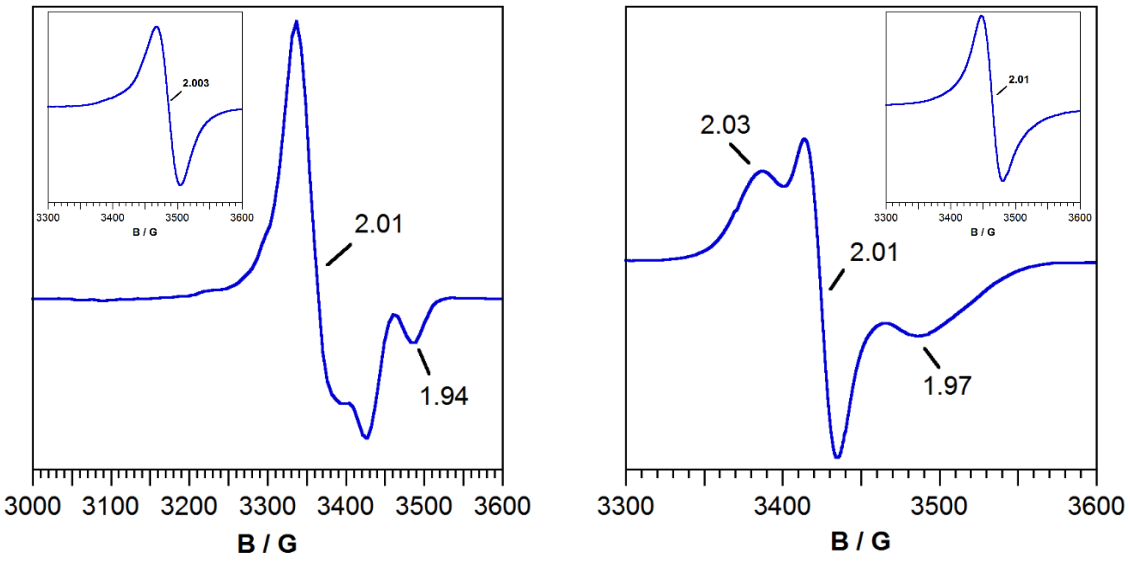

Figure 6.5. X-Band EPR spectra collected for (*left*) [[SNS$^{sq\bullet}$]Ni(PPh$_3$)]$_2$ (**14**) in frozen benzene at 77 K and (*inset*) 298 K; (*right*) [SNS$^{sq\bullet}$]Ni(PCy$_3$) (**15**) in frozen THF at 10 K and (*inset*) 298 K.

Investigation into the magnetic properties of **16-19** using nuclear magnetic resonance (NMR) revealed diamagnetic character with each species yielding characteristic $^{31}P\{^{1}H\}$ NMR shifts at room temperature in CD_3CN (**Table 6.2**). Complex **16** (PPh_3) demonstrated a sharp singlet resonance at 36.0 ppm, shifted downfield from dimer **14** (26.0 ppm). Protonated ligand backbone **18** (PPh_3) demonstrated a sharp singlet resonance at 29.0 ppm, shifted downfield from **14** and upfield from **16**. Monoanionic **17** (PCy_3) displays a singlet resonance at 33.0 ppm while protonated **19** (PCy_3) yielded a singlet resonance slightly downfield at 33.9 ppm. The protonated nitrogen was identified via ^{1}H NMR as a singlet resonance observed at 8.31 and 7.84 ppm in **18** and **19**, respectively.

Electrochemistry

Electrochemical analysis of complexes **14-19** in MeCN displayed well-behaved electrochemistry, each exhibiting at least two one-electron processes which were all referenced to $[Cp_2Fe]^{0/+}$ (**Figure 6.6**). Complex **14** demonstrated two reductive processes centered at −0.61 and −2.54 V. It should be noted that the intensity of **14** is likely due to the breaking apart of the dimer under electrochemical conditions to give a signal twice the intensity. Monoanionic **16**, revealed a shift in the resting potential with an observed single reversible reductive event and single reversible oxidative event centered at −2.54 and −0.61 V, respectively, consistent with a reduced form of **14**. Ligand protonated **18** demonstrated two reductive events, the first consisting of an irreversible event at −1.60 V and the second centered at −2.54 V. Analysis of the tricyclohexylphosphine derivatives revealed electrochemically similar events to the triphenylphoshine analogs. Complex **15** exhibited one reversible reductive event centered at −0.64 V with a second irreversible reductive event centered at −2.74 V. Monoanionic **17** demonstrated a shift in the resting potential to yield a single reversible oxidative and single irreversible reductive process at −0.64 and −2.74

V, respectively. Ligand protonated **19** reveals an irreversible reductive event at −1.76 V followed by a second irreversible reductive event centered at −2.74 V.

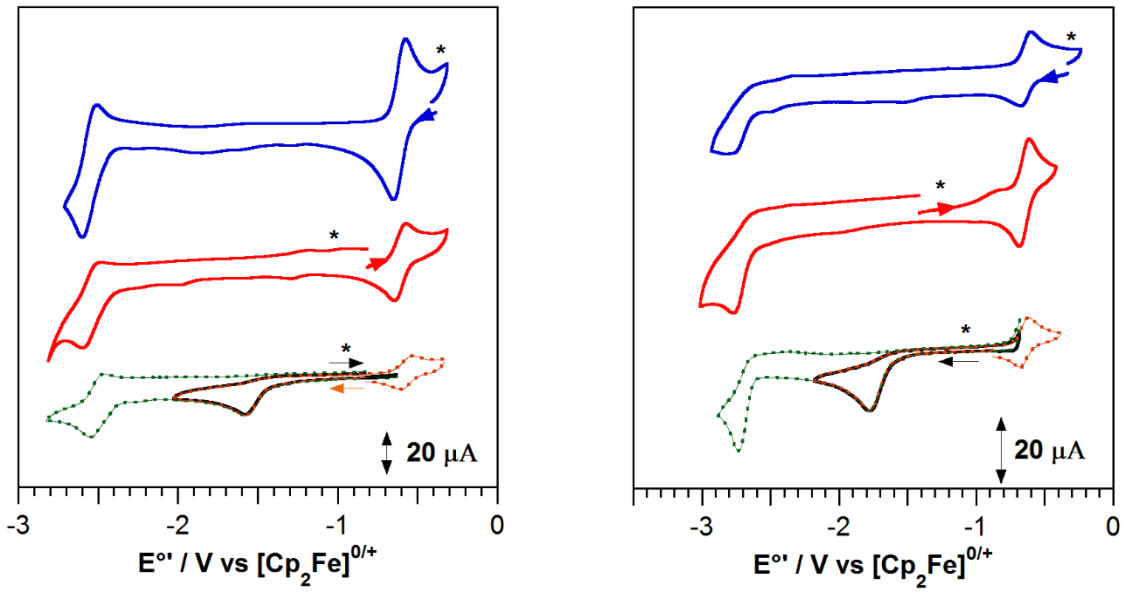

Figure 6.6. Cyclic voltammograms for (*left*) [[SNS^{sq}•]Ni(PPh$_3$)]$_2$ (**14**, blue), [[SNS^{cat}]Ni(PPh$_3$)][K] (**16**, red), and [SNHS^{cat}]Ni(PPh$_3$) (**18**, bottom); (*right*) [SNS^{sq}•]Ni(PCy$_3$) (**15**, blue), [[SNS^{cat}]Ni(PCy$_3$)][K] (**17**, red) and [SNHS^{cat}]Ni(PCy$_3$) (**19**, bottom). All voltammograms were recorded at a 1 mM analyte concentration in 0.1M [NBu$_4$][PF$_6$] in dry, degassed, MeCN under a nitrogen atmosphere using a 3 mm glassy carbon working electrode, Pt wire counter electrode, and Ag$^{0/+}$ wire pseudo-reference electrode at room temperature at 200 mV sec^{-1} scan rates.

Table 6.3. Electrochemical redox potentials for complexes **14**-**19**.

	$E_1°'$ (Ni)$^{I/II}$	E_{pc}'	$E_2°'$ ([SNS])$^{3-/2-\cdot}$
[[SNS^{sq}•]Ni(PPh$_3$)]$_2$ (**14**, *left*, blue)	−2.54	*a*	−0.61
[SNS^{cat}]Ni(PPh$_3$) (**16**, *left*, red)	−2.54	*a*	−0.61
[SNHS^{cat}]Ni(PPh$_3$) (**18**, *left*, bottom)	−2.54	−1.60[c]	−0.61[b]
[SNS^{sq}•]Ni(PCy$_3$) (**15**, *right*, blue)	−2.74[c]	*a*	−0.64
[SNS^{cat}]Ni(PCy$_3$) (**17**, *right*, red)	−2.74[c]	*a*	−0.64
[SNHS^{cat}]Ni(PCy$_3$) (**19**, *right*, bottom)	−2.74[c]	−1.76[c]	−0.64[b]

[a]Not Observed. [b]Observed after scanning past E_{pc}'. [c]Irreversible event

Comparison of the redox processes from the PPh$_3$ derivatives (**14**/**16**/**18**) to the PCy$_3$ derivatives (**15**/**17**/**19**) indicate both ligand and metal redox processes are present. A major cathodic shift in the reductive process $E_1°'$ by 200 mV is indicative of a strong influence from exchange of the appended phosphine, indicating a large amount of metal character, concluding $E_1°'$ as the Ni$^{II/I}$ couple. Analogously, a slight cathodic shift in the $E_2°'$ event by 30 mV indicates

a process less influence by substitution of the ancillary phosphine appended to the nickel center, revealing $E_2°'$ as the $([SNS])^{3-/2-\bullet}$ couple. The observed shifts in the electrochemical data to more negative potentials is directly related to the donor strength of the ancillary phosphine, whereby PCy_3 is a stronger sigma donating ligand than PPh_3 to the nickel center. The first irreversible reductive event of **18** and **19** appears consistent with the nitrogen atom of the [SNS] scaffold undergoing a structural rearrangement ($sp^3 \rightarrow sp^2$) facilitating the release of H•. Scanning past the first reductive event in each case initiates the growth of a reversible event at −0.61 (**18**) and −0.64 V (**19**), vs $[Cp_2Fe]^{0/+}$, indicative of the formation of **14** and **15** in solution. Based on the electrochemical evidence, the irreversible reductive event appears influenced by the nickel center with a change in E_{pc}' by 160 mV. This suggests that the expulsion of H• may be initiated through a Ni^I center.

Thermodynamic Reactivity

Reactivity pathways were investigated to connect each family of complexes through a thermodynamic square scheme. All reaction products were verified through EPR or $^{31}P\{^1H\}$ NMR spectroscopy (**Scheme 6.2**). Diamagnetic complex **14** and paramagnetic complex **15** could be chemically reduced using an equivalent of potassium graphite in THF to undergo an immediate color change unique to each reaction to generate diamagnetic complexes **16** and **17**. Similarly, complexes **16** and **17** could readily be chemically oxidized using an equivalent of silver triflate (AgOtf) to reform diamagnetic complex **14** and paramagnetic complex **15**, respectively. Complexes **16** and **17** could be further reacted with an equivalent of a proton source such as 4-cyanoanilinium tetrafluorborate ($pk_a^{MeCN} = 7.0$)[44] or 2,6-lutidinium tetrafluoroborate ($pK_a^{MeCN} = 14.14$)[45] to perform a proton transfer (PT) to the nitrogen of the [SNS] ligand backbone with an associated color change generating complexes **18** and **19**, respectively. Similarly, treatment of

complexes **18** and **19** using bases such as DBU (pK_a^{MeCN} = 24.34),[45] DMAP (pK_a^{MeCN} =17.95),[45] or excess 2,4,6-collidine (pK_a^{MeCN} = 14.98)[46] reformed complexes **16** and **17**. To close the square scheme, complexes **14** and **15** were treated with the hydrogen atom donor reagent TEMPOH in an attempt to perform a concerted proton-coupled electron-transfer (PCET), however, no reaction was observed. Conversely, treatment of complexes **18** and **19** with an equivalent of TEMPO• resulted in immediate hydrogen-atom abstraction to form the dark blue/green solutions of **14** and **15**, respectively. This suggests that the N–H bond of **18** and **19** is weaker than the O–H bond of TEMPOH ($BDFE^{MeCN}$ = 66.5 kcal mol^{-1}) in MeCN solutions.

Scheme 6.2. Thermodynamic square scheme for the reactivity of complexes **14-19**.

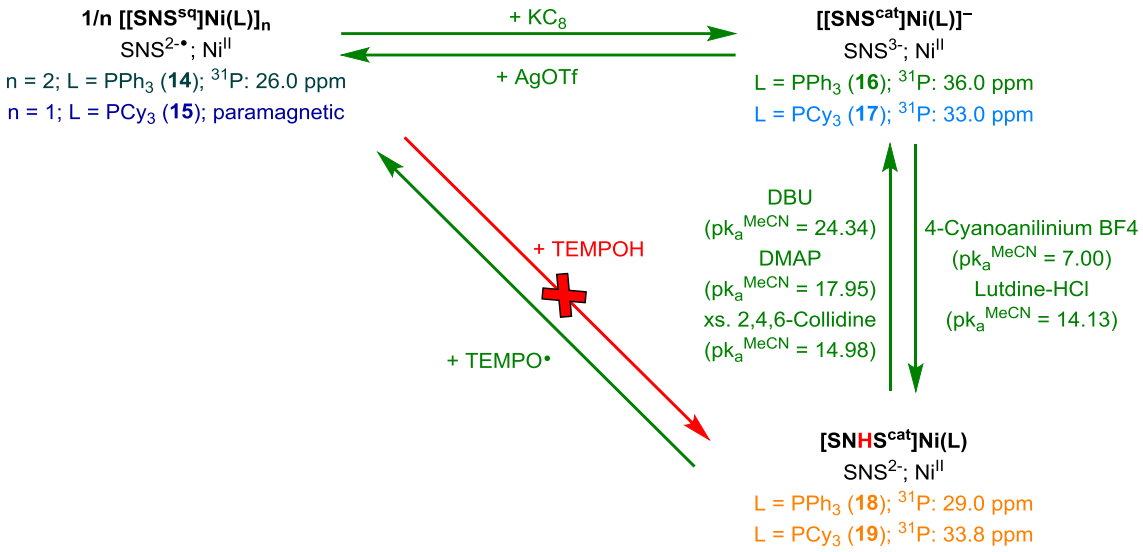

Bond Strength Determination

Hess' Law allows for the measured pK_a and E°' values to be used in the calculation of the N–H bond dissociation free energy (BDFE) using the Bordwell equation (**Equation 6.14**). By means of an approach initially outlined by Meyer *et al*. (**Scheme 6.3**), electronic absorption spectroscopy can be used to monitor an acid/base equilibrium titration to determine the equilibrium constant (K_{eq}) and pK_a for a protonated species. Cyclic voltammetry yields the potential associated with

the $E^{\circ\,\prime-/sq\bullet}$ redox event ($E_2^{\circ\prime}$) (**Table 6.3**).[45] Combination of these values through the Bordwell equation allow for the direct calculation of the N–H BDFEs for **18** and **19**.

Scheme 6.3. Square scheme for pK_a and BDFE determination.

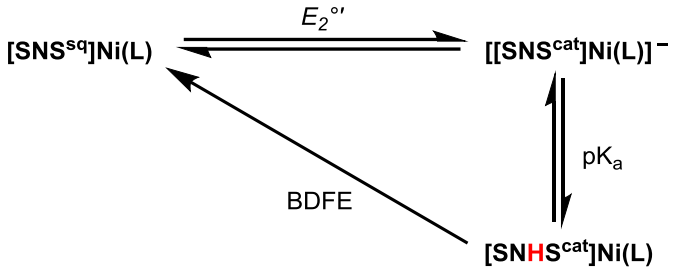

To this end, base titrations were carried out in MeCN to determine the K_{eq}, pK_a, and BDFE of complexes **18** and **19** in MeCN solutions. The complexes demonstrated complete deprotonation after the addition of more than 145 equivalents (**18**) or 4,300 equivalents (**19**) of 2,4,6-collidine (pK_a^{MeCN} = 14.98). Wavelengths were monitored at 364 nm (PPh_3) and 368 nm (PCy_3) for the growth of the charge transfer bands for the *in situ.* formation of **16** and **17**, respectively. The concentrations of [SNHS^{cat}]Ni(L) ([MH]), [SNS^{cat}]Ni(L)$^-$ ([M$^-$]), 2,4,6-collidine ([B]), and 2,4,6-collidinium ([BH$^+$]) were determined through mass balance. These concentrations allow for the determination of the equilibrium constant using equations previously outlined by Meyer *et al.*, shown below (**Equations 6.1–6.12**).[47] The absorbance due to 2,4,6-collidine and 2,4,6-collidinium tetrafluoroborate were found negligible at these wavelengths and therefore have been excluded from the calculations. **Equation 6.1** defines the initial absorbance at the monitored wavelength, prior to any addition of base.

$$A_0 = \varepsilon_{MH} b [MH]_0 \qquad (\mathbf{6.1})$$

Equation 6.2 defines the final absorbance after excess 2,4,6-collidine has been added to reach complete deprotonation of MH to form monoanionic M$^-$ *in situ.*

$$A_f = \varepsilon_{M^-} b [M^-]_f \qquad (\mathbf{6.2})$$

Equation 6.3 defines the absorbance at any time during the titration at the monitored wavelength. The subscript 't' describes titration.

$$A_t = \varepsilon_{MH} b[MH]_t + \varepsilon_{M-} b[M^-]_t \quad \textbf{(6.3)}$$

During the titration, the total concentration of nickel is equal to the initial concentration of $[MH]_0$ and the final concentration $[M^-]_f$, described by **Equation 6.4**. The equation can further be rearranged to give **Equations 6.5** and **6.6** which will be utilized later.

$$[MH]_0 = [M^-]_f = [MH]_t + [M^-]_t \quad \textbf{(6.4)}$$

$$[MH]_t = [M^-]_f - [M^-]_t \quad \textbf{(6.5)}$$

$$[M^-]_t = [MH]_0 - [MH]_t \quad \textbf{(6.6)}$$

The total concentration of base/conjugate acid at equilibrium is equal to the amount of base added ($[B]_x$), shown in **Equation 6.7**.

$$[B]_x = [BH^+]_t + [B]_t \quad \textbf{(6.7)}$$

Using mass balance, the ratio of products/reactants ($[M^-]_t/[MH]_t$) at any point during the titration can be described by **Equation 6.8** using **Equations 6.3, 6.5** and **6.6** to help simplify.

$$\frac{A(M^-)_t}{A(MH)_t} = \frac{A_t - A_0}{A_f - A_t} = \frac{\varepsilon_{MH} b[MH]_t + \varepsilon_{M-} b[M^-]_t - \varepsilon_{MH} b[MH]_0}{\varepsilon_{M-} b[M^-]_f - \varepsilon_{MH} b[MH]_t - \varepsilon_{M-} b[M^-]_t}$$

$$= \frac{\varepsilon_{MH}([MH]_t - [MH]_0) + \varepsilon_{M-}[M^-]_t}{\varepsilon_{M-}([M^-]_f - [M^-]_t) - \varepsilon_{MH}[MH]_t} = \frac{\varepsilon_{MH}(-[M^-]_t) + \varepsilon_{M-}[M^-]_t}{\varepsilon_{M-}([MH]_t) - \varepsilon_{MH}[MH]_t}$$

$$= \frac{\varepsilon_{M-}[M^-]_t - \varepsilon_{MH}([M^-]_t)}{\varepsilon_{M-}([MH]_t) - \varepsilon_{MH}[MH]_t} = \frac{(\varepsilon_{M-} - \varepsilon_{MH})[M^-]_t}{(\varepsilon_{M-} - \varepsilon_{MH})[MH]_t} = \frac{[M^-]_t}{[MH]_t} \quad \textbf{(6.8)}$$

Rearrangement of **Equation 6.8** gives **Equation 6.9**.

$$\left(\frac{A_t - A_0}{A_f - A_t}\right)[MH]_t = [M^-]_t \quad \textbf{(6.9)}$$

Combining **Equations 6.4** and **6.9** and simplifying gives **Equation 6.10**.

$$\frac{\left(\frac{A_t - A_0}{A_f - A_t}\right)[MH]_0}{\left(1 + \left(\frac{A_t - A_0}{A_f - A_t}\right)\right)} = [M^-]_t \qquad \textbf{(6.10)}$$

At equilibrium, the concentration of [M$^-$] is equal to that of [BH$^+$], whereby **Equation 6.7** yields **Equation 6.11**.

$$[B]_t = [B]_x - [M^-]_t \qquad \textbf{(6.11)}$$

The equilibrium constant equation below can then be rearranged to give **Equation 6.12**.

$$K_{eq} = \frac{products}{reactants} = \frac{[M^-]_t[BH^+]_t}{[MH]_t[B]_t}$$

$$\frac{[M^-]_t[BH^+]_t}{[MH]_t} = K_{eq}[B]_t \qquad \textbf{(6.12)}$$

The equilibrium constant, K_{eq}, is obtained through the slope of the observed trendline from a plot of $[B]_t$ vs $([M^-]_t/[MH]_t)[BH^+]_t$ (**Figures 6.7** and **6.8**). These parameters are given by **Equations 6.8**, **6.10**, and **6.11**. Using K_{eq}, the pK_a of complexes **18** and **19** could be calculated using **Equation 6.13**.

$$pKa(MH) = pKa(BH^+) - \log(K_{eq}) \qquad \textbf{(6.13)}$$

The pK_a of complexes **18** (PPh_3) and **19** (PCy_3) were found to be 15.92 ± 0.15 and 17.36 ± 0.02, respectively, using this approach. The calculated pK_a values in conjunction with the redox potential required to oxidize or reduce the ligand framework ($E_2°'$, **Table 6.3**) allowed for the direct calculation of the BDFEs for the N–H bond of **18** and **19**. These values were determined using **Equation 6.14**, where C_G is defined as 54.9 kcal mol^{-1} in MeCN.[9]

$$BDFE = 1.37\big(pKa(MH)\big) + 23.06(E'°) + C_G \qquad \textbf{(6.14)}$$

The bond dissociation free energies for the N–H bond in complexes **18** and **19** were calculated to be 62.4 ± 0.21 and 63.9 ± 0.03 kcal mol^{-1}, respectively. The results suggest that exchange of PPh_3 for the better donor PCy_3 rendered the complex an order of magnitude less acidic. Despite the

dissimilar pK_a values for the complexes, a difference of only 1.5 kcal mol^{-1} in the N–H BDFEs are observed. Experimentally, the calculated BDFEs for **18** and **19** are consistent with the observed reactivity of both complexes towards TEMPOH ($BDFE^{MeCN}$ = 66.5 kcal mol^{-1}) discussed eariler.[9] Similarly, as the O–H bond of TEMPOH is more than 2.6 kcal mol^{-1} stronger than the observed N–H bond in complexes **18** and **19**, the experimentally observed rapid hydrogen-atom transfer to TEMPO• to form **14**/**15** and TEMPOH is justified.

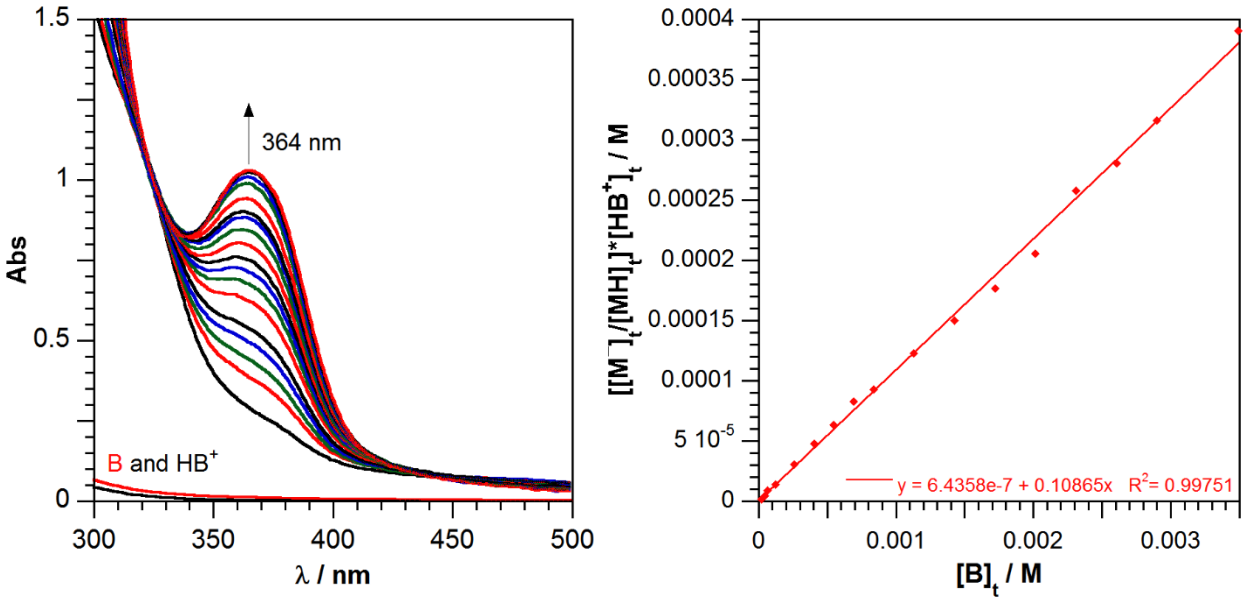

Figure 6.7. (*left*) Electronic absorption titration of [SNHS^{cat}]Ni(PPh_3) (**18**) in the presence of 2,4,6-collidine (bottom two traces correspond to absorption data collected for 2,4,6-collidine (red) and 2,4,6-collidinium tetrafluoroborate (black)); (*right*) K_{eq} determination plot using mass balance formulas.

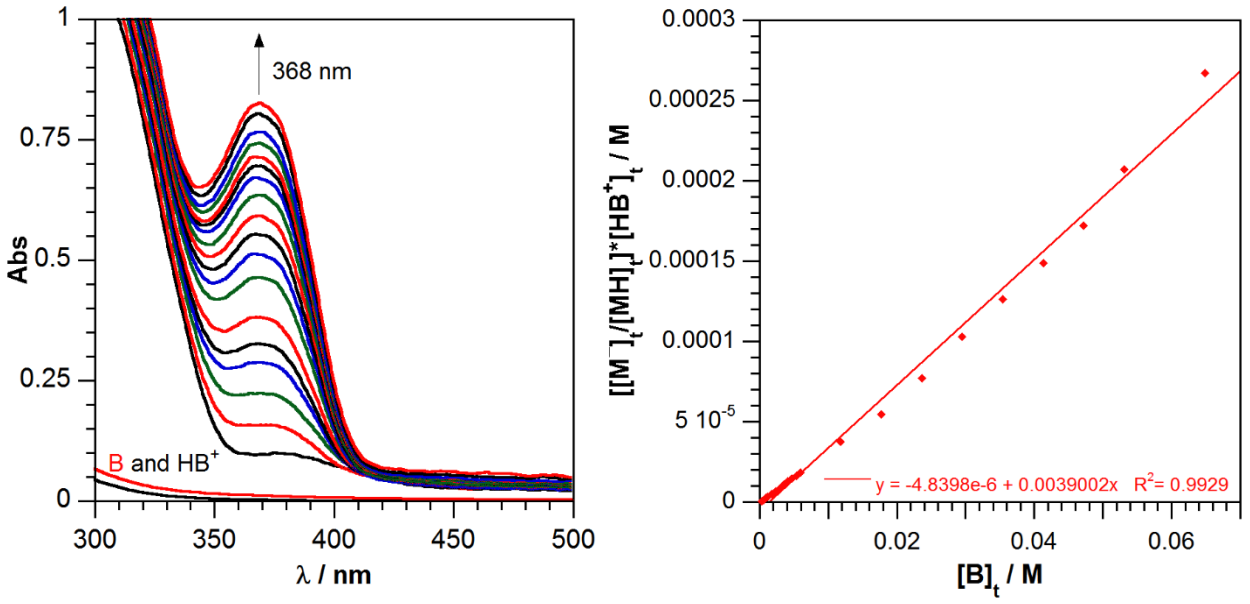

Figure 6.8. Electronic absorption titration of [SNHS^{cat}]Ni(PCy$_3$) (**19**) in the presence of 2,4,6-collidine (bottom two traces correspond to absorption data collected for 2,4,6-collidine (red) and 2,4,6-collidinium tetrafluoroborate (black)); (*right*) K_{eq} determination plot using mass balance formulas.

Theoretical Calculations

To help visualize the electronic structures of **14-19**, DFT computations were performed. Final geometry optimizations were carried out at the TPSS/TZVP level of theory after initial refinement of the solid-state structures using a more computationally inexpensive SVP basis set. The computed structures agree well with the solid-state structures. Metal–heteroatom bond distances fall within 0.02 Å of the measured values while the N–C and S–C bond distances fall within 0.005 and 0.004 Å, respectively. **Figure 6.9** shows the Kohn-Sham molecular orbitals and energies for complexes **14**, **16**, and **18**. The computed orbitals for the tricyclohexylphosphine derivatives are indistinguishable from the pictured orbitals of the triphenylphosphine derivatives with the only notable difference being in the relative energy levels of the SOMOs, HOMOs, and LUMOs.

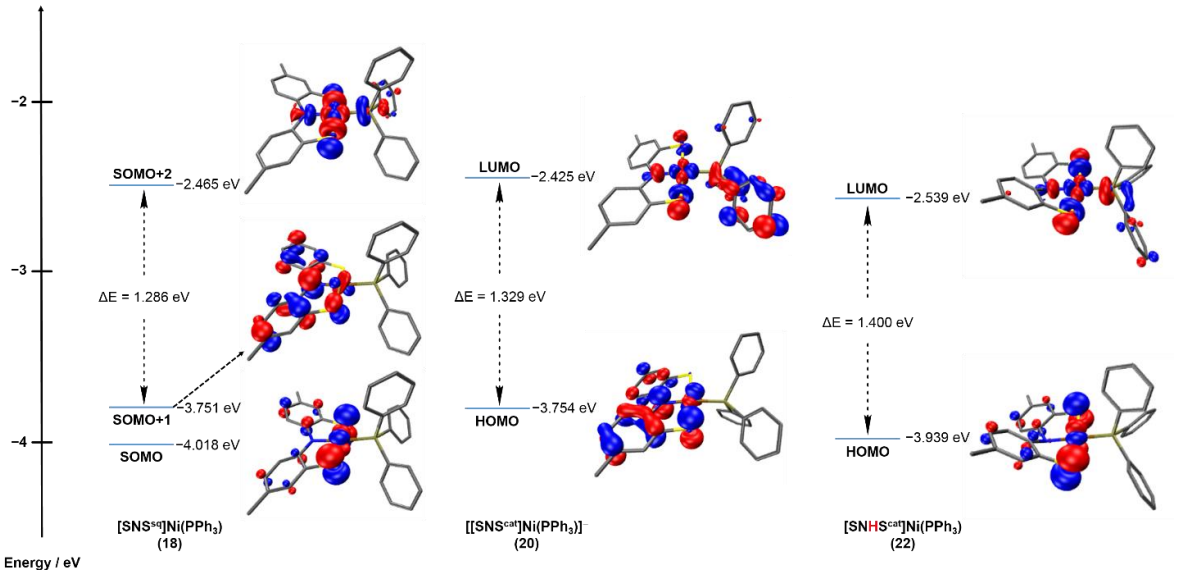

Figure 6.9. Kohn-Sham molecular orbitals and energies for (*left*) [[SNS$^{sq\bullet}$]Ni(PPh$_3$)]$_2$ (**14**, DFT run as monomer); (*middle*) [[SNS^{cat}]Ni(PPh$_3$)]$^-$ (**16**); and (*right*) [SNHS^{cat}]Ni(PPh$_3$) (**18**) using the TPSS/def2-TZVP level of theory. Rendering was performed using VMD for Windows.

Table 6.4. Mulliken population analysis distributions for complexes **14-19**.

	SOMO				SOMO+1				
	Ni (%)	S (%)	N (%)	C, P (%)	Ni (%)	S (%)	N (%)	C, P (%)	Energy Gap[b] (eV)
[[SNS$^{sq\bullet}$]Ni(PPh$_3$)]$_2$ (**14**)[a]	36.35	45.56	0.00	18.09	12.70	10.56	22.58	54.15	1.286
[SNS$^{sq\bullet}$]Ni(PCy$_3$) (**15**)	40.77	43.08	0.00	16.14	12.87	8.84	23.32	54.97	1.368
	HOMO				**LUMO**				
	Ni (%)	S (%)	N (%)	C, P (%)	Ni (%)	S (%)	N (%)	C, P (%)	Energy Gap (eV)
[[SNS^{cat}]Ni(PPh$_3$)]K (**16**)	19.79	16.86	16.91	46.43	23.33	18.26	5.19	53.22	1.329
[[SNS^{cat}]Ni(PCy$_3$)]K (**17**)	12.89	6.89	23.78	56.43	42.09	33.14	7.89	16.88	1.608
[SNHS^{cat}]Ni(PPh$_3$) (**18**)	41.13	42.28	0.54	16.04	41.14	28.06	5.71	25.09	1.400
[SNHS^{cat}]Ni(PCy$_3$) (**19**)	44.34	40.17	0.66	14.82	43.55	29.63	5.45	26.81	1.514

[a]DFT run as monomer. [b]Energy gap measured from the SOMO+1 to the SOMO+2.

Primary interest of the computational studies were to evaluate the location of the unpaired electron in complexes **14/15** (SOMO) in addition to evaluate the HOMO and LUMO molecular orbitals of the closed shell complexes **16-19**. Mulliken distributions for each complex were investigated at the SOMO, SOMO+1, and SOMO+2 energy levels for complexes **14** and **15**; and the HOMO/LUMO energy levels for complexes **16-19** (**Table 6.4**). The SOMO of **14** and **15** demonstrate high contributions from both nickel (>36%) and sulfur (>43%). The Kohn-Sham

molecular orbital visualizations demonstrate that the unpaired electron appears delocalized across both sulfur atoms with the nickel ion appearing to act as a conduit between the two. This agrees with what was observed experimentally, whereby the observed EPR signals appeared to be primarily sulfur localized with minor contributions from the nickel center. The SOMO+1 (reduction of the SOMO) of **14** illustrates that the [SNS] ligand adopts roughly 88% of the contribution, consistent with the electrochemical analysis of **14** and **15**, confirming $E_2°'$ as the $[SNS]^{sq\bullet/cat}$ redox couple. DFT calculations performed on complex **16** reveal that the HOMO energy level has large ligand based contributions (~80%) with minor contributions from the nickel center (~20%). This is consistent with the experimentally observed results which indicate that oxidation of **16** results in a ligand based oxidation through the formation of **14**. Computations on **18** reveal a HOMO energy level with large nickel (>41%) and sulfur (>40%) contributions, mimicking the contributions observed in the SOMO of **14**. The LUMO also demonstrates large nickel contributions (>41%) with lower sulfur contributions (>28%). This large contribution in the LUMO, suggests that upon reduction an electron may populate a nickel orbital and become delocalized among the [SNS] ligand scaffold. In all cases, it appears that the SOMO+2 and LUMOs all demonstrate moderately large nickel contributions, consistent with the the $Ni^{II/I}$ redox couple observed near the edge of the MeCN solvent window (> −2.50V).

Conclusion

Herein we demonstrate a synthetic approach to generate a unique set of square-planar nickel complexes supported by the [SNS] ligand scaffold. Further investigation of these nickel complexes conclude that the $[SNS]H_3$ ligand framework can act as a redox, proton, and hydrogen-atom non-innocent ligand. Characterization of the nickel complexes revealed Ni^{II} centers supported by a redox-active [SNS] ligand. Support for the [SNS] ligand being capable of redox

changes can be observed through the electronic, magnetic, and electrochemical characterization techniques applied to complexes **14-19**. Characteristic EPR signals in conjunction with a low-energy electronic transition give strong evidence for sulfur radical character and ligand oxidation in complexes **14** and **15**. The low-energy transition observed in **14** and **15** also offer a unique handle for characterization of metal complexes containing the [$SNS^{sq\bullet}$] form of the scaffold as this transition was absent in [SNS^{cat}]/[$SNHS^{cat}$] containing **16-19**. Electrochemically, all species are well-behaved with an observed ligand redox couple centered at −0.61 and −0.64 V, vs $[Cp_2Fe]^{0/+}$, for PPh_3 and PCy_3 derivatives, respectively. The N–H bond of protonated backbone **18** and **19** were found to be relatively weak (< 64 kcal mol^{-1}), with which rapid hydrogen-atom abstraction is observed upon treatment with TEMPO•. The complexes described herein provide valuable insight into the redox activity of the [SNS] ligand, illustrating the $[SNS]H_3$ ligand platform as multifunctional. The weak N–H bond in **18** and **19** is poised to readily react with a host of small molecule substrates through which H-atom transfer is necessary. Initial studies of electrochemical reduction of CO and CO_2 using monoanionic **16** and **17** are described in **Appendix A**.

Experimental

General Considerations. The compounds and reactions reported below show various levels of air- and moisture-sensitivity, therefore all manipulations were carried out using standard vacuum-line, Schlenk-line and glovebox techniques unless otherwise noted. Hydrocarbon and ethereal solvents were sparged with argon before being deoxygenated and dried by passage through Q5 and activated alumina columns, respectively. Halogenated solvents were sparged with argon and dried by passage through two activated alumina columns. To test for effective oxygen and water removal, aliquots of each solvent were treated with a few drops of a purple solution of sodium benzophenone ketyl radical in THF. CD_3CN was dried over CaH_2 and vacuum distilled prior to

use. Triphenylphosphine (sigma) and tricyclohexylphosphine (20 wt. % in toluene, sigma) were all used as received. The ligand $[SNS^{cat}]H_3$[30] and complexes, $Cl_2Ni(PPh_3)_2$[48] and $Cl_2Ni(PCy_3)_2$[48] were all prepared as previously described.

Spectroscopic Methods. Elemental analyses were conducted on a Perkin-Elmer 2400 Series II CHNS elemental analyzer. NMR spectra were collected on Bruker Avance 600 MHz spectrometer in dry, degassed CD_3CN. ^1H NMR spectra were referenced to TMS using the residual proteo impurities of the solvent (1.94 ppm for CD_3CN). All $^{31}P\{^1H\}$ NMR spectra were referenced with an external standard of phosphoric acid (H_3PO_4, 85%). Chemical shifts are reported using the standard δ notation in parts per million. Electronic absorption spectra were recorded with a Jasco V-670 absorption spectrometer or a Cary 60 UV-vis spectrometer equipped with fiber optic cables to allow for samples to remain under an inert atmosphere as solutions in dry, degassed MeCN contained in 1-cm quartz cells. Electrospray ionization mass-spectrometry (ESI-MS) data were collected on a Waters LCT Premier mass-spectrometer using dry, degassed MeCN or THF.

Electrochemical Methods. Electrochemical data were collected with a Gamry Series G 300 Potentiostat/Galvanostat/ZRA (Gamry Instruments, Warminster, PA, USA) using a 3.0 mm glassy carbon working electrode, a platinum wire auxiliary electrode, and a silver wire pseudo-reference electrode. Electrochemical experiments were performed at 25°C in a glovebox under an atmosphere of N_2. Electrochemical samples were 1.0 mM analyte solutions in MeCN containing 0.1 M $[NBu_4][PF_6]$ as the supporting electrolyte. All potentials were referenced to the $[Cp_2Fe]^{0/+}$ couple using ferrocene or decamethylferrocene as an internal standard. Ferrocene and decamethylferrocene (Acros) were purified by sublimation and tetra-*n*-butylammonium hexafluorophosphate (Acros) was recrystallized from ethanol three times and dried under vacuum.

Equilibrium Constant (K_{eq}) and pK_a Determination. In a typical experiment, a stock solution of the [SNHS^{cat}]Ni(L) species (1.67 mM – PPh_3; 1.42 mM – PCy_3) was made inside a nitrogen filled glovebox. Aliquots (200 µL) were removed from the stock solutions of analyte and diluted with 3.0 mL of MeCN to give concentrations between 60-70 µM and a total solution volume of 3.20 mL. The solution was transferred to a screw-capped 1-cm quartz cuvette. An MeCN solution of 2,4,6-collidine (380 mM for **18**) was also prepared at the same time in a 20-mL scintillation vial (concentrated 2,4,6-collidine was used for **19**). Spectra were all collected inside a nitrogen filled glovebox equipped with a Cary 60 UV-vis spectrometer equipped with fiber optic cables. After obtaining an initial optical spectrum of [SNHS^{cat}]Ni(L), the solution was titrated with 2,4,6-collidine (2.5–10 µL per addition) using a volumetric syringe. The cuvette was inverted and twisted for 20 seconds prior to acquisition of the subsequent optical spectrum.

Theoretical Calculations. All calculations were performed employing the non-empirical TPSS density functional theory using the quantum chemistry program package TURBOMOLE.[49] For computational efficiency, initial geometry optimizations were performed using moderate split-valence plus polarization basis sets (def2-SVP).[50] Structures were refined using basis sets of triple zeta valence plus polarization (def2-TZVP) quality.[51] Crystal structures obtained from X-ray diffraction experiments were used as starting points for the geometry optimization; no molecular symmetry was imposed. Complex **14** (dimer) was broken apart using Mercury 3.8 for windows whereby calculations were run as a monomer. Complexes **16** and **17** were run as monoanions to obtain the observed kohn-sham molecular orbital depictions while their respective relative energy levels were determined from calculations performed on the neutral complex (unprotected monoanion energy levels for HOMO: −0.664 eV and LUMO: +0.665 eV were obtained).

Crystallographic Methods. X-ray diffraction data were collected on a single crystal mounted on a glass fiber using paratone oil. Data was acquired using a Bruker SMART APEX II diffractometer equipped with a CCD detector using Mo Kα radiation (λ = 0.71073 Å), which was wavelength selected with a single-crystal graphite monochromator. The SMART program package was used to determine unit-cell parameters and for data collection. The raw frame data were processed using SAINT and SADABS to yield the reflection data file. Subsequent calculations were carried out using the SHELXTL program suite. The structures were solved by direct methods and refined on F^2 by full-matrix least-squares techniques. Analytical scattering factors for neutral atoms were used throughout the analyses. Hydrogen atoms were generated in calculated positions and refined using a riding model. ORTEP diagrams were generated using *ORTEP-3* for Windows.

Table 6.5. Data collection and refinement parameters for triphenylphosphine derivatives **14**, **16**, and **18**.

	[[SNS^{sq}•]Ni(PPh$_3$)]$_2$ (**14**)	[SNS^{cat}]Ni(PPh$_3$) [KCrypt] (**16**)	[SNHS^{cat}]Ni(PPh$_3$) (**18**)
empirical formula	$C_{64}H_{54}N_2Ni_2P_2S_4$ •2[CH_3CN]	$C_{32}H_{27}NNiPS_2$ •K[$C_{18}N_2H_{36}O_6$][CH_3CN]	$C_{32}H_{28}NNiPS_2$ •2[C_4H_8O]
formula weight [g/mol]	1240.80	1035.98	724.56
crystal system	Monoclinic	Monoclinic	Monoclinic
space group	$P2_1/n$	$P2_1/c$	$P2_1/c$
T [K]	88(2) K	88(2) K	128(2) K
a [Å]	13.4463(12)	13.1895(16)	13.4137(10)
b [Å]	22.515(2)	17.229(2)	20.2277(15)
c [Å]	19.8162(18)	23.327(3)	13.6316(10)
a [deg]	90	90	90
b [deg]	95.7673(11)	104.0797(17)	104.8655(9)
g [deg]	90	90	90
V [Å^3]	5968.9(9)	5141.5(11)	3574.8(5)
Z	4	4	4
refl collected	73363	62909	42087
data/restr/param	14980/0/727	12870/0/607	8686/0/430
R_1 [I > 2σ(I)][a]	0.0289	0.0377	0.0357
wR_2(all data)[a]	0.0727	0.0903	0.0980
GOF[a]	1.037	1.038	1.018

[a] $R_1 = \Sigma||F_o|-|F_c|| / \Sigma|F_o|$, $wR_2 = [\Sigma[w(F_o^2-F_c^2)^2] / \Sigma[w(F_o^2)^2]\ ]^{1/2}$, $GOF = S = [\Sigma[w(F_o^2-F_c^2)^2] / (n-p)]^{1/2}$

Table 6.6. Data collection and refinement parameters for tricyclohexylphosphine derivatives **15**, **17**, and **19**.

	[SNS$^{sq\bullet}$]Ni(PCy$_3$) (**15**)	[SNS^{cat}]Ni(PCy$_3$) [KCrypt] (**17**)	[SNHS^{cat}]Ni(PPh$_3$) (**19**)
empirical formula	$C_{32}H_{45}NNiPS_2$	$C_{32}H_{45}NNiPS_2$ •K[$C_{18}N_2H_{36}O_6$][C_4H_8O]	$C_{32}H_{46}NNiPS_2$
formula weight [g/mol]	597.49	1085.18	598.50
crystal system	Monoclinic	Triclinic	Monoclinic
space group	$P2_1/c$	$P\bar{1}$	$P2_1/n$
T [K]	88(2) K	133(2) K	128(2) K
a [Å]	8.4569(18)	10.9764(9)	13.402(2)
b [Å]	25.523(5)	12.9217(11)	15.360(2)
c [Å]	14.038(3)	22.0785(19)	14.855(2)
a [deg]	90	76.7086(11)	90
b [deg]	99.178(3)	86.4006(11)	97.142(2)
g [deg]	90	67.6215(11)	90
V [Å^3]	5968.9(9)	2817.0(4)	34245
Z	4	2	4
refl collected	35168	32815	42087
data/restr/param	7483/0/336	13223/0/599	7375/0/375
R_1 [I > 2σ(I)][a]	0.0403	0.0497	0.0362
wR_2(all data)[a]	0.1031	0.1392	0.0813
GOF[a]	1.024	1.029	0.919

[a] $R_1 = \Sigma||F_o|-|F_c|| / \Sigma|F_o|$, $wR_2 = [\Sigma[w(F_o^2-F_c^2)^2] / \Sigma[w(F_o^2)^2]\ ]^{1/2}$, $GOF = S = [\Sigma[w(F_o^2-F_c^2)^2] / (n-p)]^{1/2}$

[[SNS$^{sq\bullet}$]Ni(PPh$_3$)]$_2$ (14). In air, $Cl_2Ni(PPh_3)_2$ (1.25 g, 1.91 mmol, 1.00 equiv.) was suspended in toluene (70 mL) in a 250 mL round bottom flask equipped with a magnetic stir bar. To the suspension, $[SNS]H_3$ (504 mg, 1.93 mmol, 1.01 equiv.) was added as a toluene solution (5 mL) with no immediate color change. Triethylamine (800 μL, 5.80 mmol, 3.00 equiv.) was added via disposable syringe to afford an immediate color change from a deep blue to a forest green mixture with the evolution of gas (H_2). Reaction mixture was stirred for 30 minutes. The volatiles were removed under vacuum. The solid was re-suspended in THF and filtered using a Buchner funnel to remove Et_3NHCl as an off-white solid. The filtrate volatiles were removed under vacuum to concentrate the solution to approx. 5 mL. A solid was crashed from solution using copious amounts of pentane. A dark blue/green solid was collected on a Buchner funnel and washed with pentane (2 x 20 mL) and Et_2O (5 x 1 mL). The blue/green solid was dried under vacuum (626 mg, 56%). X-ray quality crystals were obtained from a concentrated analyte solution in MeCN at 25°C.

Anal. Calc. $C_{64}H_{54}N_2Ni_2P_2S_4$: C, 66.34; H, 4.70; N, 2.42%. Found: C, 65.97; H, 5.36; N, 2.34%. ^{1}H NMR (600 MHz, CD_3CN) δ / ppm: 7.66 (m, 2H, aryl-H), 7.64 (m, 2H, aryl-H), 7.62 (m, 4H, aryl-H), 7.60 (m, 4H, aryl-H), 7.51 (m, 15H, PPh_3), 7.44 (m, 15H, PPh_3) (note: -CH_3 resonances for [SNS] ligand were not observed as it overlapped with proteo- MeCN in CD_3CN). ^{31}P {^{1}H}-NMR (162 MHz, CD_3CN) δ / ppm: 26.0 (s). UV-vis (MeCN) λ_{max} / nm (ε / $M^{-1}cm^{-1}$): 282 (46800), 378 (sh, 13700), 661 (8200). MS (ESI+) (THF) *m*/*z*: 1194 $(M)^+$.

[SNS$^{sq\bullet}$]Ni(PCy$_3$) (15). In air, a 250 mL round bottom flask was charged with $Cl_2Ni(PCy_3)_2$ (553 mg, 0.802 mmol, 1.00 equiv.) in toluene (50 mL) to give a magenta suspension. [SNS]H_3 (208 mg, 0.797 mmol, 0.984 equiv.) was added to the suspension as a toluene solution (3 mL), no immediate color change was observed. Triethylamine (500 μL, 3.60 mmol, 3.70 equiv.) was added via disposable syringe to induce an immediate color change to a dark blue/purple solution with a precipitate formed. The reaction mixture was stirred for two hours and the volatiles were removed via roto-vap. The remaining solid was re-suspended in THF (50 mL) and stirred for 30 minutes. The mixture was filtered via Buchner funnel to remove Et_3NHCl and a powder blue solid (**17**). The green/yellow filtrate was collected and the volatiles were removed via roto-vap. The resulting solids were then dissolved in THF (5 mL) and a solid was crashed from solution using pentane. A dark blue solid was collected on a Buchner funnel (215 mg, 36%) and dried under vacuum. X-ray quality crystals were obtained from a concentrated analyte solution in MeCN at 25°C. Anal. Calc. $C_{32}H_{45}NNiPS_2$: C, 64.33; H, 7.49; N, 2.34%. Found: C, 64.29; H, 7.59; N, 2.80%. UV-vis (MeCN) λ_{max} / nm (ε / $M^{-1}cm^{-1}$): 271 (16700), 300 (14200), 376 (6100), 677 (1900). MS (ESI+) (THF) *m*/*z*: 596 $(M)^+$.

[[SNS^{cat}]Ni(PPh$_3$)][K] (16). In a 20 mL scintillation vial under a nitrogen glovebox atmosphere, a solution of [SNS]H_3 (255 mg, 0.977 mmol, 1.00 equiv.) in THF (5 mL) was deprontonated using

KH (117 mg, 2.93 mmol, 3.00 equiv.) to result in immediate white precipitate formation and the evolution of gas (H_2). Once all gas appeared to cease, solid $Cl_2Ni(PPh_3)_2$ was added (638 mg, 0.977 mmol, 1.00 equiv.). An immediate color change was observed to yield a forest green solution which was allowed to stir for two hours. The reaction mixture was filtered through celite using a fritted glass filter to remove a dark purple colored solid. The filtrate volatiles were reduced in volume to roughly 5 mL and a solid was crashed from solution using pentane (100 mL). The solid was collected on a fritted glass filter and washed with pentane (3 x 20 mL). The green solid was collected and dried under vacuum (400 mg, 83%). X-ray quality crystals were obtained by diffusion of Et_2O into an MeCN solution of the complex in the presence of 2,2,2-cryptand at 25°C. Anal. Calc. $C_{32}H_{27}NNiPS_2K$: C, 62.15; H, 4.40; N, 2.26%. Found: C, 60.16; H, 4.35; N, 2.17%. ^{1}H NMR (600 MHz, CD_3CN) δ / ppm: 7.82 (m, 5H, aryl-H), 7.43 (d, *J*=7.10 Hz, 2H, aryl-H), 7.39 (t, *J*=7.21 Hz, 10H, aryl-H), 6.80 (br. s., 2H, aryl-H), 6.43 (d, *J*=8.24 Hz, 2H, aryl-H), 2.14 (br. s., 6H, -CH_3). ^{31}P {^{1}H}-NMR (162 MHz, CD_3CN) δ / ppm: 36.0 (s). UV-vis (MeCN) λ_{max} / nm (ε / $M^{-1}cm^{-1}$): 294 (29200), 364 nm (12300). MS (ESI+) (MeCN) *m*/*z*: 617 $(M+K)^+$.

[SNS^{cat}]Ni(PCy$_3$)][K] (17). A 20 mL scintillation vial was charged with KH (43 mg, 1.1 mmol, 3.2 equiv.), THF (3 mL), and a magnetic stir bar under a nitrogen filled glovebox atmosphere. A solution of $[SNS]H_3$ (89 mg, 0.34 mmol, 1.0 equiv.) in THF (3 mL) was added to induce an immediate precipitation of a white solid with gas evolution. Once the gas had ceased to evolve, solid $Cl_2Ni(PCy_3)_2$ (236 mg, 0.343 mmol, 1.00 equiv.) was added to initiate an immediate color change to a dark green/blue solution. The reaction mixture was stirred for 30 minutes and then filtered through celite on a fritted glass filter. The filtrate was concentrated to roughly 1 mL and a blue solid was crashed from solution using copius amounts of pentane (100 mL). The solid was collected on a fritted glass filter and washed with pentane (3 x 20 mL). The baby blue powder was

collected and dried under vacuum (161 mg, 74%). X-ray quality crystals were obtained by diffusion of Et_2O into a THF solution of the complex in the presence of 2,2,2-cryptand at 25°C. Anal. Calc. $C_{50}H_{81}N_3NiPO_6S_2K$ (with 2,2,2-cryptand): C, 59.28; H, 8.06; N, 4.15%. Found: C, 58.93; H, 8.19; N, 3.80%. ^{1}H NMR (600 MHz, CD_3CN) δ / ppm: 7.27 (s, 2H, aryl-H), 6.87 (d, *J*=1.60 Hz, 2H, aryl-H), 6.36 (m, 2H, aryl-H), 2.16 (s, 6H, -CH_3), 2.06 (m, 6H, -Cy), 1.79 (m, 15H, -Cy), 1.75 (m, 3H, -CH (PCy_3)), 1.28 (d, *J*=7.78 Hz, 9H, -Cy). ^{31}P {^{1}H}-NMR (162 MHz, CD_3CN) δ / ppm: 33.0 (s). UV-vis (MeCN) λ_{max} / nm (ε / $M^{-1}cm^{-1}$): 236 nm (33600), 276 nm (31000), 368 nm (10700). MS (ESI+) (THF) *m*/*z*: 635 $(M+K)^+$. MS (ESI-) (THF) *m*/*z*: 596 $(M)^-$.

[SNHS^{cat}]Ni(PPh_3) (18). In a 20 mL scintillation vial under a nitrogen atmosphere, $Cl_2Ni(PPh_3)_2$ (655 mg, 1.00 mmol, 1.00 equiv.) was suspended in toluene (7 mL) and equipped with a magnetic stirbar. To the reaction mixture, a toluene solution (2 mL) of $[SNS]H_3$ (261 mg, 1.00 mmol, 1.00 equiv.) was added. An immediate color change was observed from a dark blue to a maroon. After 5 minutes of stirring, triethylamine (280 μL, 2.00 mmol, 2.00 equiv.) was added which resulted in the immediate precipitation of an orange solid. The solid was collected on a fritted glass filter and washed with toluene (2 x 20 mL) and pentane (3 x 20 mL). The orange solid was collected and dried under vacuum (423 mg, 73%). X-ray quality crystals were obtained from an MeCN solution of the complex at 25°C. Anal. Calc. $C_{32}H_{28}NNiPS_2$: C, 66.23; H, 4.86; N, 2.41%. Found: C, 65.37; H, 4.78; N, 2.33%. ^{1}H NMR (500 MHz, CD_3CN) δ / ppm: 8.31 (br s, 1H, -NH), 7.78 (m, 5H, aryl-H), 7.52 (m, 2H, aryl-H), 7.42 (m, 6H, aryl-H), 7.20 (m, 6H, aryl-H), 6.89 (m, 4H, aryl-H), 6.62 (m, 2H, aryl-H), 2.33 (s, 6H, -CH_3). ^{31}P {^{1}H}-NMR (162 MHz, CD_3CN) δ / ppm: 29.0 (s). UV-vis (MeCN) λ_{max} / nm (ε / $M^{-1}cm^{-1}$): 260 nm (23700). MS (ESI+) (THF) *m*/*z*: 579 $(M)^+$.

[SNHS^{cat}]Ni(PCy_3) (19). A 20 mL scintillation vial equipped with a magnetic stir bar was charged with a suspension of $Cl_2Ni(PCy_3)_2$ (673 mg, 0.977 mmol, 1.00 equiv.) in toluene (10 mL). A

solution of [SNS]H_3 (256 mg, 0.980 mmol, 1.00 equiv.) in toluene (3 mL) was added with no immediate color change observed. Triethylamine (275 μL, 1.97 mmol, 2.02 equiv.) was then added via syringe to induce an immediate color change to a dark orange solution. Reaction mixture was stirred for 30 minutes and filtered through celite on a fritted glass filter to remove Et_3NHCl. The volatiles were removed under vacuum to concentrate the solution to roughly 5 mL and pentane (100 mL) was added, no solid was precipitated. The volatiles were removed under vacuum and an orange solid began to precipitate out. The filtrate was concentrated to roughly 20 mL and the solid was collected on a glass fritted filter. The solid was washed with pentane (2 x 20 mL). An orange solid was collected and dried under vacuum (256 mg, 51%). X-ray quality crystals were obtained from an MeCN solution of the complex at 25°C. Anal. Calc. $C_{32}H_{46}NNiPS_2$: C, 64.28; H, 7.96; N, 2.13%. Found: C, 64.22; H, 7.75; N, 2.34%. ^{1}H NMR (500 MHz, CD_3CN) δ / ppm: 7.83 (br s, 1H, -NH), 6.99 (m, 2H, aryl-H), 6.85 (m, 2H, aryl-H), 6.57 (m, 2H, aryl-H), 2.19 (m, 6H, -CH_3), 2.05 (m, 6H, -Cy), 1.74 (m, 15H, -Cy), 1.28 (m, 9H, -Cy). ^{31}P {^{1}H}-NMR (162 MHz, CD_3CN) δ / ppm: 33.8 (s). UV-vis (MeCN) λ_{max} / nm (ε / $M^{-1}cm^{-1}$): 244 nm (27000), 270 nm (22500), 374 (2200). MS (ESI+) (THF) *m*/*z*: 598 $(M)^+$.

References

(1) Mayer, J. M. *Annu. Rev. Phys. Chem.* **2004**, *55*, 363–390.
(2) Cukier, R. I.; Nocera, D. G. *Annu. Rev. Phys. Chem.* **1998**, *49*, 337–369.
(3) Salamone, M.; Bietti, M. *Acc. Chem. Res.* **2015**, *48*, 2895–2903.
(4) Valgimigli, L.; Pratt, D. A. *Acc. Chem. Res.* **2015**, *48*, 966–975.
(5) Ingold, K. U.; Pratt, D. A. *Chem. Rev.* **2014**, *114*, 9022–9046.
(6) Minnihan, E. C.; Nocera, D. G.; Stubbe, J. *Acc. Chem. Res.* **2013**, *46*, 2524–2535.
(7) White, M. C. *Science (80-.).* **2012**, *335*, 807–809.
(8) Newhouse, T.; Baran, P. S. *Angew. Chemie Int. Ed.* **2011**, *50*, 3362–3374.
(9) Warren, J. J.; Tronic, T. A.; Mayer, J. M. *Chem. Rev.* **2010**, *110*, 6961–7001.
(10) Thompson, E. J.; Berben, L. A. *Angew. Chemie Int. Ed.* **2015**, *54*, 11642–11646.
(11) Henthorn, J. T.; Agapie, T. *Inorg. Chem.* **2016**, *55*, 5337–5342.
(12) Purse, B. W.; Tran, L.-H.; Piera, J.; Åkermark, B.; Bäckvall, J.-E. *Chem. – A Eur. J.* **2008**, *14*, 7500–7503.
(13) Chang, C. J.; Chng, L. L.; Nocera, D. G. *J. Am. Chem. Soc.* **2003**, *125*, 1866–1876.

(14) Chaudhuri, P.; Hess, M.; Weyhermüller, T.; Wieghardt, K. *Angew. Chemie Int. Ed.* **1999**, *38*, 1095–1098.
(15) Henthorn, J. T.; Lin, S.; Agapie, T. *J. Am. Chem. Soc.* **2015**, *137*, 1458–1464.
(16) Darkwa, J. *Inorganica Chim. Acta* **1996**, *257*, 137–141.
(17) Gan, L.; Groy, T. L.; Tarakeshwar, P.; Mazinani, S. K. S.; Shearer, J.; Mujica, V.; Jones, A. K. *J. Am. Chem. Soc.* **2015**, *137*, 1109–1115.
(18) Tolman, C. A. *J. Am. Chem. Soc.* **1970**, *92*, 2956–2965.
(19) Cordero, B.; Gómez, V.; Platero-Prats, A. E.; Revés, M.; Echeverría, J.; Cremades, E.; Barragán, F.; Alvarez, S. *Dalton Trans.* **2008**, 2832–2838.
(20) Nevondo, F. A.; Crouch, A. M.; Darkwa, J. *J. Chem. Soc. Dalt. Trans.* **2000**, 43–50.
(21) Porta, P.; Sgamellotti, A.; Vinciguerra, N. *Inorg. Chem.* **1968**, *7*, 2625–2629.
(22) Mock, M. T.; of Delaware. Department of Chemistry, U.; Biochemistry. *Synthesis and Reactivity of Thioether-supported Organoiron and Low-valent Iron Complexes and Cyanide-bridged Binuclear Complexes*; University of Delaware, 2007.
(23) Lewis, R. M.; Nancollas, G. H.; Coppens, P. *Inorg. Chem.* **1972**, *11*, 1371–1375.
(24) Van Riel, W.; Desseyn, H. O.; Van de Mieroop, W.; Lenstra, A. T. H. *Transit. Met. Chem.* **1980**, *5*, 330–332.
(25) Adam, K. R.; Antolovich, M.; Brigden, L. G.; Lindoy, L. F. *J. Am. Chem. Soc.* **1991**, *113*, 3346–3351.
(26) Meyer Jnr, E. F. *Acta Crystallogr. Sect. B* **1972**, *28*, 2162–2167.
(27) Csok, Z.; Vechorkin, O.; Harkins, S. B.; Scopelliti, R.; Hu, X. *J. Am. Chem. Soc.* **2008**, *130*, 8156–8157.
(28) J. Coles, S.; Faulds, P.; B. Hursthouse, M.; G. Kelly, D.; C. Ranger, G.; M. Walker, N. *J. Chem. Res.* **1999**, 418–419.
(29) Zarkesh, R. A.; Ziller, J. W.; Heyduk, A. F. *Angew. Chemie Int. Ed.* **2008**, *47*, 4715–4718.
(30) Shaffer, D. W.; Szigethy, G.; Ziller, J. W.; Heyduk, A. F. *Inorg. Chem.* **2013**, *52*, 2110–2118.
(31) Sproules, S.; Wieghardt, K. *Coord. Chem. Rev.* **2010**, *254*, 1358–1382.
(32) Cotton, F. A.; Murillo, C. A.; Zhou, H.-C. *Inorg. Chem.* **2000**, *39*, 3728–3730.
(33) Lum, V.; Gray, H. B. *Isr. J. Chem.* **1981**, *21*, 23–25.
(34) Yu, Q.; Ge, J.-Y.; Lv, Z.-P.; Wang, H.-Y.; Zuo, J.-L. *RSC Adv.* **2016**, *6*, 100783–100789.
(35) Schrauzer, G. N.; Mayweg, V. P. *J. Am. Chem. Soc.* **1965**, *87*, 1483–1489.
(36) Begum, A.; Moula, G.; Sarkar, S. *Chemistry* **2010**, *16*, 12324–12327.
(37) Udpa, K. N.; Sarkar, S. *Polyhedron* **1987**, *6*, 627–631.
(38) Brown, R. K.; Bergendahl, T. J.; Wood, J. S.; Waters, J. H. *Inorganica Chim. Acta* **1983**, *68*, 79–85.
(39) Moura, J. J.; Moura, I.; Huynh, B. H.; Kruger, H. J.; Teixeira, M.; DuVarney, R. C.; DerVartanian, D. V; Xavier, A. V; Peck, H. D. J.; LeGall, J. *Biochem. Biophys. Res. Commun.* **1982**, *108*, 1388–1393.
(40) Kruger, H. J.; Huynh, B. H.; Ljungdahl, P. O.; Xavier, A. V; Der Vartanian, D. V; Moura, I.; Peck, H. D. J.; Teixeira, M.; Moura, J. J.; LeGall, J. *J. Biol. Chem.* **1982**, *257*, 14620–14623.
(41) Albracht, S. P. J.; Ankel-Fuchs, D.; Van der Zwaan, J. W.; Fontijn, R. D.; Thauer, R. K. *Biochim. Biophys. Acta - Protein Struct. Mol. Enzymol.* **1986**, *870*, 50–57.
(42) Medina, M.; Williams, R.; Cammack, R.; Hatchikian, E. C. *J. Chem. Soc.{,} Faraday Trans.* **1994**, *90*, 2921–2924.

(43) Zuo, J.-L.; Yao, T.-M.; You, F.; You, X.-Z.; Fun, H.-K.; Yip, B.-C. *J. Mater. Chem.* **1996**, *6*, 1633–1637.
(44) McCarthy, B. D.; Martin, D. J.; Rountree, E. S.; Ullman, A. C.; Dempsey, J. L. *Inorg. Chem.* **2014**, *53*, 8350–8361.
(45) Albers, A.; Demeshko, S.; Dechert, S.; Saouma, C. T.; Mayer, J. M.; Meyer, F. *J. Am. Chem. Soc.* **2014**, *136*, 3946–3954.
(46) Muckerman, J. T.; Skone, J. H.; Ning, M.; Wasada-Tsutsui, Y. *Biochim. Biophys. Acta - Bioenerg.* **2013**, *1827*, 882–891.
(47) Saouma, C. T.; Kaminsky, W.; Mayer, J. M. *J. Am. Chem. Soc.* **2012**, *134*, 7293–7296.
(48) Busby, R.; Hursthouse, M. B.; Jarrett, P. S.; Lehrnann, C. W.; Malik, K. M. A.; Phillips, C. *J. Am. Chem. Soc. Dalt. Trans* **1993**, 3767–3770.
(49) Furche, F.; Ahlrichs, R.; Hättig, C.; Klopper, W.; Sierka, M.; Weigend, F. *Wiley Interdiscip. Rev. Comput. Mol. Sci.* **2014**, *4*, 91–100.
(50) Schäfer, A.; Horn, H.; Ahlrichs, R. *J. Chem. Phys.* **1992**, *97*, 2571–2577.
(51) Schäfer, A.; Huber, C.; Ahlrichs, R. *J. Chem. Phys.* **1994**, *100*, 5829–5835.

Appendix A

Electrochemical Response of $[[SNS^{cat}]Ni(L)]^{-}$

(L = PPh_3 and PCy_3) Towards CO_2 and CO

Introduction

Molecular catalysts that can perform multi-electron transformations towards the reduction of C_1 oxygentate species remains an actively pursued area of research.[1,2] A major advantage in using carbon dioxide (CO_2) or carbon monoxide (CO) as a reactant stems from their vast availability.[1,2] To investigate the reactivity of the aforementioned monoanionic square-planar nickel complexes (**16** and **17**) described in **Chapter 6**, the species were treated with CO_2 or CO under electrochemical conditions. To this end we created a custom sealed 20 mL scintillation vial cap which allowed for the purging of different C_1 oxygenate substrates into the electrochemical cell. In doing so we are able to monitor both complexes for their ability to reduce CO_2 or CO.

Results and Discussion

Electrochemistry

Initial reactivity studies on the monoanionic forms of the square-planar complexes from **Chapter 6** (**16** and **17**) were performed under electrochemical conditions to investigate the observed effects towards small molecule C_1 substrates (CO_2 and CO). **Figures A.1** and **A.2** demonstrate the electrochemical responses observed for **16** ($[SNS^{cat}]Ni(PPh_3)^-$) and **17** ($[SNS^{cat}]Ni(PCy_3)^-$), respectively, under a CO_2 and CO atmosphere. Investigation of complex **16** under a CO_2 atmosphere displayed a large increase in the current coincident with the reductive event centered at −2.54 V, vs $[Cp_2Fe]^{0/+}$. Treatment of **16** with a CO atmosphere induced an immediate color change from emerald green to a royal blue with observed shifts in the electrochemical events of the collected cyclic voltammogram. Firstly, a drastic 500 mV anodic shift in the reversible $Ni^{II/I}$ couple to more positive potentials (−2.07 V) was observed. Secondly, a slight shift (Δ = 110 mV) in the first oxidative event centered at −0.61 V was observed, indicative of a minor structural rearrangement occurring within the complex. Both of these shifts appear

consistent one of two possibilities; (i) the displacement of a PPh_3 ligand for CO or (ii) the coordination of CO through an axial coordination site to form the putative five-coordinate $[SNS^{cat}]Ni(CO)(PPh_3)$ species. While both options are plausible, we favor the latter assignment in which the CO coordinates to form a five-coordinate nickel complex because an exchange of PPh_3 for the stronger donor ligand CO, a cathodic shift to more negative potentials would be expected, however, in this case an anodic shift was observed. Performing the analogous experiments with the tricyclohexylphosphine derivative (PCy_3, **17**), a similar catalytic response appears to grow in coincident with the reductive event at −2.75 V, vs $Cp_2Fe^{0/+}$, under a CO_2 atmosphere. Unfortunately, the response that increases is observed at the edge of the MeCN solvent window and as a result does not render the complex useful for reduction of CO_2. Treatment of **17** with an atmosphere of CO displayed no observable catalytic response nor a shift in the reductive process was detected, in stark contrast to that of the PPh_3 (**16**) analog. It may be possible that the added steric bulk of the tricyclohexylphosphine group hinders the coordination of a free CO ligand to the nickel center under these conditions. Under the same conditions but in the absence of catalyst (**16** or **17**) no electrochemical processes were observed (**Figure A.3**), demonstrating that **16** and **17** may be acting as molecular catalysts. These findings offer an exciting avenue for future research in our group to further investigate the catalytic response of **16** and **17** towards small molecule activation.

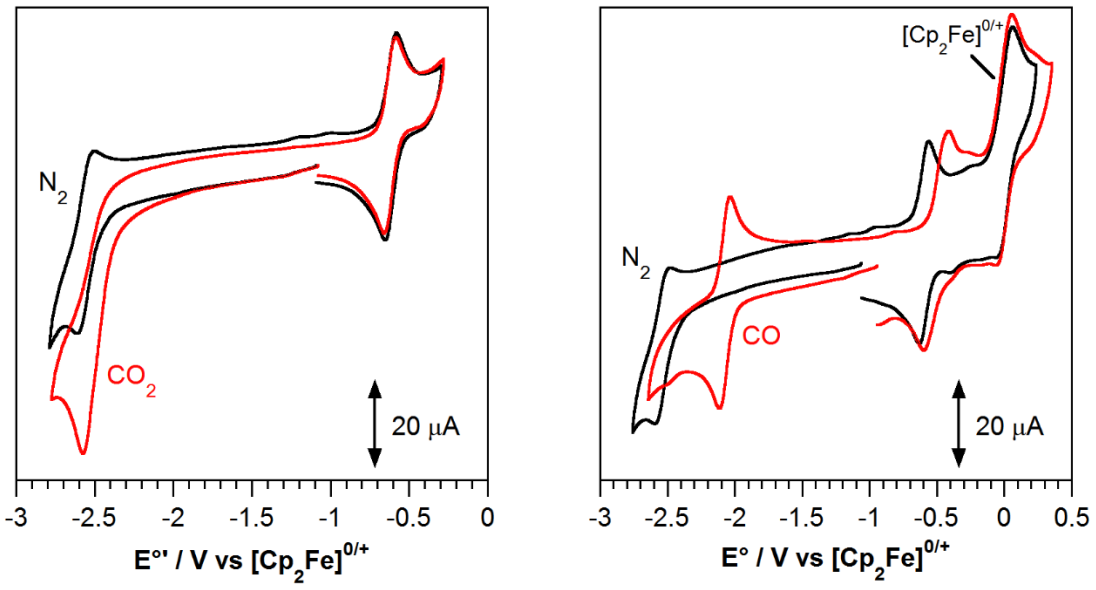

Figure A.1. Cyclic voltammograms for (*left*) [[SNS^{cat}]Ni(PPh$_3$)][K] (**16**) under a (black) N_2 atmosphere and (red) CO_2 atmosphere; (*right*) [[SNS^{cat}]Ni(PPh$_3$)][K] (**16**) under a (black) N_2 atmosphere and (red) CO atmosphere. All voltammograms were recorded at a 1 mM analyte concentration in 0.1M [NBu$_4$][PF$_6$] in dry, degassed, MeCN under a nitrogen atmosphere using a 3 mm glassy carbon working electrode, Pt wire counter electrode, and Ag$^{0/+}$ wire pseudo-reference electrode at room temperature at 200 mV sec^{-1} scan rates.

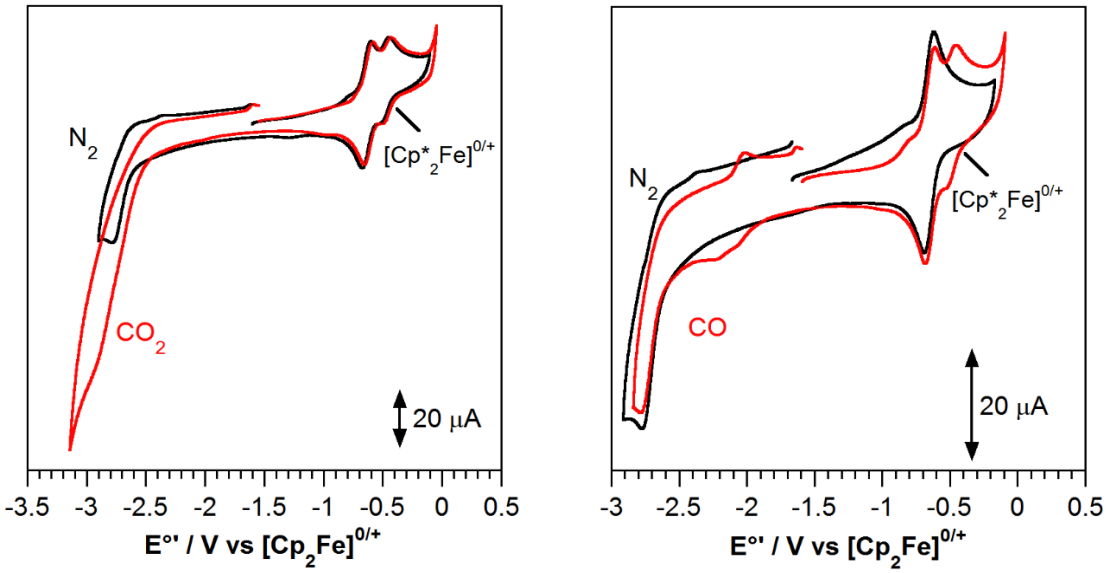

Figure A.2. Cyclic voltammograms for (*left*) [[SNS^{cat}]Ni(PCy$_3$)][K] (**17**) under a (black) N_2 atmosphere and (red) CO_2 atmosphere; (*right*) [[SNS^{cat}]Ni(PCy$_3$)][K] (**17**) under a (black) N_2 atmosphere and (red) CO atmosphere. All voltammograms were recorded at a 1 mM analyte concentration in 0.1M [NBu$_4$][PF$_6$] in dry, degassed, MeCN under a nitrogen atmosphere using a 3 mm glassy carbon working electrode, Pt wire counter electrode, and Ag$^{0/+}$ wire pseudo-reference electrode at room temperature at 200 mV sec^{-1} scan rates.

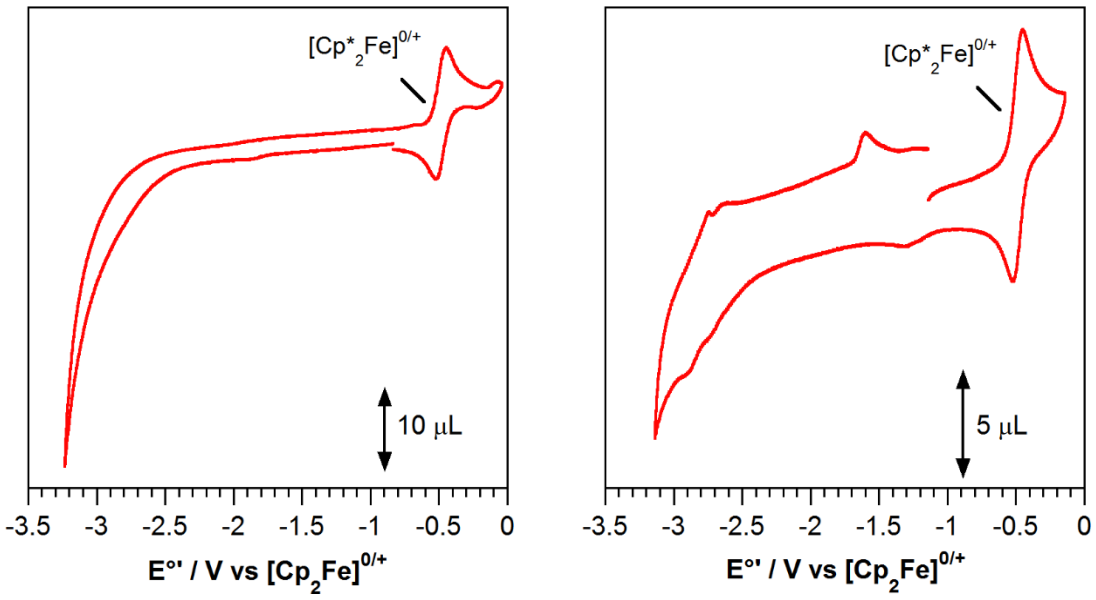

Figure A.3. Blank cyclic voltammograms collected for (*left*) Cp_2*Fe and electrolyte solution under a CO_2 atmosphere; and (*right*) Cp_2*Fe and electrolyte solution under a CO atmosphere. All voltammograms were recorded in 0.1M $[NBu_4][PF_6]$ in dry, degassed, MeCN under a nitrogen atmosphere using a 3 mm glassy carbon working electrode, Pt wire counter electrode, and $Ag^{0/+}$ wire pseudo-reference electrode at room temperature at 200 mV sec^{-1} scan rates.

Conclusion

In summary, the observed response of complexes **16** and **17** under an atmosphere of carbon dioxide (CO_2) resulted in an increase in current concurrent with the first oxidative event. This preliminary data suggests that the monoanionic species are active towards the reduction of CO_2 under electrochemical conditions. Interestingly, when the triphenylphosphine derivative (**16**) was treated with an atmosphere of CO, anodic shifts were observed. The shift in the first oxidative event by 110 mV suggests a minor structural rearrangement in the ligand oxidative process. The major shift of roughly 500 mV in the first reductive event indicates a major structural change associated with the likely coordination of a CO ligand to the nickel center. Two possible reasons for these shifts include; (i) the displacement of a PPh_3 ligand for CO or (ii) the coordination of CO through an axial coordination site to form the putative five-coordinate $[SNS^{cat}]Ni(CO)(PPh_3)$ species. Treatment of the tricyclohexylphosphine derivative (**17**) resulted in no observed reactivity, indicating that the tricyclohexylphosphine may (i) be bound stronger to the nickel center

as it is a stronger σ-donating ligand and not as easily substituted as observed in the triphenylphosphine case; and (ii) the steric bulk of the cyclohexyl groups may limit the ability for CO to bind to the nickel center. Overall, further analysis is needed for these complexes to verify they are active catalysts for the reduction of C_1 oxygenate species.

Experimental

General Considerations. The compounds and reactions reported herein show various levels of air- and moisture-sensitivity, therefore all manipulations were carried out using standard Schlenk-line and glovebox techniques. MeCN solvent was sparged with argon before being deoxygenated and dried by passage through Q5 and activated alumina columns, respectively.

Electrochemical Methods. Electrochemical data were collected with a Gamry Series G 300 Potentiostat/Galvanostat/ZRA (Gamry Instruments, Warminster, PA, USA) using a 3.0 mm glassy carbon working electrode, a platinum wire auxiliary electrode, and a silver wire pseudo-reference electrode. Electrochemical experiments were performed at 25°C under an atmosphere of N_2, CO, or CO_2 using a bubbling hose attached to a Schlenk line. Electrochemical samples were 1.0 mM analyte solutions in MeCN containing 0.1 M $[NBu_4][PF_6]$ as the supporting electrolyte. All potentials were referenced to the $[Cp_2Fe]^{0/+}$ couple using ferrocene or decamethylferrocene as an internal standard. Ferrocene and decamethylferrocene (Acros) were purified by sublimation and tetra-*n*-butylammonium hexafluorophosphate (Acros) was recrystallized from ethanol three times.

Typical Experiment Parameters. A 20 mL scintillation vial under a N_2 glovebox atmosphere was charged with a magnetic stir bar, $[NBu_4][PF_6]$ electrolyte (390 mg, 0.1 M), and analyte (1 mM) in 10 mL of dry, degassed MeCN. The electrochemical cell was sealed using a custom, "air-free," scintillation vial made by affixing a piece of rubber septa to a standard 20 mL scintillation vial cap. The cell was removed from the glovebox atmosphere and immediately bubbled with N_2

using a standard Schlenk line inlet. An initial CV was collected to ensure that the complex did not degrade upon removal from the glovebox atmosphere. After an initial scan was collected, the N_2 inlet was exchanged for an inlet of CO_2 or CO. After the solution was stirred and bubbled with the desired C_1 oxygenate substrate for 1-2 minutes, the inlet needle was raised to the headspace, stirring was ceased, and a CV trace was collected (**Figures A.1 and A.2**).

References

(1) Rakowski Dubois, M.; Dubois, D. L. *Acc. Chem. Res.* **2009**, *42*, 1974–1982.
(2) Chakraborty, S.; Zhang, J.; Krause, J. A.; Guan, H. *J. Am. Chem. Soc.* **2010**, *132*, 8872–8873.

Appendix B

Synthesis and Characterization of

a Five-Coordinate [SNS]Co(dppe) Species

Introduction

In an initial attempt to isolate the aforementioned W[SNS]$_2$Co(dppe) (**11**) complex from **Chapter 5**, a monomeric five-coordinate cobalt complex was obtained. This complex was interesting to us because it generated a pseudo-square pyramid coordination geometry with a single [SNS] ligand, the bidentate 1,2-bis(diphenylphosphino)ethane (dppe) ligand, and an open coordination site on the cobalt center. To this end, this species was independently synthesized using the technique outlined in **Chapter 6** for the monomeric square-planar nickel complexes and is fully characterized herein.

Results and Discussion

Synthesis and Structural Characterization

A monometallic cobalt complex of the formula [SNS]Co(dppe) was prepared using the synthetic strategy outlined in **Chapter 6**, whereby complex **B1** was obtained under aerobic conditions (**Scheme B.1**). Electrospray ionization mass-spectrometry (ESI-MS) data confirmed the formation of the desired complex with a parent ion signal at a *m/z* value of 715.05 $(M)^+$. Single crystals of **B1** were obtained by slow diffusion of pentane into a saturated THF solution of the complex at room temperature.

Scheme B.1. Synthesis of complex **B1**.

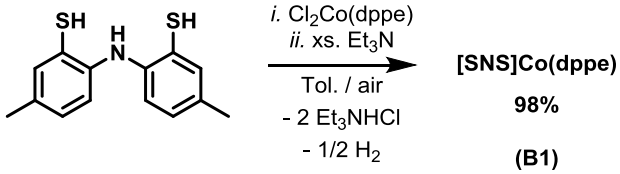

X-ray diffraction studies on single crystals of **B1** revealed a five-coordinate cobalt ion supported by a single [SNS] and dppe ligand. **Figure B.1** illustrates the structure of complex **B1** as an ORTEP diagram with a table of selected bond lengths and angles provided in **Table B.1**. Investigation into the coordination environment about the cobalt center was performed using the

angular structural parameter for five-coordinate metal centers (τ_5) established by Addison and coworkers (**Equation B.1**).[1] Using this approach, a τ_5 value of 0.00 illustrates an ideal square pyramid geometry while a τ_5 value of 1.00 demonstrates an ideal trigonal bipyramid coordination environment. Through **Equation B.1**, defining α and β as the two largest valence angles about the metal center, a τ_5 value of 0.45 was calculated for complex **B1**, consistent with a distortion from both geometries. The calculated structural parameter is supported by the observed angles about the cobalt center which revealed S2–Co–P1, S2–Co–S1, and P–Co–N angles of 95.14°, 149.9°, and 177.0°, respectively with the remaining average valence angle of 89.63°. These angles demonstrate that the cobalt center is most accurately described as adopting a either a distorted square pyramid or trigonal bipyramid coordination geometry.

$$\tau_5 = \frac{\alpha - \beta}{60} \qquad \textbf{(B.1)}$$

The oxidation state assignments of the [SNS] ligand and cobalt center is of interest. The average Co–P bond distance observed for **B1** (2.21 Å) is consistent with Co^{II}–P bond distances falling within the range of 2.205−2.230 Å.[2–5] In contrast, Co^{I}–P bond distances are expected to be severely contracted to roughly 2.108–2.154 Å while Co^{III}–P bond distances have demonstrated to appear between 2.264–2.334 Å.[5–9] The P–Co–P bite angle (89.09°) is slightly larger, yet, still consistent with other Co(dppe) complexes in the literature which demonstrate bite angles ranging between 81.10° and 87.30°.[5,9] The Co–N bond distance of 1.92 Å was found consistent with Co^{III}–N bond distances that range between 1.86 and 1.98 Å.[7,10] Analogously, comparison to Co^{II}–N bond distances in the literature revealed a lengthening in this distance (1.98–2.22 Å).[11,12] Further analysis into the Co–S bond distances demonstrate an average length of 2.21 Å which is slightly contracted from known Co^{II}– and Co^{III}–S distances found to lie between 2.24–2.37 Å.[7,13,14] Based on the solid-state metrics, a Co^{II} versus Co^{III} center cannot explicitly be assigned, however, the

average C–S bond distance (1.75 Å) observed within the [SNS] scaffold appears most similar to the average C–S bond distances obtained in complexes **14** (1.75 Å) and **15** (1.74 Å) which have been shown in **Chapter 6** to be supported by the singly oxidized [SNS^{sq}•] form of the ligand.

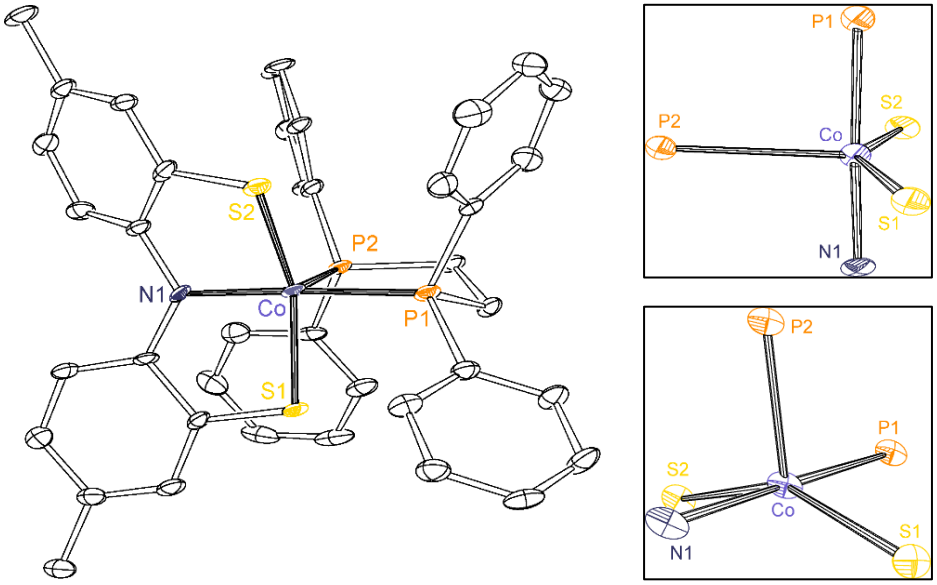

Figure B.1. ORTEP diagram for complex **B1** with thermal ellipsoids shown at 50% probability. Hydrogen atoms have been excluded for clarity. Insets shows the geometry about the cobalt center.

Table B.1. Selected bond lengths and bond angles for complex **B1**.

	[SNS]Co(dppe) (**B1**)
	Bond Lengths / Å
Co – P1	2.2109(16)
Co – P2	2.1766(16)
Co – S1	2.1954(14)
Co – S2	2.2173(15)
S1 – C2	1.747(5)
S2 – C9	1.758(6)
N1 – C1	1.396(7)
N1 – C8	1.410(7)
	Bond Angles / °
P1 – Co – P2	89.08(6)
N1 – Co – P(1)	177.00(14)
N1 – Co – S1	87.86(14)
N1 – Co – S2	86.74(14)
S2 – Co – P1	95.14(6)
S1 – Co – P1	89.35(6)
S1 – Co – S3	149.97(6)
τ_5 value	0.45

Spectroscopic Characterization

To further probe the structure of **B1**, electronic absorption spectroscopy and nuclear magnetic resonance (NMR) spectroscopy were utilized. Dissolution of **B1** in THF resulted in an intensely colored solution manifesting multiple absorbance bands within the visible region (729 (5030 $M^{-1}cm^{-1}$), 531 (4620 $M^{-1}cm^{-1}$), and 463 (3780 $M^{-1}cm^{-1}$)) indicative of charge transfer bands based on their extinction coefficients. Interestingly, complex **B1** demonstrates a low-energy transition at 729 nm (13700 cm^{-1}) which is red shifted by 1400 cm^{-1} from the previously discussed $[[SNS^{sq\bullet}]Ni(PPh_3)]_2$ (**14**, 661 nm (15100 cm^{-1})). The low-energy transition observed in **B1** is consistent with containing the singly oxidized, dianionic $[SNS^{sq\bullet}]^{2-}$ form of the ligand. Similarly, this band appears heavily dependent on the metal center, confirming this band as likely a metal to ligand charge transfer transition (MLCT, M→S).[15–17] Despite **B1** formally containing a Co^{II} center, the complex exhibits diamagnetic character with resonances in the alkyl and aryl regions of the spectrum consistent with the observed five-coordinate species. The equivalent methyl resonances of the [SNS] backbone are observed as a sharp singlet at 2.01 ppm while the methylene protons of the dppe ligand backbone are observed as a doublet at 2.87 ppm. The presence of the dppe ligand can be further established by $^{31}P\ \{^1H\}$ NMR, which revealed a sharp singlet at 79.2 ppm, concluding the solid-state structure of **B1** is maintained in solution. The spectroscopic data suggests that **B1** consists of a low spin Co^{II} ion (s = 1/2) supported by the singly oxidized, dianionic $[SNS^{sq\bullet}]^{2-}$ ligand, which allow for anti-ferromagnetic coupling between the unpaired electrons to yield the observed diamagnetic ground state.

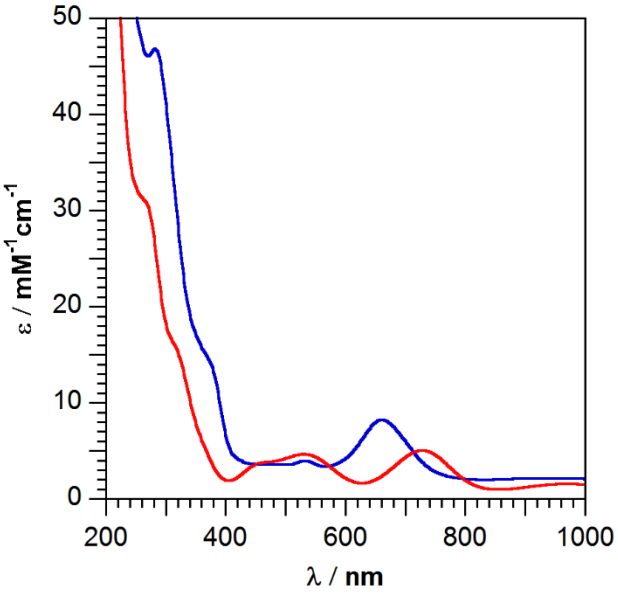

Figure B.2. Electronic absorption spectra of (red) [SNS]Co(dppe) (**B1**) collected in THF and (blue) $[[SNS^{sq}]Ni(PPh_3)]_2$ (**14**) collected in MeCN solution.

Electrochemistry

Cyclic voltammetry was performed on complex **B1** to reveal two reductive and two oxidative events in dry THF using 1 mM analyte and 0.3 M $[NBu_4][PF_6]$. The electrochemical data was referenced to $[Cp_2Fe]^{0/+}$ and is displayed in **Figure B.3** and **Table B.2**. Within the oxidative range, a reversible oxidative event at −0.13 V ($i_{pc}/i_{pa} \cong 1$) and an irreversible oxidative event at 0.64 V were observed. If the complex is best described as $[SNS^{sq\bullet}]Co^{II}$(dppe) it stands to reason that the first oxidative event may be attributed to the $Co^{II/III}$ redox couple, which happens to be consistent with previously reported cobalt complexes observed in the literature.[18–22] The 2nd oxidative process (irreversible) observed at 0.64 V may be further oxidation of the [SNS] ligand ($[SNS^{sq\bullet}]^{2-} \rightarrow [SNS^{q}]^{1-}$). The reductive region of the collected cyclic voltammograms, however, illustrate more ambiguity with a reversible event at −1.67 V and an irreversible event at −2.65 V. The first reductive event at −1.67 V appears to be consistent with two options: (i) a metal based reduction of Co^{II} to Co^{I} or (ii) a ligand based reduction of $[SNS^{sq\bullet}]^{2-}$ to $[SNS^{cat}]^{3-}$. To determine the source of the first reductive process the isolation and characterization of the singly reduced

form of the complex is needed. Monitoring the absorbance band at 729 nm via electronic absorption spectroscopy may offer evidence to support a ligand based reduction ([SNS^{sq}•]→[SNS^{cat}]) as previously observed in **Chapter 6** (**14/15→16/17**). Electron paramagnetic resonance (EPR) spectroscopy will also play a vital role in determining the location of the unpaired electron upon reduction.

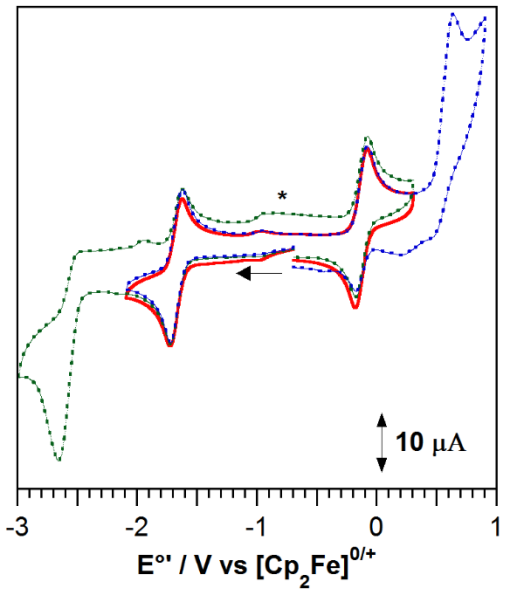

Figure B.3. Cyclic voltammogram for [SNS]Co(dppe) (**B1**). CV was recorded at a 1 mM analyte concentration in 0.3 M [NBu$_4$][PF$_6$] in dry, degassed THF under a nitrogen atmosphere using a 3 mm glassy carbon working electrode, Pt wire counter electrode, and a silver wire pseudo-reference electrode at room temperature at 200 mV sec^{-1} scan rates.

Table B.2. Electrochemical data for complex **B1** dissolved in a THF solution containing 0.3M [NBu$_4$][PF$_6$].

	E_1°′ [M]$^{2-/1-}$	E_2°′ [M]$^{1-/0}$	E_3°′ [M]$^{0/1+}$	E_4°′ [M]$^{1+/2+}$
[SNS]Co(dppe) (**B1**)	−2.65[a]	−1.67	−0.13	0.64[a]

[a]Irreversible event.

Conclusion

Two possible configurations for metal and ligand oxidation states can be made for complex **B1**. The first plausible oxidation state assignment would consist of a Co^{II} ion supported by a singly oxidized ligand ([SNS^{sq}•]). This configuration would allow for anti-ferromagnetic coupling to occur between a low-spin Co^{II} center and the ligand radical to form the observed diamagnetic

ground state. The second possible configuration is an oxidized cobalt center (Co^{III}) supported by a fully reduced $[SNS^{cat}]^{3-}$ ligand framework. Based on the limited characterization evidence described we favor the former assignment based on the observed low-energy electronic absorption band at 729 nm, however, further studies are needed to verify the exact electronic configuration of the complex. The electrochemistry is quite similar to that recorded for complexes **14-17** in **Chapter 6**. If the first reductive event at −1.67 V, vs $[Cp_2Fe]^{0/+}$, is found to correspond to a ligand based reduction then it demonstrates the metal center's ability to tune the first reductive event by roughly 1.0 V. Future studies will be performed to isolate the singly reduced and oxidized analogs to form a new family of cobalt complexes of the redox-active [SNS] ligand framework.

Experimental

General Considerations. The compound reported below is air- and moisture-stable and was synthesized under aerobic conditions. $CDCl_3$ was dried over CaH_2 and vacuum distilled prior to use. $[SNS]H_3$ was synthesized as previously described,[23] while triethylamine (sigma) and $Cl_2Co(dppe)$ (sigma) were used as received.

Spectroscopic Methods. NMR spectra were collected on a Bruker Avance 400 MHz spectrometer in dry, degassed $CDCl_3$. ^1H NMR spectra were referenced to TMS using the residual proteo impurities of the solvent (7.26 ppm for $CDCl_3$). All $^{31}P\{^1H\}$ NMR spectra were referenced with an external standard of phosphoric acid (H_3PO_4, 85%). Chemical shifts are reported using the standard δ notation in parts per million. Electrospray ionization mass-spectrometry (ESI-MS) data was collected on a Waters LCT Premier mass-spectrometer using CH_2Cl_2.

Electrochemical Methods. Electrochemical data were collected with a Gamry Series G 300 Potentiostat/Galvanostat/ZRA (Gamry Instruments, Warminster, PA, USA) using a 3.0 mm glassy carbon working electrode, a platinum wire auxiliary electrode, and a silver wire pseudo-reference

electrode. Electrochemical experiments were performed at 25°C in a glovebox under an atmosphere of N_2. Electrochemical samples were 1.0 mM analyte solutions in THF containing 0.3 M $[NBu_4][PF_6]$ as the supporting electrolyte. All potentials were referenced to the $[Cp_2Fe]^{0/+}$ couple using ferrocene or decamethylferrocene as an internal standard. Ferrocene and decamethylferrocene (Acros) were purified by sublimation under reduced pressure and tetra-*n*-butylammonium hexafluorophosphate (Acros) was recrystallized from ethanol three times and dried under vacuum.

Crystallographic Methods. X-ray diffraction data were collected on a single crystal mounted on a glass fiber using paratone oil. Data was acquired using a Bruker SMART APEX II diffractometer equipped with a CCD detector at 88 K using Mo Kα radiation (λ = 0.71073 Å), which was wavelength selected with a single-crystal graphite monochromator. The SMART program package was used to determine unit-cell parameters and for data collection. The raw frame data were processed using SAINT and SADABS to yield the reflection data file. Subsequent calculations were carried out using the SHELXTL program suite. The structure was solved by direct methods and refined on F^2 by full-matrix least-squares techniques. Analytical scattering factors for neutral atoms were used throughout the analyses. Hydrogen atoms were generated in calculated positions and refined using a riding model. ORTEP diagrams were generated using *ORTEP-3* for Windows.

Table B.3. X-ray data collection and refinement parameters for complex **B1**.

	[SNS]Co(dppe) (**B1**)
empirical formula	$C_{40}H_{36}NCoP_2S_2$
formula weight [g/mol]	715.69
crystal system	Orthorhombic
space group	$P2_12_12_1$
T [K]	88(2) K
a [Å]	10.268(2)
b [Å]	14.622(3)
c [Å]	22.608(5)
α [deg]	90
β [deg]	90
γ [deg]	90
V [Å^3]	3394.5(13)
Z	4
refl collected	30685
data/restr/param	6925/0/417
R_1 [$I > 2\sigma(I)$][a]	0.0562
wR_2(all data)[a]	0.1462
GOF[a]	1.098

[a] $R_1 = \Sigma||F_o|-|F_c|| / \Sigma|F_o|$, $wR_2 = [\Sigma[w(F_o^2-F_c^2)^2] / \Sigma[w(F_o^2)^2]\ ]^{1/2}$, $GOF = S = [\Sigma[w(F_o^2-F_c^2)^2] / (n-p)]^{1/2}$

[SNS]Co(dppe) (B1). A suspension of $Cl_2Co(dppe)$ (200 mg, 0.380 mmol, 1.00 equiv.) in 15 mL dry toluene was kept under an N_2 atmosphere in a 100 mL Schlenk flask. A solution of $[SNS]H_3$ (101 mg, 0.388 mmol, 1.00 equiv.) in 5 mL toluene was added to the reaction vessel. No immediate color change was observed. Excess Et_3N (200 µL, 1.43 mmol, 3.70 equiv.) was added in air to transform the dark green solution to a dark purple solution. Reaction mixture was stirred for two hours in air. The volatiles were then removed to concentrate the solution to roughly 5 mL. A solid was crashed from solution using 50 mL of pentane (in air). The solid was collected using a Buchner funnel, washed with water (2 x 30 mL) to remove Et_3NHCl, and pentane (3 x 10 mL). The solid was collected and dried under vacuum to yield a purple powder in 98% yield (268 mg). X-ray quality crystals were obtained by diffusion of pentane into a THF solution of the complex at ambient temperature in air, black/purple crystals obtained. ^{1}H NMR (400 MHz, $CDCl_3$) δ /

ppm: 8.37 (d, *J* = 8.02 Hz, 2H, aryl-H), 7.68 (br.s., 2H, aryl-H), 7.50 (br.s., 2H, aryl-H), 7.13 (m, 20H, aryl-H), 2.87 (d, *J* = 13.89 Hz, 4H, -CH_2), 2.01 (s, 6H, -CH_3). ^{31}P {^1H}-NMR (162 MHz, $CDCl_3$) δ / ppm: 79.2. UV-vis (THF) λ_{max} / nm (ε / M^{-1} cm^{-1}): 463 (3780 $M^{-1}cm^{-1}$), 531 (4620 M^{-1} cm^{-1}), 729 (5030 M^{-1} cm^{-1}). MS (ESI+) (CH_2Cl_2) *m/z*: 715.05 $(M)^+$.

References

(1) Addison, A. W.; Rao, T. N. *Dalton Trans.* **1984**, 1349–1356.
(2) Bertrand, J. A.; Plymale, D. L. *Inorg. Chem.* **1966**, *5*, 879–884.
(3) Falvello, L.; Gerloch, M. *Acta Cryst.* **1979**, *B35*, 2547–2550.
(4) Fryzuk, M. D.; Leznoff, D. B.; Thompson, R. C.; Rettig, S. J. *J. Am. Chem. Soc.* **1998**, *120*, 10126–10135.
(5) Kiefer, G.; Vrubel, H.; Scopelliti, R.; Severin, K. *Eur. J. Inorg. Chem.* **2013**, *2013*, 4916–4921.
(6) Levason, W.; Ogden, J. S.; Spicer, M. D. *Inorg. Chem.* **1989**, *28*, 2128–2131.
(7) Chen, Z.-N.; Zhang, H.-X.; Kang, B.-S.; Sun, J. *Synth. React. Inorg. Met. Chem.* **1998**, *28*, 245–261.
(8) Suzuki*, T.; Kaizaki*, S.; Kashiwabara, K. *Inorganica Chim. Acta* **2000**, *298*, 131–140.
(9) Nagasawa, T.; Nagata, T. *Biochim. Biophys. Acta - Bioenerg.* **2007**, *1767*, 666–670.
(10) Bill, E.; Bothe, E.; Chaudhuri, P.; Chlopek, K.; Herebian, D.; Kokatam, S.; Ray, K.; Weyhermüller, T.; Neese, F.; Wieghardt, K. *Chem. – A Eur. J.* **2005**, *11*, 204–224.
(11) Li, J.; Noll, B. C.; Oliver, A. G.; Ferraudi, G.; Lappin, A. G.; Scheidt, W. R. *Inorg. Chem.* **2010**, *49*, 2398–2406.
(12) Summers, J. S.; Petersen, J. L.; Stolzenberg, A. M. *J. Am. Chem. Soc.* **1994**, *116*, 7189–7195.
(13) Setzer, W. N.; Ogle, C. A.; Wilson, G. S.; Glass, R. S. *Inorg. Chem.* **1983**, *22*, 266–271.
(14) Halder, P.; Paine, T. K. *Indian J. Chem.* **2011**, *50A*, 1394–1402.
(15) Lum, V.; Gray, H. B. *Isr. J. Chem.* **1981**, *21*, 23–25.
(16) Yu, Q.; Ge, J.-Y.; Lv, Z.-P.; Wang, H.-Y.; Zuo, J.-L. *RSC Adv.* **2016**, *6*, 100783–100789.
(17) Schrauzer, G. N.; Mayweg, V. P. *J. Am. Chem. Soc.* **1965**, *87*, 1483–1489.
(18) Cibian, M.; Derossi, S.; Hanan, G. S. *Dalt. Trans.* **2011**, *40*, 1038–1040.
(19) Cameron, P. J.; Peter, L. M.; Zakeeruddin, S. M.; Grätzel, M. *Coord. Chem. Rev.* **2004**, *248*, 1447–1453.
(20) D'Souza, F.; Villard, A.; Van Caemelbecke, E.; Franzen, M.; Boschi, T.; Tagliatesta, P.; Kadish, K. M. *Inorg. Chem.* **1993**, *32*, 4042–4048.
(21) Vasilevskis, J.; Olson, D. C. *Inorg. Chem.* **1971**, *10*, 1228–1235.
(22) Roy, S.; Sharma, B.; Pécaut, J.; Simon, P.; Fontecave, M.; Tran, P. D.; Derat, E.; Artero, V. *J. Am. Chem. Soc.* **2017**.
(23) Shaffer, D. W.; Szigethy, G.; Ziller, J. W.; Heyduk, A. F. *Inorg. Chem.* **2013**, *52*, 2110–2118.

Appendix C

Synthesis and Characterization of a Trimetallic $W[SNS]_2[Ni(dppe)]_2$ Species

Introduction

Formation of trimetallic complexes have long been investigated to explore mixed valence chemistry. The ability to utilize the $W[SNS]_2$ coordination complex as a redox-active metalloligand lead to the isolation of the heterobimetallic nickel complexes discussed in **Chapters 2** and **3**. These complexes revealed bimetallic complexes with accessible reduction potentials between −1.0 and −2.5 V, vs $[Cp_2Fe]^{0/+}$, which could be leveraged to generate the novel heterotrimetallic complex. The ability to append two nickel centers to this system would allow for the exploration into the ability to isolate a mixed valence complex through oxidation of a single nickel center.

Results and Discussion

Synthesis and Structural Characterization

A heterotrimetallic complex (**C1**) was isolated through a similar synthetic strategy outlined for heterobimetallic complexes **1-13**, whereby reduction of $W[SNS]_2Ni(dppe)$ (**1**) using two equivalents of KC_8 was followed by the addition of an equivalent of $Cl_2Ni(dppe)$ to result in the isolation of $W[SNS]_2[Ni(dppe)]_2$ (**C1**) (**Scheme C.1**). ESI-MS data confirmed the formation of the desired trimetallic complex with a parent ion signal at a *m/z* value of 1614.3 $(M)^+$. Single crystals of complex **C1** were obtained by slow diffusion of pentane into a saturated THF solution of the complex at room temperature.

Scheme C.1. Synthesis of the heterotrimetallic complex **C1**.

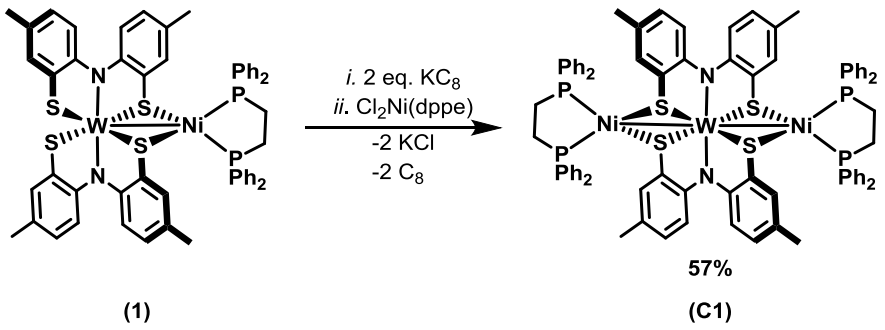

X-ray diffraction studies on single crystals of **C1** revealed a $W[SNS]_2$ center bridging two Ni(dppe) fragments. **Figure C.1** shows the structure of $W[SNS]_2[Ni(dppe)]_2$ as an ORTEP diagram and a table of bond lengths and angles are provided in **Table C.1**. The average P−Ni−P angle of 90.79° is consistent with the constricted bite angle of the dppe ligand.[1–3] The average Ni−P distance of 2.199 Å is slightly contracted from bimetallic **1**, yet, longer than those typically observed for nickel(II) complexes of the dppe ligand.[4–7] In contrast, the average Ni−S bond distance of 2.190 Å is equivalent to bimetallic **1**, however, shorter than those of nickel(II) complexes containing bridging thiolate ligands.[5–7] Within the $W[SNS]_2$ cofactor, the W−S distances range from 2.399(7) to 2.413(7) Å, which are similar to the average W−S distance of 2.367 Å in the neutral, isolated $W[SNS]_2$ complex and $W[SNS]_2Ni(dppe)$ (**1**, 2.401 Å).[8] The average W−N distance of 2.110 Å in the trimetallic complex is slightly elongated compared to the W−N distance observed for the $W[SNS]_2$ monomer (2.072 Å) and bimetallic **1** (2.091 Å). Finally, the average W−Ni distance of 2.647(4) Å falls within the sum of the covalent radii of these two metal ions (tungsten, 1.62 Å; nickel, 1.24 Å)[9] consistent with the formation of metal−metal bonds which are slightly elongated from the observed W–Ni bond in bimetallic **1** (2.536(3) Å).

Both nickel centers adopt a pseudo-tetrahedral geometry (disregarding the metal–metal bond). Calculation of the angular structural parameters for four-coordinate species (τ_4) revealed a value of 0.87 for both nickel centers. Angles about the nickel centers reveal valence angles ranging from 90.62° to 121.3°, supporting the calculated τ_4 values and illustrating that each nickel center adopts a pseudo-tetrahedral coordination geometry.

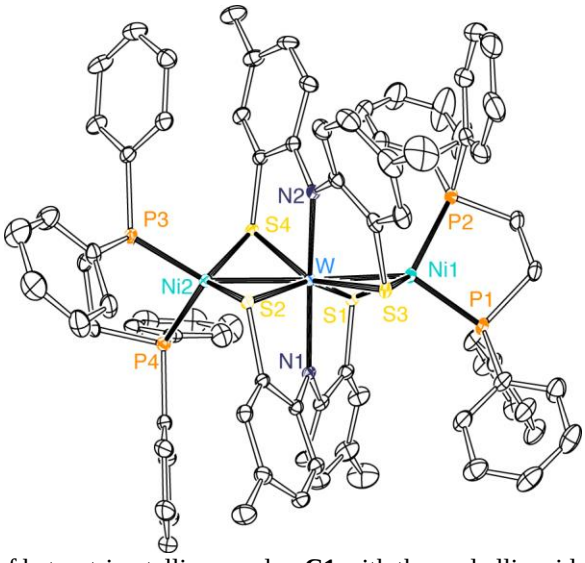

Figure C.1. ORTEP diagram of heterotrimetallic complex **C1** with thermal ellipsoids at 50% probability. Hydrogen atoms and a pentane molecule has been omitted for clarity.

Table C.1. Selected bond lengths and bond angles for complex **C1**.

	$W[SNS]_2[Ni(dppe)]_2$ (**C1**)
	Bond Lengths / Å
W – Ni1	2.6491(4)
W – Ni2	2.6443(4)
W – N1	2.114(2)
W – N2	2.106(2)
W – S1	2.3996(7)
W – S2	2.4127(7)
W – S3	2.4063(7)
W – S4	2.4044(7)
Ni1 – P1	2.1848(9)
Ni1 – P2	2.2161(8)
Ni2 – P3	2.1866(9)
Ni2 – P4	2.2074(9)
Ni1 – S1	2.1787(8)
Ni1 – S3	2.2015(8)
Ni2 – S2	2.2071(8)
Ni2 – S4	2.1744(8)
	Bond Angles / deg
S1 – W – S3	99.10(2)
S2 – W – S4	99.40(3)
P1 – Ni1 – P2	90.62(3)
P3 – Ni2 – P4	90.96(3)
S1 – Ni1 – S3	113.21(3)
S2 – Ni2 – S4	113.96(3)
τ_4 value (average)	0.87

While the isolated $W[SNS]_2$ complex shows bond angles that fall between those expected for trigonal-antiprismatic (i.e. octahedral) and trigonal-prismatic geometries, in the trimetallic complex, the $W[SNS]_2$ unit displays bond angles more consistent with a distorted trigonal antiprism. The primary measurements of trigonal prismatic versus trigonal antiprismatic geometry is defined by the twist angle (θ) between opposite trigonal faces (**Chapter 2**, **Figure 2.3**, page 22). In **C1**, two trigonal planes can be defined by the nitrogen and a single sulfur atom from one [SNS] ligand and a single sulfur from the other ligand (N(1)–S(1)–S(4) and N(2)–S(2)–S(3)). The twist angle is then defined as the torsion angle between the vertices of the trigonal planes and the centroids of those planes.[8,10] A second metrical parameter used for determining the degree of distortion for trigonal systems is the prismatic compression, defined as the ratio of the prism height (h) to the average length of the trigonal face (s). An ideal trigonal prism demonstrates a twist angle, (θ) of 0° with an s/h ratio of 1.00 while an ideal trigonal antiprism has a twist angle of 60° and a prismatic compression (s/h) of 1.22.[10] **Table C.2** displays the values calculated based off the twist angles and the observed prismatic compression. Complex **C1** displays a distorted anti-prismatic geometry with an average twist angle > 34°. These large deviations in the twist angles are consistent with the observed prismatic compression (s/h) ratio of 1.18 confirming a distortion from ideal trigonal-antiprismatic geometry.

Table C.2. Additional measured and calculated parameters for complex **C1** as defined in **Chapter 2**, **Figure 2.3**.

	$W[SNS]_2Ni(dppe)$ (**1**)	$W[SNS]_2[Ni(dppe)]_2$ (**C1**)
$\theta_{S4,N2}$	40.3°	42.41°
$\theta_{S1,S3}$	13.1°	18.18°
$\theta_{N1,S2}$	35.8°	42.44°
s/h	1.16	1.18

Spectroscopic Characterization

To further investigate the structure of **C1**, electronic absorption spectroscopy (UV-vis) and nuclear magnetic resonance spectroscopy (NMR) were utilized. Dissolution of **C1** in THF

afforded a dark solution manifesting three intense absorbance band in the visible region at 424 (27,000 $M^{-1}cm^{-1}$), 526 (11,000 $M^{-1}cm^{-1}$) and 778 (4,300 $M^{-1}cm^{-1}$) nm which are consistent with charge transfer transitions based on their extinction coefficients (**Figure C.2**). A blue shift is observed from bimetallic **1** to trimetallic **C1** from 436 nm (23000 cm^{-1}) to 424 nm (23600 cm^{-1}), respectively. The highly reducing nature of **C1** resulted in sample decomposition in $CDCl_3$ to reform complex **1** *in situ*., therefore NMRs were conducted in a solution of THF-d_8. The presence of the Ni(dppe) fragments were readily established by $^{31}P\{^1H\}$ NMR, which revealed a sharp singlet at 38.7 ppm, shifted upfield from bimetallic **1** (49.0 ppm). The characteristic proton resonances of the $W[SNS]_2$ fragment could be readily observed in the ^1H NMR spectrum through an observed sharp singlet resonance at 1.97 ppm, consistent with increased symmetry compared to bimetallic **1**. The methylene protons of the dppe ligand backbones appear as two multiplets at 2.61 and 2.30 ppm.

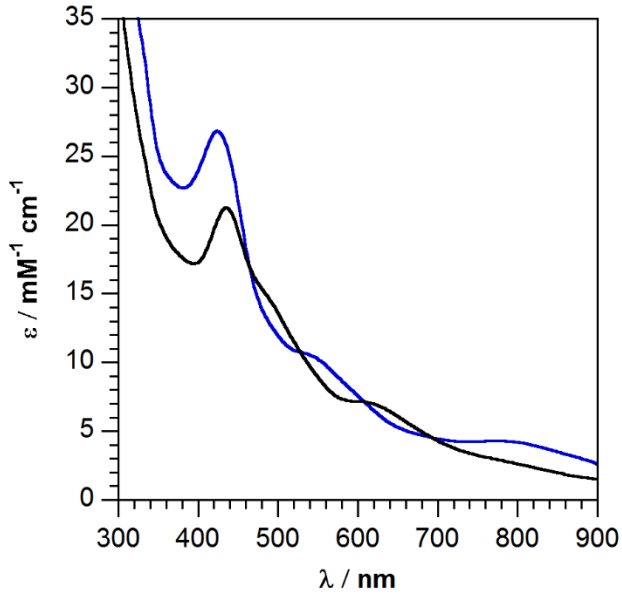

Figure C.2. Electronic absorption spectra for $W[SNS]_2[Ni(dppe)]_2$ (**C1**, blue) and $W[SNS]_2Ni(dppe)$ (**1**, black) in THF solutions.

Electrochemistry

Electrochemical analysis performed on **C1** in THF displayed rich electrochemistry with five redox processes observed. **Figure C.3** shows the cyclic voltammograms for complexes **1** and **C1** in a solution of THF containing 0.3 M $[Bu_4N][PF_6]$ as the supporting electrolyte. All potentials were referenced to $[Cp_2Fe]^{+/0}$ using an internal standard. **C1** revealed two reversible reductive events at −2.46 and −2.07 V, two reversible oxidative events at −0.70 and −0.48 V, and one quasi-reversible oxidative event at 0.28 V. The two reductive events are separated by 390 mV while the first two oxidative events are separated by 220 mV. The reductive events, $E_1°'$ and $E_2°'$, are shifted cathodically from bimetallic **1** by 320 mV and 640 mV, respectively, while the oxidative processes, $E_3°'$ and $E_4°'$, are shifted cathodically by 380 mV and 530 mV, respectively. Previously (**Chapter 2** and **3**) a trend was observed within the first oxidative process for heterobimetallic complexes **1-10** with which the appendage of $Ni(P^{R2}R'P^{R2})$ fragments tuned the redox potential of $E_3°'$. Based on previous results with the heterobimetallic systems, a similar effect appears to be observed upon the appendage of a second nickel center. In this case, the first two oxidative processes appear to correspond to nickel based oxidations ($Ni^{I/II}$ couples). Similarly, the reductive processes appear attributed to the tungsten metalloligand.

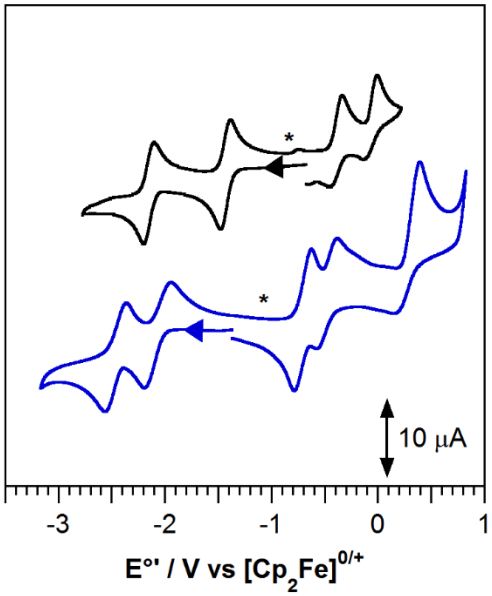

Figure C.3. Cyclic voltammograms for $W[SNS]_2[Ni(dppe)]_2$ (**C1**, blue) and $W[SNS]_2Ni(dppe)$ (**1**, black). All CVs were recorded at a 1 mM analyte concentration in 0.3 M $[NBu_4][PF_6]$ in dry, degassed THF under a nitrogen atmosphere using a 3 mm glassy carbon working electrode, a Pt wire counter electrode, and a silver wire pseudo-reference electrode at room temperature with 50 mV sec^{-1} scan rates.

Table C.3. Electrochemical potentials (V) for complexes **1** and **C1** in THF at 50 mV sec^{-1} scan rates.

	$E_1°'$ $[M]^{2-/1-}$	$E_2°'$ $[M]^{1-/0}$	$E_3°'$ $[M]^{0/1+}$	$E_4°'$ $[M]^{1+/2+}$	$E_5°'$ $[M]^{2+/3+}$
$W[SNS]_2Ni(dppe)$ (**1**, black)	−2.14	−1.43	−0.32	0.05	–
$W[SNS]_2[Ni(dppe)]_2$ (**C1**, blue)	−2.46	−2.07	−0.70	−0.48	0.28

Conclusion

A plausible metal oxidation state assignment for the trimetallic $W[SNS]_2[Ni(dppe)]_2$ (**C1**) would comprise a tungsten(IV) and two nickel(I) centers, with the unpaired electrons on each nickel center pairing with the two unpaired electrons of the tungsten metalloligand. This configuration would support the observed metal–metal bonds in addition to the diamagnetic ground state. The appendage of the second nickel center imbues the complex with interesting properties (electronic and electrochemical) and may offer a new platform to study mixed valence chemistry.

Experimental

General Considerations. The compound and manipulations reported below show various levels of air- and moisture-sensitivity, therefore all manipulations were carried out using standard vacuum-line, Schlenk-line and glovebox techniques unless otherwise noted. Hydrocarbon and ethereal solvents were sparged with argon before being deoxygenated and dried by passage through Q5 and activated alumina columns, respectively. Halogenated solvents were sparged with argon and dried by passage through two activated alumina columns. To test for effective oxygen and water removal, aliquots of each solvent were treated with a few drops of a purple solution of sodium benzophenone ketyl radical in THF. THF-d_8 was dried over NaK and benzophenone and vacuum distilled prior to use. The ligands $[SNS^{cat}]H_3$[8] in addition to complexes $W[SNS]_2$[8], $W[SNS]_2Ni(dppe)$ and $Cl_2Ni(dppe)$[4] were all prepared according to the previously reported procedures.

Spectroscopic Methods. Elemental analysis was conducted on a Perkin-Elmer 2400 Series II CHNS elemental analyzer. NMR spectra were collected on a Bruker Avance 400 MHz spectrometer in dry, degassed THF-d_8. ^{1}H NMR spectra were referenced to TMS using the residual proteo impurities of the solvent (3.58 ppm for THF-d_8). All $^{31}P\{^1H\}$ NMR spectra were referenced with an external standard of phosphoric acid (H_3PO_4, 85%). Chemical shifts are reported using the standard δ notation in parts per million. Electronic absorption spectra were recorded with a Perkin-Elmer Lambda 900 UV-vis spectrophotometer as solutions in dry, degassed THF contained in 1-cm quartz cells. Electrospray ionization mass spectrometry (ESI-MS) data was collected on a Waters LCT Premier mass spectrometer using dry, degassed CH_2Cl_2.

Electrochemical Methods. Electrochemical data were collected with a Gamry Series G 300 Potentiostat/Galvanostat/ZRA (Gamry Instruments, Warminster, PA, USA) using a 3.0 mm glassy

carbon working electrode, a platinum wire auxiliary electrode, and a silver wire pseudo-reference electrode. Electrochemical experiments were performed at 25°C in a glovebox under an atmosphere of N_2. Electrochemical samples were 1.0 mM analyte solutions in THF containing 0.3 M $[NBu_4][PF_6]$ as the supporting electrolyte. All potentials were referenced to the $[FeCp_2]^{0/+}$ couple using ferrocene or decamethylferrocene as an internal standard. Ferrocene and decamethylferrocene (Acros) were purified by sublimation under reduced pressure and tetra-*n*-butylammonium hexafluorophosphate (Acros) was recrystallized from ethanol three times and dried under vacuum.

Crystallographic Methods. X-ray diffraction data were collected on a single crystal mounted on a glass fiber using paratone oil. Data was acquired using a Bruker SMART APEX II diffractometer equipped with a CCD detector at 88 K using Mo Kα radiation (λ = 0.71073 Å), which was wavelength selected with a single-crystal graphite monochromator. The SMART program package was used to determine unit-cell parameters and for data collection. The raw frame data were processed using SAINT and SADABS to yield the reflection data file. Subsequent calculations were carried out using the SHELXTL program suite. The structures were solved by direct methods and refined on F^2 by full-matrix least-squares techniques. Analytical scattering factors for neutral atoms were used throughout the analyses. Hydrogen atoms were generated in calculated positions and refined using a riding model. ORTEP diagrams were generated using *ORTEP-3* for Windows.

Table C.4. X-ray data collection and refinement parameters for complex **C1**.

	$W[SNS]_2[Ni(dppe)]_2$ (**C1**)
empirical formula	$C_{80}H_{72}N_2Ni_2P_4S_4W \bullet C_5H_{12}$
formula weight [g/mol]	1686.93
crystal system	Triclinic
space group	*P*1bar
T [K]	88(2) K
a [Å]	14.7767(11)
b [Å]	16.5913(13)
c [Å]	16.8344(13)
α [deg]	84.3961(10)
β [deg]	75.6462(10)
γ [deg]	82.5314(10)
V [$Å^3$]	3955.2(5)
Z	2
refl collected	18811
data/restr/param	18811/0/890
R_1 [$I > 2\sigma(I)$][a]	0.0236
wR_2(all data)[a]	0.0686
GOF[a]	1.098

[a] $R_1 = \Sigma||F_o|-|F_c|| / \Sigma|F_o|$, $wR_2 = [\Sigma[w(F_o^2-F_c^2)^2] / \Sigma[w(F_o^2)^2]\ ]^{1/2}$, $GOF = S = [\Sigma[w(F_o^2-F_c^2)^2] / (n-p)]^{1/2}$

$W[SNS]_2[Ni(dppe)]_2$ (C1). To a 100 mL Schlenk flask, potassium metal (23 mg, 0.59 mmol, 1.9 equiv.) and graphite (60 mg, 0.63 mmol, 2.0 equiv.) were heated with a heat gun to form two equiv. of KC_8 as a bronze powder. The flask was charged with 20 mL of dry THF and frozen in a liquid nitrogen cold well. Upon thawing, $W[SNS]_2Ni(dppe)$ (**1**) (328 mg, 0.283 mmol, 0.986 equiv.) was added to the stirring solution to generate $K_2W[SNS]_2Ni(dppe)$ *in situ.* as a dark maroon solution with a red hue around the rim. After 10 minutes, $Cl_2Ni(dppe)$ (151 mg, 0.287 mmol, 1.01 equiv.) was added to the solution and stirred at room temperature for one hour. The reaction mixture was filtered through celite on a fritted glass filter to remove graphite and KCl to yield an orange/brown filtrate. The filtrate was concentrated to roughly 10 mL and a solid was crashed out of solution using Et_2O. The solid was collected using a glass frit and washed with pentane (2 x 10 mL) followed by Et_2O (2 x 20 mL). The trimetallic complex was collected as a dark blue powder (260 mg, 57%). X-ray quality crystals were obtained by diffusion of pentane into a THF solution of the

complex at ambient temperature, black crystals were obtained. Anal. Calc. $WS_4N_2Ni_2P_4C_{80}H_{72}$: C, 59.61; H, 4.50; N, 1.74%. Found: C, 60.00; H, 4.55; N, 1.74%. ^{1}H NMR (400 MHz, THF-d_8) δ ppm: 7.14 (m, 20H, aryl-H), 6.99 (m, 4H, aryl-H), 6.85 (m, 16H, aryl-H), 6.63 (s, 4H, aryl-H), 6.45 (d, J = 8.61 Hz, 4H, aryl-H), 6.13 (d, J = 8.41 Hz, 4H, aryl-H), 2.61 (m, 4H, -CH_2), 2.30 (m, 4H, -CH_2), 1.97 (s, 12H, -CH_3). ^{31}P {^{1}H}-NMR (162 MHz, THF-d_8) δ / ppm: 38.7 (s). UV-Vis (THF) λ_{max} / nm (ε / M^{-1} cm^{-1}): 424 (27500), 526 (11000), 778 (4300). MS (ESI+) (THF) *m/z*: 1614.3 $(M)^+$.

References

(1) Pasynskii, A. A.; Skabitskii, I. V; Karpacheva, M. V. *Russ. J. Coord. Chem.* **2013**, *39*, 229–233.
(2) Busby, R.; Hursthouse, M. B.; Jarrett, P. S.; Lehmann, C. W.; Malik, K. M. A.; Phillips, C. *J. Chem. Soc. Dalt. Trans.* **1993**, 3767–3770.
(3) Gan, L.; Groy, T. L.; Tarakeshwar, P.; Mazinani, S. K. S.; Shearer, J.; Mujica, V.; Jones, A. K. *J. Am. Chem. Soc.* **2015**, *137*, 1109–1115.
(4) Busby, R.; Hursthouse, M. B.; Jarrett, P. S.; Lehrnann, C. W.; Malik, K. M. A.; Phillips, C. *J. Am. Chem. Soc. Dalt. Trans* **1993**, 3767–3770.
(5) Carroll, M. E.; Barton, B. E.; Gray, D. L.; Mack, A. E.; Rauchfuss, T. B. *Inorg. Chem.* **2011**, *50*, 9554–9563.
(6) Redin, K.; Wilson, A. D.; Newell, R.; DuBois, M. R.; DuBois, D. L. *Inorg. Chem.* **2007**, *46*, 1268–1276.
(7) Schilter, D.; Rauchfuss, T. B.; Stein, M. *Inorg. Chem.* **2012**, *51*, 8931–8941.
(8) Shaffer, D. W.; Szigethy, G.; Ziller, J. W.; Heyduk, A. F. *Inorg. Chem.* **2013**, *52*, 2110–2118.
(9) Cordero, B.; Gómez, V.; Platero-Prats, A. E.; Revés, M.; Echeverría, J.; Cremades, E.; Barragán, F.; Alvarez, S. *Dalton Trans.* **2008**, 2832–2838.
(10) Stiefel, E. I.; Brown, G. F. *Inorg. Chem.* **1972**, *11*, 434–436.